On-Chip Characterisation and Treatment of Oral Biofilms Using Raman Spectroscopy and Microbubbles

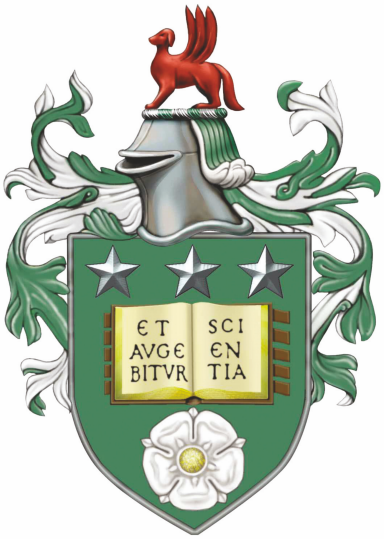

Aileen Marie Delaney

School of Physics and Astronomy

The University of Leeds

Submitted in accordance with the requirements for the degree of Doctor of Philosophy

2024

Declaration

The candidate confirms that the work submitted is their own, except where work which has formed part of jointly authored publications has been included. The contribution of the candidate and the other authors to this work has been explicitly indicated below. The candidate confirms that appropriate credit has been given within the thesis where reference has been made to the work of others. This copy has been supplied on the understanding that it is copyright material and that no quotation from the thesis may be published without proper acknowledgement.

To all the girls who think they can't do it.
And most of all to Me. I did this.

"You can never be overdressed or overeducated" - Oscar Wilde

Acknowledgements

First and foremost, I'd like to thank Professor Stephen Evans for your support and guidance throughout this whole PhD. Thank you for endlessly meeting with me when I had no idea what I was doing, and for also spending most of those meetings gossiping with me. I may not be your best student, but I hope I'm your favourite. Thank you to Dr Jonathan Vernon for teaching me all I know about microbiology, answering my endless questions, and stepping up to become my supervisor. I really valued your supervision, any future students of yours will be very lucky. Dr David Head, thank you for continuously providing feedback and support despite there now being no computing aspect in this thesis, I really appreciate it. Prof Deirdre Devine, thank you too for your support, you left me in safe hands.

Special thanks Prof Julian Moger and Dr Jessica Mansfield at the University of Exeter for use of their facility and help with SRS. Thanks to Julia for starting this project, teaching me about Raman, and providing the analysis code for this thesis. To MNP, my family that made this whole experience so much better. To Jordan, for showing me all I know about biofilms, being there to answer all of my questions, and generally being the mostly lovely supportive friend. Damien, there's no one else I would've wanted to sit behind me. Thank you for just generally helping me with all science and not thinking I'm stupid, and having endless tea (and pub) breaks with me. Please never stop sending me pictures of pints. Ash, you've made this whole process a lot easier, thank you for being the best. Your support, encouragement and thirst for pints is truly unmatched. Fern, there is no one else I would rather gossip with for 12 hours, it means the world to me, and Meghan, you deserve a medal for listening to us talk science for this long, thank you both for always being there and getting me through this.

To my desk buddy Christa, I miss staring at your face every day. Thanks for being so kind and supportive, and of course, drinking pints. Joe, we survived this together, what a team we are. Alisha, thanks for the entertainment, it's been wild. To Joel, well, yeah. Holly, Kalila, Matt B, Min, Amir, thank you for making my time in MNP (and outside) way more fun. Fiona, George, Joe, Becca, Sam, you know you're the best, what would I do without you. Alex and Dan, we came all this way, look at us go, love you. Owsh, living with you was the best 3 years, thank you for everything. Nina, you are a spark of joy, never change. To my favourite neighbour Betty, my time on Woodside Terrace was nothing without you.

Rach, Phoebe, and Becki, we met through SARSVL helpline and now you're in my life forever. Your friendship means the world to me. To my best friend Chelsea, and Kingsley of course, long distance is hard but you're worth it. Your support and voice notes are all I need, love you. To all in Cliterature Club, my legacy. You're welcome. To Greg James, Tom, Chris and everyone else at Radio 1, it's absolutely mad but you've made the last few years of my life so fun. Thanks for the nonsense and giving me confidence to lean into the creative - God help what you've done. To everyone else who has sent me support and lovely comments, it's madness thank you. The Fenton, the most special place. You hold a corner of my heart. Thank you to everyone mentioned, and anyone I have forgotten, who has spent *hours* in the pub with me. They're my favourite memories.

To my family. Mom, Dad, Shaun, Grace, Ciaran, Nuala, Olivia and Liam, and

everyone else. You may never understand this PhD, but your support along the way has meant everything. I can only apologise for all my stress induced mood swings, but thank you for understanding anyway. I love you. The last 5 years hasn't been easy, one day I may romanticise this experience or even learn to feel proud, but I know for a fact without everyone mentioned it would have been a lot worse. I love you all and surely it only gets better from here.

Abstract

Biofilms are communities of microbes encased in an extracellular matrix that protects them from harsh environments, external stresses, and antibiotics. Oral biofilms form on the hard tooth surfaces in the oral cavity and are commonly known as 'dental plaque'. If left untreated, pathogenic oral biofilms can lead to periodontal disease which is considered a global public health concern affecting over 1 billion people worldwide. Better understanding of how oral biofilms interact, grow and develop will enable preventative methods to be put in place before disease develops, or allow for informed treatment options to be put in place. Alternative treatment options to antibiotics are being sought after as antimicrobial resistance is on the rise, exacerbated by misuse and over consumption. This thesis explores using microfluidics as a method for growing *Streptococcus salivarius* and *Actinomyces naeslundii* 2-species biofilms, Raman spectroscopy (RS) for analysis, and microbubbles, ultrasound, and a synthetic antimicrobial peptide (IK8) for biofilm treatment. Combining microfluidics and RS allowed for non-destructive, label free, real time analysis of 2-species oral biofilms over the course of 5 days. Principle component analysis was able to differentiate between both planktonic species, and linear discriminant analysis was able to show how biofilms on Day 3 and 5 are similar, yet distinct from Day 1 due to the increased matrix contributions. Day 1 2-species biofilms were also most similar to *S.salivarius* biofilms at this stage. Spontaneous RS had spatial and resolution limitations, therefore Stimulated Raman Spectroscopy (SRS) was used as an alternative, providing high resolution hyperspectral SRS images and z-stacks of the high wavenumber region (2700 - 3100 cm^{-1}), as well as two-photon fluorescence (TPF) z-stacks. The CH_3 protein peak at 2937 cm^{-1} was found to be associated with bacteria cells, while CH_2 lipid/protein peaks at 2850, 2881 and 2905 cm^{-1} were predominantly matrix related. TPF detected the autofluorescence of flavins in the bacterial cells, acting as a marker to locate bacteria within the biofilm, something the SRS was not able to pick up on. IK8 was shown to work against both oral species of bacteria, and when free IK8 was combined with MBs and US there was a 68% reduction in 2-species biofilm cell density recorded. Optimisation of the treatment process is required to achieve the 3-log reduction required to be considered bactericidal.

Contents

List of abbreviations

AMP	Antimicrobial peptide
BHI	Brain Heart Infusion broth
CLSM	Confocal laser scaning microscopy
Diyne-PC	1,2-bis(10,12-tricosadiynoyl)-sn-glycero-3- phosphocholine
DLS	Dynamic light scattering
DNA	Deoxyribonucleic acid
DPPC	1,2-dipalmitoyl-sn-glycero-3phosphocholine
DSPC	1,2-distearoyl-sn-glycero-3-phosphocholine
DSPE-PEG_{2000}	1,2-distearoyl-sn-glycero-3-phosphoethanolamine-N-[methoxy(polyethyleneglycol)-2000]
DWL	Direct-write laser system
FAD	Flavin adenine dinucleotide
FISH	Fluorescence *in situ* hybridisation
FR	Fermi resonance
HB-CBA	Horse blood Columbia blood agar
HPLC	High performance liquid chromatography
IPA	Isopropanol
LDA	Linear discriminant analysis
LMBUS	Liposomes + microbubbles + ultrasound
MBs	Microbubbles
MBUS	Microbubbles + ultrasound
MBC	Minimum Bactericidal Concentration
MIC	Minimum inhibitory Concentration

MilliQ	18 MΩ ultrapure water
PBS	Phosphate-buffered saline
PI	Propidium iodide
PC	Principle component
PCA	Principle component analysis
PDMS	Polydimethylsiloxane
Re	Reynolds number
RS	Raman Spectroscopy
SRS	Stimulated Raman spectroscopy
TPF	Two-photon fluorescence
US	Ultrasound
UV	Ultraviolet

List of Tables

List of Figures

Chapter 1

Introduction and Background Theory

1.1 Bacterial Biofilms

1.1.1 Bacteria

Bacteria are ubiquitous, single cell organisms that can thrive in almost every environment on Earth. As part of the prokaryote taxonomy, bacteria do not contain a membrane-bound nucleus but instead have a nucleoid, and often plasmids, within the cellular cytoplasm that contains all genetic information in a single circular chromosome of DNA (deoxyribonucleic acid). In the cytoplasm there are also ribosomes which perform protein synthesis. The cytoplasm is enclosed by a cell membrane and cell wall. Many species have pili and/or flagellum which help with movement and adhesion [1]. **Figure 1.1** shows a schematic of a bacterial cell and its associated features.

Bacteria can be split into two categories based on the structure and composition of their cell wall and subsequent ability to hold a crystal violet (CV) Gram-stain. Bacteria which are stained pink/purple by CV are called Gram-positive, and have a thick peptidoglycan layer which is anchored to the inner lipid membrane via lipoteichoic acids. Gram-negative bacteria have a thin peptidoglyan layer in-between two lipid membrane

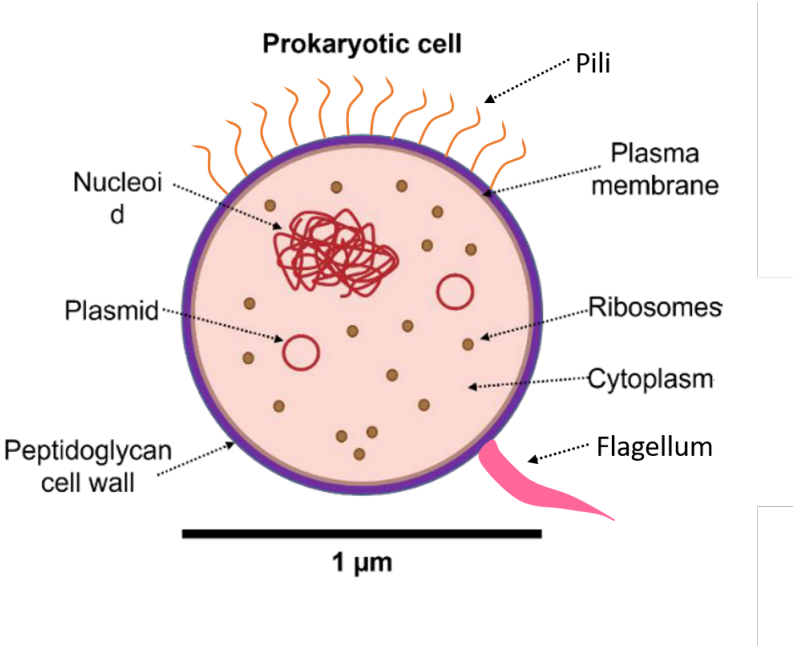

Figure 1.1: Schematic showing the structure of a prokaryote (bacteria) cell. Not all species have pili and flagellum. Figure reproduced from [2] and modified with permission.

layers, both seen in **Figure 1.2**. The inner and outer membranes are phospholipid bilayers, however the outer membrane is unique as it also contains lipopolysaccharides in the outside layer of the bilayer, which is an endotoxin potentially harmful to human health [3]. Some bacteria have external hair-like structures called flagella or pili which help with movement, attachment to surfaces, or the transfer of genetic material [1]. Teichoic acids and lipopolysaccharides provide Gram-positive and Gram-negative bacteria with an overall negative charge.

The bacteria studied in this thesis are the oral bacteria *Streptococcus salivarius* (*S.salivarius*) and *Actinomyces naeslundii* (*A.naeslundii*). Both species are Gram-positive facultative anaerobes found in the oral cavity, and are early colonisers in the development of oral biofilms.

S.salivarius is a spherical, chain forming bacteria that is found in the oral cavity a few hours after birth. Although it is generally considered harmless and in some strains can be used as a probiotic, it is still an opportunistic pathogen that on rare occasions can cause sepsis, endocarditis, or meningitis [5–8].

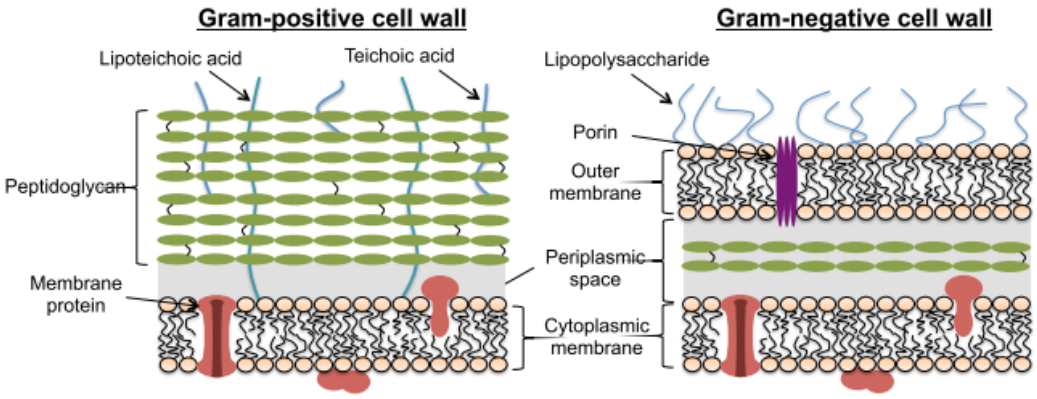

Figure 1.2: The structure of the cell wall for Gram-positive and Gram-negative bacteria. Figure reproduced from S. Moorcroft with permission [4].

A.naeslundii is a rod-shaped, non-spore forming bacterium which has fimbriae to help surface adhesion. *A.naeslundii* is also found in the oral cavity not long after birth, and is an opportunistic pathogen linked with root caries, periodontal disease and actinomycosis [9–11].

1.1.2 Biofilm formation

Individual (planktonic) bacteria in nature are vulnerable to their environment and external stresses, therefore in order to survive and prosper they form biofilms. Biofilms are surface-bound microbial communities encased in an extracellular matrix consisting of polysaccharides, lipids, proteins and DNA. Lipopolysaccharide may also be found in biofilms where gram-negative species are present. The microbes account for less than 10% of the biofilm, whereas the matrix secretion is responsible for over 90% [12].

The behaviour and lifestyle of bacteria within a biofilm is completely different to that of planktonic bacteria, making biofilms the preferred environment for microbes. The incentives to form biofilms include protection and defence from external stresses, ability for colonisation of the host, and benefits of microbial community. The presence of the matrix increases cell density and cell-cell interactions, surface adhesion, facilitates horizontal gene transfer and quorum sensing, creates oxygen and nutrient gradients altering metabolism rates, and enables the recycling of energy, DNA and nutrients from

dead bacteria. These advantages are unique to biofilms and allow bacteria to survive in scenarios that would not otherwise be possible.

The matrix also provides a physical scaffold and protectant from antibiotics, radiation, and immune responses [12–16]. As the matrix is secreted by the bacteria, it is tailored to the current environment and requirements, making biofilms ever-changing, highly adaptable and hard to treat [17]. Furthermore, persistor cells are more prevalent in biofilms making up at least 1% of the biomass. Persistors are metabolically inactive dormant cells that are highly resistant to antibiotics, but remain viable and re-populate once the antibiotic is removed [18].

It may seem counter-intuitive that microbes would willingly form a multispecies biofilm with competing species, yet this is a common occurrence with evidence showing that bacteria develop an altruistic behaviour in biofilms [19]. Microbial communities allow for the division of labour and metabolic burden, conserving energy whilst maintaining maximum efficiency. The ability to communicate and share genetic information through quorum sensing and horizontal gene transfer helps the community adapt to new stresses and further antibiotic resistance. Research is continuing into microbial communities to understand specifically the interactions within multispecies biofilms and why they occur, as multispecies biofilms are extremely common in nature.

Biofilms offer protection to encapsulated bacteria, which are commonly reported to be up to 1000x less susceptible to antibiotics than planktonic bacteria. Consequently, biofilms are becoming increasingly more threatening to healthcare as resistance rises with biofilms being responsible for approximately 80% of all chronic infections in humans [16, 20]. Biofilms thrive in open wounds, medical devices such as catheters, stents, pacemakers, and in the oral cavity where there is an abundance of soft and hard surfaces, nutrients, and warm micro-environments [21–24]. Biofilm growth on any surface follows a typical model that can be broken down into five stages: i) reversible planktonic attachment, ii) irreversible attachment, iii) proliferation, iv) maturation, and v) dispersion, (**Figure 1.3**). In cases such as oral biofilms, a salivary pellicle layer formed on the surface prior to bacteria attachment can be considered the first stage of biofilm

formation, as this provides a thin layer of proteins which aid in bacterial attachment [25].

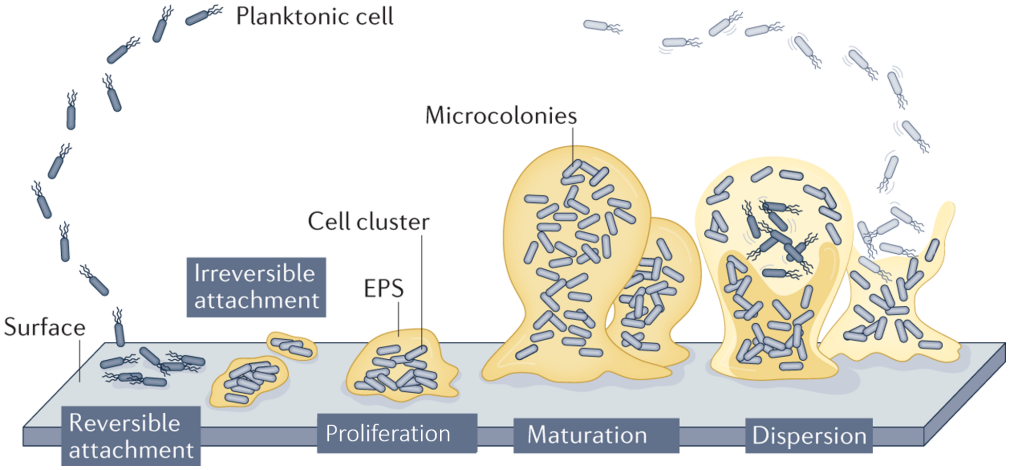

Figure 1.3: Schematic showing the five stages of biofilm formation: reversible attachment, irreversible attachment, proliferation, maturation, and dispersion. Figure reproduced with permission [26]. Copyright 2022, Springer Nature Limited.

When considering new biofilm colonisation and formation, Bacteria begin in a planktonic state, free-floating in a liquid typically under flow. The hydrodynamic forces drive bacteria over the surface, where at distances $\geq$ 50 nm Van der Waals interactions are in effect having a weak attractive force pulling bacteria from the stream and towards the surface. As bacteria approach 10 - 20 nm, repulsive electrostatic interactions between the negatively charged bacterium and surface increases, defining the reversible attachment stage. Any bacteria that is not lost at this stage drives closer overcoming the energy barrier, approaching $\ll$5 nm from the surface where specific interactions and surface receptors such as pili and flagellae bind forming physical, irreversible attachments to the surface [27, 28]. Bacteria will only attach and remain bound to a surface if the environment (nutrient content, temperature, oxygen levels) is favourable for their survival.

Bacteria will then begin to form clusters and excrete polysaccharides, lipids and DNA as the start of the extracellular matrix. As the micro-colonies develop, cells begin to communicate and regulate their gene expression through a process known as "quorum sensing". To do this, bacteria cells produce autoinducer molecules: Gram-positive bacteria produce autoinducer peptides (AiP) and Gram-negative produce acyl homoserine

lactone (AHL) [27]. This process is particularly important in biofilm formation as it allows the biofilm to improve its access to nutrients, limit the uptake of certain molecules, decide which areas are favourable to grow in, protect against threats, and survive in adverse environments [29]. The matrix continues to develop and adapt as micro-colonies grow, forming mushroom-like structures as the biofilm matures. The final stage is dispersion, where small clusters or planktonic cells break off from the main structure and begin the process again at new locations.

1.1.3 Oral Biofilms

The oral cavity is the second most diverse microbial system in the body, being host to almost 1000 species of bacteria [30, 31]. The soft and hard tissues, constant moisture, and warm temperature make it the perfect habitat for the colonisation and proliferation of multi-species biofilms. Oral biofilm formation can be broken down into three stages: early colonisers, secondary colonisers or bridging organisms, and late colonisers. Early colonisers are typically Gram-positive species such as *Streptococcus* and *Actinomyces* that are found in abundance in healthy individuals. They first bind to the salivary pellicle on the tooth surface to determine the initial composition of the biofilm and are open to co-aggregation - a process whereby genetically distinct species are able to adhere to each other via polysaccharide recognition in a mutually beneficial pairing. These are specific processes and not all species are able to bind to each other [32].

Secondary colonisers like *Fusobacterium nucleatum* are able to co-aggregate with both early and late colonisers, therefore act as a bridging organism between species which would not be able to interact or form a biofilm otherwise [33]. Late colonisers are typically anaerobic, Gram-negative, pathogenic species such as *Porphyromonas gingivalis* or *Prevotella intermedia* which are the cause of many oral diseases.

Biofilms form on the tooth surface in the supra-gingival region above the gum line, and in the sub-gingival region below the gum line. Pathogenic species thrive in the anaerobic sub-gingival regions, areas which are also harder to clean, and have the potential to allow bacteria into the bloodstream if poor oral hygiene continues. If left untreated,

sub-gingival biofilms can lead to oral diseases such periodontitis, which is estimated to effect over 1 billion people worldwide and has a huge economic burden as direct treatment accounts for 4.6% of the global health expenditure [34, 35]. Not only do oral diseases share the same risk factors as non-communicable diseases, pathogenic species are also associated with other systemic diseases in the body[36]. *P.gingivalis* alone is a key factor in Alzheimer's disease, cancer, rheumatoid arthritis and cardiovascular disease [37–41]. Inflammatory bowel disease, diabetes, and adverse pregnancy outcomes are just a few other systemic diseases associated with the oral microbiota [42–44]. It is incredibly important therefore to treat oral diseases at an early stage, or be able to recognise the development of pathogenic biofilms before they are able to form complex, resistant biofilms that are difficult to treat. Furthermore, understanding the process of how biofilms develop and the interactions within the biofilm is key to finding the best course of treatment and may suggest new methods which are not reliant on antibiotics.

1.1.4 Biofilm growth and analysis methods

There are numerous ways in which biofilms may be grown for analysis in laboratory conditions, an example of some are shown in **Figure 1.4**. A standard method is growing biofilms on the base of a 96-well plate. This method is simple, robust, and high-throughput (**Figure 1.4a**) [45, 46]. An adaptation of this method is the Calgary Biofilm Device (CBD) (**Figure 1.4b**). This is a standard 96-well microplate with a polystyrene lid attached with 96 pegs. Biofilms grow on the pegs, making this device a highly efficient method for testing and analysing multiple biofilms at once, and makes replacing the nutrients much easier as the plate can be quickly replaced. For growing oral biofilms, pegs are often coated in hydroxyapatite (HA), a naturally occurring form of calcium which builds tooth enamel. Having pegs coated in HA replicates the enamel surface allowing for a more accurate model, but also helps biofilm adhesion to the pegs [47]. A similar method to CBD is where biofilms are grown on coupons or discs in well plates or specific growth reactor (**Figure 1.4c**) . Using coupons makes nutrient replenishment simple and biofilms can be easily accessed for analysis [48].

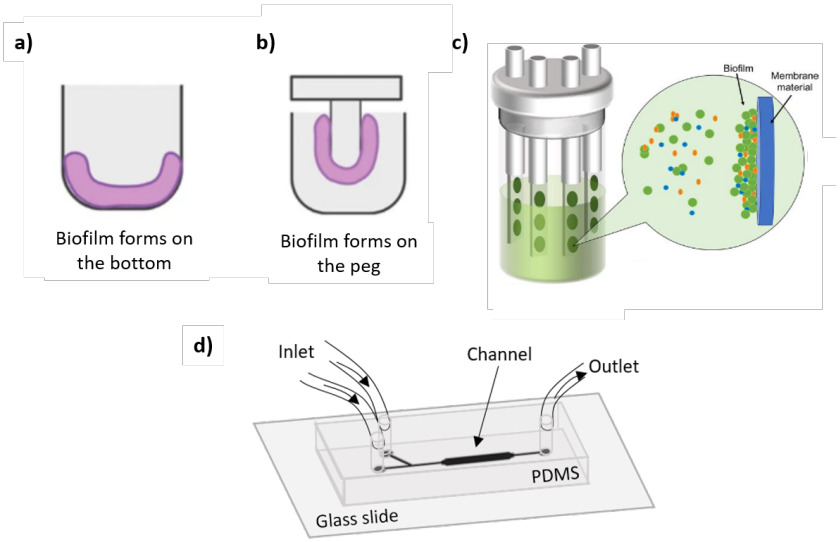

Figure 1.4: The most common methods of growing biofilms. a) Microtiter well plate with biofilm growth on the base of the well, b) Calgary Biofilm Device (CBD) where a peg is attached to the lid of a microtiter plate and inserted into the well, c) biofilm coupon reactor, and d) microfluidic device. a) and b) reproduced with permission from [49] Copyright 2023, The Korean Society of Food Science and Technology. c) reproduced with permission from [50], Copyright 2023, Taylor & Francis.

While well-plates, CBDs and coupons allow for high-throughput and require little specialised equipment, the plates are only representative of static growth conditions, have to be regularly replaced with fresh media which exposes the biofilms to air, and could cause disruption and detachment during washing steps [51]. Continuous flow influences the growth and morphology of biofilms through the transport of oxygen and nutrients, quorum sensing, shear forces, and the movement of pioneering bacterial cells causing the biofilm to spread and grow [52]. As a result flow chambers and microfluidics are becoming increasingly popular for biofilm growth for these very reasons, **Figure 1.4d**). Other work includes looking at the impact of flow induced shear stress and quorum sensing on biofilm morphology, the distribution of growth activity across the biofilm, and the effect of antimicrobial agents on orthodontic bonding materials [53–55]. Microfluidic devices are an increasingly popular choice as they are able to mimic micro-environments, require small sample sizes, and are non-destructive. A more in depth view of microfluidics for biofilm growth is given in **Section 1.2.2**.

Multiple methods of biofilm analysis are used in microbiology. The cell density

(colony forming units (CFU)/ml) can be counted by spreading the biofilm on agar plates. Crystal violet (CV) staining is used for biomass quantification and imaging. Fluorescent labelling of biofilms allows visualisation via Confocal Laser Scanning Microscopy (CLSM). Common examples of this use Filmtracer Live/Dead biofilm viability kit (SYTO9/propidium iodide), and fluorescent *in situ* hybridisation (FISH) which labels specific species within the biofilm. Gene expression is measured using qPCR, and enzymes by mass spectrometry. Other than fluorescent microscopy and CLSM, other cell imaging techniques used are transmission and scanning electron microscopy [56]. The majority of these processes are destructive, requiring the biofilm to be fixed first or removed and spread on a glass slide for microscopy.

1.1.5 Antibiotic Resistance

Antibiotic resistance is a significant threat to public health. Over recent decades there has been a surge in resistance due to over-consumption and inappropriate use of antibiotics, increase in global travel, and extensive use in agriculture [57, 58]. Antibiotics are concentration dependent treatments causing a bacteriostatic effect at low concentrations whereby bacteria proliferation is inhibited, and bactericidal effects at high concentrations where bacteria are killed [59].

Antibiotics work by three main mechanisms: targeting the cell wall, targeting protein synthesis, and targeting nucleic acid synthesis. The bacteria cell wall is made of peptidoglycan which undergoes cross-linking of peptides (D-alanyl-alanine and penicillin binding proteins (PBPs)) to strengthen the cell wall. β-lactam antibiotics target the cell wall as β-lactam mimics D-alanyl-alanine and binds to PBP, disrupting the peptidoglycan layer and preventing further synthesis, resulting in lysis of the cell [60]. Protein synthesis is interrupted by antibiotics targeting the 30S and 50S ribosomal subunits of the 70S ribosome. The 70S ribosome is responsible for all protein synthesis within the bacteria cell. Quinilone antibiotics prevent DNA replication by inhibiting the DNA gyrase which is responsible for the nicking of double-stranded DNA, introduces negative supercoils, and reseals the nicked ends. Without DNA gyrase this process cannot happen, thus causing

both bacteriostatic and bactericidal effects [60, 61].

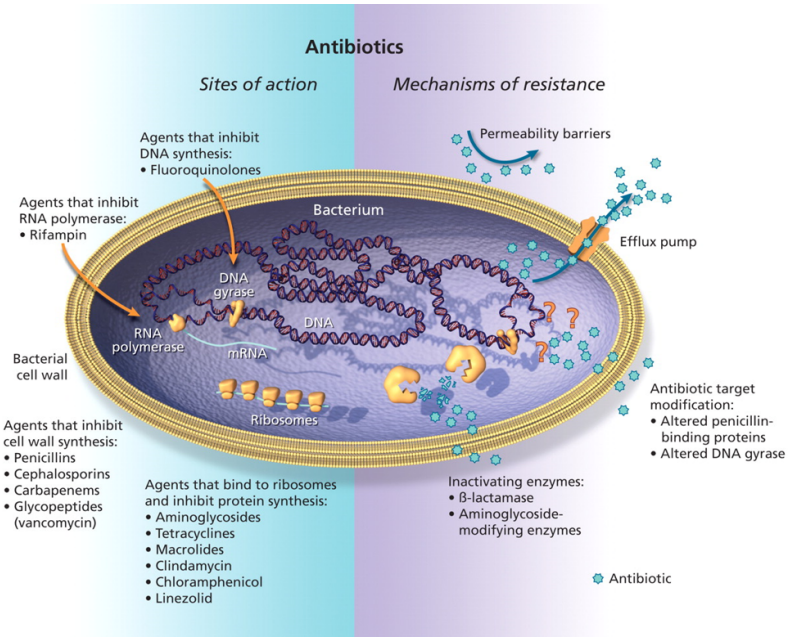

Figure 1.5: Figure showing the four common antibiotic mechanisms of action, and the four mechanisms of resistance. Reproduced with permission [62] Copyright 2009, CMAJ Group.

Resistance has emerged by bacteria adapting to these mechanisms in four ways: producing inactivating enzymes, modification of the binding site, altering the cell membrane to limit permeability, and utilising efflux pumps to dispel the drug. Enzymes are produced that inactivate β-lactums that disrupt the peptidoglycan cell wall [60]. Modification of the binding site renders the antibiotic unable to dock and inhibit the cross-linking of cell wall structures, this is the mechanism behind methicillin-resistant *Staphylococcus aureus* (MRSA). The remaining two mechanisms work by limiting the impact of the antibiotic. Efflux pumps are membrane proteins designed to remove harmful substances from the cell and have therefore evolved to remove antibiotics from the cell before they are able to take effect. Altering the cell membrane so it is less permeable to antibiotics is the final method of resistance. The lipid and protein content of the cell wall may change as well as the number of porins in the membrane which allow antibiotic entry. Resistance may also occur within the bacteria community via environment changes, horizontal gene transfer, quorum sensing, natural adaptation and mutations, as well as through the creation of persistor cells, as part of phenotypic heterogeniety [63–65]. A summary of the antibiotic mechanisms of action and resistance are given in **Figure 1.5**

1.1.6 Antimicrobial peptides

Antimicrobial peptides (AMPs) are short chain sequences of amino acids, typically 10 - 50 in length, with a positive charge. AMPs are naturally occurring in all species of life and are considered a key component in combating antimicrobial resistance [66]. Antibiotics work by disrupting the synthesis pathways of bacteria cells, whereas AMPs cause physical destruction of the negatively charged cell wall bilayer resulting in leakage of the cytoplasm, and consequently cell lysis. It is therefore less likely that resistance develops against AMPs as it is considered metabolically 'costly' for the cells to try repair themselves and mutate at a rate quicker than damage is being inflicted [67].

The efficacy of AMPs is dependent on their ability to electrostatically bind the the bacterial cell wall. They are both cationic (positively charged) and amphiphilic (contain both hydrophobic and hydrophilic properties), though have a high ratio of hydrophobic head groups [68, 69]. AMPs are characterised by their secondary structure, with the most common being α-helix and β-sheet structures. They are able to selectively bind to the surface of the negatively charged bacteria cell wall and insert their hydrophobic head groups into the bilayer causing disruption. There are three main models which describe how the peptide specifically breaks down the membrane: a) the barrel-stave model, b) the carpet model, and c) toroidal pore model, shown in **Figure 1.6**. The barrel-stave model describes clusters forming on the surface which insert themselves into the bilayer, with the hydrophobic head groups interacting with the hydrophilic ends of the bilayer, forming hydrophilic pores that lead to lysis (**Figure 1.6 a**). In the carpet model, AMPs form layers on the bacteria surface, with the hydrophobic end facing the bilayer. The AMPs cover the surface like a carpet and destroy the cell wall like a detergent (**Figure 1.6 b**). The toroidal model is similar the the barrel-stave model, however the the head groups of the AMP are always in contact with the opposing head group of the bilayer, causing the lipids within the bilayer to re-orientate themselves and curve to form a pore in the surface (**Figure 1.6 c**).

Along with natural AMPs, synthetic AMPs can be produced which are a more favourable option when considering AMPs for wide-scale use. Synthetically produc-

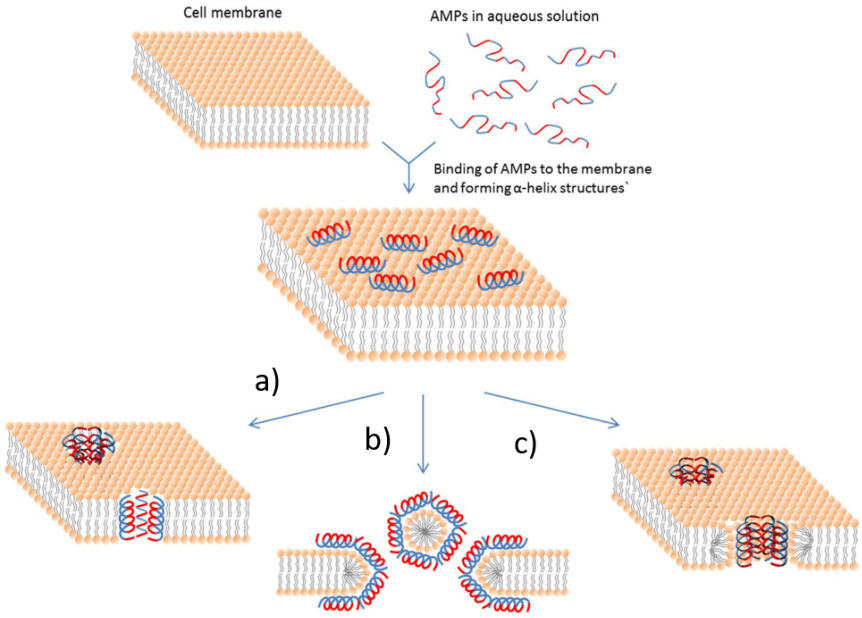

Figure 1.6: Schematic representing the AMP mechanisms of action. AMPs bind to the surface of the bacterial cell wall and disrupt the wall by one of three mechanisms. a) Barrel-stave model, b) the carpet model, or c) the toroidal model. Reproduced with permission [68]

ing AMPs allows the production of large quantities, and the ability to tailor the AMP to heighten the antimicrobial activity, and exclude any toxicity or weaknesses [70]. In this thesis a novel synthetically produced AMP known as IK8, is used to target 2-species oral biofilms [71]. IK8 is an amphiphilic β-sheet folding AMP, the structure of which is shown in **Figure 1.7**. The IK8 structure consists of recurring $(X_1Y_1X_2Y_2)_n$-NH_2 sequences where X refers to hydrophobic amino acids (Arginine (R)), Y is cationic amino acids (Lysine (K)) and n is the number of repeat units. For IK8, n=2, hence there are 8 amino acids in the sequence - IRIKIRIK-NH_2. IK8 remains a monomer in solution due to the electrostatic repulsion between Arginine and Lysine. Thus far, IK8 has shown antimicrobial activities against bacteria such as *Staphylococcus aureus*, but has not been tested against any oral species [71, 72].

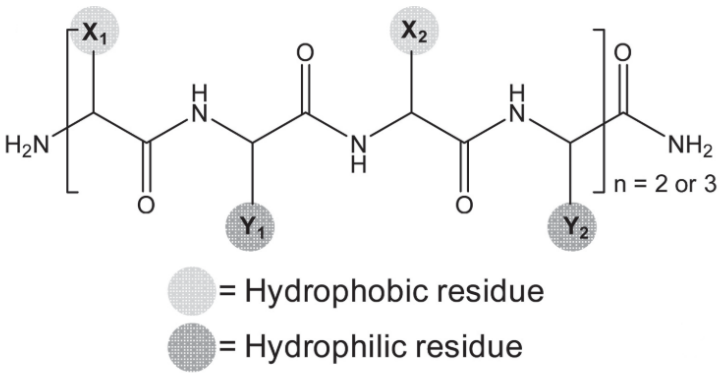

Figure 1.7: Structure of the synthetic antimicrobial peptide known as IK8, produced by Ong *et al.*. X: hydrophobic amino acids (Arginine (R)), Y: cationic amino acids (Lysine (K)) and n: number of repeat units. Figure reproduced with permission from [71]. Copyright 2013 WILEY-VCH Verlag GmbH Co. KGaA, Weinheim

1.2 Microfluidics

1.2.1 Microfluidic background

Microfluidics is the manipulation of small volumes of fluids on the micron scale, with increased control over the flow due to the presence of a laminar flow regime. Microfluidic devices have a small channel etched into either a polymer or glass, and are commonly referred to as 'Lab on a Chip' as they have the capabilities to contain an experiment from start to finish by providing the environment for sample growth (where necessary for biological samples) and subsequent analysis. Microfluidic devices are tailor made, require very small quantities of samples and reagents, can mimic micro-environments, are high-throughput, can carry out non-invasive real-time analysis, are compatible with many microscopy and spectroscopy techniques, and are low cost [73–75].

One of the main advantages of microfluidics devices is that they can be designed to specific experimental requirements, and made in-house using rapid prototyping techniques [76]. Microfluidic devices are typically fabricated from polydimethylsiloxane (PDMS), a silicone polymer that is transparent, bio-compatible, and permeable to gas [77]. The device design is cast into the PDMS and the device then bound to a glass slide

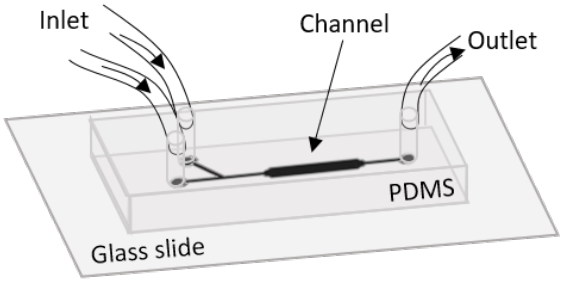

Figure 1.8: Schematic example of a single channel microfluidic device.

(or coverslip) using oxygen plasma treatment. An example of a microfluidic device is shown in **Figure 1.8**.

In order to predict and model the fluid flow in microfluidic channels, the Navier-Stokes equation can be used which describes the motion of viscous fluids. The Navier-Stokes equation for incompressible, Newtonian fluids is given in **Equation 1.1** where ν is the fluid velocity, μ is the fluid viscosity, ρ is the fluid density and p is the fluid pressure [78]. The equation describes the conservation of momentum, where each term represents a different force acting on the fluid: a) inertial forces due to fluid acceleration, b) the external pressure applied to the fluid, where fluid flows in the direction of the largest pressure change, c) viscous forces where increasing the viscosity acts to diffuse momentum, and d) represents any external forces such as gravity or electromagnetic interactions.

$$\underbrace{\rho\left(\frac{\delta\nu}{\delta t} + \nu \cdot \nabla\nu\right)}_{\text{a}} = \underbrace{-\nabla p}_{\text{b}} + \underbrace{\mu\nabla^2\nu}_{\text{c}} + \underbrace{F}_{\text{d}} \tag{1.1}$$

$$\frac{\delta\rho}{\delta t} + \nabla \cdot (\rho\nu) = 0 \tag{1.2}$$

The Navier-Stokes equation is solved along with the continuity equation given in **Equation 1.2** which represents the conservation of mass, and as the model is with an incompressible fluid, the fluid density is assumed constant reducing **Equation 1.2** to $\nabla \cdot \nu = 0$. Certain flow regimes may simplify the Navier-Stokes equation further, however to solve this model simulation software such as COMSOL Multiphysics software is often required which provides predictions of the fluid flow under various boundary conditions,

but is time intensive and potentially costly [78].

To quickly and efficiently predict fluid flow, dimensionless numbers are implemented, such as the Reynolds number (Re) [79]. Re is characterised as the ratio of inertial forces to viscous forces, shown in **Equation 1.3** where L is the characteristic linear dimension of the system dependent on the flow geometry.

$$Re = \frac{F_{inertial}}{F_{viscous}} = \frac{\rho \nu L}{\mu} \tag{1.3}$$

For rectangular channels, as is common in microfluidics, L is equal to the hydraulic diameter (D_H), which is defined in **Equation 1.4**, where A is the cross-sectional area of the channel, P is the channel perimeter, w is the width of the channel, and h is the height of the channel.

$$D_H = \frac{4A}{P} = \frac{2wh}{w+h} \tag{1.4}$$

For $Re < 2000$ viscous forces dominate and fluid flows in a continuous and smooth manner, known as laminar flow. For $Re > 4000$, the inertial forces begin to dominate causing a turbulent flow regime, where the flow is erratic and unpredictable [79, 80]. In microfluidics it is common for $Re \ll 1$, known as Stokes flow, confirming that inertial forces are negligible in these regimes. This therefore simplifies the Navier-Stokes equation to a linear, time-independent equation that is much simpler to solve, $\mu \nabla^2 \nu - \nabla p = 0$ [80].

An important factor to consider when using microfluidics to grow biofilms is the shear forces acting on the biofilm as a result of the fluid flow. This can be calculated by **Equation 1.5**, where τ is the shear stress (dynes/cm^2), μ is the fluid viscosity (Pa s), Q is the volumetric flow rate (m^{3}s^{-1}), w is the width and h is the height of the channel (m).

$$\tau = \frac{6\mu Q}{wh^2} \tag{1.5}$$

1.2.2 Microfluidics for biofilm growth

Microfluidic systems have become increasingly popular in the study of biofilms due to their ability for real-time analysis, control over the micro-environments, constant flow, and automation [81]. The versatility of microfluidics allows investigations into specific aspects of biofilm growth, such as bacterial adhesive properties, biofilm formation, the effect of shear stresses, antibiotic susceptibility and resistance, to name a few [82–87]. The microfluidic devices used can vary from a simple straight channel device, to those with complex geometries to control flow and concentrations, multiple channels, multiple layers, or sensors depending on the experimental outcomes [88–91].

Guanju Wei and Judy Yang studied the impact of fluctuating flow on *Pseudomonas putida* biofilms, using a serpentine channel with differing number of turns to determine the frequency of the fluctuation. Low frequency fluctuations promoted biofilm growth while high frequency fluctuations inhibited growth - a finding that could be used as a strategy to control biofilm formation in diverse natural and engineered systems [85]. Núria Blanco-Cabra *et al.* developed a microfluidic platform with electrode sensors on the base of the biofilm growth chamber, which are able to monitor biofilm growth an treatment without any external interference [91].

Oral biofilms have been grown using microfluidics, with William C Nance *et al.* demonstrating the success of using a BioFlux microfluidic system to qualitatively and quantitatively assess the impact of antimicrobials on a multi-species oral biofilm using live/dead fluorescent staining and CLSM [92]. An 'artificial teeth' device was developed by Raymond H. W. Lam *et al.*, where a device contained 128 individual chambers to perform simultaneous cultivation and analysis on *Streptococci spp* and *F.nucleatum* under different conditions such as nutrient composition and oxygen levels [93]. The versatility of microfluidic devices makes them an attractive choice for biofilm growth, especially with the benefit of *in situ*, real-time analysis and direct easy compatibility with microscopy and spectroscopy techniques, which is not possible with other traditional biofilm growth methods. In this thesis microfluidic devices are used for mono- and multi-species biofilm growth to allow for the long term, non-destructive characterisation of biofilms using

Raman spectroscopy.

1.3 Raman Spectroscopy

1.3.1 Raman Background

Raman spectroscopy (RS) is a form of vibrational spectroscopy where light interacts inelastically with matter to produce a spectrum showing the molecular fingerprint of that sample [94]. It was first described theoretically by Smekal in 1923 followed by Kramers and Heisenberg developing a quantum theory of scattering in 1925, furthered by Dirac in 1927. Raman scattering was first observed by C.V. Raman and K.S. Krishnan in 1928, of whom the scattering is named after [95].

Since its discovery RS has been extensively used in scientific analysis as it can be used on most materials, it's highly specific so can differentiate similar chemical structures and small changes in material structure, it's non-destructive, no sample preparation is typically required, and can be used with aqueous solutions [96]. For these reasons RS has become a popular analysis tool to investigate biological samples such as colorectal cancer cells, brain tumours, coronary artery, cornea, bacteria and biofilms [97–102].

Not all molecules are considered "Raman active", and a molecule may not be Raman active in all it's modes of vibration. Raman scattering is induced by a change in polarisability of the molecule, therefore a molecule undergoing a symmetric stretch may cause a change in polarisability while its bending mode may not. Infrared (IR) absorption is considered complimentary to Raman scattering as not all molecules are "IR active", as for IR to occur the dipole moment of a molecule must change during vibrations. For molecules with a centre of symmetry, a Rule of Mutual Exclusion applies whereby if a molecule is Raman active in one mode of vibration it is therefore IR in-active, and vice-versa [103].

The theory behind Raman scattering can be explained in a classical and quantum context, as presented in the sections below.

1.3.2 Classical theory

Raman scattering can be explained by the classical theory of electromagnetic radiation [104–106]. The electric field strength of a fluctuating, time-dependent, electromagnetic wave is given by

$$E = E_0 cos(2\pi\nu_0 t) \tag{1.6}$$

where E_0 is the vibrational amplitude and ν_0 is the frequency of the incident light. If a molecule is in the presence of an electric field, the surrounding electron cloud is disrupted resulting in an induced dipole moment, μ:

$$\mu = \alpha \cdot E = \alpha \cdot E_0 \cos(2\pi\nu_0 t) \tag{1.7}$$

If a molecule is vibrating at frequency ν_m, then the nuclear displacement q is given as

$$q = q_0 cos(2\pi\nu_m t) \tag{1.8}$$

where q_0 is the vibrational amplitude. The molecular polarisability, α, denotes how easy it is to distort the electron cloud of a specific molecular bond. Nuclear vibrations affect the polarisability, so in order to see the dependence of α on these vibrations, q, a Taylor expansion is performed for small deviations

$$\alpha = \alpha(q) = \alpha_0 + \left(\frac{\partial\alpha}{\partial q}\right) \cdot q + ... \tag{1.9}$$

Combining these equations, we obtain a final equation for the time dependent induced dipole moment,

$$\mu(t) = \alpha_0 E_0 \cos(2\pi\nu_0 t) + \left(\frac{\partial\alpha}{\partial q}\right) \cdot E_0 q_0 \cos(2\pi\nu_0 t)\cos(2\pi\nu_m t) \tag{1.10}$$

Using the trigonometric identity $2cos(A)cos(B) = cos(A+B) + cos(A-B)$, the above equation can be expressed as

$$\mu = \underbrace{\alpha_0 E_0 \cos(2\pi\nu_0 t)}_{\text{Rayleigh Scattering}} + \left(\frac{\partial\alpha}{\partial q}\right) \cdot \frac{E_0 q_0}{2} [\underbrace{\cos((\nu_0 - \nu_m)2\pi t)}_{\text{Stokes}} + \underbrace{\cos((\nu_0 + \nu_m)2\pi t)}_{\text{anti-Stokes}}] \quad (1.11)$$

It is clear from the **Equation 1.11** that the the induced dipole moment oscillates at three distinct frequencies. The first term oscillates at the same frequency as the incident radiation therefore the light scattering is elastic and known as Rayleigh Scattering. This term also has no dependence on the nuclear vibrations. The second term is dependent on the difference between the incident frequency (v_0) and the molecular normal mode frequency (ν_m). This represents inelastic scattered light and more specifically that of a lower frequency, this is known as Stokes scattering. The third term is also inelastic scattering but is instead dependent on $(\nu_0 + \nu_m)$ so the scattered light has a frequency greater than that of the incident, known as Anti-Stokes scattering [105]. From the above equation it is evident that for Raman scattering to occur the rate of change of the polarisability with respect to vibration must be nonzero,

$$\left(\frac{\partial\alpha}{\partial q}\right) \neq 0 \quad (1.12)$$

As the change in polarisability would be relatively small, the detected Raman signal is weak compared to Rayleigh scattering. The polarisability of a molecule can be graphically represented by an ellipsoid [108]. If the size, shape, or orientation of the ellipsoid changes during a molecular vibration, the molecule is Raman active. **Figure 1.9** shows the molecular vibrations for a CO_2 molecule, along with a graph showing how the polarisability changes with the vibration coordinate. The symmetric vibration (ν_1) is the only mode which completely changes the polarisability ellipsoid and produces a non-zero value of $\partial\alpha/\partial q$. For the bending and symmetric stretching vibrations the ellipsoid is the same at $\pm q$ so for small displacements there is no change in polarisability so these modes are not Raman active.

The frequency at which the molecules vibrate can be calculated by modelling them as

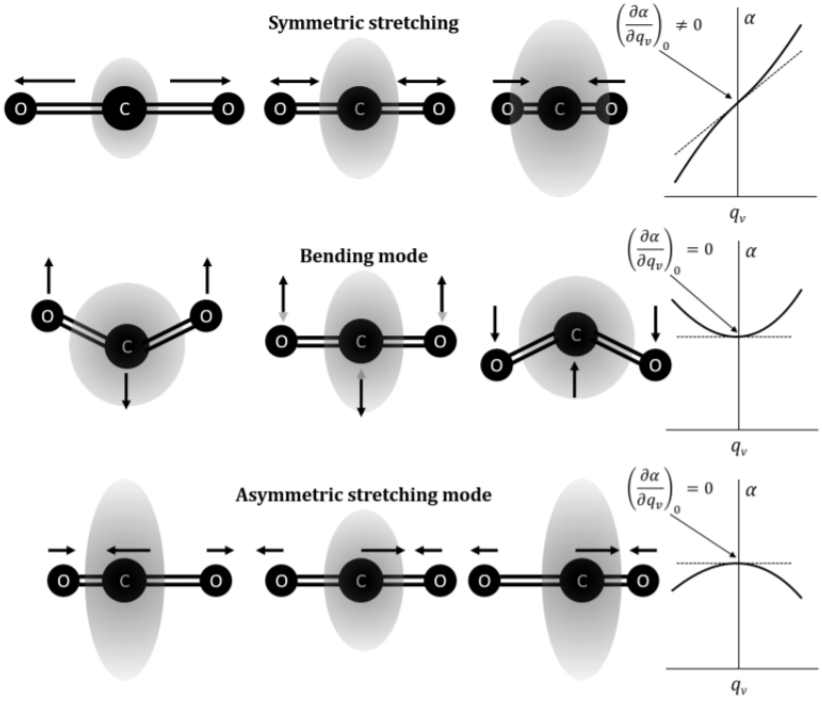

Figure 1.9: Schematic showing how the polarisability, represented by an ellipsoid, changes during the molecular vibrations of a CO_2 molecule, along with the graphical representation of the change in polarisability with vibration coordinate. Only the symmetric stretching has a non-zero representation of Equation 1.12, therefore is the only Raman active mode [107].

two balls attached to a spring (diatomic molecule). This two atom system follows simple harmonic motion, where the amplitudes of the vibrations are inversely proportional to the masses, thus keeping the centre of mass stationary. The frequency of the harmonic oscillations is given by Equation 1.13, where k is the spring force constant (which is a function of the bond energy) and μ_m is the reduced mass of the two atoms, m_1 and m_2.

$$\nu_v = \frac{1}{2\pi}\sqrt{\frac{k}{\mu_m}} \qquad \mu_m = \frac{m_1 m_2}{m_1 + m_2} \tag{1.13}$$

Equation 1.13 shows that the frequency of molecular bonds are unique as they're dependent on the force constant and the atomic masses involved in that interaction. The value of the force constant, k, can be approximated for different bonds: 3 - 6 (single), 10 - 12 (double), and 15 - 18 (triple), showing that the stronger double/triple bonds will have a higher frequency [109]. Heavier atoms will result in a higher reduced mass and therefore a lower frequency. If a bond is strongly polarised, such as O-H, C-O, N-O, the vibration will only have a small resultant effect on the polarisation, so will only be weakly Raman active. Strong Raman scatterers tend to be those with covalent bonds such as C≡C, C-S, S-S, or aromatics [110].

While the classical theory explains well the nature of polarisation, it does have some limitations. Many approximations were made, such as assuming harmonic motion and a Taylor expansion only to the first order. Considering anharmonicity introduces overtones which are generally much weaker than fundamentals [109]. Furthermore, by considering only the first order Taylor expansion the theory is limited to linear Raman scattering, whereas further expansions and consideration of the susceptibility of the material leads to non-linear scattering processes such as Stimulated Raman Scattering, coherent anti-Stokes Raman or coherent Stokes Raman scattering [107, 111].

1.3.3 Quantum theory

Quantum mechanics states that energy is quantised, therefore molecules can only exist in quantised energy levels (electronic, vibrational and rotational). For this reason we

know that vibrational energy cannot be continuous but must have discrete values. For a harmonic oscillator all vibrational energy levels are equidistant and a molecule can only transition to its neighbour states, that is $\Delta v = \pm 1$. The vibrational energy levels for a harmonic oscillator can be found using Equation 1.14,

$$E_v = \left(v_v + \frac{1}{2}\right) h\nu \qquad v_v = 0, 1, 2... \tag{1.14}$$

where ν is the vibrational frequency of the oscillator, v_v is the quantum number which can only be whole integers, and h is Plank's constant. The zero point energy occurs when $v = 0$, $E = \frac{1}{2}h\nu$, showing that even in the vibrational ground state the molecules still undergo vibrational motion, which agrees with Heisenberg's uncertainty principle as if the molecule were to stop moving it would be possible to define both the position and momentum simultaneously [112].

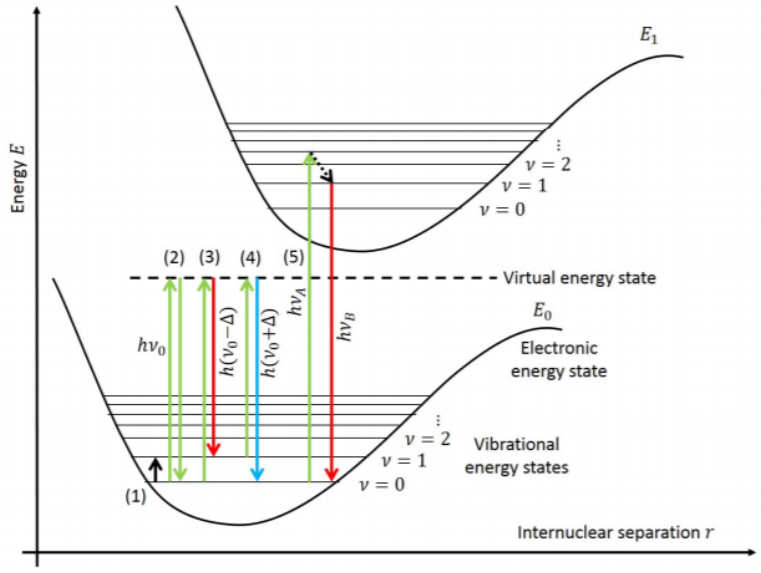

Figure 1.10: Jablonski Energy diagram showing the difference between (1) IR absorption, (2) Rayleigh scattering, (3) Stokes and (4) anti-Stokes Raman scattering, and (5) Fluorescence. The energy state E_0 and E_1 show different electronic states. Colours were used to indicate the shift in energy/frequency of the photon (either to red or to blue). Figure reproduced with permission from [107].

For scattering to occur, the molecule must be excited to a "virtual" energy level according to quantum mechanics. Classically this "virtual" state does not exist. After any scattering event, the conservation of energy must be maintained. For elastic Rayleigh

scattering, the molecule transitions back from the virtual state to its original energy level, emitting a photon of equal energy to the incident photon. During Raman scattering, the molecule ends up in a higher or lower energy state than it began in, therefore the emitted photon either has lower energy (Stokes) or higher energy (anti-Stokes), so the total energy of the system remains the same.

Figure 1.10 shows a Jablonski diagram which demonstrates the different energy level transitions for infrared absorption (1), Rayleigh scattering (2), Stokes and anti-Stokes Raman scattering (3,4), and fluorescence emissions (5). IR absorption is the transition between vibrational energy states, and fluorescence is the excitation of a photon to a higher electronic state (absorption), followed by the non-radiative transition to a lower electronic state, and then the return of the photon to the ground state (emission). Fluorescence is an absorption and emission process and only occurs during resonance, when the incident photon matches the energy difference between the ground state and a higher electronic energy level state. Fluorescence is a relatively much slower process, taking on the order of nanoseconds. [113]. RS is an inelastic scattering process which is fundamentally different to the absorption/emission process of fluorescence. It is a non-resonant process causing excitation to a virtual energy state. It is an instantaneous process of energy coupling from the photon to the molecular vibrations, and back again. If the scattered photon gains energy it is known as anti-Stokes scattering, and if it loses energy it is known as Stokes scattering.

1.3.4 Non-linear Raman Spectroscopy

Coherent RS techniques such as CARS and SRS, unlike spontaneous RS involve multiple incident laser sources therefore non-linear optical polarisation must be considered due to the effects of multi-wave mixing [114]. Both linear and non-linear optical effects can be understood by considering the effect of the electromagnetic wave on the charge particles in a material. The applied electric field induces a dipole moment by causing a small displacement of bound electrons from their equilibrium position. The induced dipole

moment is defined as

$$\mu(t) = -e \cdot r(t) \tag{1.15}$$

where e is the charge of the electron and r is the displacement. r is dependent on how tightly bound the electrons are to the nucleus, and for small displacements can be modelled as a harmonic oscillator as previously mentioned.

The polarisation of the material, P, is the sum of the electric dipoles in a unit area, N,

$$P(t) = N\mu(t) \tag{1.16}$$

and for weak electric fields, the displacement of the electrons is directly proportional to the electric field, thus the polarisation can be written as

$$P(t) = \epsilon_0 \chi E(t) \tag{1.17}$$

where ϵ_0 is the electric permittivity and χ is the susceptibility of the material. The susceptibility is a dimensionless proportionality constant that describes the degree of polarisability of a material with respect to the applied electric field. Equation 1.17 therefore states that for small displacements, the polarisability is linearly proportional to the electric field.

Non-linear optical effects are introduced when there is a strong field causing large electron displacements or multiple electric fields are involved, meaning that the displacement can no longer be modelled as a harmonic oscillator and anharmonicity can no longer be ignored [115].

For non-linear optics the polarisation can now be expressed as a power series to the nth order

$$P(t) = \epsilon_0[\chi^{(1)}E(t) + \chi^{(2)}E^2(t) + \chi^{(3)}E^3(t) + ...] = P^{(1)}(t) + P^{(2)}(t) + P^{(3)}(t) \tag{1.18}$$

The physical processes that occur at the second order, P^2, are distinct from the third order, P^3. Second order non-linear polarisation can only occur in non-centrosymmetric

crystals (crystals that lack inversion symmetry), therefore for liquids, gases, amorphous solids (such as glass), and some crystals, $\chi^{(2)}$ vanishes. Third-order nonlinear optical interactions described by $\chi^{(3)}$ can occur for both centrosymmetric and non-centrosymmetric systems [116].

Coherent, non-linear raman spectroscopy techniques such as CARS and SRS are as a result of the third order polarisation, P^3, and are thus dependent on $\chi^{(3)}$.

1.3.5 Stimulated Raman spectroscopy (SRS)

SRS is a coherent, non-linear process involving two photons instead of one. The result is an enhanced signal with non-resonant background, and acquisition rates much faster than spontaneous RS. SRS is not completely background free, with self-phase modulation and laser background still having an impact, though is much less than in spontaneous RS. For SRS, two photons are incident on the sample - a pump photon of frequency ω_p, and a Stokes photon of frequency ω_s. If the frequency difference ($\Delta\omega = \omega_p - \omega_s$) between these photons matches a specific molecular vibration, the occurrence of this transition is enhanced.

During spontaneous RS, where only the pump beam is incident on the sample, the probability of a vibrational transition resulting in Raman scattering is low. The inclusion of the Stokes beam, which is spatially and temporally synchronised with the pump beam, stimulates the vibrational transition to increase scattering by $\sim 10^8$ and also increases the relaxation rate to the vibrational state, making SRS a much faster process than spontaneous RS [117]. **Figure 1.11** compares and demonstrates the energy transitions for spontaneous RS and SRS. During the transition, a pump photon is lost while a Stokes photon is gained, resulting in the output pump and Stokes beams showing a respective energy loss and gain. The energy loss or gain in the beams are modulated and used to determine the SRS signal [118, 119].

The speed and significant enhancement properties of SRS make it a desirable spectroscopic tool in all fields. There are other RS processes, such as Coherent anti-Stokes

Raman Spectroscopy (CARS) which is significantly stronger than RS and much easier to implement, which uses three photons but has lower signal intensity than SRS [105]. Surface-enhanced Raman Spectroscopy (SERS) utilises the enhancement properties of rough metal surfaces or nanoparticles to enhance local signals by several orders of magnitudes [120]. The type of RS used is dependent on the sample and the desired outcome, but all are increasingly being used for biological analysis.

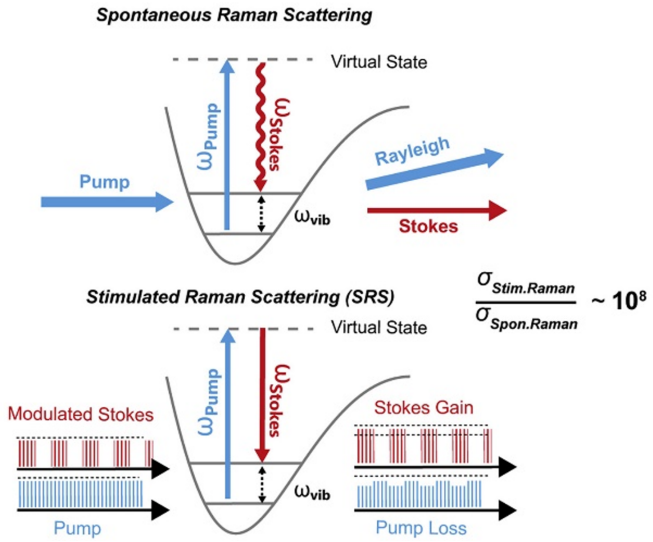

Figure 1.11: Comparison of spontaneous RS (top) and SRS (bottom) energy transitions. RS induces spontaneous Stokes scattering with one incident photon, whereas during SRS the additional Stokes photon stimulates the transition, and results in the output having a pump loss and Stokes gain. Reproduced with permission from [117]. Copyright 2021, Elsevier.

1.3.6 Raman spectroscopy of oral biofilms

Raman spectroscopy has gained a lot of interest in the biofilm community as it provides label free, non-destructive spectral analysis with high spatial resolution. This process enables rapid microbial detection and has been shown to identify individual species of bacteria, identify bacteria in different metabolic states, test antibiotics and resistant strains, and even identify bacterial species within a multispecies biofilm [121–124]. The first document of using RS to investigate oral bacteria was in 2003 by Andrew J. Berger & Qingyuan Zhu, where RS and cluster analysis were used to successfully identify four oral *streptococci* species [121]. This group pioneered research into oral bacteria and biofilm

using RS. They went on to show that RS can be used to identify and quantify bacteria (*Streptococcus mutans* and *Streptococcus sanguis* (now reclassified as *S.sanguinis*) within a poly-microbial mixture [125], and later advanced their methods to identify and map bacterial species within 2-species biofilms [126, 127]. The model used combined principle component analysis and a linear regression model to predict the species of bacteria present in each voxel of a mapped area of biofilm, accurately predicting 94% *S.mutans* and 92% *S. sanguinis* species correctly.

The biofilm matrix of mono- and dual-species *E. faecalis* and *A. naeslundii* biofilms has been studied to identify the biochemical composition and structure of these biofilms [128]. The main spectral differences of these two species were found in the spectral regions around 1270 – 335 cm^{-1} and 1000 – 1125/800 – 980 cm^{-1}, which were assigned to protein and polysaccharides, respectively. Further work by this group has shown that the composition of the biofilm matrix varies significantly between mono- and dual-species biofilms, indicating that the two species influence each other on a biochemical level during growth [129].

Recent work by Kriem *et al.* used RS and statistical modelling to differentiate between 5 common types of subgingival oral bacteria: *F.nucleatum, S.mutans, Veillonella dispar, A.naeslundii* and *Prevotella nigrescens*. Using the spectra from planktonic samples as a reference, they were able to successfully identify each biofilm with 90% accuracy by using a 2-way orthogonal Partial Least Square with Discriminant Analysis (O2PLS-DA) [130]. Further work by Kriem *et al.* mapped and identified *Actinomyces denticolens* and *Streptococcus oralis* bacteria in dual-species biofilms, using CLSM and FISH to identify bacteria morphology and distribution, which supported and confirmed the Raman map cluster analysis [124]. This process of using Raman maps and cluster analysis to analyse multi-species biofilms is the most advanced and detailed RS analysis of oral biofilms to date. There is however room to build on this method as thus far all biofilms were fixed prior to analysis (killing and preservation of the cells), therefore analysing biofilms in real-time would allow for long term studies and mapping of biofilm growth over time. This method is also limited to a spatial resolution of 1μm, and the long acquisition times associated with taking Raman maps with spontaneous RS. It is important

to determine how far scan times can be reduced without diminishing the quality of the maps. It would also be beneficial to look at Raman maps across the z-axis to see the variation across the biofilm depth.

SRS imaging has only recently been used for biofilm analysis, though at the point of writing there has been studies on oral biofilms. SRS has been used to study the real-time antibiotic effect of vancomycin on *S. aureus* biofilms, finding that the penetration into the biofilm is limited and non-uniform, showing eradication of thin areas of biofilm while thick areas remain viable [131]. The high resolution, enhanced signals and high speed of SRS makes it an ideal method for real-time analysis of biofilms.

1.4 Microbubbles and Ultrasound

1.4.1 Microbubble background

Microbubbles (MB) are defined as a gas core with a diameter 1 - 10 μm [132]. The gas core, typically air or perfluorocarbon, is stabilised by a lipid, polymer, or protein monolayer, which increases the lifetime of the MB. Since their discovery in the 1960's MBs have been widely used as ultrasound (US) contrast agents due to the high acoustic impedance mismatch between their gas core the surrounding medium. This causes significantly enhanced echo-scattering (or echogenicity), reducing the signal-to-noise ratio and makes the area of interest distinguishable from surrounding tissues [133]. Having a gas core and relatively flexible shell means MBs are compressible, therefore when subject to an US wave the MB will experience volumetric oscillation. If the frequency of oscillation is too high, the MB will collapse in a process called cavitation. This feature makes MBs an ideal method for controlled drug delivery and release [134, 135].

MBs are only clinically approved for use as US contrast agents at this point, and are most routinely used in echocardiography [136]. In order for MBs to fit through vasculature and not cause embolism, clinically accepted MBs are <8 μm, with the average size being 1-3 μm, [136–138]. This size of MBs have a resonant frequency of 2–15 MHz

which fortunately overlaps with the frequency range that is commonly used in diagnostic US [139]. One further benefit of MBs is that they can be tailored for a specific purpose. The composition of the shell and choice of gas core determines the acoustic response and stability of the MB, however it is possible to incorporate drugs or antibiotics into the MB by attaching to the outside of the MB, incorporating into the monolayer, or via encapsulation within the MB [140, 141].

1.4.2 Formulation and stability

The first discovery and use of MBs were just air bubbles with no shell. Many naturally occurring MBs are just air bubbles, such as those created during teeth cleaning with ultrasonic toothbrushes [142, 143]. Creating MBs with a phospholipid shell and a high molecular weight gas core, as is used in this thesis, increases the stability and longevity of the MB. The stability of a MB sample is often described in terms of how the size of the population changes over time, that being the rate of diffusion of gas across the monolayer to the surrounding medium. If the internal pressure of the MB is greater than the external pressure, the MB will shrink. This relationship between internal and external pressures is known as the Laplace pressure, as shown in Equation 1.19

$$\Delta P = P_{int} - P_{ext} = \frac{2\sigma}{r} \tag{1.19}$$

where P_{int} is the internal pressure of the MB, P_{ext} is the external pressure of the surrounding medium, σ is the surface tension, and r is the radius of the MB.

MB stability is modelled by the Epstein-Plesset equation (Equation 1.20) which considers the surface tension of a lipid shell and diffusivity of the gas core to calculate the rate of MB dissolution:

$$-\frac{dr}{dt} = \frac{H}{\frac{r}{D_w} - R_{shell}} \left(\frac{1 + \frac{2\sigma}{P_\alpha r} - f}{1 + \frac{4\sigma}{3P_a r}} \right) \tag{1.20}$$

where $-\frac{dr}{dt}$ is the change in MB radius over time, D_w is the gas diffusivity into the surrounding medium, R_{shell} is the encapsulation mass transfer resistance, σ is the surface

tension of the lipid shell, P_α is atmospheric pressure, f is the degassing factor, and H is the Ostwald coefficient:

$$H = \frac{C_a}{C_g} \tag{1.21}$$

where C_a is the gas concentration in the aqueous phase, and C_g is the gas concentration in the gas phase.

Adding a lipid shell to a gas MB therefore drastically improves the stability and lifetime of the MB, creating a physical barrier between the internal and external medium, reducing the Laplace pressure. The most common phospholipids used for the MB shell are DPPC and DSPC, with chain length 16 and 18 respectively [144–147]. Longer chain lipids increase MB stability by forming thicker monolayers with increased van der Waals attraction between the chains, and show enhanced resistance to gas permeation and MB dissolution [148]. Lipid MBs also have an emulsifier component, such as DSPE-PEG2000 which aids in MB formation and prevents coalescence [149]. MBs can be produced via mechanical agitation, where the MB lipid solution is saturated with gas and vigorously shaken, or by using microfluidics whereby a stream of gas is directed through the lipid solution and pinched off, creating MBs [150].

1.4.3 Therapeutic Microbubbles

MBs are small, non-toxic, versatile carriers which can be ruptured upon US exposure, making them an ideal candidate for therapeutic drug delivery. **Figure 1.12** demonstrates the four main methods of using MBs for drug delivery. Hydrophobic drugs can be loaded within a thick oil layer in between the shell and gas core. This was one of the first methods developed, though the loading capacity needs to be considered as the oil layer may alter the echogenicity of the MB and cause instability [132]. Hydrophobic drugs, or just the hydrophobic end of the drug, may be inserted into the shell of the MB for delivery [151, 152]. Hydrophilic drugs can bind to the surface of the MB shell through electrostatic interactions by designing the MB so that the phospholipids are of opposite charge to the drug [153]. Finally, drugs may be loaded into other small vesicles such as nanoparticles or liposomes which are then attached to the MB via avadin and

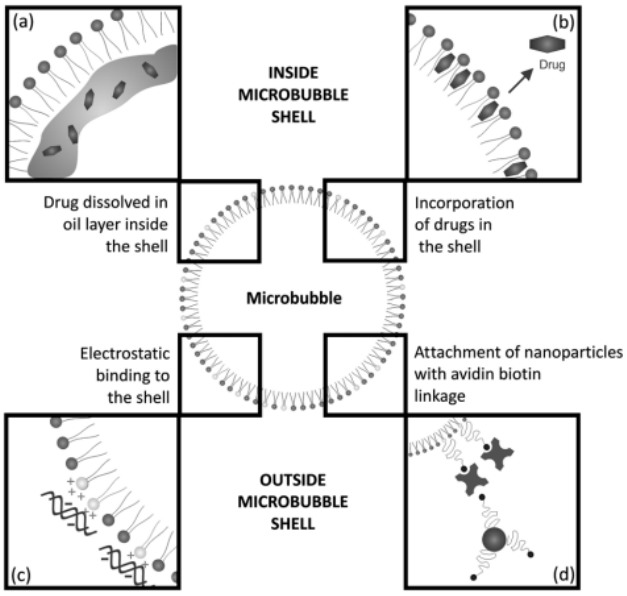

Figure 1.12: Schematic showing the possible methods of drug loading a microbubble. a) Drugs loaded in an oil layer between the gas core and shell, b) incorporated in the microbubble shell, c) electrostatic attachment to the outside of the shell, d) small, drug loaded vesicles, attached to the shell. Figure reproduced with permission from [140]. Copyright 2009 RSC.

biotinylated lipids. Liposomes are 100 - 500 nm in size, consisting of an aqueous core stabilised by a lipid bilayer. By incorporating biotinylated lipids into the lipids shells, the MB and liposome bind to avadin and load approximately 10^5 liposomes to the surface of a MB [152–154].

Using MBs as a carrier, drugs can be delivered to the site of interest and released on demand with US exposure. The effects of US induced cavitation alone can cause damage to a surface, in a process know as sonoporation. The mechanisms of MB destruction with US and sonoporation effects are detailed in **Section 1.4.4**. Targeted MBs are continuing to be developed to ensure MBs are delivered to the intended site, and are delivered at a concentration high enough to take effect. This is particularly important when treating tumours or delivering chemotherapeutic agents [155, 156]. Nicola InGram *et al.* developed therpautic MBs that targeted a tumour endothelial marker (VEGFR2) using a biotin-neutravadin linker and VEGFR2 antibody [157]. The study found that after ultrasound exposure the efficacy of the cytotoxic drugs was enhanced, and ultrasound

triggered release was essential to achieve these effects. Magnetically targeted MBs using superparamagnetic iron oxide nanoparticles have been used to treat brain tumours, and also enables direct visualisation of the drug delivery using MRI [158].

Targeted MBs for biofilm treatment has only started to gain interest in recent years as the need for alternatives treatment strategies intensifies. Caudwell *et al.* bound MBs to *S.aureus* using a protien affimer which targets the clumping factor A (ClfA) virulence factor. Bound MBs were able to withstand flow rates of 250 μl/min, and led to a 25% decrease in biomass of the biofilm after US exposure [159]. Kouijzer *et al.* chemically coupled vancomycin to the lipid shell of MBs and demonstrated the specific binding to *S.aureus* biofilms, which remained successfully attached under shear stress rates of 0 – 12 dyne/cm^2, and after US had a 28% reduction in biomass [160]. The sonoporation effects alone cause sufficient damage to the biofilm surface, and also drastically increase the drug uptake. However sonoporation is shown to have the most effect when MBs are bound to, or are extremely close to the biofilm surface (or any desired surface), therefore it is desirable to develop targeted MBs for biofilm use [161, 162].

1.4.4 Ultrasound

Ultrasound (US) is a sound wave with frequencies above 20 kHz, which is beyond the upper limit of human hearing [163]. Sound waves are longitudinal waves that propagate energy through the compression and rarefaction of particles in a medium. The particles move parallel to the direction of sound wave, however there is no net transport of the particles themselves. The compression of particles corresponds to high pressure regions, and rarefaction is low pressure, as shown in **Figure 1.13**. When MBs are exposed to an US wave, they too oscillate in tune with the high and low pressure regions.

$$v = \lambda f \tag{1.22}$$

The speed of US (v) is dependent on the wavelength (λ) and frequency (f) of the wave, as shown in Equation 1.22, and varies according to the medium US is travelling

through. For example, the speed of US in air is 330 ms^{-1}, water 1480 ms^{-1}, and soft human tissue 1540 ms^{-1} [164, 165]. These variations are due to differences in density, elasticity, and stiffness of the medium.

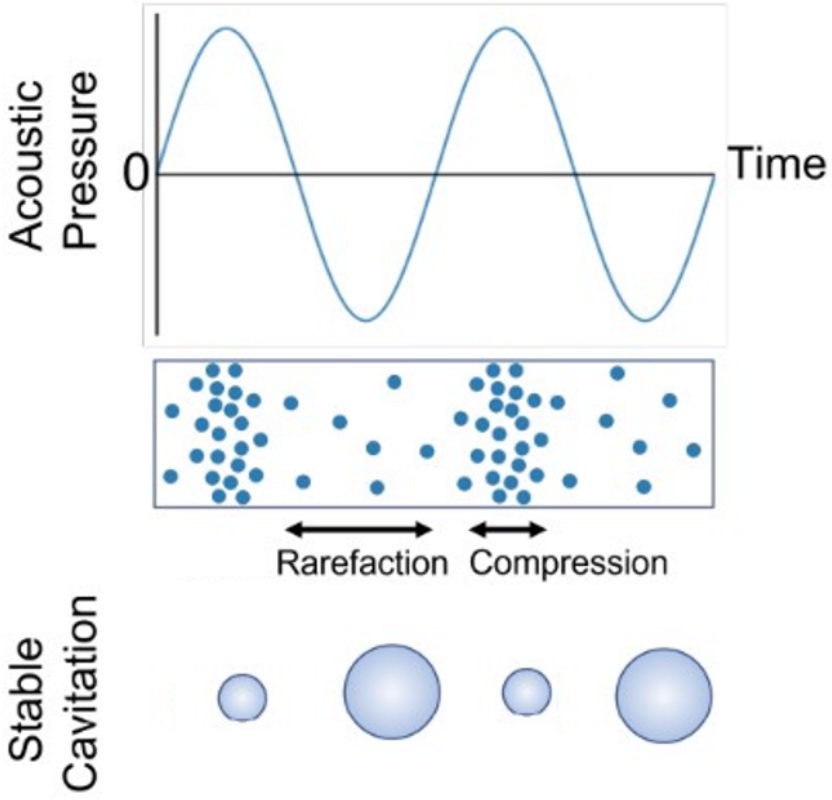

Figure 1.13: Ultrasound (US) waves are longitudinal pressure waves with high acoustic pressure during compressions, and low pressure during rarefactions. MBs expand and contact in tune with the US wave in a process called stable cavitation. Schematic reproduced with permission from [166].

US waves are generated by a transducer which contains a piezoelectric crystal that converts electrical current into sound waves. Once sound waves traverse the material, the reflected signal is detected by the same transducer. As previously mentioned, MBs will undergo volumetric oscillation in tune with the US wave, expanding and contracting with each rarefaction and compression. The presence of the lipid MB shell allows the MBs to withstand higher energy before reaching the point of cavitation. At low acoustic pressures the MB will oscillate linearly, with small, symmetrical oscillations. As acoustic pressure increases, the oscillations become non-linear and eventually result in the violent

collapse of the MB in a process known as inertial cavitation [167].

1.4.5 Microbubble, Ultrasound and Biofilm interactions

Combining MBs and US for therapeutic use against biofilms has many advantages, not limited to the ability to deliver drugs to a specific site. The response of MBs to changing acoustics pressure can lead to two forms of cavitation: stable and inertial, both of which can result in the permeation of biofilm surfaces in a process known as sonoporation.

Low magnitudes of acoustic pressure result in stable cavitation. If the MB is positioned near a surface, microstreaming occurs creating a vortical flow of the surrounding fluid, as demonstrated in **Figure 1.14 a**. Experiments have shown that microstreaming velocities can reach a few mm s^{-1}, at distances over 1mm away [168]. This bulk fluid flow results in shear stresses being exerted on the nearby surface, directing planktonic bacteria away from the biofilm, and potentially causing pores to form. The constant expansion and contraction of MBs during stable cavitation exerts push and pull forces on the biofilm, leading to the eventual breakdown of the surface, shown in **Figure 1.14 b**.

Inertial cavitation occurs when the acoustic pressure is above a certain threshold causing the rapid and unstable expansion of the bubble, where the diameter more than doubles in size within one acoustic cycle. When the MB violently collapses the resulting shockwaves and micro-jets perforate the biofilm surface, **Figure 1.14 c and d**. Micro-jets occur as a result of the close proximity to the surface. During MB collapse, liquid on opposing sides of the MB move differently creating a pressure gradient, which causes a jet of fluid to pass through the MB and penetrate the surface at force [169]. In general, inertial cavitation creates larger pores in the boundary surface than stable cavitation, and is thus preferred for application such as biofilm removal and drug delivery [170].

The efficacy of biofilm disruption is dependent on how close the microbubble is to the surface. While microstreaming can have effects over 1mm away, permeability of cells has been shown to decrease with distance from the surface. Meng *et al.* have shown that the

distance between the cell and the microbubble should be no more than 0.68 the diameter of the microbubble for maximum destruction[161]. It is increasingly popular therefore to create targeted microbubbles which attach to the biofilm surface, maximising cavitation effects.

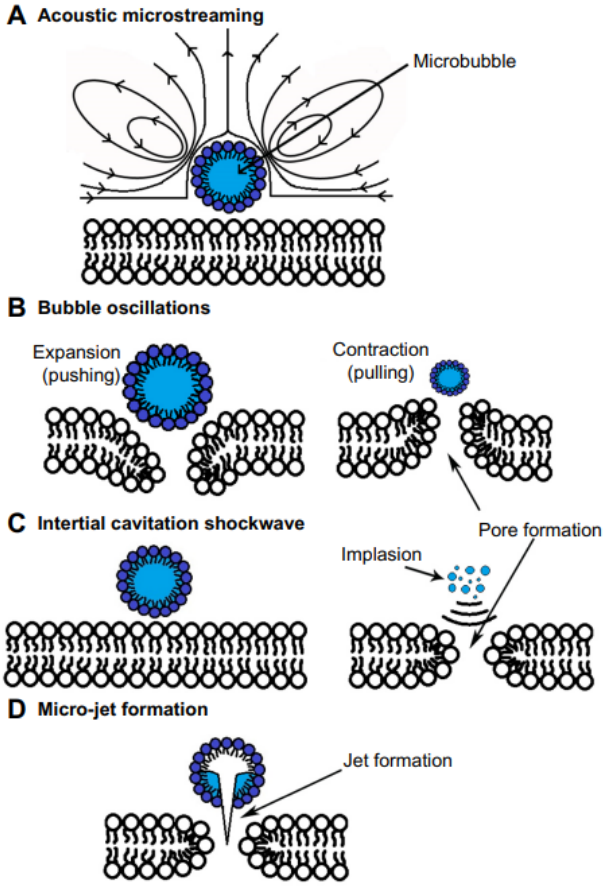

Figure 1.14: Bioeffects of ultrasound induced microbubble cavitation near a surface. Stable cavitation: a) microstreaming, b) pushing/pulling on the surface. Inertial cavitation causing Mb destruction: c) shockwaves, d) micro-jet formation. Figure reproduced with permission from [171].

Many studies have shown that the therapeutic effects of drugs and antibiotics are increased when used in tandem with MBs . In a 2017 study, Lattwein *et al.* coined the term 'sonobactericide', a biofilm treatment strategy that combines US exposure and MBs, with or without therapeutic agents [172]. Their proof-of-principle study demonstrated that the most effective treatment of *S.aureus* biofilms were those treated with antibi-

otics, a recombinant tissue plasminogen activator, MBs and US. A study by Dong *et al.* found *Staphylococcus epidermidis* biofilms treated with MB and US were more sensitive to vancomycin, compared to those treated with US alone or no treatment [173]. A recent study by Xiu *et al.* were the first to include chemical degradation of the biofilm as part of the sonobactericide treatment. The antibiotic piperacillin and Fe_3O_4 nanoparticles formed the MB shell which surrounded an air core. The Fe_3O_4 nanoparticles chemically degrade the biofilm matrix and induces a biofilm immune response of macrophage polarisation into a pro-inflammatory phenotype, which combined with piperacillin achieves increased cell death [174].

LuTheryn *et al.* used nitric oxide MBs with and without antibiotics to treat *Pseudomonas aeruginosa* biofilms. Nitric oxide gas is a signalling molecule that is known to disperse bacteria, and has shown therapeutic properties in wound healing. Nitric oxide MBs caused a 99.8% reduction in biomass when combined with antibiotics, compared to only 84.7% without antibiotics [175]. Previously mentioned studies by Caudwell *et al.* and Kouijzer *et al.* used targeted microbubbles that bound to the biofilm surface to further increase the sonobactericidal effect [159, 160].

When the MB payload is contained in an attached liposome or other nanoparticle, the delivery mechanism is the same. The sonoporation effects can propel the liposome into the biofilm delivering the drug further into the biofilm than would have been achieved otherwise. Liposomes protect sensitive drugs and antimicrobial from external elements that would otherwise degrade them [176]. For example, the antimicrobial peptide IK8 used in this thesis can be degraded by proteolytic enzymes within the bloodstream, therefore to ensure the peptide is delivered intact and safely, encapsulation within a liposome is recommended. Depending on the location of biofilm this may not always be necessary, as treating oral biofilms has the benefit of direct access and does not require MB transport in the bloodstream, however the benefits of encapsulated delivery in conjunction with MB and US may enhance antimicrobial uptake .

Thus far there have been no studies using lipid MB and US, with or without antimicrobials, for the treatment of oral biofilms. However, MBs are well known to have

anti-biofilm effects on oral biofilms as jet streams of naturally occurring air MBs (with no shell) are commonly produced as a result of ultrasonic toothbrushes [142]. Furthermore, microbubbled water, cavitating jet streams, and water flosssers with MBs have all been investigated as ways to remove oral biofilms and improve oral health care [177–180]. Therefore, combining MBs, US and therapeutic agents has promising outcomes on the control and treatment of oral biofilms.

1.5 Project aims and thesis outline

The aim of this project was to develop a method of using microfluidics and RS to characterise *S.salivarius* and *A.naeslundii* multi-species oral biofilms over time, and use MBs, US and IK8 as an alternative method of biofilm treatment. The combination of these techniques in this unique way allows the entire process to be conducted in one self-contained microfluidic environment.

Chapter 2 provides details on the methodologies used to undertake this research on *S.salivarius* and *A.naeslundii* oral biofilms, microfluidics, RS and MBs.

Chapter 3 initially describes the development of a microfluidic platform for multi-species biofilm growth, that is optimal for long term growth, RS analysis, and MB treatment. The chapter goes on to demonstrate how spontaneous RS was used to differentiate between planktonic *S.salivarius* and *A.naeslundii*, and characterise mono- and 2-species biofilms over 5 days using PCA and LDA.

Chapter 4 uses SRS and TPF to further analyse biofilms in ways that were not possible with spontaneous RS in chapter 3. SRS hyperspectral images, SRS z-stacks, and TPF z-stacks were taken of mono- and 2-species (fixed) biofilms on Day 1 and Day 5. Numerous methods of analysis were demonstrated, however k-means clustering was considered reliable and used throughout. The work in this chapter was performed at the EPSRC funded CONTRAST Facility at the University of Exeter.

Chapter 5 describes the use of liposomes, MBs, US and IK8 for 2-species biofilm

treatment. Multiple treatment methods were applied to biofilms grown in 96-well plates, with analysis methods including colony counting and confocal imaging.

Chapter 6 provides a summary of the work in this thesis and discusses how this work can be developed and continued in future works.

Chapter 2

Materials and methods

2.1 Multi-species Biofilm Growth

The oral biofilm model and methods used in this thesis are based on a 5-species biofilm developed by Monika Naginyte [181]. The original 5-species model was a pathogenic biofilm consisting of early colonisers *Streptococcus salivarius* and *Actinomyces naeslundii*, a bridging organism *Fusobacterium nucleatum*, and two pathogenic species *Porphorymonas gingivalis* and *Prevotella intermedia*. The work in this thesis could be extended to the 5 species model, however a 2-species model using *Streptococcus salivarius* and *Actinomyces naeslundii* was chosen to begin with while the method of on-chip Raman analysis was being developed. In the oral cavity, the biofilm typically builds in order from early coloniser to pathogenic, therefore the early colonisers were chosen for the 2-species biofilm as they are the basis of this pathogenic biofilm. This also allowed for extension of the biofilm model if time allowed. For this reason, the 2-species biofilm in this thesis is not the type of sub-gingival pathogenic biofilm one might be looking to treat in oral healthcare, but is a starting model to understand the process of growing multi-species biofilms on-chip, using Raman spectroscopy as a non-invasive real-time method of biofilm analysis, and as a model biofilm for studying treatment using microbubbles.

2.1.1 Bacterial growth

Frozen stocks of *Streptococcus salivarius* and *Actinomyces naeslundii* were stored in a 40% glycerol solution at -80 °C. To culture the bacteria, using a sterile plastic loop 10 μl of each frozen stock was spread onto 5% Horse Blood Columbia Agar (HB-CBA) (Sigma-Aldrich) plates and incubated in an aerobic environment at 37°C for 24 hours, to achieve single colony formation. Three or four single colonies were then transferred to 5 ml of Brain Heart Infusion broth (BHI) (Sigma-Aldrich) and incubated at 37°C, shaking at 200 RMP for 24 hours.

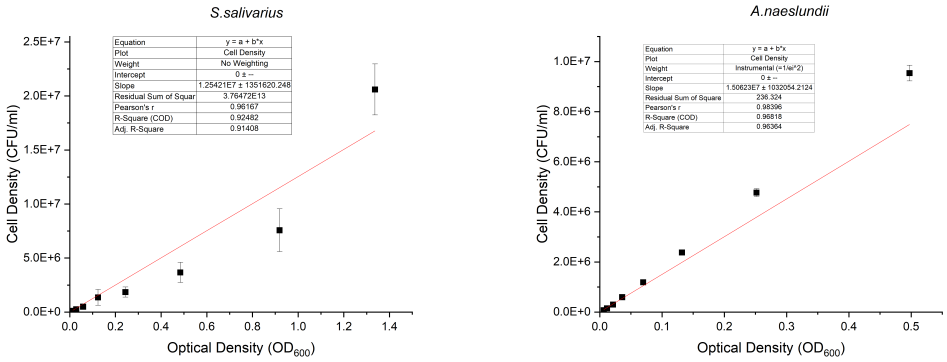

(a) **(b)**

Figure 2.1: Cell density (CFU/ml) v Optical density (OD_{600}) bacterial calibration curves for a) *S.salivarius* and *A.naeslundii*. For OD_{600} = 0.2, CFU/ml = 2.5×10^6 and 3×10^6 for *S.salivarius* and *A.naeslundii* respectively.

Cell density (CFU/ml) v optical density (OD_{600}) calibration curves for *S.salivarius* and *A.naeslundii* were taken. Bacteria was grown in broth as described above for 24 hours, diluted 8 times in a 2-fold serial dilution. The optical density of each dilution was taken, and the sample then spread on an agar plate and incubated at 37°C for 24 hours. After 24 hours, the number of colony forming units were counted for each dilution and plotted against the corresponding OD_{600}. The calibration curves for both species are shown in **Figure 2.1**.

2.1.2 Media composition

Media used for biofilm culture is designed to be more reflective of the oral environment in vivo, than standard nutrient media, thus is a composite of 3 media types - basal medium, artificial saliva, and fetal bovine serum. Specific details of basal medium and artificial saliva can be found in **Table 2.1**. Basal medium is a nutrient-rich medium which was successfully used to culture multispecies oral biofilms by McKee *et al* [182] , and was later modified by Bradshaw *et al* [183] to include artificial saliva. Previous work by Naginyte found that a protein rich media combination was optimal for this specific biofilm growth: 20% fetal bovine serum (Sigma-Aldrich), 20% basal medium, and 60% artificial saliva [184].

Biofilm Media Composition		
Basal Media	Proteose peptone (Sigma-Aldrich)	10 (g/L)
	Tryptose peptone (Sigma-Aldrich)	5 (g/L)
	Yeast extract (Fisher Scientific)	5 (g/L)
	L-Cysteine hydrochloride (Sigma-Aldrich)	0.5 (g/L)
	Hemin (Sigma-Aldrich) *	0.00002 (g/L)
	Menadione (Fluorochem Ltd)*	0.00004 (g/L)
Artificial Saliva	Hog gastric mucin (Sigma-Aldrich)	2.5 (g/L)
	NaCL (Sigma-Aldrich)	0.381 (g/L)
	KCl (FIsher Scientific)	1.114 (g/L)
	KH_2PO_4 (Sigma-Aldrich)	0.738 (g/L)
	Ascorbic Acid (Fisher Scientific)	0.002 (g/L)
	Urea (Fisher Scientific)*	9 mM
	Arginine (Sigma-Aldrich)*	5 mM

Table 2.1: Composition of media components. *filter-sterilised, added after autoclaving. The pH of the media were adjusted to 7.4.

2.1.2.1 Heat-inactivation of Serum

Fetal-Bovine serum, used in culture media, was heat-inactivated to inactivate the complement cascade. Serum was heated to 56°C for 30 min in a water bath, aliquoted to 50 ml and stored at -20°C.

2.1.2.2 Human Saliva Sterilisation

Human saliva was sterilised using the protocol by Palmer et al [185]. A volunteer was asked to drool saliva into a falcon tube at least 1.5 hours after eating, drinking and tooth brushing. Saliva was stimulated via mastication of Parafilm and stored on ice. DL-dithiothreitol (Sigma-Aldrich) was added for a final concentration of 2.5 mM, and gently stirred on ice for 10 minutes to reduce protein aggregation. Saliva was then centrifuged at 17,000 g for 25 minutes. The saliva supernatant was removed and diluted 50% in sterile PBS. Diluted saliva was filtered through a 0.22 μm pore-size low-protein-binding filter (Millex-GV, Merck), and frozen at -20°C in 1 ml aliquots. To check the efficiency of the protocol, 50 μl saliva was inoculated onto HB-CBA plates and incubated at 37°C for 24 hours.

2.2 Microfluidic Device Fabrication

Microfluidic device fabrication was a three step process: device designs were first created in AutoCAD, photolithography was used to create a negative photo resist master wafer of the design, and the PDMS devices finally created using soft lithography.

The original device used in the microfluidic set up version 1, was designed by Dr Julia Gala de Pablo. The device used in version 2 and all subsequent experiments was designed and fabricated by Aileen Delaney.

2.2.1 Photolithography

A 3-inch (76.2 mm) diameter silicon wafer (PI-KEM Ltd, Tamworth, UK) was cleaned with acetone, MilliQ, and dried with compressed air. The wafer was placed in an oven at 200°C for 30 minutes to fully dehydrate. The wafer was then removed and left to cool to room temperature, **Figure 2.2a**. The SU-8 2075 negative photoresist (MicroChem, Warwickshire, UK) has a high viscosity so was removed from the fridge and left to reach room temperature for 1 hour to aid in pouring. Approximately 3 ml of SU-8 2075 was spin-coated onto the wafer. A maximum spin rate of 1350 RPM was applied to achieve SU-8 coating thickness between 150 - 170 μm. A series of incrementally higher spin speed steps were used to encourage the even spread of the SU-8 photoresist across the surface of the wafer, **Figure 2.2b** . To remove any solvent remnants, the wafer underwent a soft bake whereby the wafer was placed on a room temperature hot plate, the temperature was increased to 55°C (which took approximately 5 minutes to reach), and then left for 55 minutes to bake, **Figure 2.2c**. The hot plate was then turned off and the wafer was left to cool for 30 minutes.

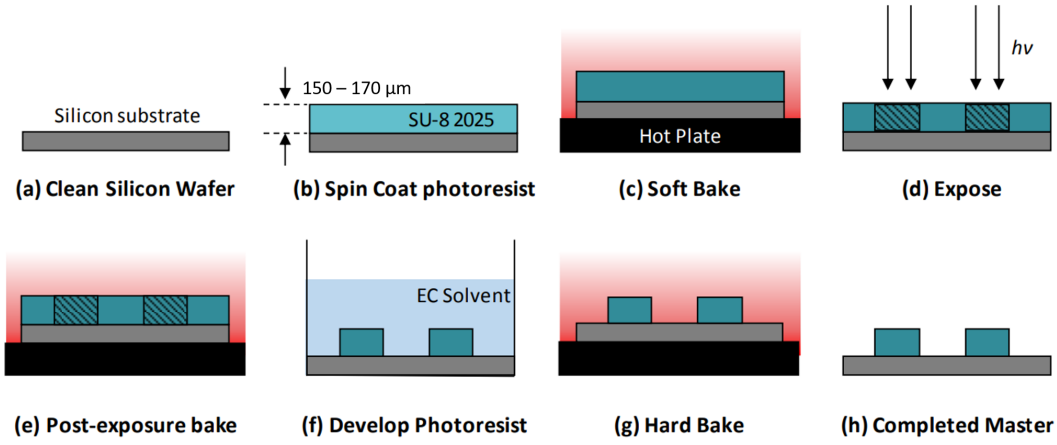

Figure 2.2: Schematic demonstrating the photolithography process for creating an SU-8 silicon master for microfluidic devices. a) clean silicon wafer, b) spin coat photoresist, c) soft bake, d) exposure, e) post-exposure bake, f) develop photoresist, g) hard bake, and h) completed master. Figure reproduced with permission from [186].

Microfluidic designs were created in AutoCAD (AutoDesk, San Rafael, CA, USA) and arranged across the wafer using CleWin (WieWeb, Hengelo, The Netherlands). As the SU-8 is a negative photoresist, it crosslinks when exposed to UV-light. Direct-write

laser (DWL) lithography was used to etch the designs onto the SU-8 layer using a 2 μm, 375 nm laser. Only the areas etched with the laser become crosslinked, leaving the rest of the wafer still soluble, **Figure 2.2d**. A dose of 400 mJ/cm^2 was used for these microfluidic designs. A low dose is useful for small features and precision etching but may result in adhesion problems between to wafer and SU-8, whereas a high dose can cause overexposure and result in bell-shaped channels which are wider than desired.

The wafer then underwent a post-exposure bake to complete the polymerisation of the SU-8 using the same temperature control as the soft-bake, **Figure 2.2e**. The wafer was then left to cool for 30 mins. Wafers were developed by submerging in ethylene carbonate (EC) solvent for 10 mins to remove any non-crosslinked SU-8, and rinsed with isopropanol (IPA) to ensure all remnants had been removed, **Figure 2.2f**. The wafer underwent a final hard bake at 180°C, slightly below SU-8 glass transition temperature of 210°C, for 15 mins to remove any cracks in the SU8, **Figure 2.2g**. The wafer was then complete and ready for PDMS device fabrication, **Figure 2.2h**. The height of the developed devices were measured using a surface profiler (Dektak® XT, Bruker, Billerica, MA, USA). A 2 μm stylus tip performed a line scan across the channels, using a force of 2 mg, to measure the height profile of the devices at several positions. Profiles of the measured heights were obtained and averaged to determine the overall height of individual devices.

2.2.2 Soft lithography

Microfluidic devices were made by casting the wafer design into polydimethylsiloxane (PDMS). PDMS was prepared by mixing the elastomer base and curing agent (Sylgard 184, Dow Corning, Midland, MI, USA) at a 10:1 ratio, and centrifuging at 4000 RPM for 2 mins to remove any air bubbles. The PDMS mixture was poured onto the wafer in a petri dish to achieve a 1 mm thickness, **Figure 2.3a**, and left under vacuum for 1 hour to remove any excess gas dissolved in the PDMS. The PDMS was then cured in an oven at 75°C for at least 1 hour. Once set the solid PDMS was peeled off the wafer, **Figure 2.3b**, the devices cut out with a scalpel and the inlet/outlet holes were punched

out using a 2 mm biopsy puncher, **Figure 2.3c**.

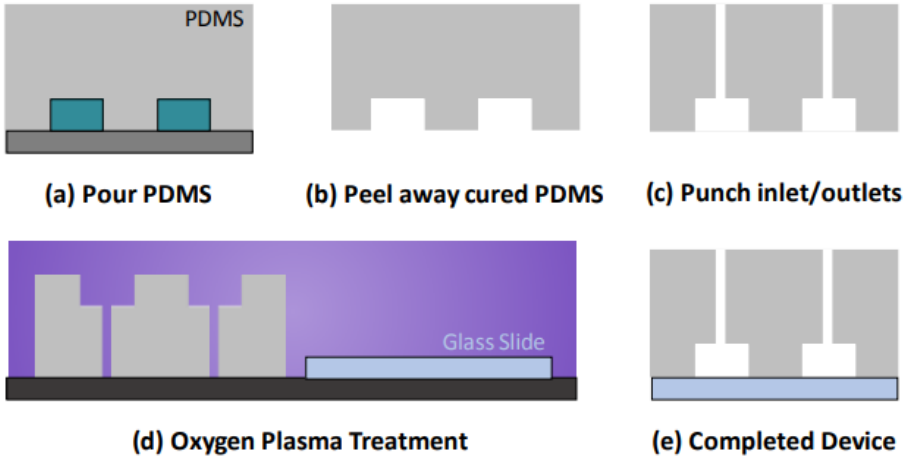

Figure 2.3: Schematic showing the soft lithography process of creating PDMS microfluidic devices. a) PDMS poured over the master wafer, b) cured PDMS peeled away from the wafer, c) devices cut out and inlets/outlets punched using biopsy punch, d) PDMS and glass slide undergo oxygen plasma treatment, and e) PDMS and glass slide are bound together and devices are completed. Figure reproduced with permission from [186].

Individual devices were bound to glass cover slips (Thorlabs Inc. Newton, NJ, USA) using oxygen plasma treatment. Magic tape was applied to the PDMS and cover slips to remove any debris, which were then placed inside the plasma cleaning chamber (Zepto, Diener electronic GmbH, Ebhausen, Germany) and treated for 30 s at 0.3-0.5 mbar O_2, **Figure 2.3d**. Plasma treatment oxidises the PDMS and glass substrates. Plasma treatment with oxygen replaces hydrocarbon groups with hydroxyl groups, increasing the number of Si-O-H groups present on the surface. The PDMS and glass cover slips were then pressed together with light pressure, forming strong covalent Si-O-Si bonds, **Figure 2.3e** [187]. The devices were then placed in the oven at 75°C for 30 mins.

Devices were created at a 1 mm thickness to reduce ultrasound attenuation during experiments. Though not all experiments would require ultrasound, devices were the same across all experiments for consistency. Due to the thin PDMS layer, an extra 5 mm block of PDMS was bound to the inlet/outlet ends of the device to increase the stability of the tubing attachments. These were bound using oxygen-plasma treatment. Note: due to time limitations, no experiments were performed where ultrasound was used on chip.

2.3 Biofilm Growth

2.3.1 Microfluidic set up

The microfluidic device, shown in **Figure 2.4a**, had a single chamber with two inlets, one for media and one for bacteria, buffer and fluorescent dye injection, and one waste outlet. The growth chamber was 12 mm x 2 mm x 150 μm. Sections of 1.3-mm ID Tygon tubing (Masterflex, Cole-Parmer) were cut to length, as described in **Figure 2.4b**. Tubing, metal device connectors, media flasks and waste flasks were all sterilised for 15 minutes at 121°C in a vacuum autoclave (Sun 23L Class B, MingTai, Ningbo, China).

Two- and three-way taps and luer lock connectors were soaked in 70% ethanol for 30 minutes and dried under UV for 15 minutes in a sterile class II cabinet (Guardian MSC T800, Monmouth Scientific Ltd). Following sterilization, the full system was assembled, and 4 mm diameter 0.22 μm filters were attached to the lids of media and waste lids to allow pressure equalization. 70% ethanol was then injected into the system, filling the microfluidic device, and irradiated with UV for 30 minutes for final sterilisation. The system was then rinsed with 10 ml of PBS to remove any traces of ethanol. A 5 ml Plastipak syringe of PBS was attached to the buffer inlet and a 20 ml syringe of Biofilm Media was attached to the media inlet. 1 ml media was injected to fill the tubing.

2.3.1.1 Microfluidic Biofilm Growth

A salivary pellicle on the surface of the chamber better mimics the tooth surface and helps with bacterial adhesion. 500 μl sterile human saliva was injected into the chamber via the injection loop and all taps were closed to prevent fluid flow. The device was incubated for 1 hour at 37°C, then rinsed with 500 μl PBS at a constant rate of 20 μl/min to remove any excess.

Bacterial solution was diluted to OD_{600} = 0.2 using a SpectraMax M2e well plate reader (Molecular Devices LLC), corresponding to 2.5×10^6 and 3×10^6 CFU/ml for

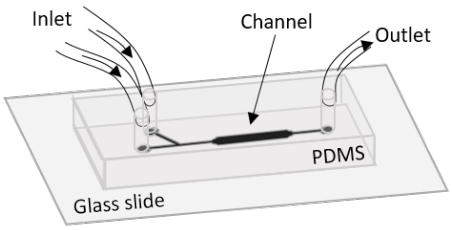

(a)

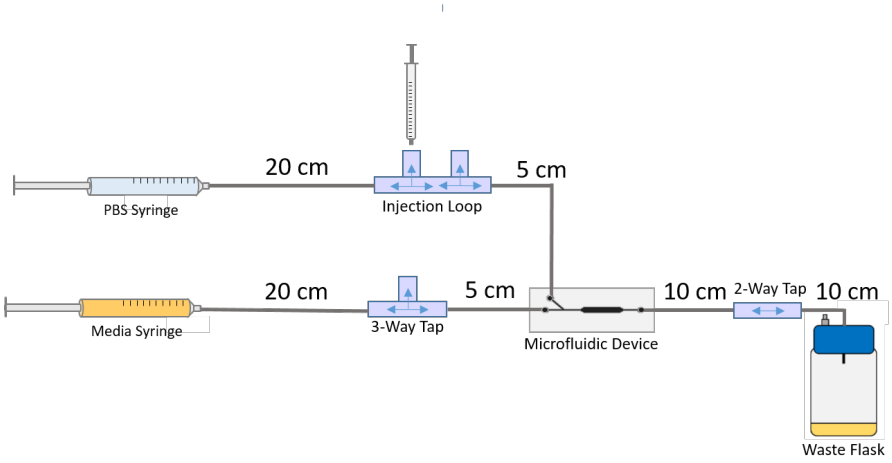

(b)

Figure 2.4: a) Microfluidic device. Chamber dimensions 12 mm x 2 mm x 150 μm. b) Microfluidic biofilm growth system. Each section of ID 1.3 mm Tygon tubing is cut to a specific length, 20 ml syringes used for inlets, 1ml syringe for bacteria injection.

S.salivarius and *A.naeslundii*, respectively. Mono-species and 2-species biofilms were grown. For 2-species, *S.salivarius* and *A.naeslundii* were mixed at a 1:3 ratio and 500 μl of bacterial solution was injected into the injection loop. The system was transferred to the incubator and connected to the syringe pump (**Figure 2.5**). Bacteria was injected into the chamber at a rate of 20 μl/min for 25 minutes after which all taps were closed and the device was incubated statically at 37°C for 1.5 hrs to allow bacteria to adhere to the surface. After 1.5 hrs the media flow was started at a constant rate of 20 μl/min (or a shear stress of 0.33 dynes/cm^2). The syringe media was replenished every 24 hours. The biofilm was cultured for either 1,2,3,4 or 5 days.

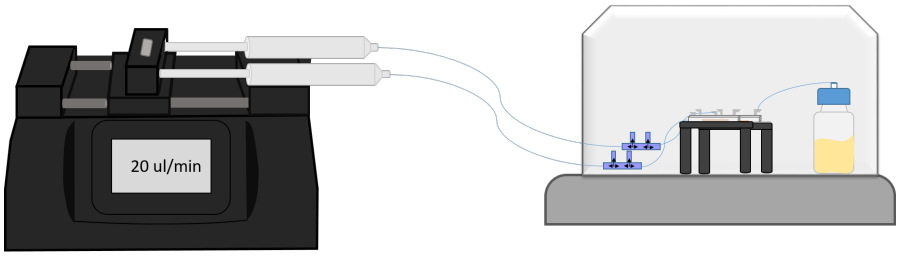

Figure 2.5: Schematic showing the microfluidic biofilm growth set up. Fluid flow is controlled by a dual syringe pump (allowing 2 biofilms to be grown at once), tubing is fed into an incubator where the microfluidic chip is placed, and connected to a waste flask.

Following biofilm growth, waste was emptied into a container of 1 % Virkon solution (Virkon disinfectant powder; DuPont), and all two- and three- way taps, luer lock and metal device connectors were first rinsed with and then soaked in Virkon for 24 hours. Following that, all parts were rinsed 3 times in DI water and a pipe cleaner was used to remove any remaining debris. Tubing and microfluidic devices were autoclaved at 121°C for 15 mins and disposed of.

2.3.1.2 On Chip Fluorescent staining of biofilms

Biofilms were live/dead stained using the Filmtracer™ LIVE/DEAD Biofilm Viability Kit containing SYTO™ 9 and propidium iodide (PI). 3 μl of each dye were added to 1 ml MilliQ. 500 μl was added into the injection loop and then injected on chip by the syringe pump at 20 μl/min. The chip was covered in foil and left for 20 mins. The chip was rinsed with PBS for 20 mins at 20 μl/min to remove any remaining stain.

	S.salivarius	***A.naeslundii***
Oligo name	STR405	ANA103
DNA/RNA	DNA	DNA
Sequence	tagccgtccctttctggt	cggttatccagaagaagggg
Length	18	20
End modification dye	5':Cyanine 3 3':	5':Cyanine 5 3':
Ex/em	555/569 nm	651/670 nm
Probe Concentration	20 ng/ml	20 ng/ml

Table 2.2: FISH probes purchased from Biomers.net (Germany) for *S.salivarius* and *A.naeslundii*. Protocol from Thurnheer *et al* 2001 and 2004 [188, 189].

2.3.1.3 FISH on planktonic bacteria

Fluorescent probes were purchased from Biomers.net (Germany), details of which are described in **Table 2.2**, and details of the hybridisation and washing buffers used are shown in **Table 2.3**. FISH protocols were followed from Thurnheer *et al* 2001 and 2004, and Lee Lab protocol [82, 188, 189]. Bacteria samples were washed via centrifugation and fixed in 50% ethanol overnight at -4°C. 20 μl bacteria was dried onto a clean glass coverslip for 30 mins in a class II cabinet. Once dried onto the slides, samples were permeabilised by adding 20 μl Lysozyme (70,000 U/ml) (3.5 mg/ml dissolved in Tris/HCl pH 7.5 and 5 mM EDTA) to the slide for 15 min at 37°C. Slides were rinsed with MilliQ, then bacteria dehydrated sequentially with 50%, 80% and 99% ethanol for 3 min each. Slides were rinsed and gently dried with compressed air.

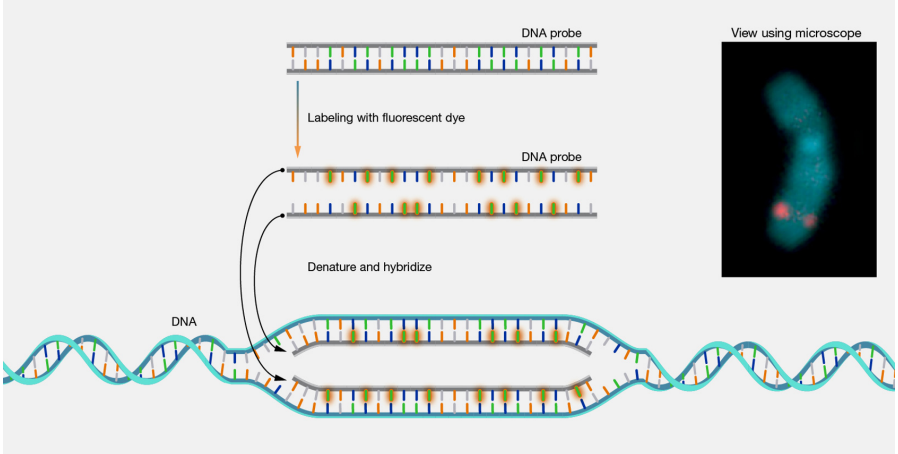

Figure 2.6: Fluorescence *in situ* hybridisation (FISH) process. DNA probes are fluorescently labelled, the sample denatured and probes hybridised to the sample. Figure reproduced from National Human Genome Research Institute with permission [190].

	Hybridisation Buffer	Washing Buffer
S.salivarius	0.9 M NaCL 20 mM Tris/HCL 0.01% SDS 25% Formamide	0.159 M NaCL 20 mM Tris/HCL 0.01% SDS 5 mM EDTA
A.naeslundii	0.9 M NaCL 20 mM Tris/HCL 0.01% SDS 10% Formamide	0.45 M NaCL 20 mM Tris/HCL 0.01% SDS

Table 2.3: Hybridisation and washing buffer concentrations used during FISH, for probes binding to *S.salivarius* and *A.naeslundii*. Formamide concentration is dependent on the probe, which determines the NaCl concentration. EDTA is only required for formamide concentrations above 20%. Protocol followed from Thurnheer *et al* 2001 and 2004, and the Lee Lab protocol [82, 188, 189].

50 ml Falcon tubes were used as hybridisation chambers. A section of paper towel was first soaked in hybridisation buffer and placed into the Falcon tube to maintain humidity during the process. 20 μL of buffer containing 20 ng/μl of probe was added to the sample, and the slide carefully placed horizontally into the falcon tube and sealed. The sample was incubated at 46°C for 90 mins. 50 ml of washing buffer was prepared in a Falcon tube and pre-heated to 48°C. The hybridisation process can be seen in **Figure 2.6**. After hybridisation, the slide was removed and gently rinsed in washing buffer, and then submerged in a washing buffer tube for 20 mins at 48°C. Samples were protected from photo-bleaching by being covered in foil. When working with a mixed bacteria sample, the sample which has the highest formamide concentration was performed first, then the whole process repeated for the second sample. In this case, *S.salivarius* was hybridised first. After the final washing step, the samples were rinsed in cold MilliQ, gently dried with compressed air, and stored in a cool place in a sealed petri dish covered in foil. A schematic of this process can be seen in **Figure 2.7**.

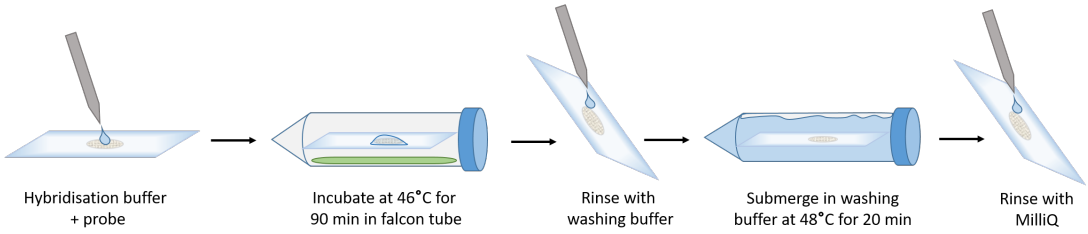

Figure 2.7: Schematic showing hybridisation and washing steps for fluorescence *in situ* hybridisation (FISH) on planktonic bacteria. First hybridisation buffer containing the probe is added to the dried sample, then placed in a falcon tube with a paper towel soaked in buffer to maintain humidity, then rinsed with washing buffer, submerged, then rinsed in MilliQ.

2.3.1.4 FISH on Chip

Performing FISH on microfluidic chips follows the same general protocol as described in **Section 2.3.1.3** but requires some modifications and more stringent planning. To ensure each step smoothly follows on from one another, the amount of dead volume in the tubing had to be kept to a minimum as any deviation from the protocol could reduce the efficacy of the process. Tubing connecting the injection loop to the chip was reduced to 3.5 cm (approx. 50 μl volume) to reduce time and dead volume. As previously, the process is performed first with the probe containing the highest formamide concentration, *S.salvarius*, then repeated with *A.naeslundii*.

Biofilms were first fixed with 4% paraformaldehyde, which was injected on chip at 20 μl/min and incubated for 1 hour at 4°C. Biofilm was rinsed with PBS for 20 mins. 200 μl lysozyme was injected on chip, incubated for 15 min at 37°C, then rinsed with PBS for 20 mins. The biofilm was dehydrated with 50%, 80% and 99% ethanol under flow. 100 μl of 50% ethanol was first injected into the injection loop middle chamber (which holds 300 μL), followed by 100 μl of 80% and 100 μl of 99% ethanol. Ethanol was then injected on chip at 20 μl/min until all 300 μl had pass through the chip. The biofilm was rinsed with PBS for 5 mins. 300 μl of hybridisation buffer containing the first probe, *S.salivarius*, was added into the loop and injected on chip and incubated at 46°C for 90 min. 300 μl of washing buffer was then added into the loop and injected on chip, incubated at 48°C for 15 min. The hybridisation and washing process was then repeated with the *A.naeslundii* probe. Finally, the biofilm was rinsed with MilliQ for 5

mins, and stored at 4°C covered in foil until use.

2.3.2 Well plate biofilm growth

Well plate biofilms were grown in a way to best replicate those grown microfluidically. 100 μl saliva was injected into wells of a 96-well plate (μClear, Greiner Bio-One Ltd, Kremsmünster, Austria) and incubated statically at 37°C for 1 hour. Each well was rinsed thrice with PBS. Bacteria was diluted to OD_{600}=0.2 in BHI, mixed together at 1:3 (*S.salivarius*:*A.naeslundii*) and 200 μl was added to each well and incubated statically at 37°C for 2 hours. After incubation the innoculum was removed from the wells and 200 μl of biofilm media was added. Plates were incubated at 37°C, shaking at 200 RMP for 24 or 48 hours.

2.3.2.1 Crystal Violet Staining

Crystal violet (Alfa Aesar, Haverhill, MA, USA) solution was prepared to a stock concentration of 1% (mass/vol). Crystal violet powder was dissolved in DI water with 1% (vol/vol) methanol added to aid solubility, and then diluted to give a 0.1% solution for use as a biofilm stain. Biofilms were first fixed with 200 μl methanol for 30 minutes and washed a further three times with PBS. To stain, 100 μl of 0.1% crystal violet solution was added to each well and left at room temperature for 15 minutes. Wells were then washed five times with DI water to remove excess CV stain until the removed waste was visibly clear. Biofilms were then left to dry overnight at 37°C to remove the remaining wash fluid. CV stain was solubilized with 200 μl 33% acetic acid solution. Well plates were shaken at 200 RPM for 15 minutes to aid this process, and the absorbance at 570 nm was measured using a well plate reader using either a point scan or 9-point well scan.

2.3.2.2 Fluorescent staining

Live/dead staining of well plate biofilms was performed using SYTO™ 9 and propidium iodide (PI) stain kit. The stain was prepared to the required volume, adding 3 μl of each dye for every 1 ml MQ. 100 μl of stain was added to each well and covered in foil for 20 minutes. Wells were washed three times with PBS to remove any remaining stain solution. A well plate reader was used to measure the fluorescence of SYTO™ 9 (Ex: 485 nm / Em: 498 nm) and PI (Ex: 535 / Em: 617 nm).

2.4 Microbubble Formation

2.4.1 Lipid preparation

The standard microbubble (MB) lipid composition used was 95 mol% DPPC (Lipoid GmbH, Ludwigshafen, Germany) and 5 mol% DSPE-PEG2000 (Lipoid GmbH, Ludwigshafen, Germany). All lipids were purchased in powdered form and stored at -80°C. Stock solutions were prepared by dissolving the lipids in a 1:1 mixture (vol/vol) of chloroform:methanol and stored at -20°C. Lipids were added to a glass vial at their required mol% and dried under a steady stream of nitrogen for 40 mins to form a thin film. Once dried lipids were placed in a vacuum desiccator overnight to remove any remaining solvent. Dried lipids were either used immediately or stored at -20°C until further use.

MB lipids were resuspended in a PBS-1% glycerol solution to a concentration of 2 mg/ml. Lipids were resuspended by vortexing and then tip sonication for 30 mins until the lipid solution was a cloudy white mixture.

2.4.2 MB production via mechanical agitation

MBs are produced when a vial of lipid solution saturated with gas is vigorously shaken. This method of MB production was preferred for its simple and rapid generation of MBs. MB lipid solution was prepared as previously described in a 1 ml vial, and perflu-

orobutane gas was bubbled through the solution for 2 mins until the vial head-space was saturated. The vial was sealed with para-film to prevent leakage and placed in a dental amalgamator (ESPE CapMix™, 3M, Saint Paul, MN, USA) and shaken for 45 seconds at a rate of 4300 oscillations per minute.

2.4.3 MB analysis

The size and concentration of MBs samples was determined via image analysis using a MATLAB (The MathWorks Inc, Natick, MA, USA) script written by Damien Batchelor [191].

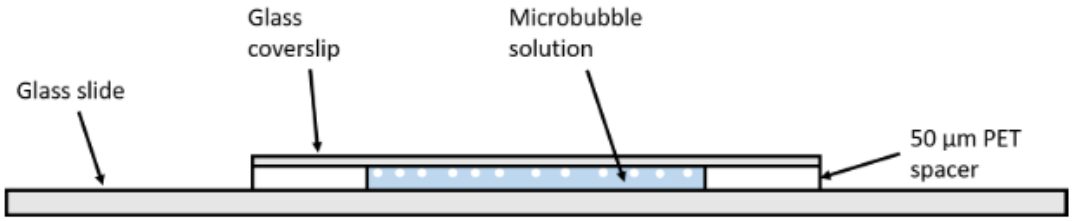

Figure 2.8: Schematic of a 50 μm chamber used to capture bright-field images of MBs for analysis. Schematic reproduced with permission from [2].

The MB samples were imaged using a 50 μm chamber as shown in **Figure 2.8**. The chamber consisted of two 50 μm thick polyethylene terephthalate (PET) film spacers (Goodfellow Cambridge Ltd, Huntingdon, UK) placed approximately 20 mm apart on a 1 - 1.2 mm thick glass slide, with a 20 x 20 mm glass coverslip on top. The MB solution was typically diluted 50x in PBS and injected into the chamber between the glass slide and coverslip using capillary action. The slide was inverted 3 minutes before imaging to allow all MBs to rise to the same focal plane. 10 - 15 bright field images were taken per sample using 60x objective on a Nikon 90i microscope, and the images ran through the MATLAB script for analysis.

The MATLAB script increases the contrast of the images, performs a binarization, fills circular objects, measures the circularity, and applies user set parameters to the fittings to obtain optimal results. The user can set the binarization threshold, which was typically chosen to be between 0.45 - 0.55, as well as the circularity detection threshold

which was set to be 0.75 - 0.85. The images were scaled accordingly so the size of the MBs could be determined based on number of pixels, and the concentration calculated using the dilution factor and number of MB detection's per image area. A histogram is produced detailing the average size and concentration of the sample, an example of which is seen in **Figure 2.9**.

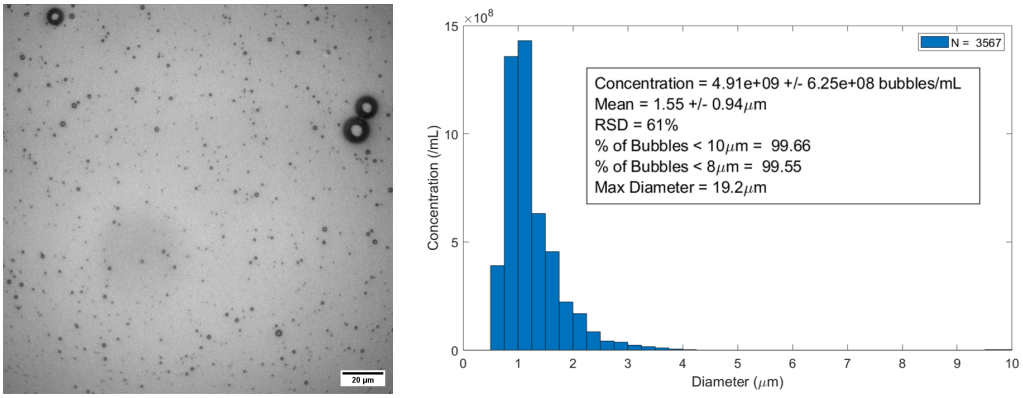

(a) **(b)**

Figure 2.9: MB image and size and concentration histogram produced by a MATLAB script which analyses MB images. Script written by Damien Batchelor [191].

2.5 Liposomes

2.5.1 Liposome formation

Liposomes were typically comprised of 32.5% DSPC (Lipoid GmbH, Ludwigshafen, Germany), 32.5% 23:2 Diyne-PC (Avanti Polar Lipids, AL, USA), 30% Cholesterol (Sigma-Aldrich, St Louis, MO, USA), and 5% DSPE-PEG2000 (Lipoid GmbH, Ludwigshafen, Germany). Liposomes without Diyne-PC were formed at (65:30:5) ratio of DPSC:Cholesterol:DSPE-PEG2000. Lipids were dried to a mass of 10 mg/ml.

Diyne-PC was dissolved in chloroform and dried under nitrogen to form lipid films at 10 mg/ml, and stored at -80°C until needed. Lipids were combined at the desired concentration in an amber 1 ml vial and dried under nitrogen for 40 mins to form a thin film. Once dried the vials were placed in a vacuum desiccator overnight to remove any

remaining traces of chloroform:methanol. Lipid films were either used immediately or stored at -80°C until needed.

To form liposomes, 1 ml of resuspension solution was added to the vial, placed on a hot plate and heated to 65°C, which is 10°C above the gel-fluid transition temperature of the most abundant lipid (DSPC T_m = 55°C). The solution was left on the hot plate gently stirring for 20 mins to form vesicles. The resuspended lipid solution was extruded through 800 nm then 400 nm polycarbonate membrane filters (Whatman plc, Maidstone, UK) 11 times to homogenise the liposome sample. The extrusion block was pre-heated to 65°C to maintain constant temperature. Liposomes were stored at 4°C until use.

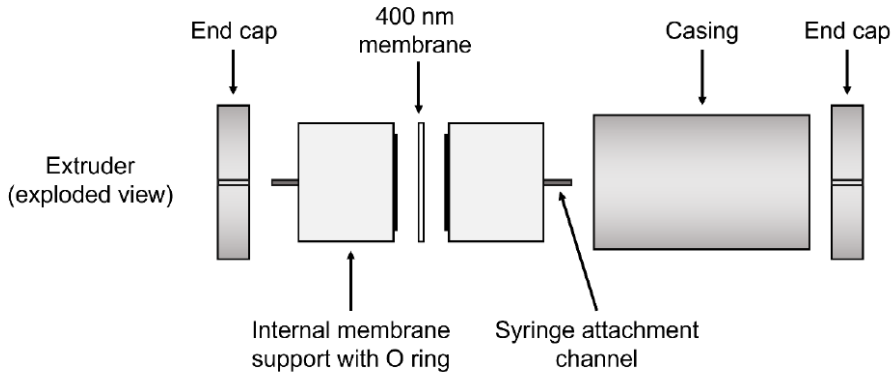

Figure 2.10: Components of the extruder used for liposome homogenisation. Not shown, the glass syringes used for sample transfer [2]

2.5.2 Fluorophore-loaded liposomes

Calcein was the fluorophore of choice for a liposome leakage assay. Calcein was dissolved in PBS and a few drops of 10 M NaOH at 100 mM so that it was in its self-quenched state. NaOH is required to ensure calcein remains in solution at such a high concentration. Liposomes were prepared as described above in **Section 2.5.1** with 100 mM calcein as the resuspension solution, and stored at 4°C. A Sephadex G-25 size chromatography column was used to clean the liposome sample, removing excess calcein. PBS was then gently flowed through the column until twice the volume of the column had passed through the gel. The calcein-liposome suspension was then added to the surface of the

gel and was gently eluted using PBS. When the solution exiting the column became slightly coloured, the solution was then collected in 0.5 ml increments.

2.5.3 AMP loaded liposomes

IK8 loaded liposomes were fabricated by rehydrating the thin lipid film in 5 mg/ml IK8 dissolved in 95 % MilliQ and 5% x10 PBS. Following extrusion, liposomes were stored at 4°C. A 0.5 – 3 ml 20 kDa MWCO Slide-A-Lyzer™ cassette (ThermoFisher Scientific, Waltham, MA, USA) was placed in DI water for 2 minutes to hydrate. Liposomes were transferred into the cassette using a needle, and the cassette was allowed to float in a 2 L bucket of DI water, stirring at 200 RPM. Water was replaced after 6 hours to maintain a sufficient diffusion gradient. After 18 - 20 hours the liposome sample was removed and transferred to an eppendorf. This process is demonstrated in **Figure 2.11**. Samples were stored in the fridge at 4°C until required.

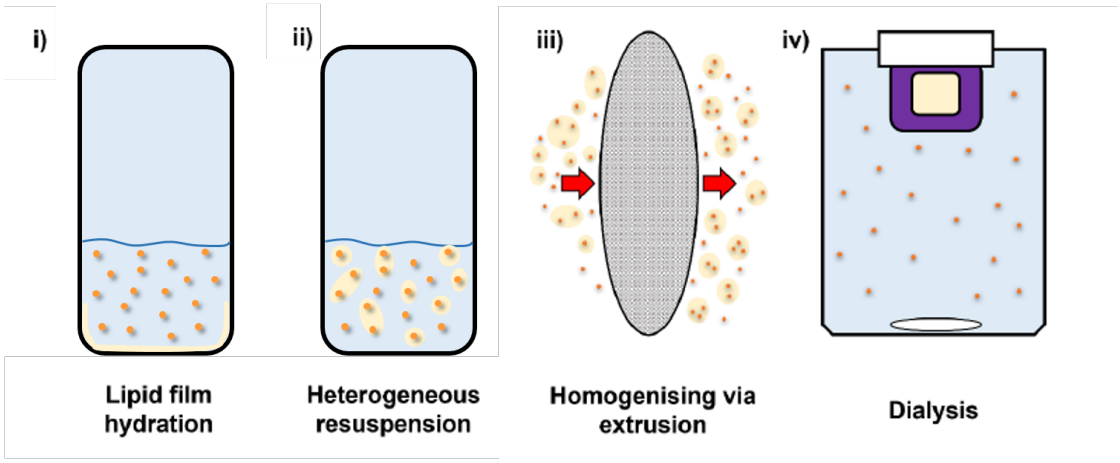

Figure 2.11: Schematic summarising the liposome fabrication process used to prepare AMP-loaded liposomes. From left to right, i) lipid film (yellow) hydration with IK8 solution (orange), ii) the resulting heterogenous liposome suspension (yellow circles) following 20 mins of heated resuspension, iii) liposomes homogenised via extrusion, iv) removal of un-encapsulated IK8 by dialysis using a 20 kDa MWCO dialysis cassette. Figure modified from [2].

2.5.4 UV polymerisation of Diyne-PC liposomes

After liposome fabrication and necessary cleaning steps, liposomes containing Diyne-PC were cross-linked using a 254 nm lamp (2.8 mW/cm^2). Liposomes were placed in a 1 ml quartz cuvette, 1 cm distance from the lamp, and exposed to UV for 15 mins. For control samples, liposomes were exposed to UV for a range of 0 - 90 mins.

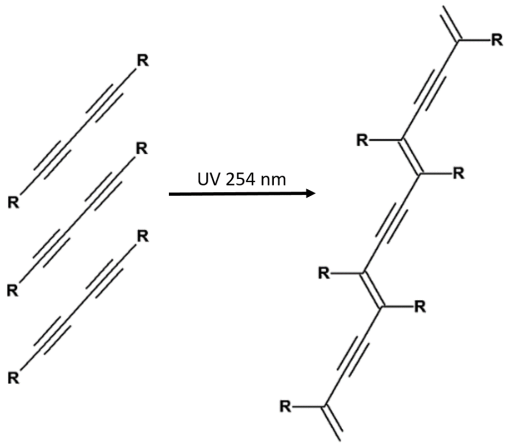

Figure 2.12: Polymerisation reaction of Diyne-PC.

2.6 Liposome Characterisation Techniques

2.6.1 Dynamic light scattering

Dynamic light scattering (DLS) is a technique used to determine the size distribution of particles within a solution. DLS was performed using a Zetasizer Nano ZS with a 4 mW He-Ne laser at 633 nm and a measurement angle of 173°. Liposome samples were typically diluted 10,000x in MilliQ, added to a polystyrene cuvette, and measured three times, of which the average was taken to find the size distribution and polydispersity.

In order to determine the size of particles within a solution, a monochromatic laser source is incident on the sample creating a scattering pattern as light is scattered by the particles and interferes constructively or destructively. As the particles are constantly diffusing with Brownian motion, the intensity of the scattering patterns fluctuates therefore

information regarding the dynamic motion of the particles may be obtained by observing the scattering intensity fluctuations over time, otherwise known as the autocorrelation function. For a monodisperse sample, the autocorrelation function can be written as an exponential with a time decay,

$$g(t) = e^{-q^2 Dt} \tag{2.1}$$

determined by the translational diffusion coefficient of a particle, D, and the length of the scattering vector q, where $q = \frac{4\pi n}{\lambda} \sin \frac{\theta}{2}$. The hydrodynamic radius of the solute, R, can be extracted from this equation by relating the translational diffusion coefficient to the Stokes-Einstein equation

$$D = \frac{k_B T}{6\pi\eta R} \tag{2.2}$$

where k_B is Boltzmann's constant, T is the absolute temperature and η is the viscosity of the suspension medium.

2.6.2 Single particle tracking

Single particle tracking is a technique used to determine the size and concentration of particles in a sample, however unlike DLS which uses bulk averages, this technique tracks the scattering of single particles and their motion through the medium to provide a concentration value based off a certain number of particle within a volume.

Liposomes were diluted 1000x in MilliQ and measured using Nanosight NS300 (Malvern Panalytical, Malvern, UK). A microfluidic chamber was fixed atop a laser module. A 1 mL syringe was used to introduce the sample into a microfluidic chamber with a computer-controlled syringe pump unit. Samples were flowed through the microfluidic device at a continuous flow rate of 30 μL min-1 and irradiated using a 50 mW 532 nm laser. The scattered light from individual particles was observed using a 20$\times$ objective located above the flow chamber. Five 60 second videos were recorded under continuous flow conditions for each sample. Tracking analysis software was then used to measure the Brownian motion of the particles to obtain a radius estimate using the Stokes-Einstein equation. The concentration was obtained by measuring the number of

particles that passed through the imaging area using the set flow rate, and then applying the dilution factor. Particle sizing and concentrations values for individual videos were averaged to give a final value.

2.6.3 UV-Visible spectroscopy

UV-Vis spectroscopy is a type of absorption spectroscopy which measures how much light is absorbed by a sample, within the ultra-violet and visible light region of the electromagnetic spectrum. UV-Vis was used to characterise the level of polymerisation of Diyne-PC within the liposome bilayer, as a notable change in absorption can be seen at 490, 525 and 600 nm which correlates to UV exposure time, Figure 2.13.

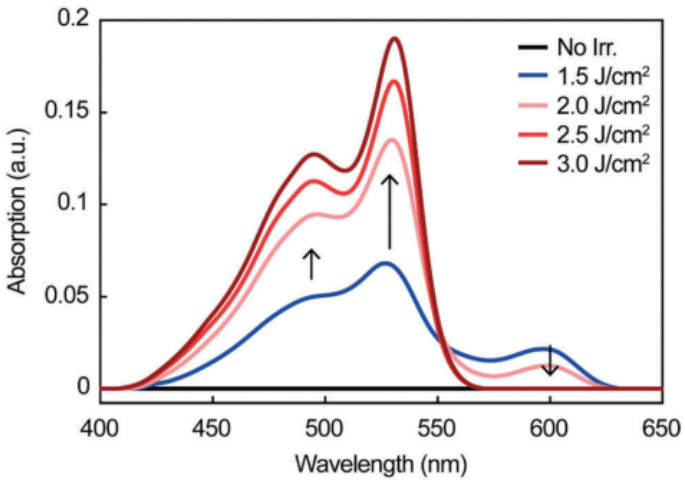

Figure 2.13: UV-Vis spectra of DOPC:Diyne-PC vesicles for different UV doses. Reproduced from [192] with permission from the Royal Society of Chemistry.

Measurements were carried out on Agilent Technologies Cary 5000 UV-Vis-NIR absorption spectrophotometer. Liposomes samples were diluted 1000x in MilliQ and added to a polystyrene cuvette for measurements. A 'blank' MilliQ sample was first measured and automatically subtracted from all sample measurements. Absorption scans were taken with a wavelength range of 400-800 nm.

2.6.4 Raman spectroscopy

Raman spectroscopy is a form of vibrational spectroscopy which detects the inelastic scattering of light to provide a chemical fingerprint of a sample. Polymerised Diyne-PC shows Raman peaks at 1500 and 2100 cm^{-1}, which correlated to UV exposure time, therefore Raman can be used as a non-destructive method of characterising polymerisation as well as as a label free method of liposome detection. More detail about Raman Spectroscopy and the system used in this thesis can be found in Section 2.8.

10 μL of liposome samples were aliquoted onto glass slides and left to air dry in a class II hood for 1 hour. Measurements were taken on a Renishaw inVia Spectrometer integrated with a Leica DMi8/SP8 laser scanning confocal microscope, 532 nm laser, 1% laser power, 1 s exposure, and 5 accumulations.

2.6.5 High performance liquid chromatography (HPLC)

High performance liquid chromatography (HPLC) was used to quantify the concentration of IK8 encapsulated within liposomes as prepared in **Section 2.5.3**. From this the encapsulation efficiency can be calculated. Post dialysis, liposomes were diluted 5x in MilliQ, and 10 μL of 1% Triton-X was added to the sample and vortexed to lyse the liposomes and release the encapsulated IK8. 20 μl of sample was used per HPLC run which was conducted over 5 mins. A UV-vis spectrometer was used to measure the absorbance at 220 nm. The peak corresponding to IK8 was seen after approximately 1.6 - 1.8 minutes, as seen in **Figure 2.14**.

A strong Triton-X peak can be seen at 4 minutes. An IK8 calibration curve was prepared with a series of 2-fold dilutions ranging between 400 - 6.25 μg ml^{-1}. The concentration of IK8 was calculated by integrating beneath the peak and comparing to the IK8 calibration curve. The encapsulation efficiency was calculated using **Equation 2.3**, where the IK8 mass remaining after dialysis (M_{final}) was compared to the mass of IK8 used in lipid film rehydration ($M_{initial}$).

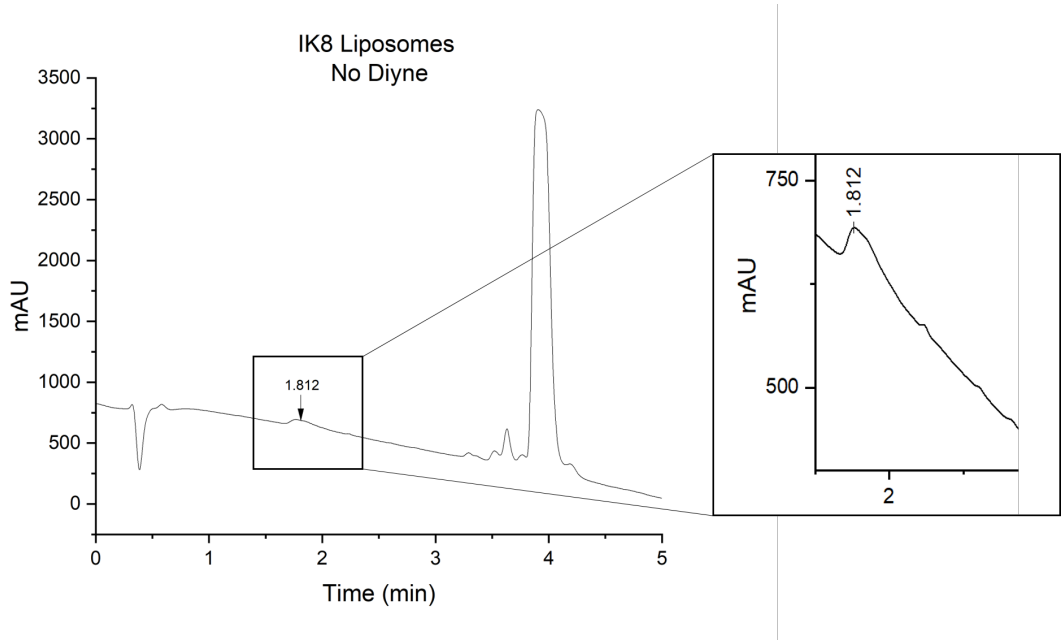

Figure 2.14: A HPLC chromatograph used to quantify the concentration of IK8 in a sample without Diyne-PC. The presence of IK8 can be seen at 1.812 minutes. The large peak at 4 minutes is due to Triton-X in the sample.

$$Encapsultation\ Efficiency\% = \frac{M_{final}}{M_{Initial}} \times Dilution\ Factor \times 100 \qquad (2.3)$$

2.7 Bacterial Treatment with IK8

2.7.1 Minimum Inhibitory Concentration (MIC) and Minimum Bactericidal Concentration (MBC)

Minimum inhibitory concentration (MIC) is a method of finding out the minimum antimicrobial concentration required to inhibit visible bacterial growth in a solution commonly over 18 hours [193].

0.5 McFarland standard stocks of *S.salivarius* and *A.naeslundii* were prepared and diluted a further 100 times to give a concentration of 10^5 - 10^6 CFU ml^{-1}. A 5 mg/ml stock solution of IK8 was made up in MilliQ from which a series of 2-fold serial dilutions from 800 - 6.25 μg/ml were prepared using BHI. Wells of a 96-well plate were filled with

100 μl of bacteria and 100 μl of IK8 at double the required final concentration. Wells with no IK8 were filled with 10 0μl BHI. Control wells of BHI and PBS were added to check sterility. Six replicate wells were performed for each IK8 concentration. The optical density of each well was measured at 600 nm after 18 hours. The MIC was identified visually as the concentration of IK8 that resulted in no bacterial proliferation.

Minimum bactericidal concentration (MBC) is the lowest concentration of antimicrobial that causes cell death over 18 hours. It is quantified by counting the colony forming units (CFUs). Once the MIC was determined, bacteria from each well was 10-fold serial diluted 1-5 times, and 10 μl of 10^{-3}, 10^{-4}, and 10^{-5} diluted bacteria was spread onto a Horse-blood CBA agar plate which had been divided into 6. Agar plates were incubated overnight at 37°C. Blank plates and PBS/BHI were plated to check for sterility. Bacteria colonies were counted by eye, and the cell density (CFU/ml) was calculated by **Equation 2.4**, where the volume factor was 100 based off 10 μl being spread onto the agar plate.

$$CFU/ml = CFU\ count \times Dilution\ Factor \times Volume\ Factor \tag{2.4}$$

2.7.2 Time-kill study

A time-kill study is a method used to determine the rate at which an antimicrobial kills bacterial cells. For this study, the rate was determined for *S.salivarius* and *A.naeslundii* by testing a range of concentrations above the MIC - 0, 25, 50, 100, and 200 μg/ml for *S.salivarius*, and 0, 6.25, 12.5, 25, and 50 μg/ml for *A.naeslundii*. Three replicates of 6 wells were prepared. The well plates were incubated at 37°C for 24 hours. Samples were removed at set time points and serially diluted between 1-5 times. Dilutions were spread across Horse-blood CBA plates as described in **Section 2.7** and incubated overnight at 37°C. This process was performed at 0, 1, 2, 4, 6, and 24 hours. The well plate was returned to the incubator after each time point samples had been removed.

2.7.3 Biofilm treatment with free IK8

2-species biofilms were grown in 96-well plates as described in **Section 2.3.2**, and washed three times with PBS. IK8 was 2-fold serial diluted from 800 - 6.25 μg/ml in BHI, and 200 μl of each concentration was added to 6 repeat wells. Biofilms containing no IK8 were filled with 200 μg/ml BHI, and as a control 1% Virkon was added to biofilms as a positive kill control. Biofilms were incubated for 3 or 24 hours, after which IK8 was removed and biofilms were washed 3 times with PBS. Multiple analysis methods were used: biofilms were either stained with live/dead or crystal violet solution, and the fluorescence or absorption measured, respectively, or biofilms were aspirated and spread on agar plates (as described in **Section 2.7**) to quantify the cell density.

2.7.4 Biofilm treatment with IK8, liposomes, MBs + US

Biofilms were grown in 96-well plates as described in **Section 2.3.2** and washed three times with PBS. Biofilms were grown in every other column to avoid ultrasound crossover. Each column in the well plate was exposed to a different treatment method, and the results of 3 wells per treatment were average for the final result. 2-species biofilms were exposed to five different treatments:

1. Microbubbles + Ultrasound (MBUS)
2. free IK8 + MBUS (x1 exposure)
3. free IK8 + MBUS (x3 exposures)
4. IK8 loaded liposomes + MBUS (LMBUS) (x1 exposure)
5. LMBUS (x3 exposures)

Untreated wells and wells treated with 1% virkon were used as controls. For all wells, the final volume of treatment solution was 200 μl.

MBs were prepared, sized and concentration determined as described in **Section 2.4**. MBs were diluted so that the final concentration in the well was 2.5×10^8 bubbles/ml. For wells with free IK8 + MBUS, 100 μg IK8 was added to each well along with MBs. For LMBUS treated wells, IK8 loaded liposomes were prepared as described in **Section 2.5.3**. Based on the HPLC results of the encapsulation efficiency, 1 ml of liposomes should contain 206 μg/ml of IK8. For a final IK8 concentration of approximately 100 μg/ml within the well, 100 μl of liposomes were added to the well with the remaining 100 μl made up of MBs and PBS.

Ultrasound was applied up through the base of the well for 5 seconds, as shown in **Figure 2.15** , immediately after MBs were added to the well. For those only receiving one treatment exposure, after US the biofilms were incubated at 37 °C for 3 hours before rinsing three times with PBS and being analysed. Biofilms which received three treatment exposures had the same process repeated three times, with only 1 hour incubation period between each exposure instead of 3 hours. Biofilms were rinsed three times with PBS after incubation, before the next treatment. Treatment effectiveness was measure by spreading the bacteria on agar plates and counting cell density.

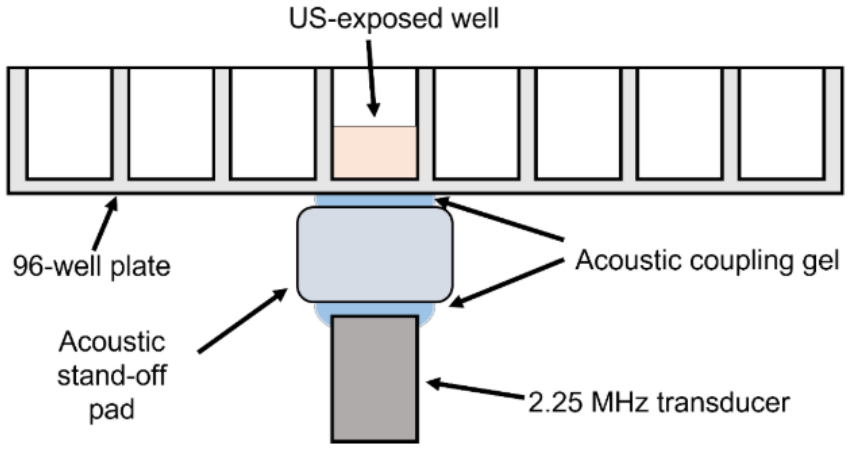

Figure 2.15: Schematic showing how ultrasound was applied to biofilms grown in a 96-well plate. The 2.25 MHz transducer was positioned beneath the well plate and ultrasound was applied through a 2cm thick acoustically transparent stand-off pad with acoustic coupling gel on either side. Schematic reproduced with permission from [2].

2.8 Raman Spectroscopy

2.8.1 Raman System

The Raman system used for this thesis is a Renishaw inVia Spectrometer integrated with a Leica DMi8/SP8 laser scanning confocal microscope. **Figure 2.16** shows the spectrometer optics. There are two laser options: a 532 nm DPSS Diode visible laser or a 785 nm Diode near IR laser. For this thesis the 532 nm laser was used, which had power of 50 mW, 22 mW at the sample. Two detectors are available: a Renishaw CCD array detector near infra-red enhanced, best suited for 785 nm excitation (100 mW, 45 mW at the sample), and an Andor EMCCD (Electron multiplying charged coupled device) high sensitive back-illuminated detector for UV/Vis measurements, suitable for the 532 nm excitation (50 mW, 22mW at the sample). Renishaw WiRE 4.2 software was used to control all acquisition settings during the scans.

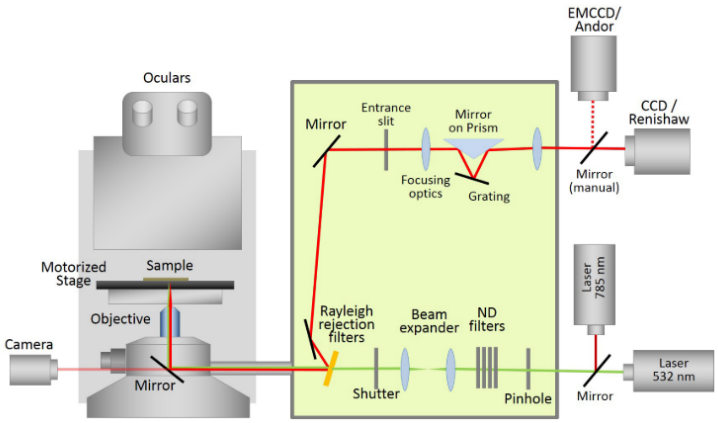

Figure 2.16: Optical configuration of the Renishaw inVia Raman Microscope, simplified for clarify. Figure reproduced with permission from [107].

The laser beam travels through a pinhole which is used to improve the beam profile and spatial resolution. Neutral density (ND) filters and a beam expander were used to control the power output of the laser reaching the sample. The light then passes through a motorised shutter, a series of mirrors, an entrance slit, grating, and the chosen objective before hitting the sample in an inverted configuration. The spectral resolution is affected by the slit size and grating used for each experiment. A smaller slit size results in a higher

Objective	FWD (mm)	N.A
10x	inf	0.3
20x	0.62	0.75
40x	0.21	0.85
63x air	2.6 - 1.8	0.7
63x oil	0.14	1.4
100x oil	0.13	1.4

Table 2.4: Summary of the available objectives in the Raman-Confocal microscope and their resolution, where FWD stands for Free Working distance and N.A. for Numerical Aperture.

resolution. A diffraction grating with a higher groove density has a higher dispersion angle, and therefore greater spectral resolution. However, this consequently reduces the spatial resolution, which can be overcome by using a movable grating to scan across all wavenumbers in sections which can be stitched together at the end. The objectives available for this system are: 2.5x, 10x 40x, 50x, 60x oil, and 100x oil, though 100x oil was only used in this thesis. Details of the resolution of the objectives is given in 2.4. The samples sit on the stage in 3D printed holders, which are magnetically attached to prevent movement during acquisition. The stage is automated and moves in an X-Y direction, while the Z-height is controlled by adjusting the objective.

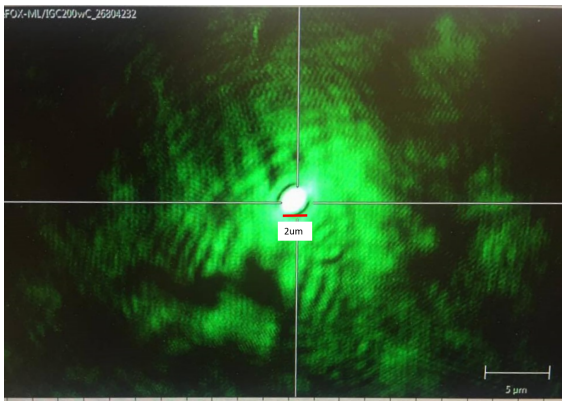

Figure 2.17: Laser spot calibration for Raman Spectroscopy. Scattered light is collected by the camera so the laser spot can be observed and aligned to the crosshairs.The spot size for 532 nm laser with 100% laser intensity is approximately 2 μm.

Some of the scattered light is reflected into the camera so the laser spot can be observed and aligned to the crosshairs, shown in **Figure 2.17**. The spot size of the laser can change with laser intensity due to internal reflections within the microscope, or it

may be purposefully increased using a beam expander. The work in this thesis used the 532 nm laser with 100% intensity, producing a spot size of approximately 2 μm. The majority of light is reflected onto Rayleigh reflection filters which eliminates wavenumbers less than 100 cm^{-1}. The entrance slit controls the degree of confocality of the system, with settings of 65 μm for standard confocality or 20 μm for high confocality. There are two gratings available, 1800 lines/mm for the 532 nm and 1200 lines/mm for the 785 nm laser. There are two scan types possible: synchro-scan or step scan. A synchro-scan collects the one continuous spectrum in high resolution. A step scan collects the spectrum in separate parts which are stitched together at the end to produce one full spectra. Step scan is recommended for samples that are strong Raman scatterers which might saturate the detector.

Unless otherwise stated, for the experiments in this thesis the following settings were used: the 532 nm laser with a 1800 lines/mm grating, 100x oil objective, high confocality mode, step scan and Andor detector. Due to the short working distance of the 100x oil objective, glass coverslips were used throughout all experiments. Immersion oil is required for 100x objective as the high magnification results in increased loss of light in the air gap between glass and lens due to refraction, so by adding oil (with the same refractive index as glass) between the lens and coverslip the air gap is eliminated and the refracted light is directed back to the camera, providing crisp, high resolution images.

2.8.2 System calibration

To ensure reproducibility and to account for the drift in motors over time, before every use the Raman system is calibrated to a standard Silicon sample, which shows a strong sharp peak at 520.5 cm^{-1} (**Figure 2.18**). Calibration is specific to the objective and settings used, so should match those used for the experiment for optimum calibration. Any value between 520.3 - 520.7 cm^{-1} was accepted as calibrated, with the aim of 520.5 cm^{-1}. If the peak is not in the acceptable range, the alignment can be re-calibrated to the correct value using the 'peak offset' function in Wire 4.2.

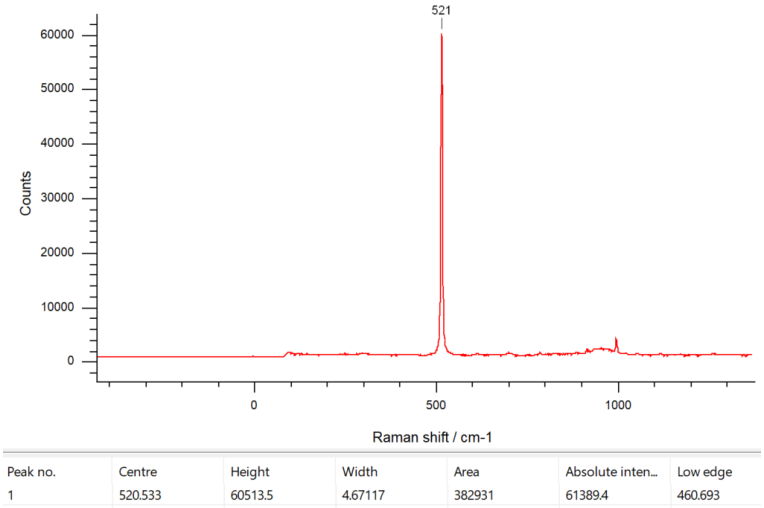

Peak no.	Centre	Height	Width	Area	Absolute inten...	Low edge
1	520.533	60513.5	4.67117	382931	61389.4	460.693

Figure 2.18: Example of the Silicon peak the Raman system is calibrated to, 520.533 cm^{-1}. Taken with 100x oil objective, 100% laser power, 1s acquisition time.

2.8.3 Raman spectroscopy of planktonic bacteria

Raman spectra of single species planktonic bacteria was obtained by drying bacteria samples onto a glass coverslip and taking multiple Raman spectra of the bacteria. To remove any traces of growth media which would contribute to the Raman spectra, planktonic bacteria were washed via centrifugation at 6,000xg for 10 mins, the supernatant removed and replaced with MilliQ. This was repeated three times. Glass coverslips were rinsed in 99% ethanol and dried under nitrogen before 10 μl of bacteria was added to the surface and left to dry in a class II hood for 1 hour.

The sample was focused using the bright field, focusing the centre of the cross hairs on the bacteria as this is the focus point of the laser spot, which is approximately 2 μm. An example of this can be seen in **Figure 2.19a**. Background spectra was also taken of the glass, in the same plane, where no bacteria were present. As bacteria is dried onto the slide and the focus point is very small, there will be glass detected in the Raman spectra that will need to be removed during analysis. Example spectra can be seen in **Figure 2.19b**. All scans were taken with 532 nm laser, 10% laser power, 10 s exposure time, 5 accumulations. A lower laser power is required to prevent burning of the sample.

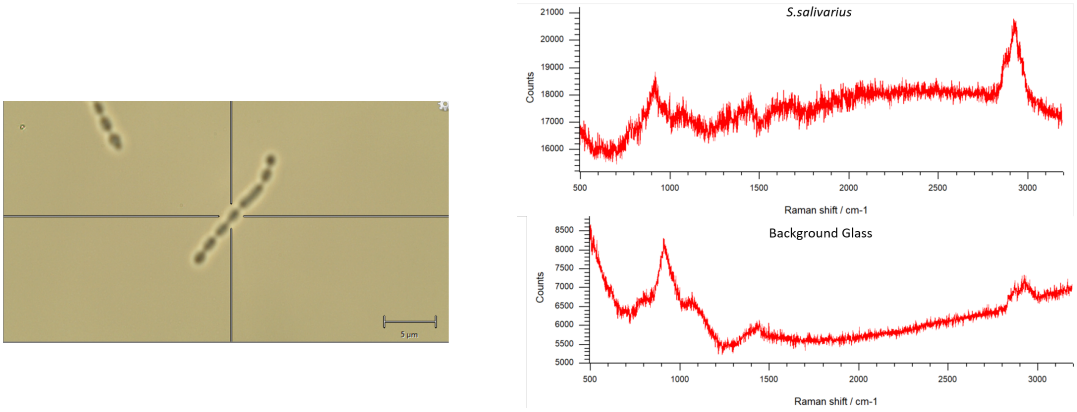

(a) **(b)**

Figure 2.19: a) Example of the centre of the cross hairs focused on bacteria, the point at which the scan would be taken, b) *(Top)* Raw spectrum of *S.salivarius* and *(Bottom)* raw spectrum of background glass, showing that the glass has a contribution in the sample spectra.

2.8.4 Raman of biofilms on-chip

One of the main aims of the project was to use Raman spectroscopy to analyse biofilms over time. By growing biofilms microfluidically, Raman spectra could be taken of the same biofilm over the course of 5 days.

Biofilms were grown as described in **Section 2.3.1.1**. Biofilms were rinsed for 20 mins at 20 μl/min with PBS to remove any traces of biofilm media which would have a strong contribution to the Raman spectra. All 2- or 3-way taps in the microfluidic system were closed so the biofilm could be scanned under static conditions, and importantly to prevent any disruption of the biofilm during transport between labs. The microfluidic chip was placed on the stage and secured using 3D printed magnetic holders. Single point Raman scans of the biofilm were taken using 532 nm, 100x oil objective, step-scan, 10 s exposure, 10 accumulations, and "high confocality". Spectra were acquired at random points across the whole biofilm to gain an average. A minimum of 25 spectra from different points were taken per biofilm.

2.8.5 Raman analysis

2.8.5.1 Raman pre-processing

Raman spectra of similar samples may have varying baseline contributions due to the differing levels of scattering and auto-fluorescence. In order to reliably analyse data and compare results from different experiments, each Raman spectra should be carefully pre-processed in the same way before moving forward. Pre-processing here was done using WiRE 4.2, and MATLAB script written by Dr Julia Gala de Pablo, which was used, reproduced, and adapted with permission, and can be found with more detail in [107]. Briefly, the pr-processing steps were: cosmic ray removal, alignment to calibration peak, baseline subtraction, background removal (when necessary), and smoothing. The following example used to illustrate the pre-processing steps is a spectrum of planktonic *S.salivarius*. Cosmic rays were rarely seen in spectra, but were removed using the feature in the WiRE software prior to exporting the data. All files were saved as `.wdf` files, which were read into the MATLAB code using `WdfReader` function provided by Renishaw.

The first step was to ensure all spectra were aligned to the same silicon peak calibration value. Each spectrum was interpolated to provide a step of 0.5 cm^{-1} so all spectra were aligned. The next step was baseline subtraction, performed using `f_baseline_corr`, an algorithm developed by Koch *et al* [194]. An example of the baseline subtraction can be seen in **Figure 2.20**.

For planktonic samples, a background subtraction step was included to remove the glass background that contributed to the spectra. This step was not necessary for thicker biofilms as there was no noticeable background contribution from the glass or PDMS as the growth chamber and sample area were large enough so this could be avoided. Background spectra were imported and processed as above, averaged and then smoothed using a Savitzki-Golay filter (function `sgolayfilt`), with polynomial order of 2 and frame width 17. This step was performed first to ensure minimal noise was added to the spectra during subtraction. Background removal from planktonic spectra can be seen in **Figure 2.21**.

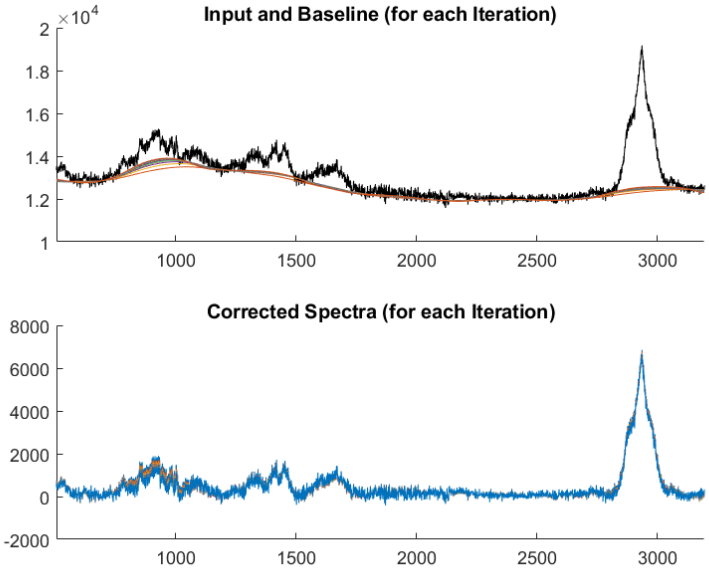

Figure 2.20: Example the first, more aggressive, baseline subtraction on *S.salivarius* using the Koch *et al* algorithm with 15 iterations, frame = 500, smooth width= 40 [194].

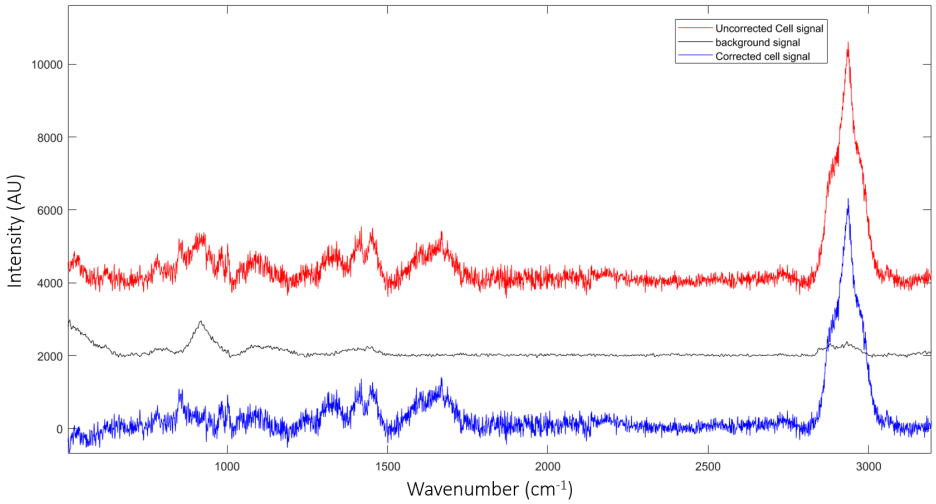

Figure 2.21: Example of background removal of glass from planktonic *S.salivarius* spectra. Offset spectra of planktonic *S.salivarius* (red), background glass (black), and corrected spectra (blue).

Corrected spectra were then smoothed using the Savitzki-Golay filter (function `sgolayfilt`), with polynomial order 2, and frame width9, and truncated to 500 - 3020 cm^{-1} (or to the fingerprint region 500 - 1800 cm^{-1} if necessary). It was found that including the 'silent' region during later multivariate analysis could impact the classifications as baseline contributions could be misinterpreted as important spectral information, so it was easier to remove, or 'zap', the region 1800 - 2750 cm^{-1} from the spectra. Finally, the spectra were then normalised to the Amide I peak, the maximum between 1650 - 1660 cm^{-1}, and averaged. The final processed average plot with standard error is shown in **Figure 2.22**. This process was repeated in the same way for all planktonic and biofilm spectra. From the MATLAB script: `DataMatrix, Average spectra, Error, and Xvalues` were saved as `.csv` files so figures could be plotted in OriginPro.

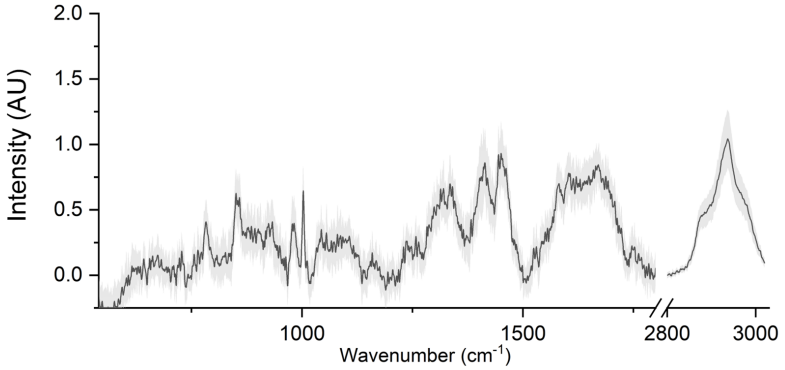

Figure 2.22: Example average spectrum of *S.salivarius*, normalised to Amide I, and plotted with standard error. N = 27. Acquisition conditions: 532 nm, 100x oil objective, 10 s exposure, 10 accumulations.

2.8.5.2 Multivariate Analysis

Principle Component Analysis (PCA) is a method used to reduce the dimensionality of large data sets whilst preserving the variability, thus maximising the variance between data sets and allowing visualization of complex multidimensional data [195]. MATLAB scripts were used to run multi-variate analysis, written by Dr Julia Gala de Pablo [107]. Zapped spectra were used (500-1800 and 2800-3020 cm^{-1} where the silent region was removed), and all data was first standardised using Standard Normal Variate where each

spectrum is normalised by subtracting the mean and making its standard deviation of 1. PCA scores and loadings were saved from MATLAB as `.csv` files and plotted in OriginPro, where a 95% confidence ellipse was added to the figures. Linear Discriminant Analysis (LDA) is a supervised algorithm that works to maximise difference between classes. LDA was performed using MATLAB script, where scores and loadings were exported and plotted in OriginPro.

2.8.6 Stimulated Raman spectroscopy (SRS)

SRS is a type of Coherent Raman spectroscopy that produces a Raman image at a specific wavenumber, usually in the high wavenumber region (**Figure 2.23**). Unlike spontaneous Raman scattering where the scan length can be long, taking seconds or minutes per pixel, SRS takes milliseconds. Due to this time limitation, taking Raman maps or z-stacks of biofilms with the Renishaw system was unfeasible and produced unreliable data as the stage and motors would drift out of focus over the period of the scan. SRS and SRS hyperspectral images of biofilms were therefore taken at The CONTRAST Facility at the University of Exeter using their custom built Narrowband Spectrally Focused Coherent Raman. The system also allowed for complimentary techniques such as Second Harmonic Generation (SHG) and Two Photon Fluorescence (TPF) to be taken at the same time.

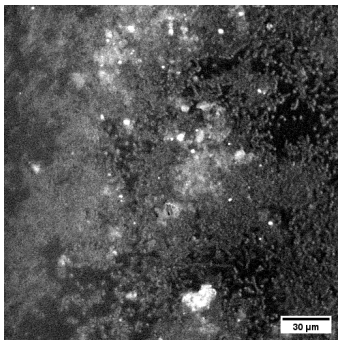

Figure 2.23: Example SRS image of *S.salivarius* Day 1 biofilm at 2930 cm^{-1}. Scale bar = 30 μm.

2.8.6.1 Sample Preparation

Day 1 and 5 mono-species and 2-species biofilms were grown microfluidically and taken for analysis. Three repeats of each sample were taken, e.g 3x Day 1 *S.salivarius* biofilm, 3x Day 3 *S.salivarius* biofilm... An extra biofilm for 2 species Day 1 and 5 were grown and FISH stained for analysis. Biofilms were fixed before travel by injecting 4% paraformaldehyde on chip at 20 μl/min and incubating for 15 mins at 4°C, then rinsed with PBS. PDMS chips were sealed by filling the punctured holes with the PDMS that was discarded during the original biopsy punch, then a layer of superglue on top to seal and prevent any leakage. Samples were discarded after use.

SRS Samples		
S.salivarius	*A.naeslundii*	2-species
Day 1	Day 1	Day 1
Day 1	Day 1	Day 1
Day 1	Day 1	Day 1
Day 5	Day 5	Day 5
Day 5	Day 5	Day 5
Day 5	Day 5	Day 5
		FISH Day 1
		FISH Day 5

Table 2.5: Mono-species and 2-species biofilm samples taken for SRS analysis.

2.8.6.2 SRS system

The custom built system was powered by an InSightX3 fs laser, providing a tuneable output between 680-1300 ns and a fixed wavelength output at 1045 nm. The 2 beams are combined in the SF-TRU spectral focusing unit. This unit controls the laser power applied to the sample and the time delay between the beams. It also provides the intensity modulations in the Stokes beam necessary for SRS and chirps the beams from fs to ps pulses. The imaging is carried out on a modified confocal inverted microscope (Olympus Flouview3000 and IX81). The light is focused on the sample with a 1.2NA water objective and transmitted light collected with a water condenser. For transparent samples SRS and CARS are measured in the forwards direction, however for thicker samples there is an option to collect backscattered CARS in an epi channel. Second

Harmonic Generation (SHG) and TPF are also available. The system is set up for 3D imaging, large area scans and rapid hyperspectral imaging [196].

Biofilm samples were placed on the stage and focused by adjusting the objective height. At least two areas per biofilm were imaged for analysis. A hyperspectral SRS image, SRS Z-stack, SHG and TPF were all taken at the same position.

For SRS hyperspectral images and z-stacks, a 1045 nm fixed "Stokes" laser and 802 nm tuneable "pump" laser were used. For hyperspectral images where each scan is taken at a different wavenumber, the stage delay position was chosen to be 90-92 mm with 101 positions corresponding to the CH_2/CH_3 region from 2740 - 3084 cm^{-1}. For z-stacks the same settings were used without the delay stage, but tuned to the CH_3 band at 2930 cm^{-1} . For TPF, an 802 nm femto-second pulsed laser was used for excitation, and 575 nm band pass filter used for detection (which collects from 550 - 600 nm).

For FISH samples, two wavelengths were used sequentially to excite both fluorescent probes attached to each species. For the Cy3 probe (Ex: 555 *nm*, *S.salivarius*), 1040 nm laser was used for excitation and 575 nm band pass filter for detection. For Cy5 (Ex: 651 nm, *A.naeslundii*) a 1220 nm laser line was used, with a 660 nm band pass filter for detection. Image resolution was: 0.14 μm/pixel and typically collected over a 212 x 212 μm region.

2.8.6.3 SRS Analysis

Hyperspectral SRS: To ensure each image was analysed in the same way and to maximise the amount of information taken from the images whilst keeping the process simple, each hyperspectral image was divided into a 15 x 15 grid using a Python script, details found in Appendix 1. Each individual square measured 14.14 μm^2, and the average spectrum from each square was extracted and saved to an Excel file. All spectra were plotted in Origin Pro. To produce a hyperspectral image with a 15 x 15 grid, the brightest and clearest image from the stack was chosen in ImageJ as a representative, and a 15 x 15 grid overlaid using a macro found in Appendix 1. One row or column of

the grid was chosen for analysis, and the corresponding spectrum plotted.

K-means Clustering: Another method of hyperspectral image analysis is to use K-means clustering, which aims to group similar data points together, minimise within-cluster variances, and discover underlying patterns [197]. K-means clustering is a non-supervised method that separates the data into a user-defined number of clusters (K). It randomly picks K number of data points to define the cluster centroids, then assigns the remaining data points to the nearest centroid (that with the nearest mean). The algorithm performs iterations to optimise the centroid until the centroids have stabilised, or the maximum number of iterations has been reached. The final cluster centroid is an average of all data points. The spectra corresponding to each cluster is plotted and the image colour coded into clusters, shown in **Figure 2.24**. This method is complimentary to the manual spectra extraction method described above, but may prove to be accurate enough to a reliable method on its own. A MATLAB script was used for this analysis, provided by the CONTRAST Facility at the University of Exeter (See Appendix 1). 4 clusters were chosen, with a min threshold of 10,000 and max threshold 1,000,000.

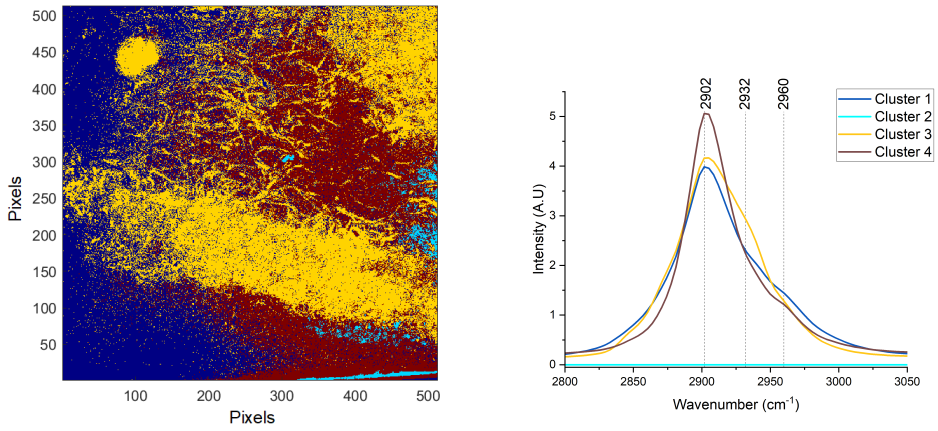

(a) **(b)**

Figure 2.24: K-means clustering data of hyperspectral SRS Day 5 2-species *S.salivarius* and *A.naeslundii* Day 5 biofilms. K- means clustering colour map, Cluster 1 (dark blue), cluster 2 (light blue), cluster 3 (yellow), cluster 4 (red),

SRS and TPF z-stacks: Z-stacks were imported into ImageJ, brightness adjusted, and 4-6 slices from the stacks were used to represent the biofilm. Composite images of

SRS and TPF were made where SRS were false coloured green, and TPF coloured red.

FISH z-stacks: FISH z-stacks of 2-species biofilms were imported into ImageJ, brightness adjusted, 4-6 slices from the stack were chosen to represent the biofilm. The *S.salivarius* channel was false coloured green and *A.naeslundii* red, before merging into a composite image.

2.9 Confocal Laser Scanning Microscopy (CLSM)

Confocal Microscopy was used to capture high resolution fluorescence images and z-stacks of biofilms. The confocal laser scanning microscope (CLSM) system (SP8, Leica Microsystems GmbH, Wetzlar, Germany) has 405, 488, 552, and 638 nm excitation lasers. The 488 and 552 nm lasers were used for the excitation of SYTO9 and Propidium Iodide. The system was equipped with 2.5×, 10×, and 40× dry objectives, and higher magnification 63× and 100× oil immersion objectives. A schematic showing the optical set up can be seen in **Figure 2.25a**. For imaging biofilms on chip, the 10x and 100x oil objective were most commonly used as the 10x gave a clear overview of the whole biofilm while to 100x oil allowed for imaging of individual species. Z-stacks taken with 100x oil objective had a 1 μm step size. All images were processed in ImageJ, with live/dead images being false coloured green/red, respectively. 3D z-stacks were rendered in the Leica software where images and videos could be saved, an example of which is shown in **Figure 2.25b**.

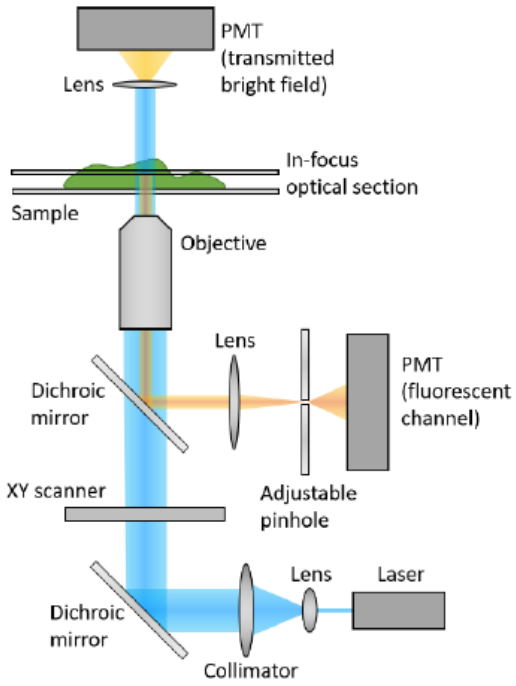

(a)

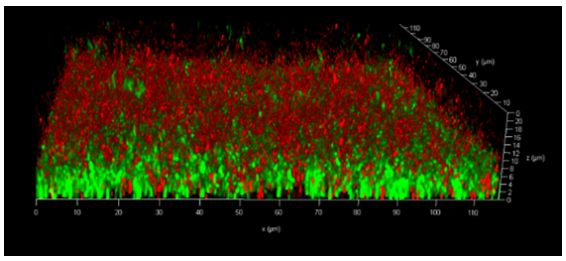

(b)

Figure 2.25: Schematic showing the light paths involved in an inverted CLSM. The excitation laser is passed across the surface of a sample using an XY scanner. The fluorescent signal emitted by the sample is passed back through the objective and towards a PMT for detection. The adjustable pinhole allows refinement of the depth of the optical section. A portion of the excitation and emission light is transmitted through the sample and dispersed to give a bright-field view of the sample. Figure reproduced with permission from [2].

Chapter 3

On-Chip Raman Spectroscopy of Multi-species Oral Biofilms

3.1 Aims and Motivations

The aim of this chapter is to analyse how multi-species oral biofilms develop and change over time, using Raman Spectroscopy (RS). Traditional methods of biofilm analysis are often destructive or require fixation, making it impossible to study the same biofilm over time [198, 199]. Here we aim to develop a microfluidic growth system that allows biofilms to be grown under continuous flow, yet can be easily transported for non-destructive, label free analysis using RS. It is hoped that the molecular fingerprint provided by RS will allow for a deeper understanding of the structure of the biofilm at different stages of maturity, as well as giving an insight to inter-species interactions.

3.2 Biofilm Growth System Development

3.2.1 Version 1: Piezo-pump System

The initial version of the microfluidic growth system was based on the set up configured by J.Tinkler and modified by Dr Julia Gala de Pablo [2]. The result was a self-contained microfluidic system with continuous flow driven by piezo-pumps, which allowed the whole system to sit compact and undisturbed in an incubator, while being easily transportable for analysis.

3.2.1.1 Microfluidic Device

The first iteration of the microfluidic device was designed by Dr Julia Gala de Pablo, and can be seen in **Figure 3.1.** The device has two inlets to prevent contamination, the far left inlet for injecting bacteria and fluorescent stains, and the central inlet for media. The growth chamber itself is 6 mm (l) x 4 mm (w) x 140 μm (h), with rounded corners to reduce flow stagnation and air pockets. As the chamber is relatively large, pillars were added to support the top of the chamber to prevent any potential collapse. Devices were bound to 22 $\times$ 50 $\times$ 0.13 mm glass coverslips to allow for high magnification objectives to be used during RS and confocal imaging.

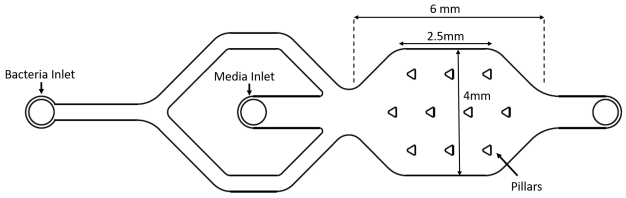

Figure 3.1: First iteration of the microfluidic device design. The chamber dimensions are 6 mm (l) x 4 mm (w) x 140 μm (h), with pillars added to prevent roof collapse. Separate inlets were used for media flow and bacteria injection to prevent contamination.

When growing a biofilm under flow, the shear stress exerted on the biofilm is more important than the flow rate itself, as the shear stress tells you the impact of the flow on the biofilm whereas the flow rate is independent and has little meaning without knowing

the dimensions of the chamber. Growing biofilms under flow increases the transport of nutrients and signalling molecules during biofilm formation [87], and has shown to produce thicker biofilms at a higher shear stress, as well as [200, 201]. If the shear stress is too high however, the shear force will overcome the adhesive forces and remove the biofilm. From the literature, a shear stress of approximately 0.3 dynes/cm^2 (0.03 Pa) have been deemed suitable to encourage biofilm proliferation, whilst not causing damage [200].

3.2.1.2 Growth System

The growth system is based on that designed by J.Tinkler, where a microfluidic device has two inlets, one for nutrients (media) and one for injecting rinsing buffer, bacteria, and fluorescent stains, as well as an outlet for waste, as shown in **Figure 3.2a**. There are 2- and 3-way taps connected to all tubing to stop flow and remove any air bubbles that may get trapped in the system. The buffer inlet has an injection loop, which is two 3-way taps connected, where bacteria and stains are manually injected into the central chamber (volume = 300 μl), and then injected on chip by the pump, **Figure 3.2b**. By injecting the bacteria via the injection loop instead of at the end of the tubing, the time taken for the bacteria to get on chip is reduced and any air bubbles can be removed before getting on chip.

3.2.1.3 Piezo-pump

The growth system was designed to be as compact as possible to allow for ease of use and portability. Choosing a piezo-pump to drive the flow of media allowed for this. The mp6 pump (Bartels Mikrotechnik) used worked like a beating heart, using alternate valves to push fluid through the system, in one direction,. **Figure 3.3a** demonstrates how the mechanism of the pump worked by using a piezoelectric diaphragm and passive check valves, so when a voltage is applied the brass membrane is deformed and pushed downwards, forcing the medium into the next chamber, the direction of which determined by the check valves.

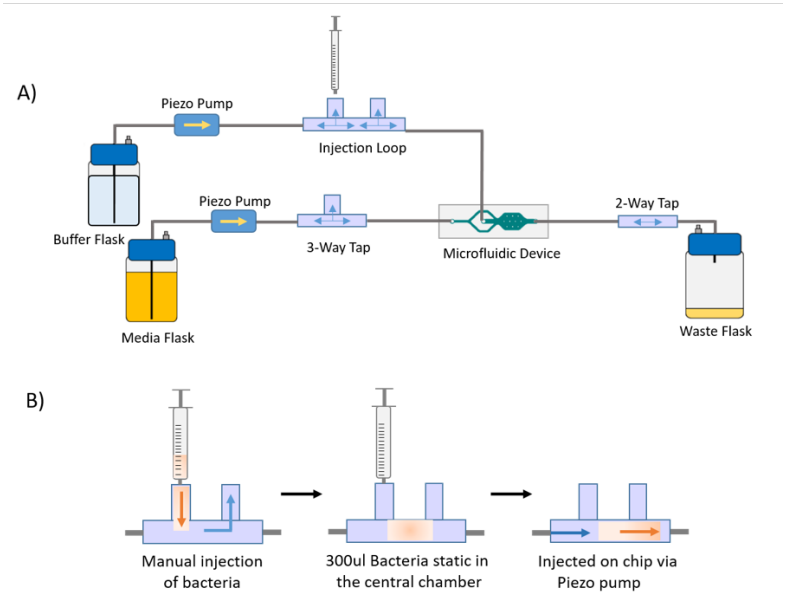

Figure 3.2: A) Simplified schematic showing the piezo-pump driven microfluidic system. 2- and 3-way taps are used to stop flow, remove air bubbles, and serve as an injection loop, B) Schematic showing how the injection loops works. Bacteria (or other) is manually injected into the central chamber of the loop (300 μl) and the displaced liquid is forced out of the loop outlet. The bacteria is then pumped on chip by the piezo pump and at controlled rate.

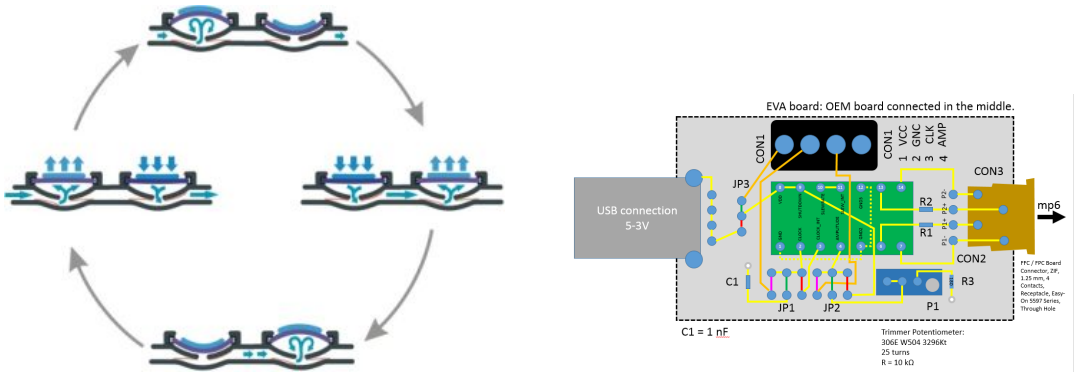

(a) **(b)**

Figure 3.3: The working mechanisms of the mp6-pump used to drive fluid flow in the biofilm system. a) A piezoelectric diaphragm is deformed when a voltage is applied, forcing the membrane downwards and pushing the medium into the next chamber, when the cycle continues. Figure reproduced from the manufacture's website; Bartels Mikrotechnik. b) The evaluation board which controlled the mp6 pump, powered by a USB battery pack. [202].

The pump is attached to, and controlled, by an evaluation board which is powered by a USB battery pack, shown in **Figure 3.3b**. The flow rate of media through the system is controlled by the voltage (amplitude of deformed membrane) and frequency of the pump. The relationship between voltage, frequency, and flow rate are as follows:

1. Flow rate increases linearly with amplitude (voltage).
2. Flow rate decreases linearly with back pressure
3. Flow rate increases linearly with frequency up to the resonant point. This is 100 Hz for water. After this point flow rate decreases again as the frequency is too high causing the pump to be ineffective as it becomes 'too slippy'. The resonant frequency depends on the viscosity of the liquid.

Various voltage and frequency combinations were tested and flow rates measured. It was found that varying the frequency had the greatest effect on flow rate, thus for further testing the voltage was kept constant (85 Vpp). The frequency was defined by varying the capacitance, where 1 - 10 nF corresponded to 226 - 65 Hz. As the only way to vary the capacitance was by turning an unmarked screw on the board, only the minimum and maximum were tested. The flow rates can be seen in **Table 3.1**.

	Media Flow (ml/min)
(1 nF) 226 Hz, 85 Vpp	1.41
(10 nF) 65 Hz, 85 Vpp	0.81
(330 nF) 3.4 Hz, 270 Vpp	0.062

Table 3.1: Flow rates for the piezo-pump are determined by varying the voltage (Vpp) and frequency (Hz). The frequency is controlled by varying the capacitance (nF). Flow rates through the microfluidic system are given in ml/min.

The maximum and minimum frequency resulted in flow rates of 1.14 and 0.81 ml/min respectively. To further reduce the flow rate, a 330 nF capacitor was added to give a frequency of 3.4 Hz, and a 0.062 ml/min flow rate. The lowest flow rate, 0.062 ml/min, would provide a shear stress calculated to be 0.79 dynes/cm^2 for this device. To achieve the desired shear stress of approximately 0.3 dynes/cm^2, a flow rate of 0.025 ml/min would be required. The piezo-pumps were therefore unable to provide the desired flow rate.

Further experiments demonstrated that the piezo-pump was unable to reliably function at 0.062 ml/min; flow would cease after a short period of time due to high back pressure. High back pressure also caused the tubing to detach from the device on occasion. Despite the benefits of using a piezo-pump, the required flow rates for this experiment meant that the pump was incompatible, thus another method was developed.

3.2.2 Version 2: Syringe pump driven system

A syringe pump was used in place of the piezo-pump as it was known to reliably function at the low flow rates required and had the option to automate the flow to make the experiments less labour intensive. The one drawback of using a syringe pump was that the system was a lot larger than planned, it was no longer compact and easily able to fit into an incubator, and due to the working temperature required of the syringe pumps, the pumps had to remain outside the incubator, as shown in **Figure 3.4**. This created a lot of dead volume in the tubing but was incorporated into the section before the injection loop (arrow A on **Figure 3.4**), so that the tubing volume between the injection loop and microfluidic chip was as minimal as possible (arrow B on **Figure 3.4**), to reduce the time taken to inject bacteria or fluorescent stains on chip. The tubing volume was reduced to 5cm (approx. 50μl).

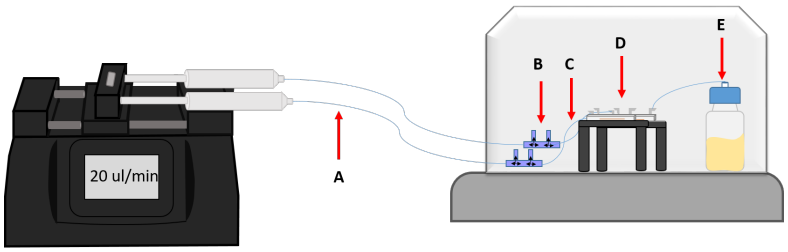

Figure 3.4: Schematic showing the syringe pump driven microfluidic system, where the pump has to remain outside the incubator. Arrow A shows the dead volume in the tubing connecting syringes to B) the injection loop, C) tubing connected to D) microfluidic device, and E) waste flask. Schematic not to scale.

Two syringe pumps were trialled. The Harvard PHD Ultra pumps were better quality and more user friendly than the Aladdin pumps (World Precision Instruments, Florida, USA), which often stalled and would incorporate more human error due to the manual

programming system. A flow rate of 25 μl/ml was easily achieved and consistent over the growth period. Using a 50 ml syringe allowed for uninterrupted flow over 48 hours.

The microfluidic device was redesigned to a long straight channel as it was noted that in future experiments with microbubbles and ultrasound, the ultrasound transducer which would be positioned on top on the PDMS, would not fit between the inlets and outlets of the current device (**Figure 3.5C)**. A 12 mm x 2 mm x 160 μm channel was designed, **Figure 3.5A**, and the slight change in dimensions meant the flow rate could be reduced to 16μl/min to achieve the same shear stress (approx 0.3 dynes/cm^2). The bacteria inlet channel was re-positioned and fed into the main inlet channel, to simplify the device and prevent any blockages that could occur with extra channels.

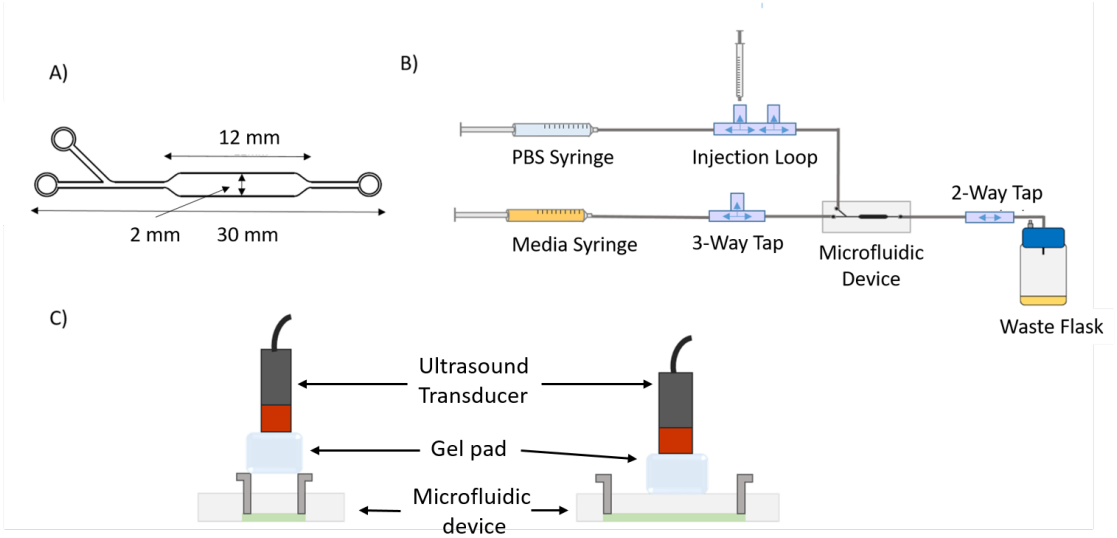

Figure 3.5: A) Straight channel microfluidic device B) simplified schematic showing the syringe pump driven system with the straight channel microfluidic device, C) (left) the original microfluidic device showing how the inlet and outlet were too close together thus the transducer and gel pad required for ultrasound would not fit, (right) the straight channel device which is longer and designed to allow room for the transducer and gel pad.

The mechanisms of the growth system are the same as in Version 1. There are two inlets, an injection loop, and waste outlet, shown in **Figure 3.5B**. In the previous system, the media was in a 100 ml flask that would last the course of the experiment, whereas in Version 2 the maximum syringe volume was 50 ml, thus had to be replaced more regularly.

3.3 Biofilm Growth

3.3.1 Biofilm Growth

This thesis studied 2-species oral biofilms, consisting of *S.salivarius* and *A.naeslundii*. These species are considered early colonisers in the oral cavity, attaching to the supra- and sub-gingival tooth surface, starting the formation of biofilms and creating the perfect environment for pathogenic species to colonise. These two species are part of a larger 5-species biofilm studied by Monika Naginyte, consisting of *S.salivarius, A.naeslundii, F.nucleatum, P.gingivalis* and *Prevotalla intermedia* [184]. Understanding how these multi-species pathogenic biofilms grow and interact over time is the long term aim in this research. However, starting with a 2-species biofilm model was appropriate to first develop this novel method of using microfluidics and RS to characterise multi-species biofilms over time. RS has been used to study multi-species biofilms grown off chip [124, 203], and single species biofilms on chip [122], yet to date there has been no studies showing RS for the analysis of multi-species biofilms on chip, over time.

The microfluidic devices were first coated with sterilised human saliva to replicate the oral environment by providing a pellicle layer of salivary glycoproteins, phosphoproteins, and lipids which both species initially bind to. Mono-species and 2-species biofilms were grown for 5 days at 37°C under constant flow. An example of how 2-species biofilms grow and develop over time can be seen in the bright field images shown in **Figure 3.6**. Biofilm growth begins in small aggregates across the chamber rather than one blanket biofilm, and favours attachment to the chamber walls, as seen in Day 1. Biofilm aggregates in the centre of the chamber get washed away over the days, while those attached to the walls grow thicker and denser and eventually represent the most mature point of the biofilm, with the path of fluid flow through the chamber clearly carved out around the biofilms. One advantage of the chip design is that the transparent chamber allows for the biofilm growth to be seen by eye, and on the occasion where the biofilm were contaminated with other species or fungal bacteria, it was instantly noticeable as there would be excessive growth in the chamber which was not consistent with these

2-species biofilms.

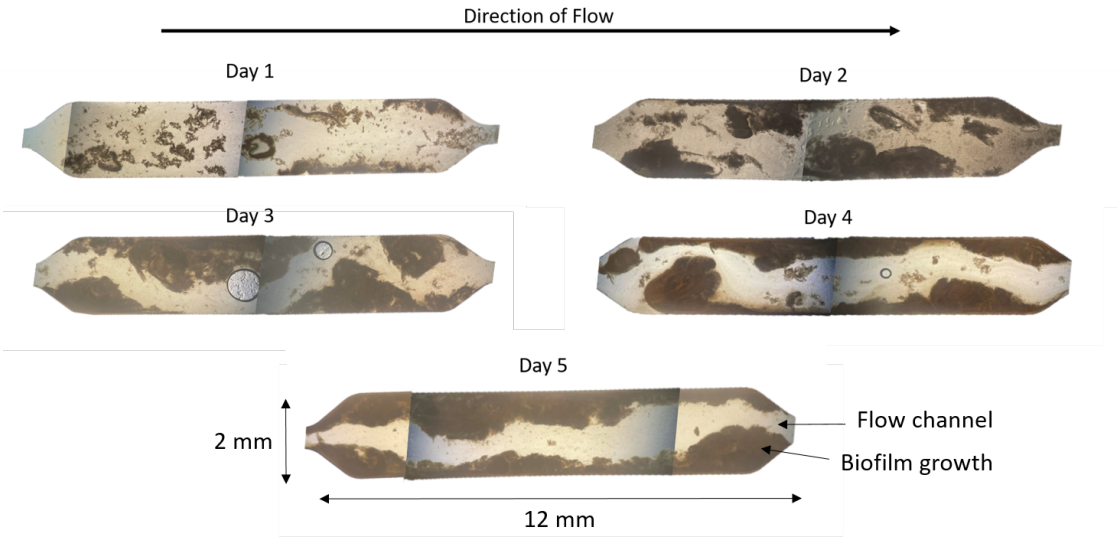

Figure 3.6: Bright field images of *S.salivarius* and *A.naelsundii* 2-species biofilm growth at Day 1 - Day 5. The chamber dimension are 12 mm x 2 mm x 160 μm, and images of the chamber are stitched together from separate images taken using a Confocal microscope and 10x magnification. Fluid flow is from left to right, 20 μ/min, shear stress 0.3 dynes/cm^2. Occasionally air bubbles would pass on chip, as seen in the Day 3 sample.

Preventing air bubbles from flowing on chip was a major concern as they have the potential to disrupt the biofilm completely. **Figure 3.6** shows small air bubbles on the Day 3 biofilm, which in this instance likely caused limited biofilm disruption as the air bubbles are small and the biofilms at this stage are well developed and are more resistant to stress. However, larger air bubbles or those that appear during early biofilm formation can remove a significant portion of the biofilm, providing inconsistent biofilm growth. To prevent incorporating air into the system, media was warmed to room temperature before connecting to the syringe pump. Any visible air bubbles were removed via the 3-way taps or injection loop. Despite this, some small air bubbles did still arise in the system. This was potentially due to air seeping in through the 2- and 3-way tap connectors, or dissolved gas within the media forming air bubbles.

3.3.2 Confocal fluorescence imaging of Biofilms

Confocal laser scanning microscopy (CLSM) is a useful technique that can provide high resolution 3D imaging of biofilms, and can be used to distinguish between individual species within a biofilm. Using a live/dead stain is a common analysis method for biofilms, where the SYTO9 is a green-fluorescent nucleic acid stain that permeates the cell wall, binding to all live and dead cells, while propidium iodide (PI) is a red-fluorescent membrane impermeable DNA stain that will only stain dead cells. PI will cause a reduction in SYTO9 fluorescence in dead cells, and thus dominate [204]. CLSM in this thesis was performed on an inverted microscope system, so all images shown are taken looking up through the bottom of the biofilm, as shown in **Section 2.9**.

Images of 2-species biofilms were taken at 10x and 100x magnification. Images taken with the 10x magnification give a broad overview of the biofilm structure. Examples of fluorescent CLSM images of Day 1 - Day 5 biofilms can be seen in **Figure 3.8**. These images show the x-y plane of z-stack composites, looking up through the base of the biofilm, shown in **Figure 3.7**. Confocal images of mono-species biofilms were not taken in order to save time, as it was thought they would not provide enough information to inform on the growth of the 2-species biofilms and the new interactions taking place. Confocal images were considered to be a useful visual addition to the Raman data, however in the future if the nature of the live/dead bacteria was the main focus, images of mono-species would also be taken.

These CLSM images provide an insight into the general structure and growth patterns of biofilms. In all images where there are large aggregates of biofilms, the inner portion and base of the biofilm is dead (red), with a live (green) band surrounding the edge of the biofilm. This is particularly prominent in Day 3 and 4. This is consistent with the literature which suggests that as biofilms develop and grow, there is a nutrient gradient across the z-axis of the biofilm, resulting in the bacteria at the base of the biofilm becoming nutrient deficient and dying first [205–207]. This is also true along the x-y axis when a biofilm is attached to the wall of the chamber. The outer edge of the biofilm is directly in the flow of nutrients, growing and excreting matrix making the

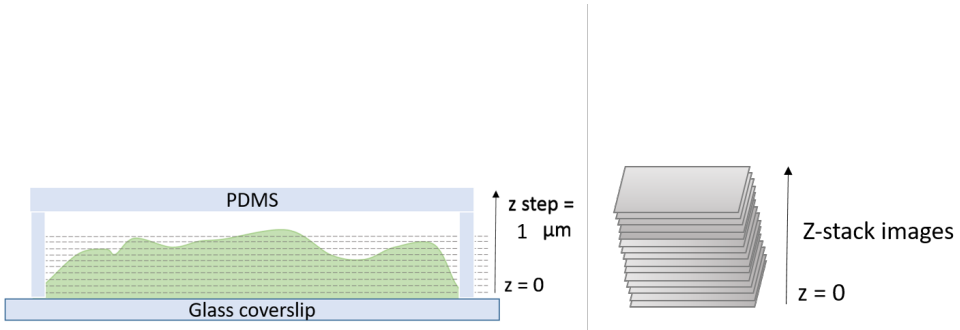

Figure 3.7: Schematic demonstrating z-stacks taken of biofilms on chip, from the base up (z = 0), and the z-stack projection of images. Z-stacks taken with a 1 μm step, unless otherwise stated. Z-height varies per biofilm.

biofilm thicker. The Day 3 image specifically shows this as the green central channel of live bacteria is the media flow between the thicker biofilms on either side. Nonetheless, caution must be advised when analysing these images, as it is also possible that PI is not just binding to DNA in dead cells, but also to eDNA in the extracellular matrix therefore over-estimating the dead cells in areas they may be dense extracellular matrix.

For the particularly dense areas of biofilm, as in Day 2, 4 and 5, this dead (red) fluorescence at the base of the biofilm does however fade to black, where no signal is shown despite there being biofilm present. This was one of the main limitations found of this imaging technique. These black areas are either caused by the fluorescent stains not being able to penetrate the depth of the biofilms thus showing no fluorescence, this is quite likely as it is known that antibiotics often fail to treat biofilms due to lack of penetration into the biofilm matrix. For this reason, conclusions drawn from these images are limited as the full depth of the biofilm cannot be analysed. Taking a closer look at the biofilm with the 100x oil immersive objective provides a different insight into the biofilm structure and growth, one which shows the individual species and their formation within biofilm clusters.

An example of z-stack images taken of Day 1 biofilms with 100x oil magnification can be seen in **Figure 3.9**. Highlighted on the images are the individual species, where

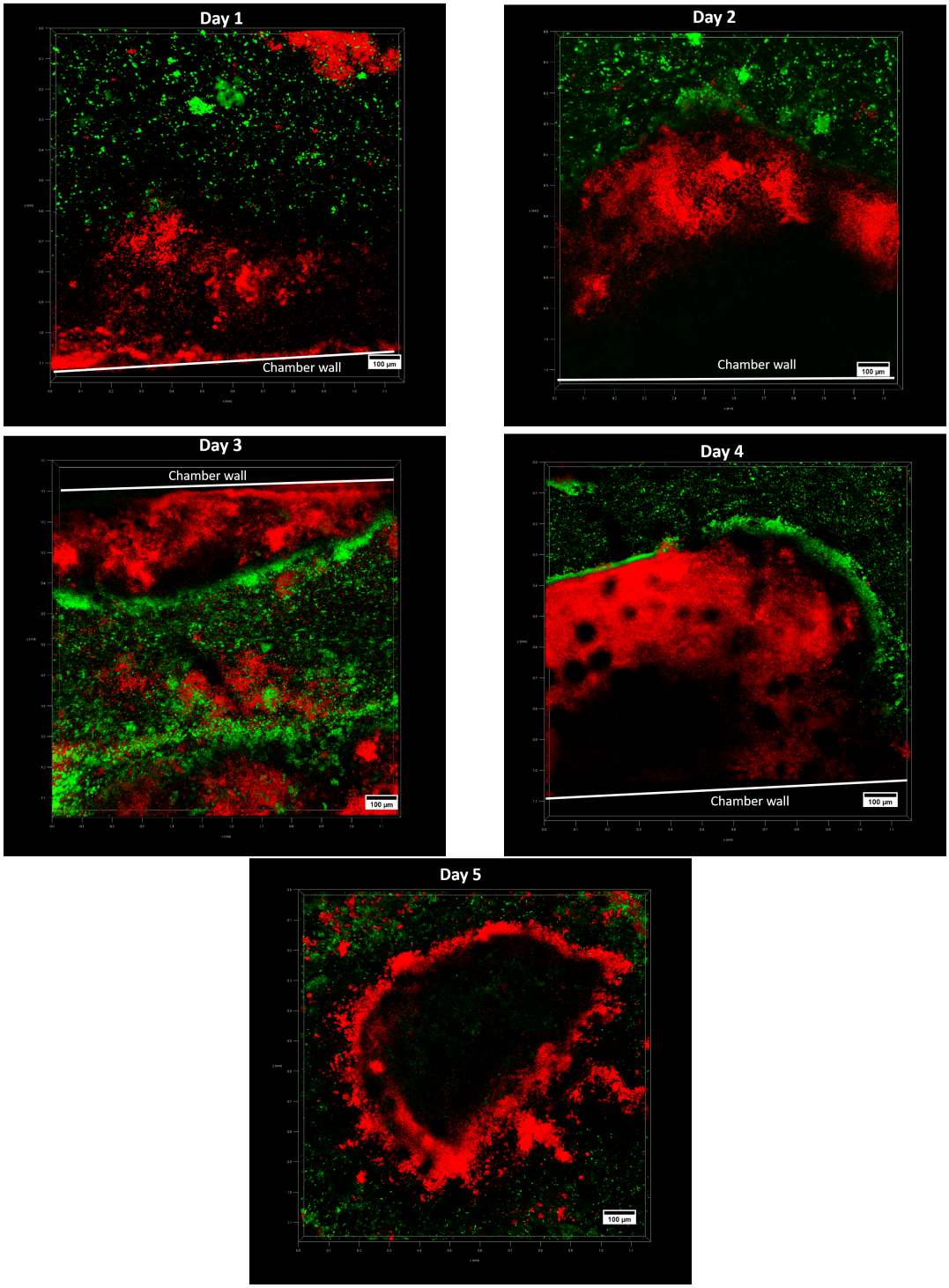

Figure 3.8: Fluorescent CLSM images of live/dead (SYTO9/PI) stained 2-species biofilms from Day 1 - Day 5, taken with 10x magnification. Live bacteria is shown in green and dead shown in red. The white line shows the edge of the chamber wall for reference. Images are z-stack composites viewed through the x-y plane, looking up through the base of the biofilm. The image area is 1200 x 1200 μm, and the scale bar shows 100 μm.

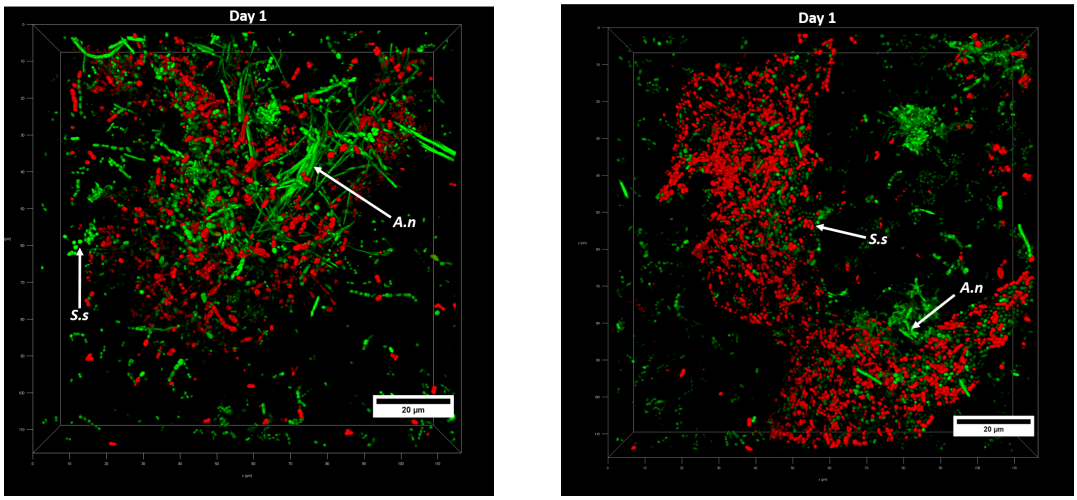

Figure 3.9: Fluorescent CLSM images of live/dead stained 2-species biofilms on Day 1, taken with 100x oil objective at different points of the biofilm. Live bacteria are shown in green, and dead in red. *S.salivarius* (S.s) are spherical cocci, *A.naeslundii* (A.n) are rod like. Images are z-stacks viewed through the x-y plane and are 120 x 120 μm, with a 20 μm scale bar.

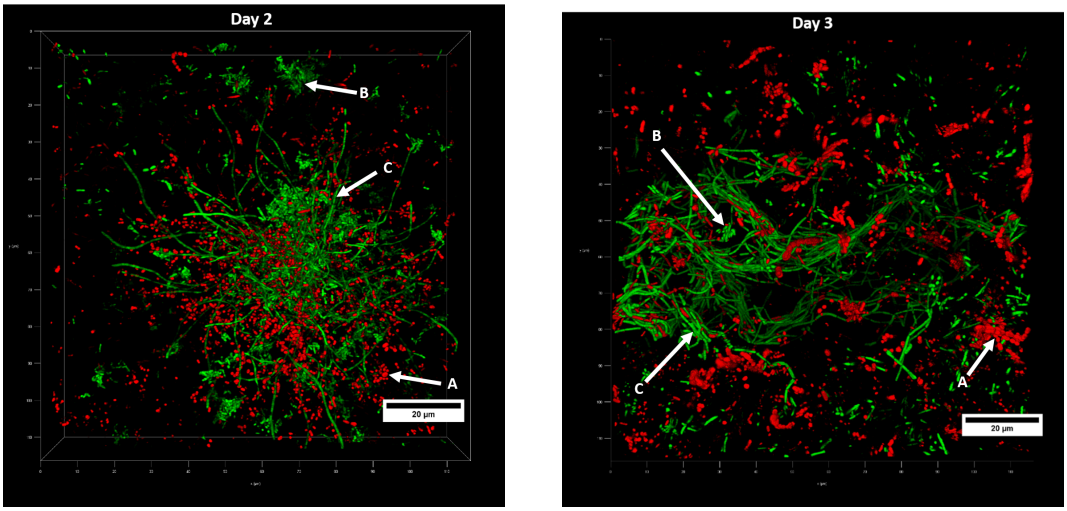

(a) **(b)**

Figure 3.10: Fluorescent CLSM images of live/dead stained 2-species biofilms on a) Day 2 and b) Day 3. Live bacteria is shown in green, and dead in red. *S.salivarius* are spherical cocci, *A.naeslundii* are rod like. Images were taken with 100x oil magnification, and are z-stacks viewed through the x-y plane. 120 x 120 μm, with a 20 μm scale bar.

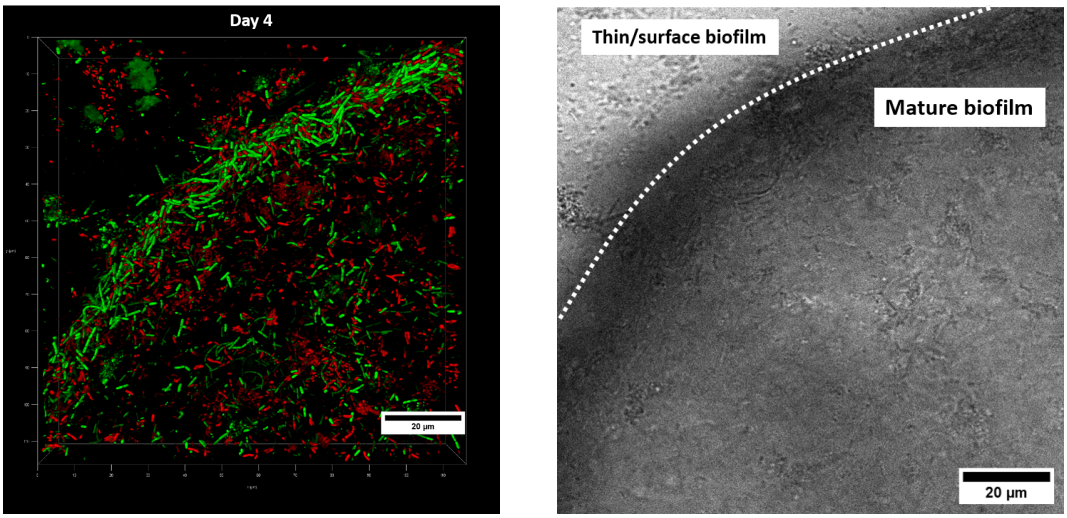

(a) **(b)**

Figure 3.11: a) Fluorescent CLSM images of live/dead stained 2-species biofilms on Day 4. Live bacteria is shown in green, and dead in red. *S.salivarius* (S.s) are spherical cocci, *A.naeslundii* (A.n) are rod like. Images were taken with 100x oil magnification, and are z-stacks viewed through the x-y plane. b) Corresponding bright field image showing the boundary of the 2-species biofilm with the dotted white line. Both image dimension are 120 x 120 μm, with a 20 μm scale bar

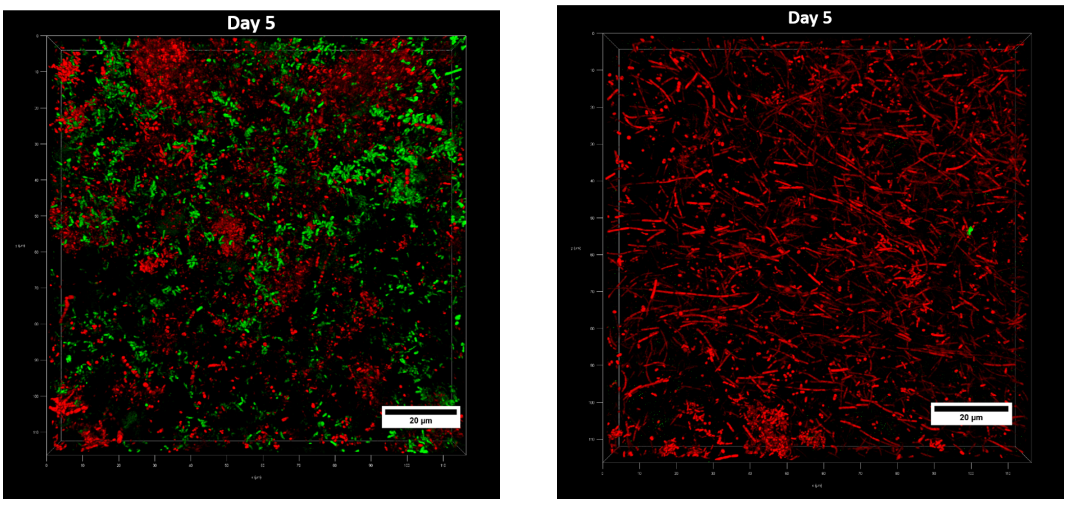

(a) **(b)**

Figure 3.12: Fluorescent CLSM images of live/dead stained 2-species biofilms on Day 5, taken at different areas of a biofilm. Live bacteria are shown in green, and dead in red. *S.salivarius* are spherical cocci, *A.naeslundii* are rod like. Images were taken with 100x oil objective, and are z-stacks viewed through the x-y plane. 120 x 120 μm, with a 20 μm scale bar

the spherical *S.salivarius* (S.s) can be seen individually or forming long chains. The rod like *A.naeslundii* (A.n) are clearly distinguishable due to their long rod like chains. The images suggest that *S.salivarius* is more abundant in Day 1 than *A.naeslundii*, which is not unexpected as *S.salivarius* has a faster growth rate. This naturally explains why there also appears to be more *S.salivarius* dead cells. Examples of images taken at Day 2 and 3 can be seen in **Figure 3.10**. These images, particularly Day 2 and 3, show how bacteria develop in clusters and branch out. *S.salivarius* clusters are labelled "A" and are mostly dead in both Day 2 and 3 images, dispersed throughout the biofilms, and small clusters of *A.naeslundii*, "B", are seen, but it is more common so see long chains intertwined, "C". Interestingly, images of Day 4 in **Figure 3.11 a** show how the outer perimeter of a biofilm consists of live bacteria, primarily *A.naeslundii* in this instance, while the inner areas are populated with more dead bacteria. **Figure 3.11 b** shows the corresponding bright field image highlighting where the boundary of the biofilm is with a white dotted line. The boundary of the biofilm is closest to the flow of nutrients therefore it is unsurprising that this area has a high density of live bacteria.

Day 5 images in **Figure 3.12** show an even distribution of live and dead bacteria across the biofilm in **Figure 3.12a**, while some areas show complete coverage of dead bacteria, **Figure 3.12b**, which is something not seen in previous days. Up to Day 5, image have show an approximately even distribution of live and dead bacteria, most of which was *S.salivarius*. These high magnification images allow for the identification of individual species within 2-species biofilms and give an indication of the structure of the biofilms. As with the previous CLSM images, these images alone are not enough to accurately provide information on the variation between biofilms at different days, but show examples of 2-species biofilms on the micron scale.

3.4 Raman Spectroscopy

To better understand the structure of 2-species biofilms and how they change over the course of 5 days, RS was used as it is a non-destructive, label free method of analysis, meaning that the same biofilm can be analysed over time. RS provides a spectra (In-

tensity (A.U) v Wavenumber (cm^{-1})) denoting the molecular fingerprint of the biofilm. In this thesis, spectra were primarily recorded in the "fingerprint" region, between 550 - 1850 cm^{-1}, which contains most biological information, and the high wavenumber region, from 2800 - 3020 cm^{-1} which shows the CH_2 and CH_3 peaks prominent in proteins and lipids. The region from 1850 - 2800 cm^{-1} is known as the "cellular silent region" as there is typically no biological information in this region.

Multi-species biofilms are complex, ever-changing organisms with inter-species interactions and a growing extracellular matrix. By comparing Raman spectra of 2-species biofilms over 5 days, we hoped to show how these biofilms change over time. In order to understand *S.salivarius* and *A.naeslundii* 2-species biofilms, it was first necessary to examine the planktonic species and mono-species biofilms, see how these species differ with RS, and then use this to inform and compare to 2-species biofilms.

All Raman spectra were pre-processed, which included cosmic ray removal, baseline subtraction, truncating, normalising to Amide I at 1659 cm^{-1}, and smoothing. Principle component analysis (PCA) and linear discriminant analysis (LDA) were used as a tool to maximise the separation between biofilm species, details given in **Section 2.8.5.2**.

3.5 Raman of Planktonic Bacteria

Planktonic samples of *S.salivarius* and *A.naeslundii* were washed to remove any traces of media that may interfere with Raman spectra and air-dried onto glass coverslips. Samples were air dried as in solution bacteria were free to move around and drift out of focus during scans. Raman spectra of each individual species was taken with 100x oil objective. The average spectra of each species (n = 27, taken over 3 experimental repeats) can be seen in **Figure 3.13**.

Figure 3.14 a shows the planktonic spectra annotated with dashed lines showing key peaks that appear in the spectra of both species. Both species show a strong lipid peaks at 2937 cm^{-1}, and the shoulder of a peak at 2880 cm^{-1}, associated with the symmetric stretching of CH_3 and the asymmetric stretching of CH_2, respectively [208].

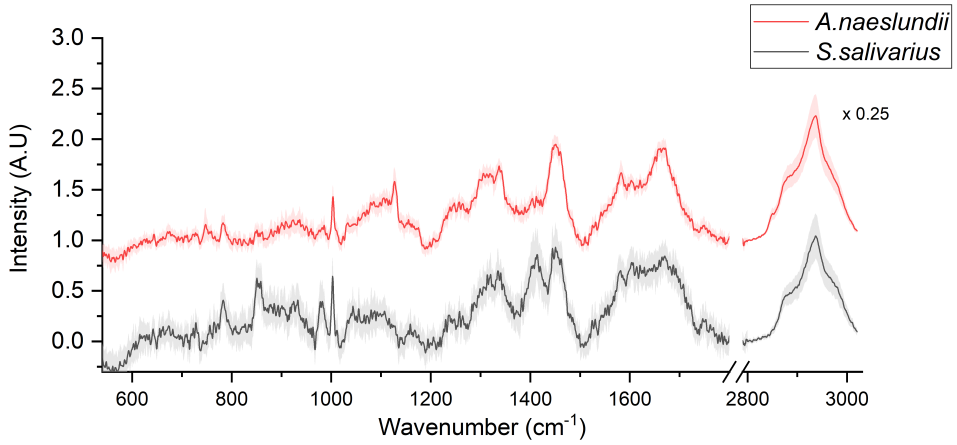

Figure 3.13: Average Raman spectra of planktonic *S.salivarius* (black) and *A.naeslundii* (red) taken with 100x oil objective. The spectra show the fingerprint region from 550 - 1800 cm^{-1} and the high wavenumber region from 2800 - 3020 cm^{-1}. High wave number region x0.25. Each spectrum is the average of n = 27 spectra across repeats, and the shaded region shows the standard deviation. 2800 - 3000 cm

Within the fingerprint region, both species show similar peaks at 1670 cm^{-1} (Amide I), 1450 cm^{-1} (CH_2 bending, lipids), and 1003 cm^{-1} (phenylalanine) which are expected within biological spectra [209, 210]. 1583 cm^{-1} is also attributed to C=C stretching of phenylalanine, and 644 cm^{-1} is either the C-C twisting of phenylalanine or tyrosine [209, 211–213]. 1337 cm^{-1} CH_2 wagging, and 783 cm^{-1} is the phosphodiester symmetric stretching in DNA [211, 214–217].

Figure 3.14 b shows the differences in the spectra, where the dashed line and black text shows peaks only found in *S.salivarius* and the dotted line and red text shows those only found in *A.naeslundii*. *A.naeslundii* has fewer distinct peaks, notably a small shoulder at 2850 cm^{-1} (CH_2 symmetric stretching), 1127 cm^{-1} (C-N stretch of proteins), and 784 cm^{-1} (DNA) [208, 211]. *S.salivarius* shows additional peaks at 728 cm^{-1} (adenine), 980 cm^{-1} (proteins), 1414 (CH stretch/DNA), 850 and 1604 cm^{-1} (tyrosine) [210, 211, 218–221]. Although Raman spectra of bacterial species can be very similar, these small distinct peaks allow for the spectra to be differentiated.

PCA is a useful tool in Raman analysis as it reduces the dimensionality of the data whilst maintaining the most information. It maximises the variance in the data so that the first principle component, PC1, contains the most variance, PC2 contains the next

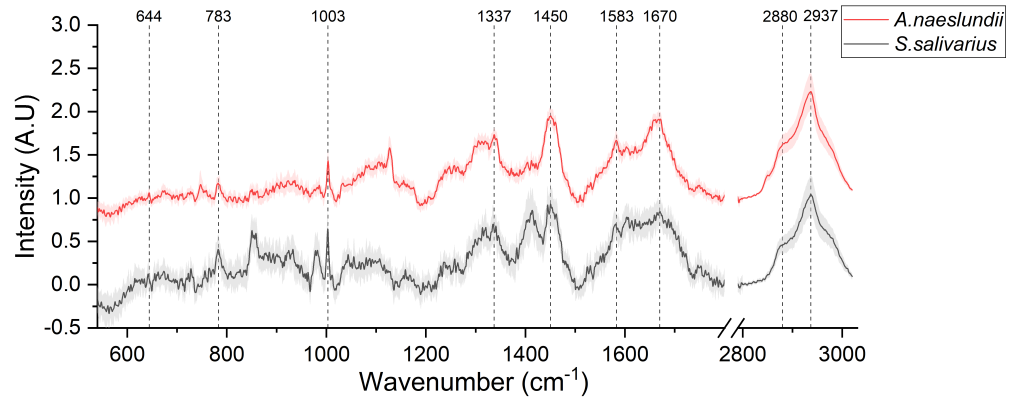

(a)

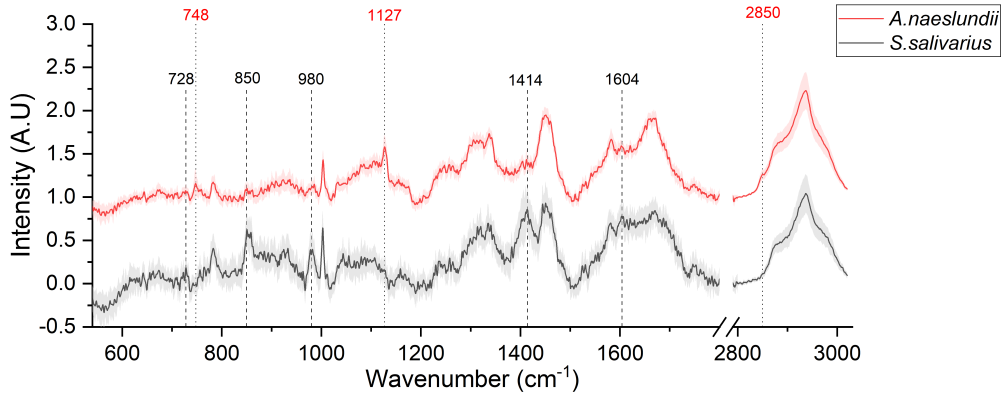

(b)

Figure 3.14: Average Raman spectra of planktonic *S.salivarius* (black) and *A.naeslundii* (red) where a) uses a dashed line to show peaks which are present in both spectra, and b) uses a dashed line and black text to show peaks only present in *S.salivarius,* and a dotted line and red text showing those only present in *A.naeslundii.*

amount, and so on. These PC's can be portrayed on 2 or 3D plots, making visualisation of the data much easier.

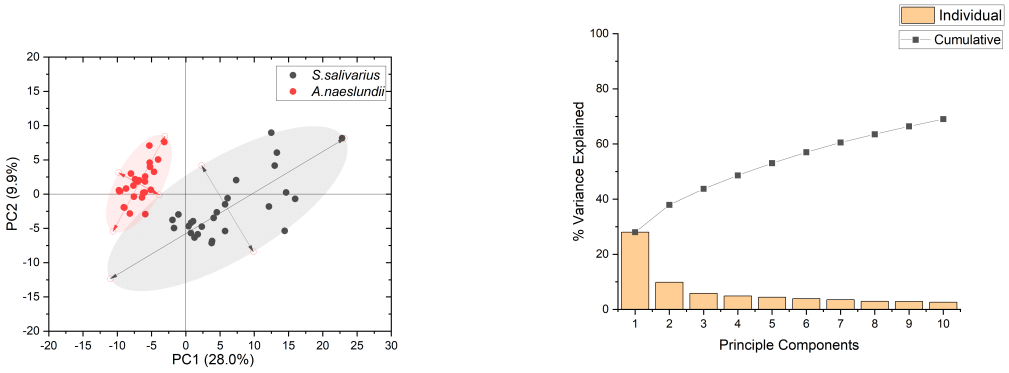

(a) **(b)**

Figure 3.15: PCA of planktonic *S.salivarius* and *A.naeslundii* Raman spectra, where a) shows the score plot of PC1 v PC2, *S.salivarius* are black and *A.naeslundii* red, with 95% confidence ellipse, and b) shows the % variance explained of PC1 - PC10, with the bars showing the individual variance and the line showing the cumulative variance. n= 27 per species.

PCA of planktonic Raman spectra was performed and **Figure 3.15a** and **b** shows the scatter plot of PC1 v PC2, and the variance explained. Each species shows clear clusters, thus showing that Raman can be successfully used to identify and differentiate between planktonic species of bacteria. *S.salivarius* has a broader spread than *A.naeslundii* showing a greater variability across the PC1 and PC2 axis. The most significant separation between the two species is along the PC1 axis, where *A.naeslundii* has a negative PC1 loading while *S.salivarius* has a majority positive PC1 loading. The loadings show how strongly that variable influences the component, the bacteria species in this case. A positive loading has a strong influence or relation to the component, a negative loading is unrelated or lacking any influence from that variable. The PC loadings for PC1 and PC2 can be see in **Figure 3.16a**, and a plot of PC1 loadings with peak annotations can be seen in **Figure 3.16b**. The distribution of the scores on the scatter plot show that for the loadings of PC1, all the peaks in the negative direction correspond to *A.naeslundii* (738 - 738, 1127, 1510, 2850 cm $^{-1}$), and the positive are *S.salivarius* (850, 978, 1410, 1580-1660, 1660-1730 cm^{-1}), which encompass the peaks identified by eye in **Figure 3.14**. PCA was able to successfully identify the two species and provide good spectral

information on both species through the PC1 and PC2 components, therefore no further LDA analysis was required. LDA would also not be possible on just 2 bacteria species as for LDA the number of components is the number of classes (species) minus one, therefore LDA could only provide 1 component which would not work.

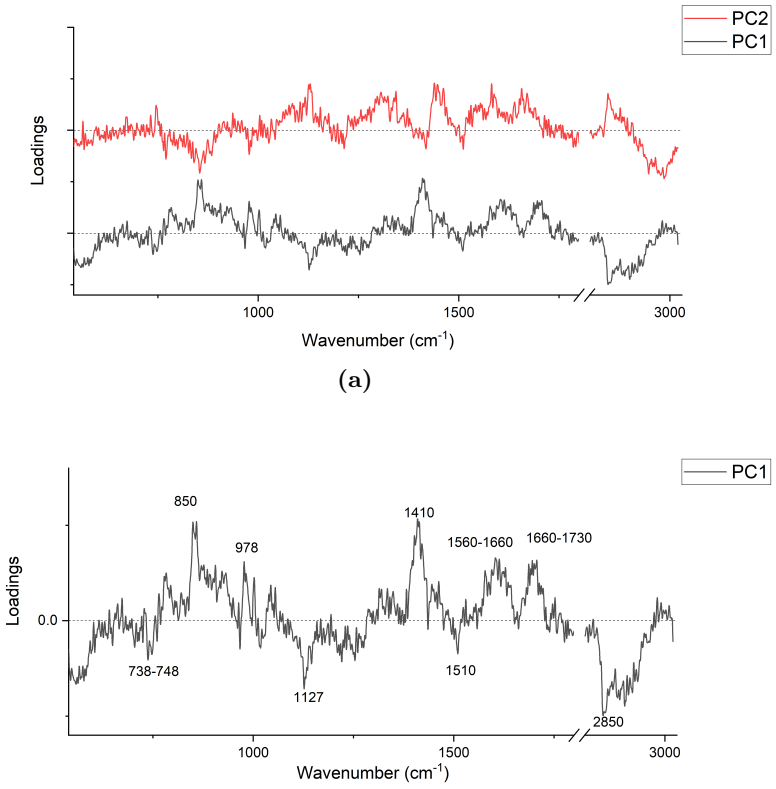

Figure 3.16: a) PC1 and PC2 loadings of *S.salivarius* and *A.naeslundii* planktonic species, b) PC1 loading with each significant peak labelled, where negative peaks are associated with *A.naeslundii* and positive peaks *S.salivarius*

3.6 Raman on-chip: Mono-species biofilms

Taking Raman spectra of mono-species biofilms is the natural progression of trying to understand these species and how they, and their spectra, change over time as they secrete extracellular matrix and form biofilms. Understanding how these single species grow on their own will make understanding 2-species biofilms easier, and highlight what, if any, features are exclusive to multi-species biofilms. Raman spectra of *S.salivarius*

and *A.naeslundii* mono-species biofilms were taken every day from Day 1 - Day 5, with a minimum of 25 spectra taken across three biofilms and the average of each spectrum from each day plotted. The Raman peaks were identified based on the literature and can be found in **Table 3.2**.

Wavenumber (cm^{-1})	**Peak Assignment**	**Reference**
602	DNA	[209, 211]
614	DNA	[209, 211]
710	DNA	[209, 211]
728	Adenine	[218]
746	DNA	[209, 211]
781	Cytosine	[210, 211]
784	DNA	[208, 211]
850	Tyrosine	[220]
920	C-C	[209, 211]
980	protein	[211]
1003	Phenylalanine	[209, 210]
1127	C-N stretch (proteins)	[222]
1168	Tyrosine	[223]
1250	Amide III	[224]
1297	CH_2 twisting	[211]
1305	CH_2, nucleic acids	[225]
1337	CH_2 wagging	[214]
1414	DNA/CH	[219, 226]
1450	CH_2 bending	[209, 210]
1581	DNA	[222]
1604	Tyrosine	[221]
1670	Amide I	[209, 210]
2850	CH_2 symmetric	[211]
2874	CH_2 sym and asym of lipids and proteins	[227]
2881	CH_2 symmetric	[228]
2905	CH_2 fermi resonance, CH stretch	[211]
2930	CH_3 symmetric	[211]
2960	out of plane asymmetric CH_3 stretch	[211]

Table 3.2: Raman peak identifications based on literature that have studied bacterial and mammalian cells.

3.6.1 *S.salivarius* Mono-species Biofilm

Figure 3.17 shows the Raman spectra of *S.salivarius* mono-species biofilms taken over 5 days, the planktonic spectrum in black is inlcuded for reference. Key peaks which

visually change over time are labelled with a dashed line. Some peaks that are present in the planktonic spectra are not present in the biofilm spectra, such as 728 and 980 cm^{-1}, while there are others that are not present in the planktonic and only feature in the biofilms; 602, 614, 710, 746, 1127, 1297, 2850, and 2905 cm^{-1}.

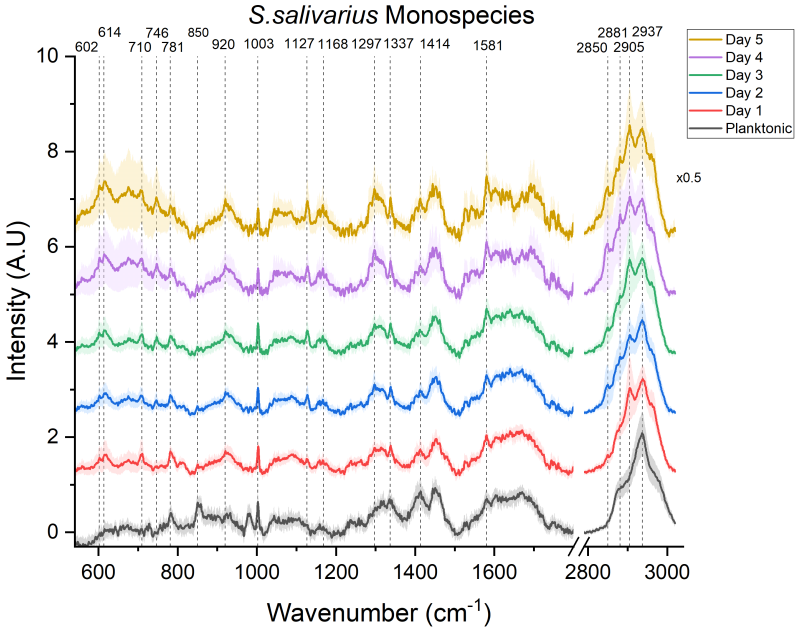

Figure 3.17: Raman spectra of *S.salivarius* mono-species biofilms taken everyday for 5 Days. *S.salivarius* planktonic spectra is shown in black for reference, Day 1 (red), Day 2 (blue) Day 3 (green), Day 4 (purple), Day 5 (gold). Key peaks are labelled with a dashed line. All spectra normalised to the Amide I peak 1670 cm^{-1}.

Figure 3.18 shows the intensity over time of significant peaks, with peaks showing similar trends grouped together. **Figure 3.18a** shows 602, 614, 710 and 746 cm^{-1}, which are all labelled as DNA. All peaks were not present in the planktonic spectra thus suggesting these DNA peaks are associated with the extracellular matrix. 746 cm^{-1} is the only peak that shows a linear increase over time. 602, 614 and 710 cm^{-1} all show an increase between Day 3 - 5, suggesting some significant metabolic activity during this stage of biofilm growth. **Figure 3.18b** shows 781 and 920 cm^{-1}, which are cytosine and the C-C stretch of lactic acid, respectively. Both are present in planktonic and also show the greatest increase between Day 3 - 5.

Figure 3.18c shows 1127 (C-C), 1337 (CH_2 wagging) and 1581 (DNA) cm^{-1} linearly

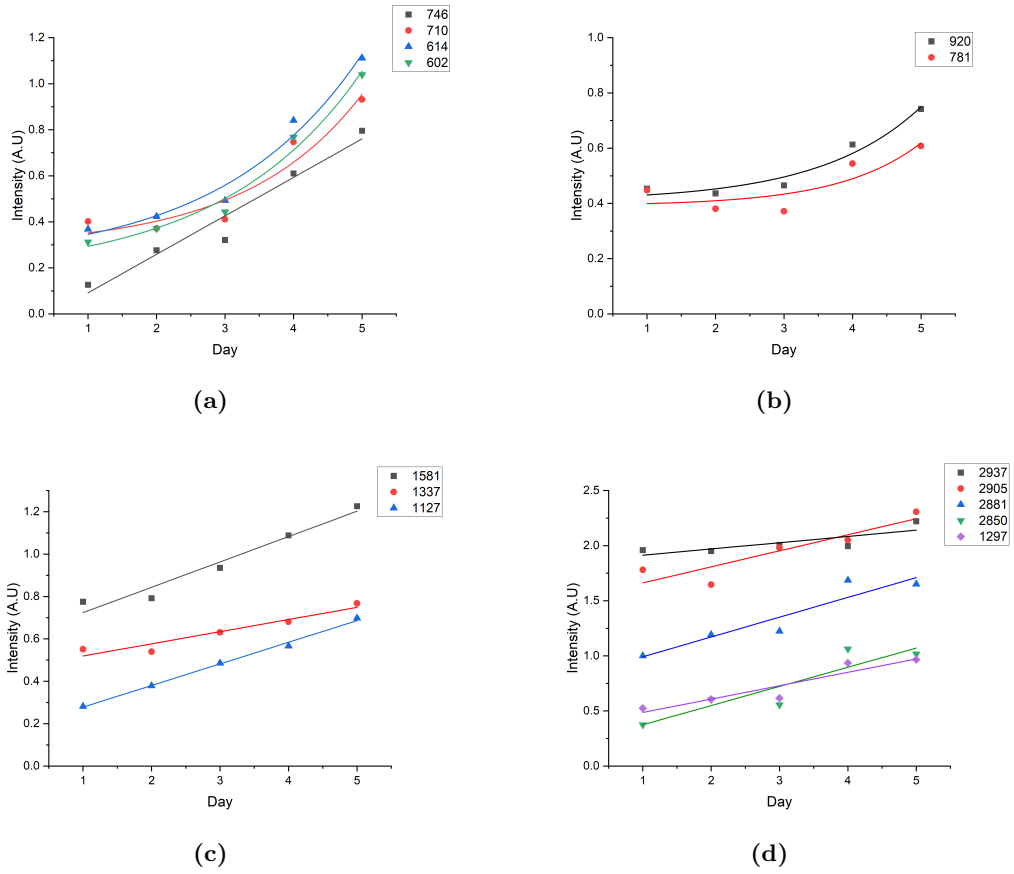

Figure 3.18: Raman peak intensity over time of *S.salivarius* biofilms, where peaks are grouped by biological relevance: a) (DNA) 602, 614, 710, 746 cm^{-1} b) 920 (C-C), 781 (cytosine) cm^{-1}, c) 1127 (C-C), 1337 (CH_2 wagging), 1581 cm^{-1} (DNA) d) 1297 (CH_2 twisting), 2850 (CH_2 symmetric), 2881 (CH_2 asymmetric), 2905 (CH_2 FR), 2937 (CH_3 symmetric) cm^{-1}. Curves fitted with a linear or exponential curve fit.

increase over the 5 days, showing the increase in protein and DNA production as bacteria not only proliferates, but excretes matrix. The linear growth of DNA fshown in this figure may represent bacterial cell growth, and explain the difference in growth from that in **Figure 3.18a**, which may be more representative of matrix. **Figure 3.18 d** shows the CH_2 and CH_3 peaks primarily in the high wavenumber region, representing lipids and proteins. All peaks show a linear increase over time, although 2937 cm^{-1} has a gradient of 0.06, showing that this peak remains approximately stable over 5 days. The CH_2 peaks, 1297 twisting, 2850 symmetric, 2881 asymmetric, and 2905 fermi resonance cm^{-1}, all show fluctuations around Day 3, but have an overall linear trend. One common theme amongst these figures is the increase in intensity from Day 3 - Day 5. This may suggest the most significant changes are during the mature stages of the biofilm, or there is an increase in metabolism or new bacterial growth stage occurring at Day 3.

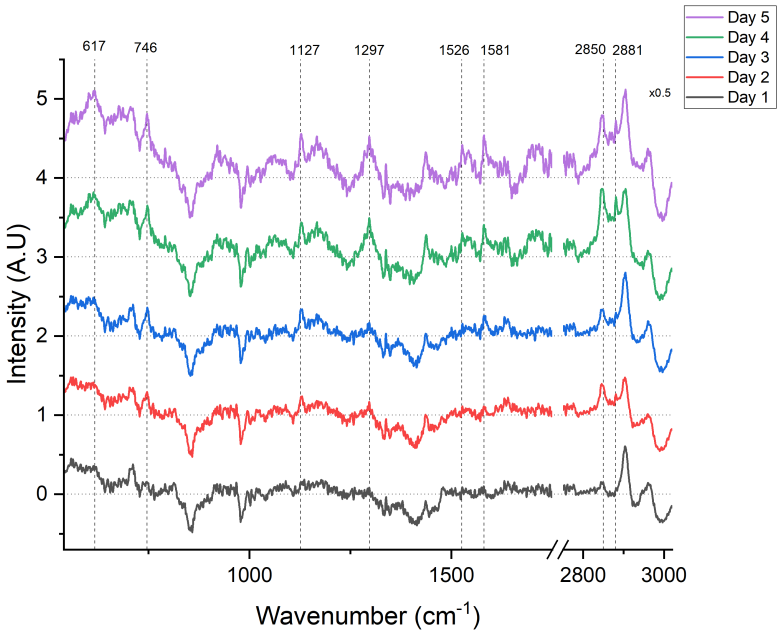

Figure 3.19: The resulting Raman spectra after *S.salivarius* planktonic spectra was subtracted from the mono-species biofilms. The dotted line for each spectra is the 'zero' baseline. For each Day, the spectra above the dotted line is considered to be the extracellular matrix contribution. T

To understand the matrix production of *S.salivarius* mono-species biofilms and how this varies as the biofilm grows, the planktonic spectra was subtracted from the biofilm

spectra, leaving what should be, in theory, the Raman spectra of the matrix contribution, seen in **Figure 3.19**. For each Day, everything above the horizontal dotted line is considered to be matrix. Peak which increase from Day 1 - 5 are labelled with a dotted line. On Day 1 the only significant contribution is DNA in 500-800 cm^{-1} and CH_2 FR at 2905 cm^{-1}. By Day 5 distinct peaks appear across the matrix spectra showing the increase in DNA (617, 746 and 1414 cm^{-1}), proteins and lipids (1127, 1297, 2850, 1526, 2881 cm^{-1}). The increase in matrix intensity shows increased density and thickness of biofilms. Each species secretes a unique matrix composition and thus far, Raman can identify *S.salivarius* matrix components and how they change over time, which may be unique compared to *A.naeslundii* and allow for differentiation, or at least comparison, with multi-species biofilms.

3.6.2 *A.naeslundii* Mono-species Biofilm

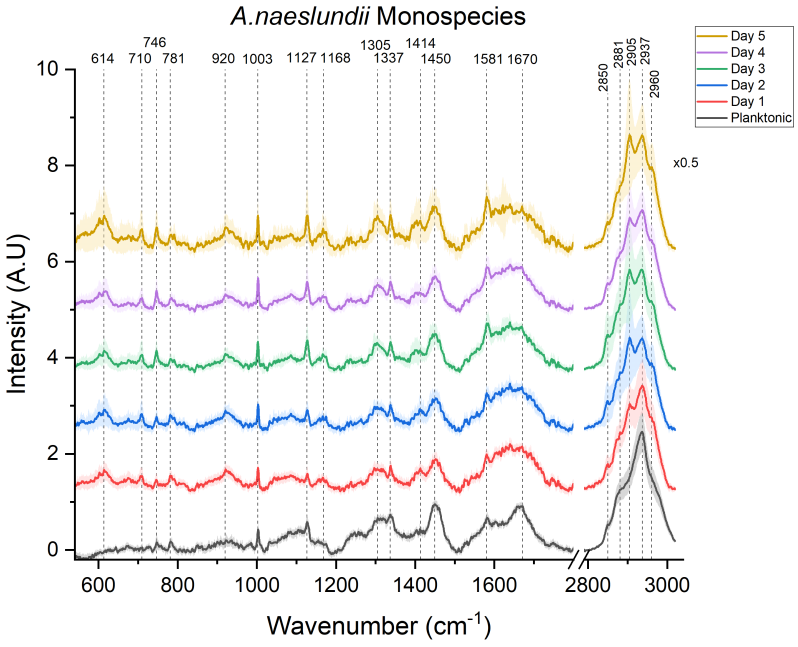

Figure 3.20: Average Raman spectra of *A.naeslundii* mono-species biofilms taken everyday for 5 Days. *A.naeslundii* planktonic spectra is shown in black for reference and key peaks are labelled with a dashed line. 2800 - 3020 cm^{-1} region is multiplied by 0.5 for scale. Each Day shows the average (n=75) and the shaded region is the standard error. Spectra normalised to the Amide I peak 1670 cm^{-1}.

Raman spectra of *A.naeslundii* mono-species biofilms from Day 1 - Day 5, along with the planktonic spectra for reference can be seen in **Figure 3.20** with key peaks labelled with a dashed line. Many peaks are similar to those found in *S.salivarius* biofilms: 746, 781, 1003, 1127, 1168, 1337, 1581, 2850, 2881, 2905, and 2937 cm^{-1} (present in planktonic), and 614, 710, 920, and 1414 cm^{-1} (not present in planktonic). The only noticeable peak that is unique to *A.naeslundii* is 1305 cm^{-1} (CH_2, nucleic acids). This peak was not one identified as a notable peak in the PCA performed on planktonic species in **Figure 3.15**, therefore this peak must be matrix related. The *A.naelsundii* spectra remains consistent over time and is less noisy by Day 5 than *S.salivarius*, potentially due to *A.naeslundii* growing and producing matrix at a slower rate.

The intensity of key peaks over time are shown in **Figure 3.21**, grouped by similar features and trends. **Figure 3.21a** shows 602, 614, 710, 746 (DNA) cm^{-1}. 602 and 614 cm^{-1} remain constant throughout the biofilm growth, until there is an exponential increase between Day 4 - 5 where the intensity almost doubles. 710 and 746 cm^{-1} both show a linear increase. As suggested previously, this difference in DNA growth profile may represent DNA associated with matrix and bacterial cells.

Figure 3.21b shows 781 (DNA) and 920 (C-C) cm^{-1} have no overall increase in intensity over the course of 5 days. This is **Figure 3.21c** shows 1127 (C-C), 1305 (CH_2/nucleic acid), 1337 (CH_2 wagging) and 1581 (DNA) cm^{-1}, all following a linear increase over 5 days. Aside from 1305 cm^{-1} which is not present in *S.salivarius*, these peaks follow the same trend as for *S.salivarius* biofilms. **Figure 3.21 d** shows the intensity for all peaks in the high wavenumber region; 2874, 2850, 2881 and 2937 cm^{-1}. 2850 and 2881 cm^{-1} remain stable across the 5 days, having a gradient of 0.003 and 0.02, respectively. 2905 cm^{-1} shows the greatest increase, with a gradient of 0.19, while 2937 cm^{-1}, has a smaller increase and gradient of 0.06. Compared to *S.salivarius*, *A.naeslundii* shows smaller change in intensity for most peaks over 5 days, and has more peaks remaining stable. An exponential increase in some DNA peaks are seen between Day 4 - 5, suggesting an increase in metabolism at this stage.

The sole matrix contribution for each Day is seen in **Figure 3.22**, with key peaks

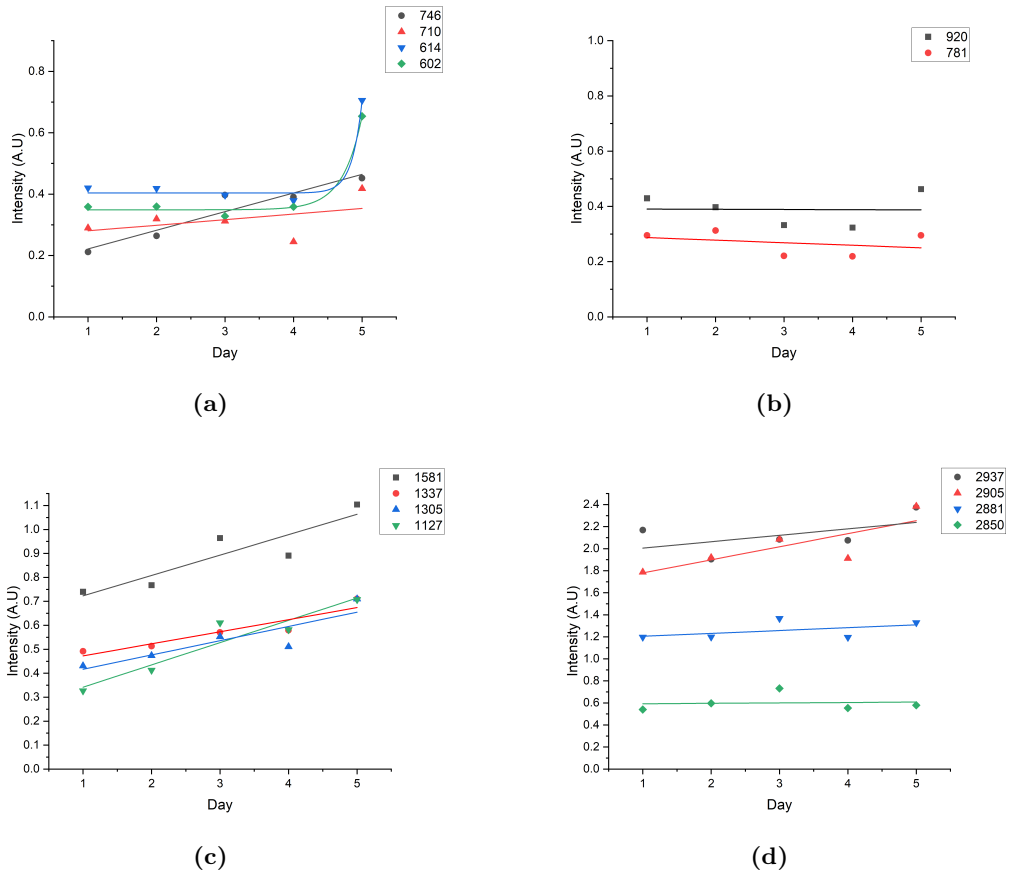

Figure 3.21: Raman peak intensity over time of *A.naeslundii* biofilms, where peaks are grouped by similar features: a) (DNA) 602, 614, 710, 746 cm^{-1}, b) 781 (DNA) and 920 (C-C) cm^{-1}, c) 1127 (C-C) 1305 (CH_2, nucleic acid) , 1337 (CH_2 wagging), 1581 (DNA) cm^{-1}, d) 2850 (CH_2 symmetric), 2881 (CH_2 asymmetric), 2905 (CH), 2937 (CH_3 symmetric) cm^{-1}. All plots fit to a linear or exponential curve fit.

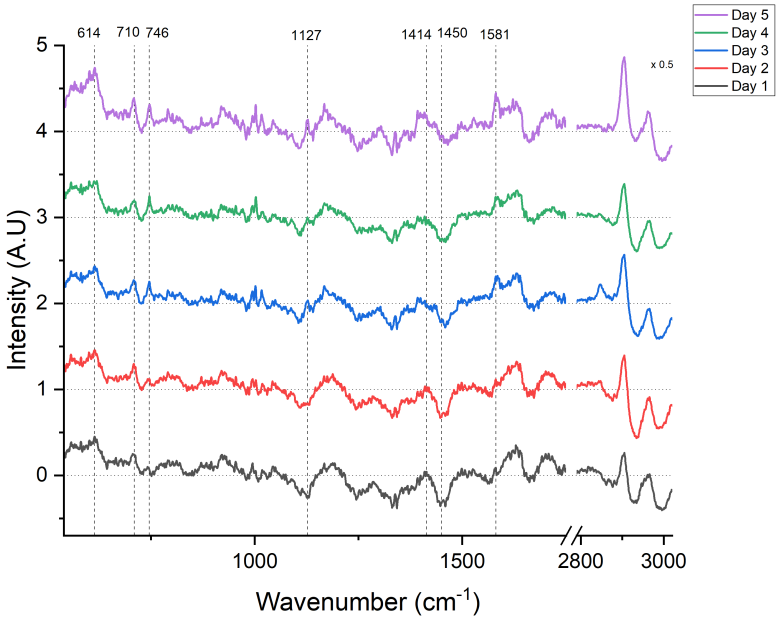

Figure 3.22: The resulting Raman spectra after *A.naeslundii* planktonic spectra was subtracted from the mono-species biofilms. For each Day, the spectra above the dotted line is considered to be the extracellular matrix contribution.

that change over time highlights with a dotted line. 614, 710, 746, 1414 and 1581 cm^{-1} are DNA peaks that show clear increase over 5 days and are thus DNA peaks that are associated with *A.naeslundii* matrix production. 1127 cm^{-1} (C-C) which could be related to proteins shows a strong peak by Day 5. 1450 cm^{-1} does not show a positive peak, however does increase in intensity over time showing an increasing matrix contribution to the CH_2 peak, likely related to the lipid and proteins in the matrix. The 2905 cm^{-1} peak is present at Day 1 and only increases by Day 5, showing this peak to be indicative of *A.naeslundii* matrix, whereas the lack of 2937 cm^{-1} peak suggests this CH_3 peak is related to bacterial cells.

Both *S.salivarius* and *A.naeslundii* grow thick biofilms within 5 Days. The key features of which, DNA, proteins, lipids, can be detected and tracked using RS. For *S.salivarius* biofilms, the trend in peaks suggested the most growth between Day 3 and 5. This increase is mostly matrix, with a strong increase in DNA in the 500 - 800 cm^{-1} region, and specific peaks in the high wavenumber region; 2850, 2881, and 2905 cm^{-1} all

representing the increasing CH_2 and CH_3 lipid and protein contribution. The increase in spectral intensity over time for *A.naeslundii* biofilms was less intense than *S.salivarius* biofilms, with the sharpest increases happening between Day 4 - 5. When looking at the matrix contribution, *A.naeslundii* has fewer peaks in the high wavenumber region, yet both species of biofilm are lacking in the 2937 cm^{-1} peak, therefore this peak could be considered an indicator of the bacteria cells and not the matrix.

3.7 Raman on-chip: 2-species biofilms

Understanding Raman spectra of *S.salivarius* and *A.naeslundii* in planktonic and mono-species biofilm form provides a foundation of knowledge when wanting to look at a more complex 2-species biofilm system. When looking at how the 2-species biofilm changes over time, Raman spectra of biofilms at different Days are compared to see these changes, if any at all. Where the appearance of new peaks or changes in peak intensity can be seen, based on peak assignment we are able to identify what is changing and broadly infer what is the cause, for example peaks in the 2800-3000 cm^{-1} region are associated with CH_2 and CH_3 in proteins and lipids, thus an increase likely indicates cell growth and matrix production. However, knowing that *S.salivarius* has a distinct peak at 2881 cm^{-1} on Day 5 when *A.naeslundii* does not, suggests that *S.salivarius* is the main contributor behind this peak within a multi-species system.

What is difficult about 2-species biofilms is that there is now inter-species interactions taking place, making them more complex than simply the sum of the two mono-species counterparts. Comparing Raman spectra of 2-species biofilms to the mono-species biofilms is important as it tells you the influence each species may be having on the biofilm at that point, but crucially shows what is different and therefore what makes a 2-species biofilm inherently different from the mono-species.

The average Raman spectra of *S.salivarius* and *A.naeslundii* 2-species biofilms taken Day 1 - Day 5 can be seen in **Figure 3.23**. Key peaks are annotated, which are the same as those highlighted in the mono-species biofilms. From this figure, an initial visual

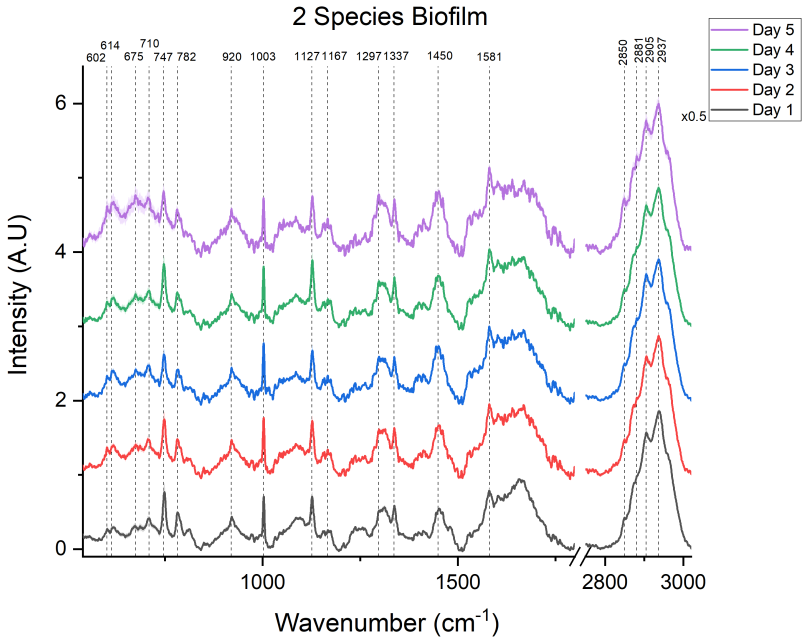

Figure 3.23: Average Raman spectra of *S.salivarius* and *A.naeslundii* 2-species biofilms taken everyday for 5 Days. Day 1 (black), Day 2 (red) Day 3 (blue), Day 4 (green), Day 5 (purple). Key peaks are labelled with a dashed line. 2800 - 3020 cm^{-1} region is multiplied by 0.5 for scale. Biofilms were grown microfluidically and the same biofilm analysed over time. Each day shows the average of 3 experimental repeats (total spectra n=75) and the shaded region is the standard error. Spectra normailsed to Amide I peak 1670 cm^{-1}.

comparison of the spectra shows an increase in intensity in the 500 - 800 cm^{-1} region (DNA), strong prominent peaks at 747, 1003, and 1127 cm^{-1} across all days (cytosine, phenylalanine, C-C protein), and the emergence of 2850 and 2881 cm^{-1} (CH_2 sym and asym) peaks by Day 5. Compared to mono-species, individual peaks appear more distinct with greater intensities, 747 and 1003 cm^{-1} for example. The increase in intensity of the DNA region from 500 - 800 cm^{-1} is most similar to the *S.salivarius* matrix production, which had a broad increase in intensity particularly by day 4 and 5, as demonstrated in **Figure 3.19**. The 2850 cm^{-1} peak is most likely an indication of *S.salivarius* matrix, as the contribution was much greater in *S.salivarius* than *A.naeslundii*. The 2905 cm^{-1} peak present in Day 1 2-species biofilms is due to *A.naeslundii* matrix, however is present in both species matrix thereafter.

The variation in intensity over time of these peaks is shown in **Figure 3.24**. For DNA 602, 614 and 710 cm^{-1}, **Figure 3.24a**, the greatest increase in intensity is seen between Day 4 - 5, with 746 cm^{-1} showing a linear increase. **Figure 3.24b** shows 781 and 920 cm^{-1} remain stable over 5 days. Thus far, these peaks follow the same trends as *A.naeslundii* biofilms. **Figure 3.24c** shows the DNA peak 1581 cm^{-1} have a linear increase over time, with gradient 0.08, where as 1127 and 1337 cm^{-1} have a much smaller change with a linear gradient of 0.02. The high wavenumber region in **Figure 3.24d**, shows small linear increases in intensity over 5 days, with 1297, 2850 and 2881 cm^{-1} all having similar gradients (0.06), while the smallest change is seen for 2937 cm^{-1} (0.03 gradient).

The peak trends of 2-species biofilms are most similar to *A.naeslundii* biofilms, particularly in **Figure 3.24a** and **Figure 3.21a** comparing the DNA peaks which only show increase between Day 4 - 5. The stability of 781 and 920 cm^{-1} peaks over the 5 days is also similar to *A.naesludnii*.

To see if 2-species biofilms at different time points can be individually identified, linear discriminant analysis (LDA) was performed. Unlike PCA, which is an unsupervised model used to find the maximum variance within the data-set, LDA is supervised (which takes a portion of the data set to train the algorithm which then processes the remaining

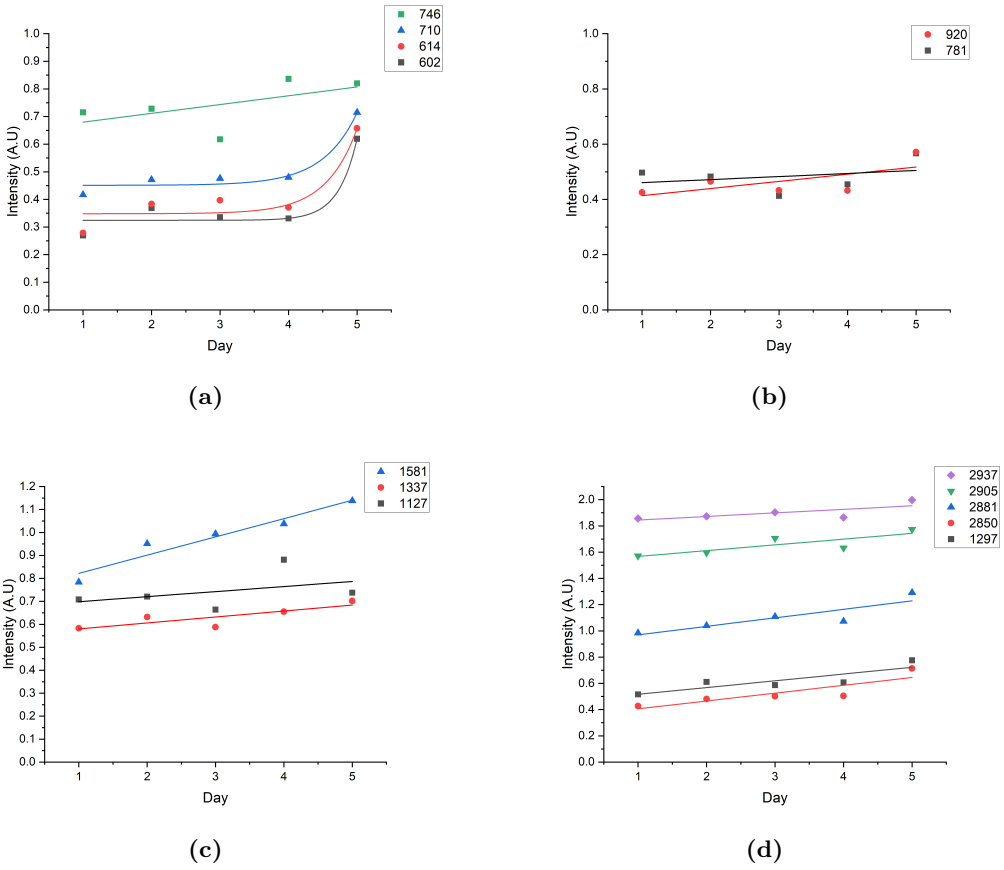

Figure 3.24: Raman peak intensity over time of *S.salivarius* and *A.naeslundii* 2-species biofilms, where peaks are grouped by similar features: a) (DNA) 602, 614, 710, 746 cm^{-1}, b) 781 (cytosine) and 920 (C-C) cm^{-1}, c) 1127 (C-C), 1337 (CH_2 wagging), and 1581 cm^{-1}, d) 1297, 2850 (CH_2 symmetric), 2874 (CH_2), 2881 (CH_2 asymmetric), 2905 (CH_2 FR), 2937 (CH_3 symmetric) cm^{-1}. All plot fit to a linear or exponential curve fit.

data) and aims to find the maximum separation between the defined classes - which are in this case Day 1, 3 and 5. LDA was the preferred method for this analysis as the Raman data across all days was so similar, the variance between the days was not different enough to warrant any information.

A scatter plot of LDA for 2-species biofilms at Day 1, 3, and 5 is shown in **Figure 3.25**. Day 1, 3 and 5 were chosen to simplify the analysis and to show the greatest changes over the 5 days. LD1 and LD2 show the discriminants that have the most separation. From this we see that there is substantial overlap with Day 3 and 5, but Day 1 can be separated from them both. Day 3 and 5 are extremely similar, although Day 5 has much wider spread than Day 3. For mono-species biofilms, *S.salivarius* demonstrated the greatest difference between Day 3 - 5, and *A.naeslundii* between Day 4 - 5, which is reflected in the LDA plot. This data suggests that by Day 3 for 2-species biofilms, the biofilm reaches a new stage of growth lasting until at least Day 5, which is distinct from Day 1. This LDA model however only shows an accuracy rate of 73 $\pm$ 1.5 %, sensitivity of 85 $\pm$ 2%, and specificity of 95 $\pm$ 0.5 %, when doing a 5-fold cross validation. This lower rate of accuracy reflects the similarity of the biofilms across the days, particularly Day 3 and 5 which have large overlap. The average Raman spectra across each biofilm is able to differentiate between biofilm days, but not at high accuracy, therefore looking at specific areas of the biofilm in isolation, such as the top or bottom, may show more significant differences and allow for higher accuracy LDA.

3.7.1 Comparison of 2-species and mono-species biofilms

The change taking place within 2-species biofilms over time are still unclear, however learning what separates them from mono-species biofilms would be a step towards improving our understanding. LDA was used to compare *S.salivarius* and *A.naeslundii* 2-species and mono-species biofilms on Day 1 and Day 5.

The LDA results for Day 1 are shown in **Figure 3.26**, with an accuracy of 87.7 $\pm$ 1 %, sensitivity of 89.1 $\pm$ 1.6 %, and specificity of 97.6 $\pm$ 0.6 %. The scatter plot shows clear and defined biofilm clusters, with 2-species located in the middle of the mono-

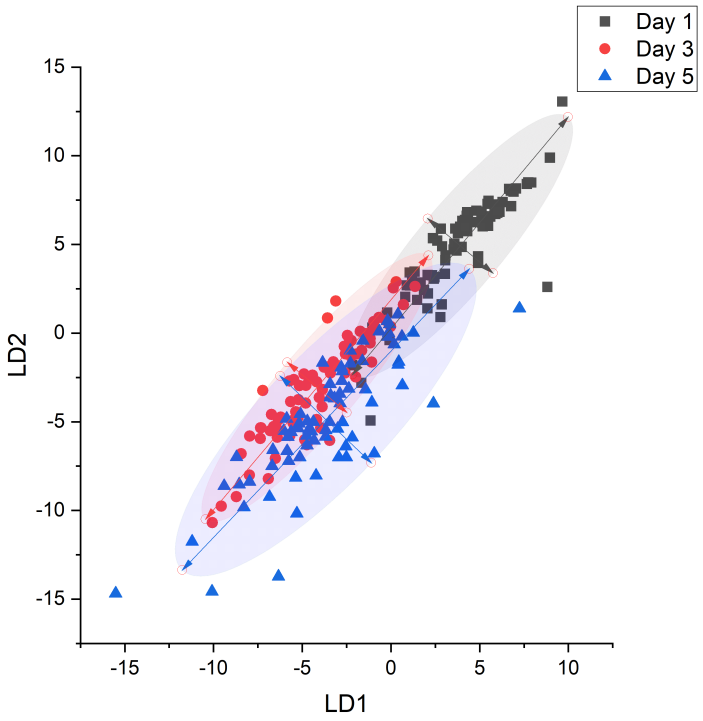

Figure 3.25: LDA of *S.salivarius* and *A.naeslundii* 2-species biofilms at Day 1, 3 and 5. Scatter plot of the classes showing LD1 v LD2 where Day 1 (black), Day 3 (red) and Day 5 (blue), with 95% confidence ellipse. For each day, n=75.

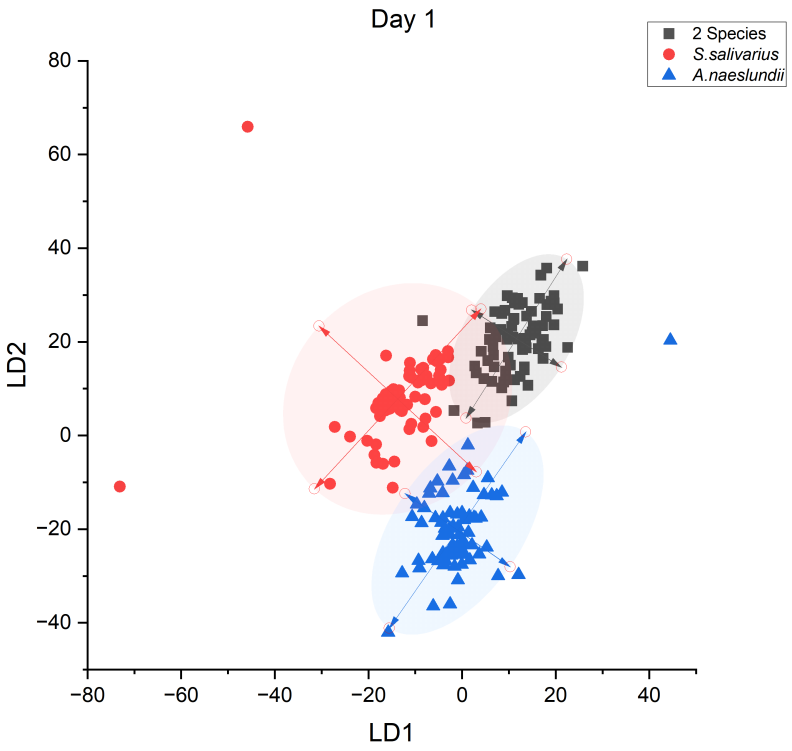

Figure 3.26: LDA of Day 1 *S.salivarius* and *A.naeslundii* mono-species and 2-species biofilms. Scatter plot of the classes showing LD1 v LD2 where 2-species (black), *S.salivarius* (red) and *A.naeslundii* (blue), with 95% confidence ellipse. For each biofilm, n=75.

species along the diagonal axis. The biofilms are well separated along both LD1 and LD2. Along the LD1 axis 2-species biofilm has most overlap with *A.naeslundii*, whereas on LD2, which also shows the greatest separation, 2-species biofilm has overlap with only *S.salivarius*. As the 2-species cluster is not located directly on top of the two mono-species clusters, this suggests there are influences specific to 2-species biofilms causing this greater separation. The accuracy of these results differentiating between mono- and 2-species biofilm on Day 1 (87.7%) is greater than comparing 2-species biofilms on different days (73%).

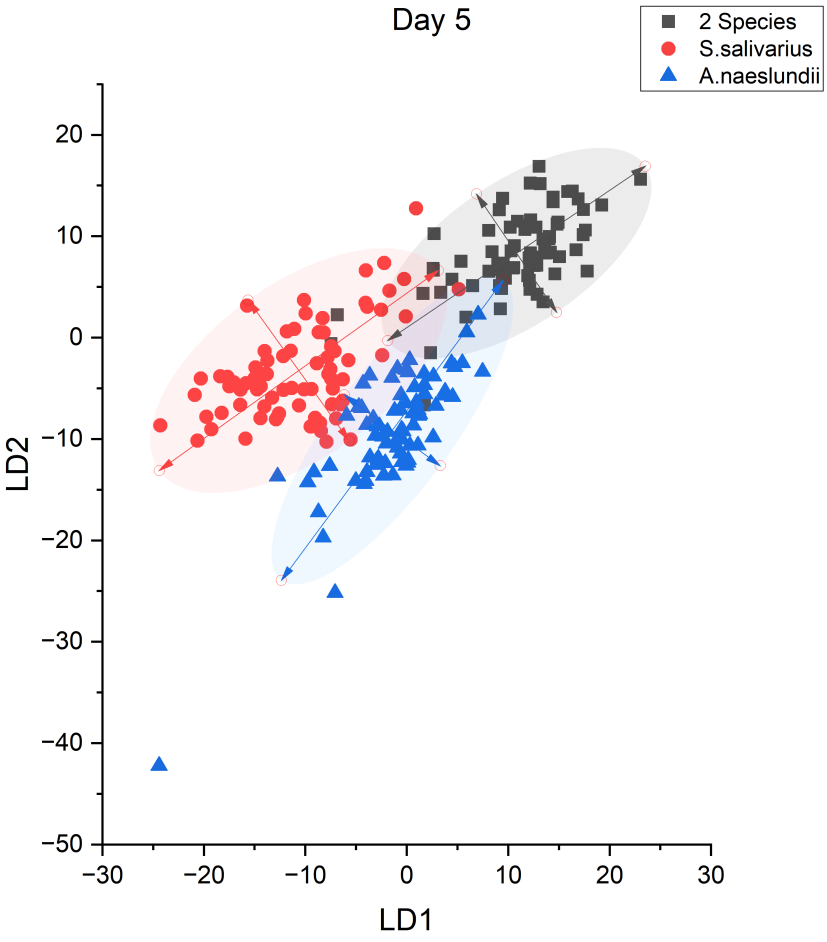

Figure 3.27: LDA of Day 5 *S.salivarius* and *A.naeslundii* mono-species and 2-species biofilms. a) Scatter plot of the classes showing LD1 v LD2 where 2-species (black), *S.salivarius* (red) and *A.naeslundii* (blue), with 95% confidence ellipse, b) LD1 and LD2 class distribution shown in a box plot, c) Raman spectra corresponding to LD1 (black) and LD2 (red). For each biofilm, n=75.

Now when looking at Day 5 biofilms, the LDA results show similar clustering in **Figure 3.27a** and **b**, though all days have a broader spread. The accuracy of LDA is 85.8 ± 1.2 %, sensitivity 84.2 ± 2.1%, and specificity 95.6 ± 0.8 %. The accuracy is slightly lower than for Day 1 biofilms (87.7%), however as the biofilms have matured and have increased matrix, the biofilms may become more similar and slightly harder to differentiate. The 2-species biofilm cluster is mostly situated in the positive LD1 and LD2, where both mono-species biofilms are mostly negative LD1 and LD2. There is therefore something about these two species being combined in a multi-species biofilm that creates a new environment that is completely different from their parts. The combination of each species and their respective matrix contribution makes a unique 2-species environment, however how these species grow together and the intricacies of their relationship within the biofilm is not able to be seen in detail at this stage with this data. We are are to see the difference between the two mono-species and how these species grow individually, and their respective matrix contributions, and using this we can compare mono-species biofilms to 2-species biofilms at each day. We are also able to see how these biofilms change over time. By looking at the peak trends, the 2-species biofilm had most similarities to *A.naeslundii* over time, yet all biofilms show most changes over Day 3 - 5, therefore it can be concluded that a new biofilm growth stage occurs between Day 3 - 5.

What we do not know is if there is a difference in the Raman spectra of live and dead bacteria, and whether such differences could be signifiers of dead bacteria in the biofilm. For example, Runze Li *et al* found that the difference in live and dead *Escherichia coli* was the emergence of a peak around 1400 cm^{-1}, caused by the denaturing of proteins when exposed to UV [229]. It is most likely that bacteria within the biofilm would die due to starvation caused by a nutrient gradient across the depth of the biofilm, and the effect of this on the morphology and metabolism of *S.salivarius* and *A.naeslundii* biofilms has yet to be reported. The relative proportion of live and dead bacteria within the biofilm will affect the Raman spectra in ways such as the appearance of new peaks or peak intensity. If there is a high proportion of dead bacteria, there may be a slowing down of matrix production which is reflected in the peak intensities of the corresponding peaks. The Raman spectra of nutrient deficient bacteria should be studied, as well as

bacteria under hypoxic conditions too as the oxygen gradient within the biofilms may cause aerobic species trapped in an anaerobic environment to die.

For all biofilms, Raman spectra were taken at 75 points across the whole biofilm and averaged to produce one final spectrum seen in **Figure 3.17, 3.20 and 3.23**. This method provides a broad overview of the biofilm and as shown above, provides valuable information about how the contents of the biofilm changes over time, and can be used to successfully differentiate between mono- and 2-species biofilms. However, in order to maximise the potential of RS as a tool for label free, non-destructive biofilm analysis, Raman spectra and in particular Raman maps should be taken at specific known locations (e.g. inner/outer edge, top/bottom) to show what is happening in an area of biofilm at these points, and then demonstrate how these areas differ from each other. Having a visual map of the area and knowing the location can help explain why certain Raman features are present. The behaviour and structure of the biofilm at a point on the bottom inner edge, shielded from nutrients, compared to a point on the top outer edge which is in the flow of nutrients, will likely be very different, so knowing the location and taking a Raman map of the area will provide detailed specific information.

Unfortunately, it was not possible to take Raman maps of biofilms for this part of the work as maps required long scan times ($\gg$4 hours), during which the 100x oil objective would drift out of focus. Raman maps have recently been used to identify bacterial species within a 2-species biofilm , and in theory has the potential to separate live and dead bacteria, as well as understand inter-species interactions within the biofilm, by looking at metabolite production or species density, for example [124]. Surface Enhanced Raman Spectroscopy (SERS) is an alternative method of RS where a metallic substance such as silver is added to the sample, either on the surface or via nanoparticles, resulting in a Raman enhancement factor of 10^{10} - 10^{11} [230]. This enhancement may be what is needed to show the small differences between biological spectra as has already been used to study the matrix production of bacteria at different growth phases, and together with PCA-LDA has demonstrated the response of *Pseudomonas syringae* biofilms to a viral contaminant at varying doses [120, 231]. Stimulated Raman Spectroscopy (SRS) is a resonance enhancement, vibrational imaging technique that can map the distribution of

chemical bonds in 3-dimensions and real time [232]. SRS can produce Raman maps 1000 times faster than spontaneous RS, making it a favourable choice for biofilm analysis, and has recently been used to show that penetration of vancomycin within *Staphylococcus aureus* biofilms is shallow and non-uniform due to vancomycin attachment to bacteria cells [233].

In order to gain further understanding of multi-species oral biofilms using RS, care should be taken when choosing areas of biofilm to scan, as the information gathered at more localised areas along with the knowledge of location and potential map images, will provide greater insights into the biofilm structure and what exactly is causing this. Other Raman techniques such as SRS or SERS have the advantage of enhancement factors and faster scan time, making data acquisition easier and higher quality.

3.8 Chapter Conclusions

This chapter developed a microfluidic platform for the growth of multi-species biofilms under continuous flow, which had multiple inlets to allow all analysis and treatments to occur on chip. Using microfluidics as the method of growth allowed biofilms to be analysed in real time using non-destructive RS. Initially, RS of planktonic *S.salivarius* and *A.naeslundii* was performed and the spectra of each species compared, with peaks associated with *S.salivarius* identified as 728, 850, 980, 1414, and 1604 cm^{-1}, and *A.naeslundii* as 746, 1127 and 2850 cm^{-1}. PCA was able to successfully identify and cluster each species, demonstrating that RS can be used a a method of species identification.

RS of mono- and 2-species biofilms were taken every day for 5 days and the trends of key peaks over time were plotted and assessed. For all species most peaks show a linear increase over time, except for DNA peaks at 602 and 614 cm^{-1}, which for *S.salivarius* showed an exponential increase between Day 3 - 5, and for *A.naeslundii* and 2-species biofilm this occurred between Day 4 - 5. The matrix contribution of mono-species biofilms at each day was seen by subtracting the planktonic spectrum from the biofilm spectra, leaving what should in theory be just matrix contribution. For both species a

strong CH_2 2905 cm^{-1} peak was present which could be used to identify matrix, whereas the 2937 cm^{-1} was not present in both spectrum, suggesting this peak is associated with bacterial cells. *S.salivarius* matrix had a strong broad increase in intensity over the DNA region 500 - 800 cm^{-1} which was also seen in the dual species, and the 2850 cm^{-1} peak had the strongest contributions from *S.salivarius*, which were both seen in the 2-species biofilms. The 614 cm^{-1} DNA peak for *A.naeslundii* is also very strong in the matrix, and has great contributions to the 2-species biofilm.

LDA was used to show the differences between 2-species biofilms on Day 1, 3 and 5, with an accuracy of 73 %. Day 3 and 5 showed considerable overlap, but both were distinct from Day 1, showing that by Day 3 the 2-species biofilm must reach a new growth stage and thus have a biofilm composition that remains relatively unchanged up to Day 5. LDA was also used to see the differences and similarities between mono- and 2-species biofilms on Day 1 and 5. Day 1 and 5 LDA were both able to distinctly cluster all 3 biofilms with little overlap, showing that 2-species biofilms are not just the sum of the mono-species part, but there are specific 2-species interactions taking place that makes multi-species biofilms unique from mono-species. Day 1 was able to identify clusters with an accuracy of 88 % and Day 5 86%. The 2-species biofilm cluster sits in between the two species clusters, however on Day 1 the 2-species had most overlap with *S.salivarius*, suggesting a Day 1 2-species biofilm may be most like *S.salivarius* biofilm.

Using RS we are able to identify the planktonic species, monitor mono- and 2-species biofilms over time, and see RS of the individual matrix components. Spectra can be compared and the peak intensities tracked over time, however LDA can be used to further the analysis and separation between the biofilms, particularly when spectra is relatively similar. This data is able to infer relationships between the biofilm, such that a 2-species biofilm may be most similar to *S.salivarius* on Day 1, however this method is unable to identity individual species within the biofilm, or show specifically how the biofilm change in relation to metabolites or other inter-species interactions, due to the limitations on scan speed, resolution, and ability to take Raman maps. Furthermore, the contribution of dead bacteria within the biofilm is unknown and should be considered for future works.

Chapter 4

Stimulated Raman Spectroscopy and Two-Photon Fluorescence of Oral Biofilms

4.1 Aims and motivation

Due to the limitations of spontaneous RS when it comes to analysing multi-species biofilms, such as speed of acquisitions and limited spatial resolution, another method of RS was sought out which was capable of penetrating the depth of the biofilm and taking z-stacks to provide high quality Raman data of biofilms over time. This chapter uses Stimulated Raman Spectroscopy (SRS) which is able to provide high resolution images, z-stacks, and hyperspectral images of biofilms much faster than spontaneous RS. The nature of the equipment used meant that Two-Photon Fluorescence (TPF) could also be acquired at the same time. During SRS only the high wavenumber region (2740 - 3080 cm^{-1}) is captured, therefore only this region is discussed in this chapter.

The process of taking SRS, hyperspectral SRS and TPF of biofilms on chip has not been previously reported and represents a novel approach. This chapter explores SRS as

a method of biofilm characterisation, and looks into the best method of analysing and presenting the data. The work in this chapter was undertaken at the EPSRC supported CONTRAST facility at the University of Exeter. As samples were prepared in Leeds and needed to be transported to Exeter, due to the need to take samples on public transport, all biofilms were fixed with 4% para-formaldehyde.

4.2 *S.salivarius* Mono-species Biofilms

4.2.1 Day 1

4.2.1.1 Hyperspectral SRS

Specific Point Analysis Method

Hyperspectral SRS images of biofilms form a stack of 101 images, where each image is an intensity map taken every 3.44 cm^{-1} from 2740 - 3084 cm^{-1}. **Figure 4.1** demonstrates how the stack of images corresponds to wavenumbers. Each pixel of the image (512 x 512 pixels) contains the intensity information at that wavenumber therefore when analysing the stack of images, the information of a pixel or region of interest can be extracted from each slice and the Raman spectra plotted (intensity (A.U) v wavenumber cm^{-1}).

The hyperspectral SRS image of a *S.salivarius* Day 1 biofilm is shown in **Figure 4.2**. The image used in this figure was taken at 2925 cm^{-1} which had the greatest intensity across the stack, and is used here for demonstration purpose. All analysis was performed on the whole stack. The yellow square inset of **Figure 4.2** shows a zoomed in section of the hyperspectral image with each pixel having a specific intensity. This area demonstrated the high resolution of SRS as planktonic bacteria, small chains, and clusters of *S.salivarius* can be seen attached on the surface. Brighter regions appear to show areas of biofilm which are thicker and denser in bacteria. This image at 2925 cm^{-1} is associated with the CH_3 (protein) peak and therefore may be indicative of the

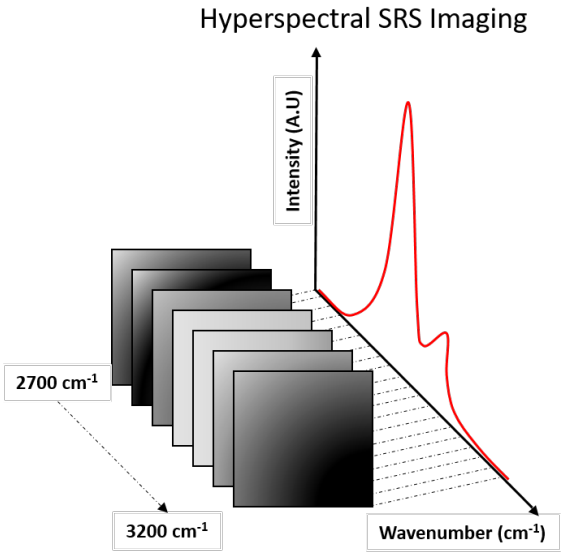

Figure 4.1: Schematic showing how hyperspectral SRS stacks correspond to wavenumbers. Each image in the stack is taken at a specific wavenumber, where each pixel of that image shows the intensity at that wavenumber. The stack can therefore be plotted as Intensity (A.U) v Wavenumber cm^{-1}.

bacteria rather than the matrix.

As mentioned, when selecting regions of interest on the hyperspectral images, the Raman intensity of that area can be averaged and plotted. **Figure 4.3a** shows six regions of interest and the associated spectra in **Figure 4.3b**. The six regions were chosen for comparison based on visual assessment of the SRS image, as they appear to show varying degrees of biofilm thickness and bacteria density, with point 1 (red) showing the surface with no apparent biofilm, up to point 6 (gold) which is the brightest and densest area of biofilm. Point 1 (red) shows a very low intensity shallow 2900 cm^{-1} peak which could be associated with remnants of saliva on the surface or traces of biofilm matrix. Point 2 (green) shows an area of uniform bacteria (potentially planktonic or with minimal matrix based on visual assessment), which has a low spectral intensity but broad peaks at 2902 and 2932 cm^{-1}. It is unclear if the bacteria has began to secrete extracellular matrix at this stage which could be contributing to this spectra.

Point 3 (dark blue) is a low intensity area, lower than point 2 where bacteria are visible present, whereas the neighbouring point 4 (light blue) is brighter and more intense.

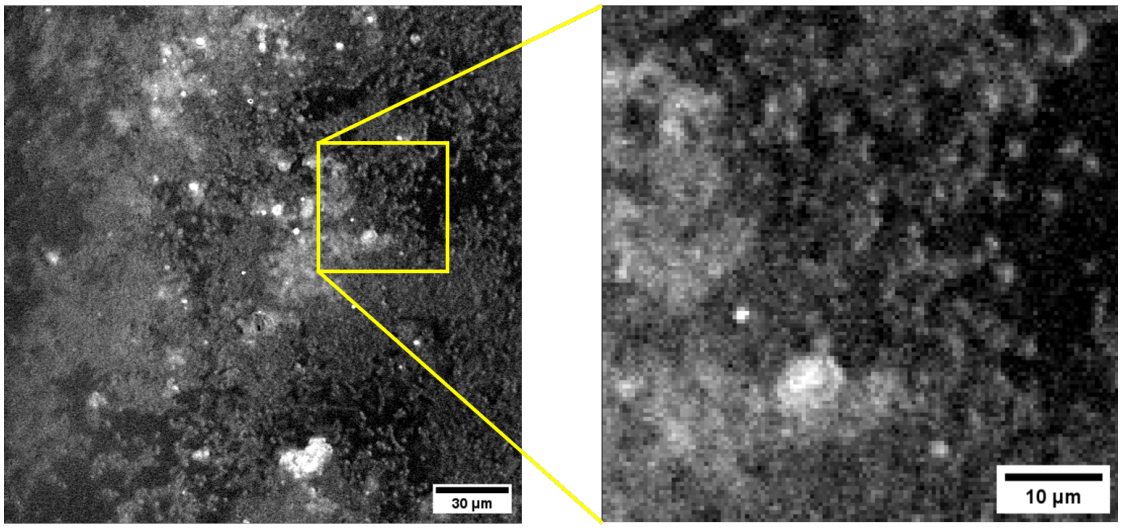

Figure 4.2: SRS hyperspectral image of *S.salivarius* Day 1 biofilm. The image is the slice with the maximum intensity, 2925 cm^{-1}, taken from a stack 2700 - 3200 cm^{-1}. The yellow square shows a zoomed in area of the SRS hyperspectral image, where each pixel contains a Raman spectra.

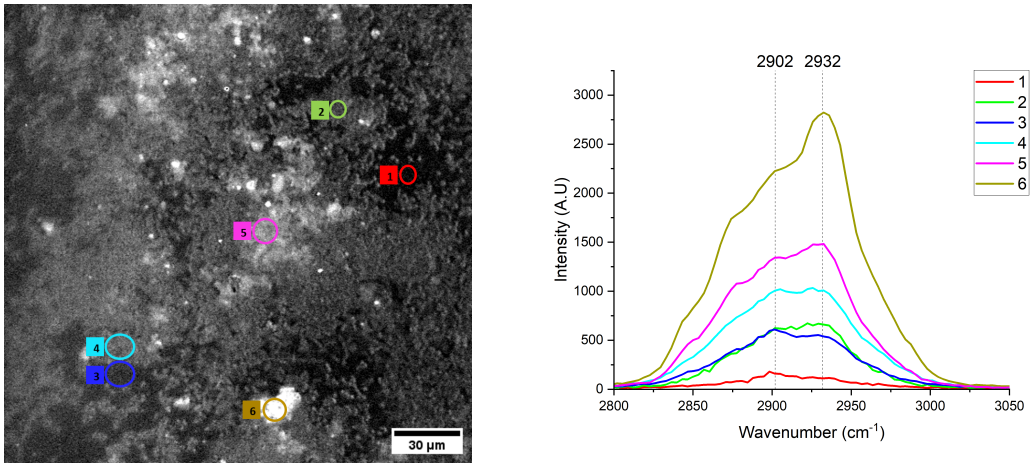

(a) **(b)**

Figure 4.3: a) SRS hyperspectral image of *S.salivarius* Day 1 biofilm. Each pixel of the image contains a Raman spectra from 2700 - 3200 cm^{-1} . Circled areas show different regions of interest (ROI) across the biofilm and the average spectra within the ROI are plotted in b).

This visual comparison suggests point 4 may have bacteria and matrix contributions whereas point 3 may just be matrix. The corresponding spectra for these areas show that point 3 (dark blue) has a stronger 2902 cm^{-1} peak, whereas point 4 (light blue) has approximately equal 2902 and 2935 cm^{-1} peaks. This comparison of neighbouring areas which look visually different suggests that *S.salivarius* has a stronger and identifiable 2935 cm^{-1} contribution, and the matrix which may also contribute to 2935 cm^{-1}, has a stronger 2902 cm^{-1} contribution. The intensity of point 4 is also double that of point 3 owing to the increased density of biofilm. Point 5 (pink) shows increased intensity of both 2902 and 2935 cm^{-1} and the emergence of peaks at 2850 and 2880 cm^{-1} which likely represent more matrix contribution. Finally point 6 (gold) is the most intense and densest area of biofilm, which is reflected in the spectra. The clear dominating 2935 cm^{-1} peak shows this area is high in density of *S.salivarius* bacteria, with matrix contribution at 2902, 2880 and 2850 cm^{-1}. This agrees with the findings of spontaneous RS in Chapter 3, where the matrix contribution of mono-species biofilms had a strong clear 2905 cm^{-1} peak, whereas the 2937 cm^{-1} was notably missing, therefore suggesting this peak is representative of bacteria cells.

Significant peaks in *S.salivarius* Day 1 biofilms are therefore 2850 ($\nu_s CH_2$), 2880 ($\nu_{as} CH_2$), 2902 ($\nu_{as}^{FR} CH_2$), and 2935 ($\nu_s CH_3$) cm^{-1}, as explained in **Table 4.1**. 2902 cm^{-1} is tentatively assigned as the fermi resonance of $\nu_{as} CH_2$ though this assignment is nontrivial and has also been associated with C-H stretching [234, 235].

Wavenumber (cm^{-1})	**Assignments**	
2850 (2848 - 2852)	$\nu_s CH_2$	lipids, proteins
2880 (2871 - 2881)	$\nu_{as} CH_2$	lipids
2902 (2900 - 2905)	$\nu_{as}^{FR} CH_2$ (tentative)	lipid
2935 (2925 - 2937)	$\nu_s CH_3$	protein, lipid

Table 4.1: Raman peak assignments. ν: stretching vibration, ν_s: symmetric stretching, ν_{as}: asymmetric stretching, FR: fermi resonance. [211, 234].

It was noted that throughout the hyperspectral image, bright spots can be seen that are not consistent with the biofilm, highlighted as point 1 (red) and 2 (green) in **Figure 4.4a**. The spectra in **Figure 4.4b** is distinct from that seen previously, showing a sharp yet broad spectra between 2840 - 2932 cm^{-1} and a peak at 2877 cm^{-1}. There is no

obvious assignment for this spectra within the literature, though these peaks are slightly red-shifted from the CH_2 and CH_3 peaks mentioned previously, which can occur when a sample becomes more crystalline. It is possible therefore that these bright spots could be crystalline lipid artefacts from the biofilm nutrients, or as a result of the fixing process of these biofilms.

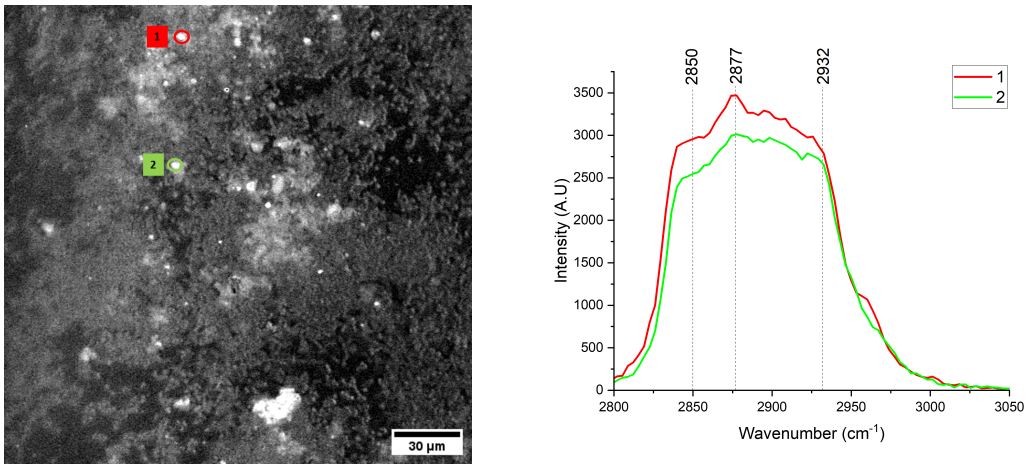

(a) **(b)**

Figure 4.4: a) SRS hyperspectral image of *S.salivarius* Day 1 biofilm. Each pixel of the image contains a Raman spectra from 2740 - 3084 cm^{-1} . Bright points 1 (red) and 2 (green) across the biofilm are circled and the average spectra of these points are plotted in b).

A great deal of information can be gained from hyperspectral SRS images of biofilms, however this method of selecting specific points from the image to plot is subjective and not consistent when comparing multiple biofilms. To make analysis consistent and uniform across data sets, the hyperspectral images were divided into a grid from which spectra were withdrawn, as now described.

Grid Analysis Method

To have a consistent method of hyperspectral image analysis across all sets of data, the images were divided into a 15 x 15 grid, where each grid is 14.14 μm^2 (34 $pixels^2$), **Figure 4.5a**. The average spectra from each grid was collected. From the grid, one row or column which best represented the biofilm was chosen for analysis, highlighted in yellow in **Figure 4.5a**. This method was able to cut down the large amount of data

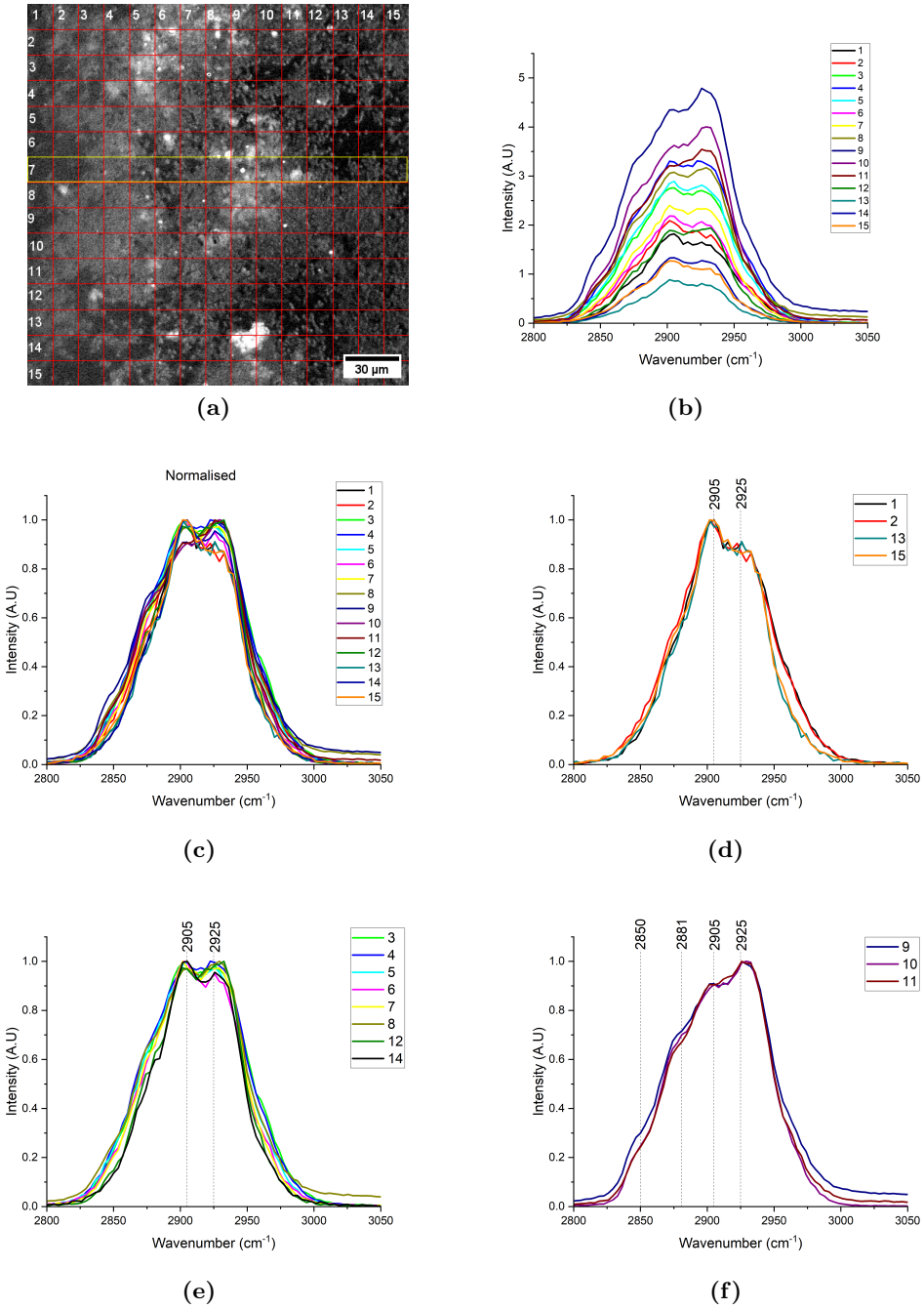

(a) **(b)** **(c)** **(d)** **(e)** **(f)**

Figure 4.5: a) SRS hyperspectral image of *S.salivarius* Day 1 biofilm analysed using a 15 x 15 grid. Each pixel contains a spectra and the average spectra in each 14.14 μm^2 square (34 $pixels^2$) was plotted for analysis. Row 7, highlighted in yellow, was chosen for analysis. b) Average spectra for row 7 plotted for grid 1 - 15, c) average spectra normalised to the max intensity which are also grouped by similar features and plotted separately on d), e) and f) for clarity.

from each image into a reasonable, comparable dataset.

Figure 4.5b shows the 15 spectra for row 7 of *S.salivarius* Day 1 biofilm. The most intense spectra are 9 - 11 across the densest area of biofilm, which has a dominant 2925 cm^{-1} peak. Thinner areas of biofilm such as 3 - 6 show a dominant 2903 cm^{-1} peak. These spectra are normalised to their maximum peak in **Figure 4.5c** which are then grouped by similar features and plotted separately in **Figures 4.5d - f** for clarity.

Those spectra with a dominant 2902 - 2905 cm^{-1} peak in **Figures 4.5d** are 1, 2, 13, and 15. Grid 1 and 2 show areas of mostly matrix and little bacteria, while 13 and 15 show areas of sparse bacteria on the surface. The spectra for 13 and 15 are an average of bacteria and the surface, therefore these areas are not as specific as those found previously in **Figure 4.3**, however the overall spectra agrees with the findings where the surface (point 1) and just matrix (point 3) has a more prominent 2902 cm^{-1} peak. **Figures 4.5e** shows spectra with approximately equal 2905 and 2925 cm^{-1} peaks, grid points 3 - 8, 12, and 14. These are areas which show both matrix and bacteria contribution. Grid points 3 - 5 show are clearly areas of growing biofilm and show shoulders developing at 2850 and 2881 cm^{-1} due to the matrix, whereas peaks points 12 and 14 are mostly bacteria on the surface and do not have these shoulders. It is suggested therefore, that the 2850 and 2881 cm^{-1} CH_2 lipid peaks are indicators of biofilm matrix. **Figures 4.5f** shows spectra 9 - 11, the densest area of biofilm in terms of both bacteria and matrix. There are distinct shoulders developing at 2850 and 2881 cm^{-1} caused by increased matrix production.

This method of analysis shows the detail and variation of SRS spectra across the biofilm, without losing detail or over averaging the data. If needed, specific areas could still be chosen for analysis, as performed in **Figures 4.3**. While this method is a good method of directly analysing the hyperspectral data by reducing the size of data, it is still a time consuming method which requires manual labour. A final suggested method of analysis is using K-means clustering, an unsupervised machine learning algorithm that sorts data into a pre-defined number of clusters.

K-means clustering

K-means clustering is a non-supervised method that separates the data into a pre-defined number of clusters (K). It randomly picks K number of data points to define the clusters centroids, then assigns the remaining data points to the nearest centroid. The final cluster centroid is an average of all data points. The average spectra are plotted and the colour map of the hyperspectral image is produced, as shown in **Figure 4.6a and b**. Four clusters were defined, three of which represent the biofilm and one (cluster 3, yellow) is the surface with zero intensity. The three defined biofilm clusters are similar in profile to those found previously using the grid method in **Figure 4.5**. Cluster 1 (dark blue) represents moderate biofilm growth with approximately equal 2905 and 2935 cm^{-1} peaks, and shoulders at 2850 and 2881 cm^{-1}. Cluster 2 (light blue) shows denser areas of biofilm with a dominating 2935 cm^{-1} CH_3 protein peak, and cluster 4 shows areas with matrix and little bacteria, having a dominating 2902 cm^{-1} peak. The colour map of **Figure 4.6a** visually represents these areas, drawing similar details and likeness to the original hyperspectral SRS image.

The deconvolution of each spectra for cluster 1, 2 and 4 are seen in **Figure 4.6c, d, and e** respectively. Deconvolution of the spectra allows the contribution of each peak to be seen and therefore the provide more details about the biofilm structure. All spectra have peaks at approximately 2850, 2873, 2902, 2935 and 2965 cm^{-1}, and appear in the same intensity order (relatively), with 2935 cm^{-1} having the greatest intensity, then 2902 and 2873 cm^{-1}. 2850 and 2965 cm^{-1} fluctuate in intensity though are always the least intense.

One way to compare spectra is to look at the ratio of 2935/2902 cm^{-1} for each spectra. Cluster 1 and 2 have similar 2935/2902 cm^{-1} ratios at 1.19 and 1.18 respectively, while cluster 4 is 1.07, showing a much greater 2902 cm^{-1} CH_2— lipid contribution. For cluster 1 and 2, as the 2935/2902 cm^{-1} ratios are similar, the peak that is causing cluster 1 to be broader than cluster 2 and have approximately equal 2935 and 2902 cm^{-1} peaks is the 2973 cm^{-1} CH_2 peak. During the deconvoltution process, iterations are performed to provide the best fit, which allows the peak position, full width half

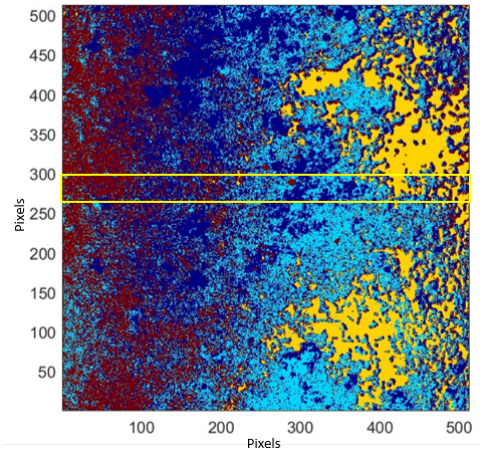

(a)

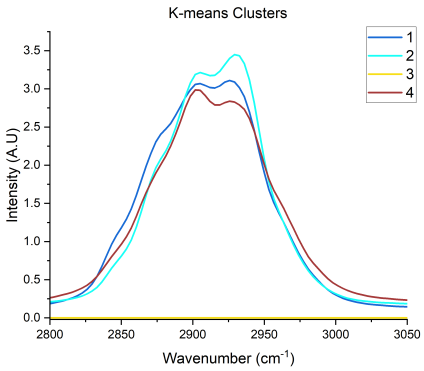

(b)

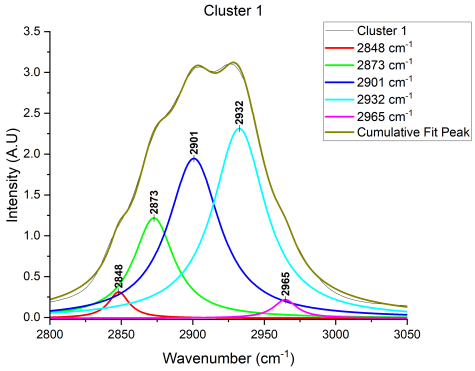

(c)

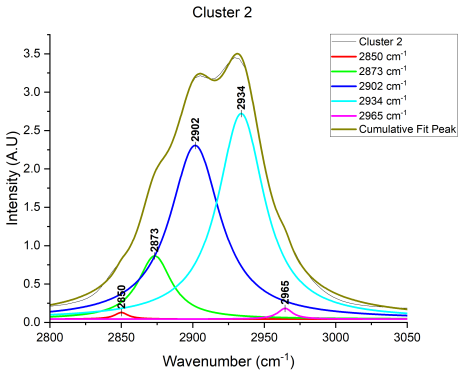

(d)

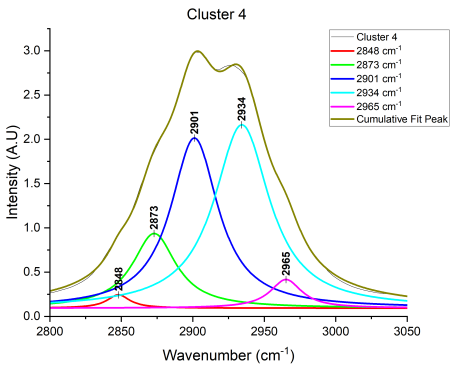

(e)

Figure 4.6: K-means clustering of *S.salivarius* Day 1 mono-species biofilm hyperspectral SRS data. 4 clusters are defined: Cluster 1 (dark blue), cluster 2 (light blue), cluster 3 (yellow), cluster 4 (red). a) Hyperspectral image of the biofilm identified into clusters. The yellow rectangle highlights the area used for analysis in **Figure 4.5**. b) The average spectra for each cluster, c), d) and e) show the de-convoluted spectra of cluster 1, 2 and 4, respectively.

maximum (FWHM) and area to change, hence why some peaks are slightly shifted from the expected positions. Fixing the peak position would often cause the fitting of the peaks to not converge, causing an error. Hence the deconvolution was the best approximation of the peaks present.

K-means clustering analysis has proved a quick, reliable, and accurate method of hyperspectral SRS analysis by defining clusters with spectra that correspond to those found by manual analysis using specifics points or the grid method. Going forward, k-means clustering will be used as the sole analysis method for hyperspectral SRS biofilm analysis.

4.2.1.2 Z-stacks and two-photon fluorescence (TPF)

Hyperspectral biofilm images were taken at one fixed point on the z-axis, gaining data on a whole spectral region. Z-stacks of the biofilm, at the same x-y position as the hyperspectral images, were also taken to see how the biofilm varies with depth. In order to vary the z-position, the wavenumber at which the SRS images were taken was fixed to the CH_3 2930 cm^{-1} peak, resulting in a spectral intensity that varies with z-position (μm), demonstrated in **Figure 4.7a**. As found in the previous section, **4.2.1.1**, the 2930 cm^{-1} CH_3 protein peak is indicative of *S.salivarius* bacteria cells, hence the z-stacks are expected to show how the profile of bacteria within the biofilm changes with height. Images were taken every 0.5 μm and the z-height was dependent on the biofilm, **Figure 4.7b**.

TPF z-stacks were also taken at the same point, at same increments as SRS z-stacks, with an excitation of 802 nm (two photons are absorbed therefore the actual excitation is 401 nm) and detection at 575 nm (band pass filter allowing 550 - 600 nm). TPF is a non-linear process where the fluorescence intensity scales quadratically with excitation intensity ($I_F \propto I_E^2$), resulting in highly localised fluorescence as the focal point of the laser beam is the only point where two photons can be delivered and absorbed simultaneously [236]. TPF shows the presence of endogenous fluorophores within the biofilm, the fluorescence spectra of which are shown in **Figure 4.8** and **Table**

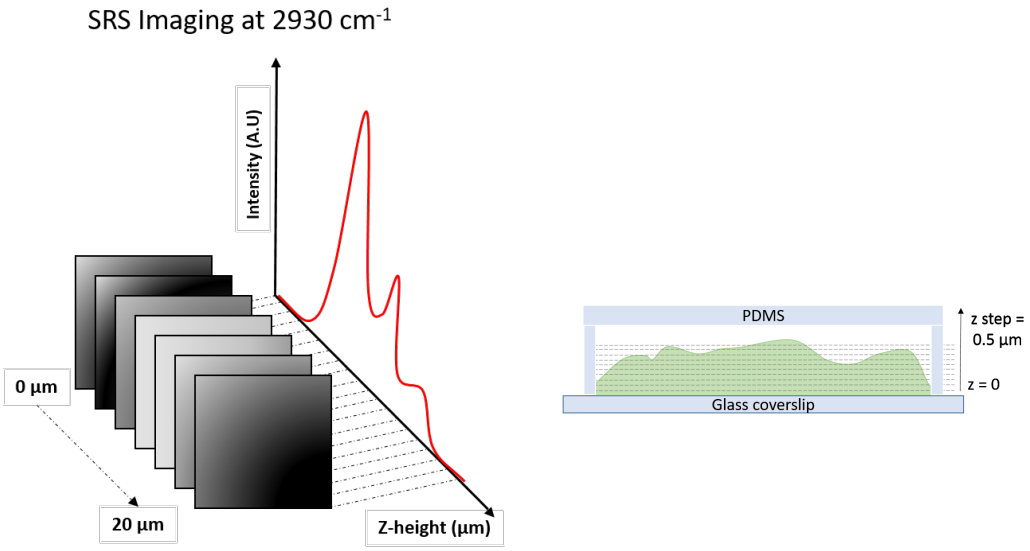

(a) (b)

Figure 4.7: a) Schematic showing SRS z-stack imaging of biofilms. SRS imaging was fixed to the CH_3 2930 cm^{-1} peak, and each image of the stack was taken at a 0.5 μm intervals. The spectral intensity is plotted as a function of z-height μm, b) schematic demonstrating how the z-stacks of the biofilm were taken, starting at the base of the biofilm, 0 μm, and increasing in 0.5 μm steps.

4.2. The fluorophore which corresponds to the excitation/emission of 401/575 nm used for TPF is likely flavins or its derivative, flavin adenine dinucleotide (FAD) and flavin mononucleotide (FMN) which are part of the metabolism process playing a key role in the conversion of energy from acetyl CoA to ATP, and auto-fluoresce in the green [237–239].

Fluorophore	Excitation (nm)	Emission (nm)
Tryphtophan	280	340
Collagen	365	420
Elastin	365	420
NADH	365	490
Flavins	450	550
Lipo-fuscin (pigments)	532	570
Porphyrins	405	620 - 700

Table 4.2: The excitation and emission of common endogenous fluorophores [241].

The SRS and TPF z-stacks, and composite images, for *S.salivarius* Day 1 biofilm can be seen in **Figure 4.9**. The biofilm stack is 10.5 μm, and images at z = 0, 5, 7.5 and 10.5

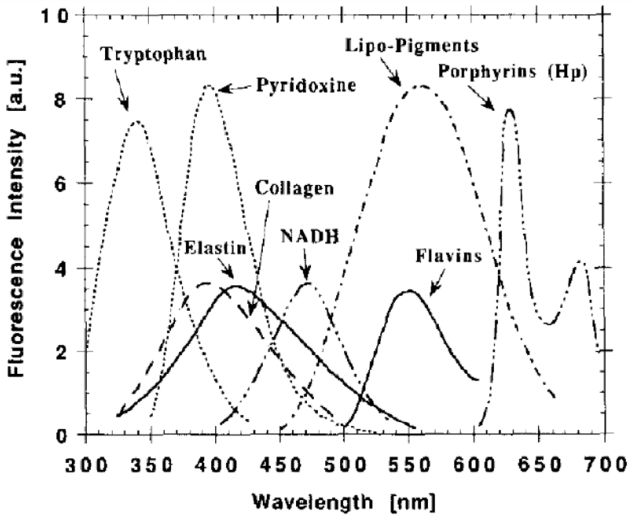

Figure 4.8: Fluorescence emission spectra for common endogenous fluorophores. Reproduced with permission from [240] with license CC BY-NC 4.0.

μm are presented for comparison. In **Figure 4.9a** at z = 0 μm, the SRS image (at 2930 cm^{-1}) shows only little intensity gradient on the left side of the image, likely where the bulk of the biofilm is attached to the surface. The TPF image shows specific detailing of areas with dense bacteria caused by flavins within the cell. The SRS image in **Figure 4.9b** at z = 5 μm shows a clear base layer of the biofilm matrix, while the TPF shows a similar profile to that at z = 0 μm but with a greater intensity. The TPF intensity is also at its maximum at z = 5 μm. and the maximum intensity across the stack. It is not evidently clear, but there is very low intensity fluorescence across the whole biofilm where bacteria is seen to be present, showing a similar map to **Figure 4.9c** SRS image. Therefore, the autofluorescence of flavins (FAD or FMD) are a bacteria marker, the intensity of which increases with concentration [242]. It is noted that the bright dots in the the SRS image, which were previously attributed to be crystalline lipid droplets, are not picked up in the TPF thus are not bacterial cells.

While the greatest intensity and most detail for TPF is seen at 5 μm, for SRS this is seen in **Figure 4.9c** at 7.5 μm. The TPF image does not pick up the same details as SRS, confirming that there is no fluorescence in the matrix. **Figure 4.9d** at 10.5 μm shows the top of the biofilm, with both SRS and TPF having little detail.

SRS and TPF are complimentary methods which show different details about the

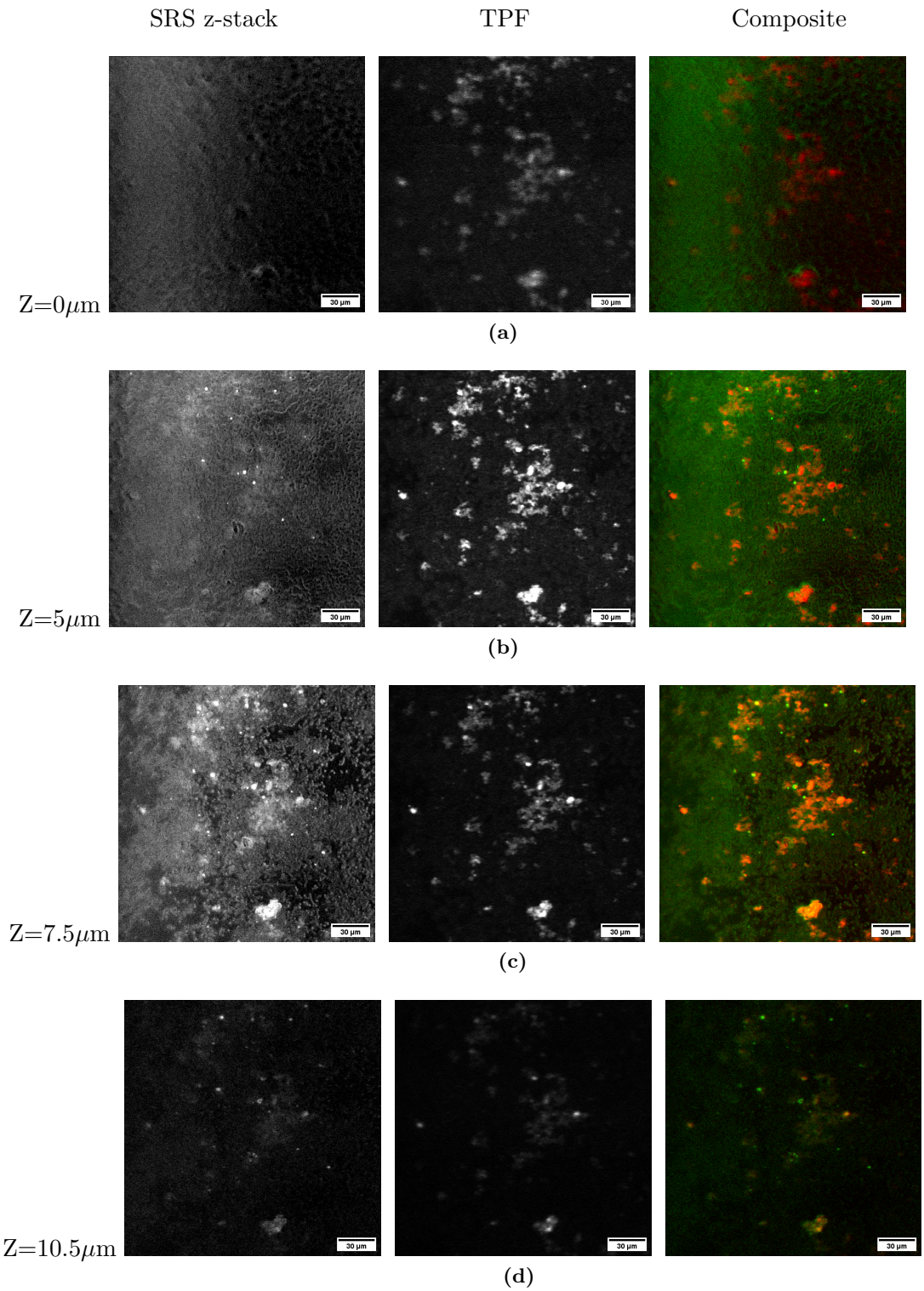

Figure 4.9: Day 1 *S.salivarius* biofilm showing z-stacks of SRS at 2930 cm^{-1} (left), TPF (middle), and SRS (green) + TPF (red) composite (right). Each slice is 0.5 μm and taken at a) 0 μm, b) 5μm, c) 7.5 μm, d) 10.5 μm. (Scale bar = 30 μm).

biofilm. TPF is a good bacterial marker, showing the distribution of bacteria cells within the biofilm, however as the biofilms used in this chapter were fixed prior to analysis, it is unlikely that any conclusions can be drawn from TPF about the metabolic activity of the biofilm. Flavins are a key part of the metabolic system and it has been documented that bacterial autofluorescence increases when cells are under stress, by antibiotics for example. Research by Jérémy Surre *et al.* found that bacteria exposed to antibiotics show increased flavin autofluorescence due to the rapid increase in gene expression and metabolic production to cope and adapt to the stresses, showing the relationship between fluorescence and metabolic activity [237]. Dead (or fixed) bacteria cells are however associated with a lower fluorescence intensity [243]. More information would therefore be gained by looking at live biofilm samples, nevertheless, TPF is a useful tool for bacteria identification within the biofilms.

4.2.2 Day 5

4.2.2.1 Hyperspectral data

Hyperspectral data of Day 5 *S.salivarius* mono-species biofilms can be seen in **Figure 4.10a**. Visually, compared to Day 1, the Day 5 *S.salivarius* biofilm looks thicker and denser across the majority of the biofilm. There is a particularly intense area spanning the outer edge of the biofilm. The outer edge is closest to the flow of nutrients thus is developing quickly with high rates of metabolism, which would explain why this area appears particularly dense.

The K-means analysis of the hyperspectral data is shown in **Figure 4.10b - f**. Dominant peaks are at approximately 2850, 2881, 2902, and 2930 cm^{-1}. Cluster 2 (light blue) and 3 (yellow) encompass the main features of the biofilm, with cluster 2 having a dominant 2930 cm^{-1} peak while cluster 3 has a dominant 2881 cm^{-1} peak. This differs from Day 1 biofilms as 2882 cm^{-1} was not a dominant feature, only presenting as a shoulder, the same is true for 2850 cm^{-1}, therefore the CH_2 lipid contribution is much greater in Day 5 biofilms as a result of the developed matrix and density of the biofilms.

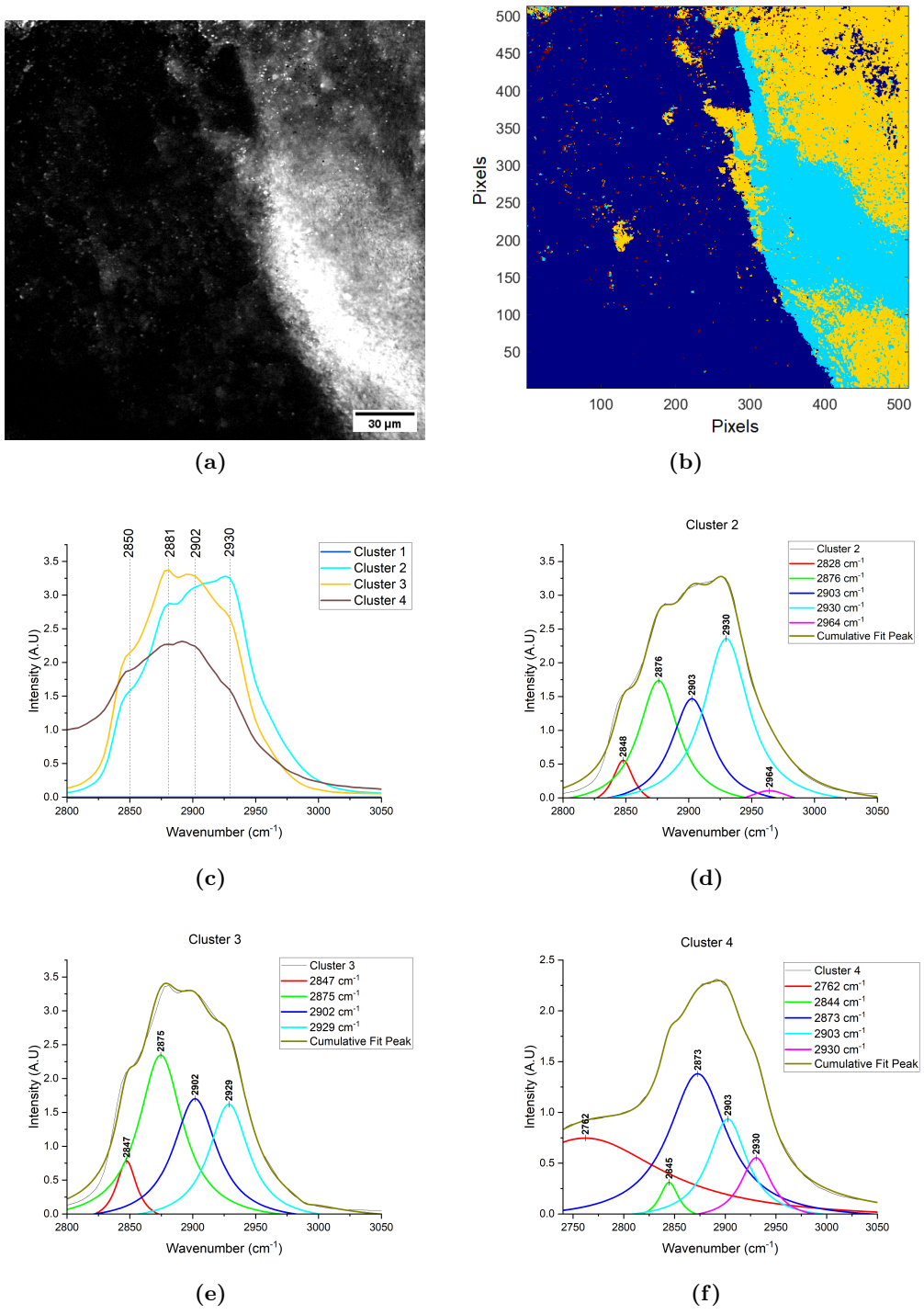

Figure 4.10: Hyperspectral SRS data of *S.salivarius* Day 5 biofilms. a) Hyperspectral image, b) K-means clustering colour map, Cluster 1 (dark blue), cluster 2 (light blue), cluster 3 (yellow), cluster 4 (red), c) average Raman spectra of the 4 k-means clusters, d), e) and f) show the deconvolution of cluster 2, 3 and 4 respectively. A Lorentzian fit was used for multiple peak deconvolution.

The deconvoluted spectra of each cluster in **Figure 4.10d - f** further demonstrates the differences between the clusters. Cluster 2, which maps onto the edge/inner biofilm and the area which appears to be the most dense, is confirmed to have a leading CH_3 2930 cm^{-1} peak, associated with proteins and bacteria cells. Supporting the theory that this area would have the highest growth and metabolism rates. The dominant 2873 (2873-2881) cm^{-1} peak of cluster 3 shows areas with matrix but fewer bacteria cells, and/or thinner areas of biofilm. Cluster 4 (red) defines very small irregular features of the biofilm, mostly small points on the surface where no biofilm is present, or bright dots seen across the top right of the hyperspectral biofilm image. This spectra has a broad profile with a peak at 2762 cm^{-1}, corresponding to a CH stretch of possibly phospholipids [244]. As cluster 4 represents small points across the biofilm, it is likely that these areas are not bacteria related, and likely artefacts of the biofilm.

Overall, compared to *S.salivarius* Day 1 biofilms, Day 5 hyperspectral data shows increased density of the biofilms with a much stronger matrix (lipid and protein) contribution. The hyperspectral data is able to identify regions of high bacterial density using the CH_3 2930 cm^{-1} peak as an identifier for *S.salivarius* bacteria.

4.2.2.2 Z-stacks and two-photon fluorescene (TPF)

SRS and TPF stacks were taken of *S.salivarius* Day 5 biofilms and images at 0, 7.5, 10 and 24.5 μm can be seen in **Figure 4.11**. At 0 μm in **Figure 4.11a**, there is no SRS information and only a small amount of flavin autofluorescence present in the TPF channel, mapping out the edge of the biofilm. **Figure 4.11b** at 7.5 μm shows significant, yet different detail in both SRS and TPF. The SRS shows a uniform biofilm on the right, with less intense small regions attached to the surface on the left. From the SRS it is difficult to discern matrix from bacteria. The TPF however provides the specific detail and mapping of bacteria within the biofilm, highlighting dense regions of bacteria along the biofilm edge, and picking up bacteria on the surface that wasn't as clear in the SRS. TPF is also the most intense at this z-position. The composite image shows how both SRS and TPF compliment each other to provide maximum detailing of the biofilm.

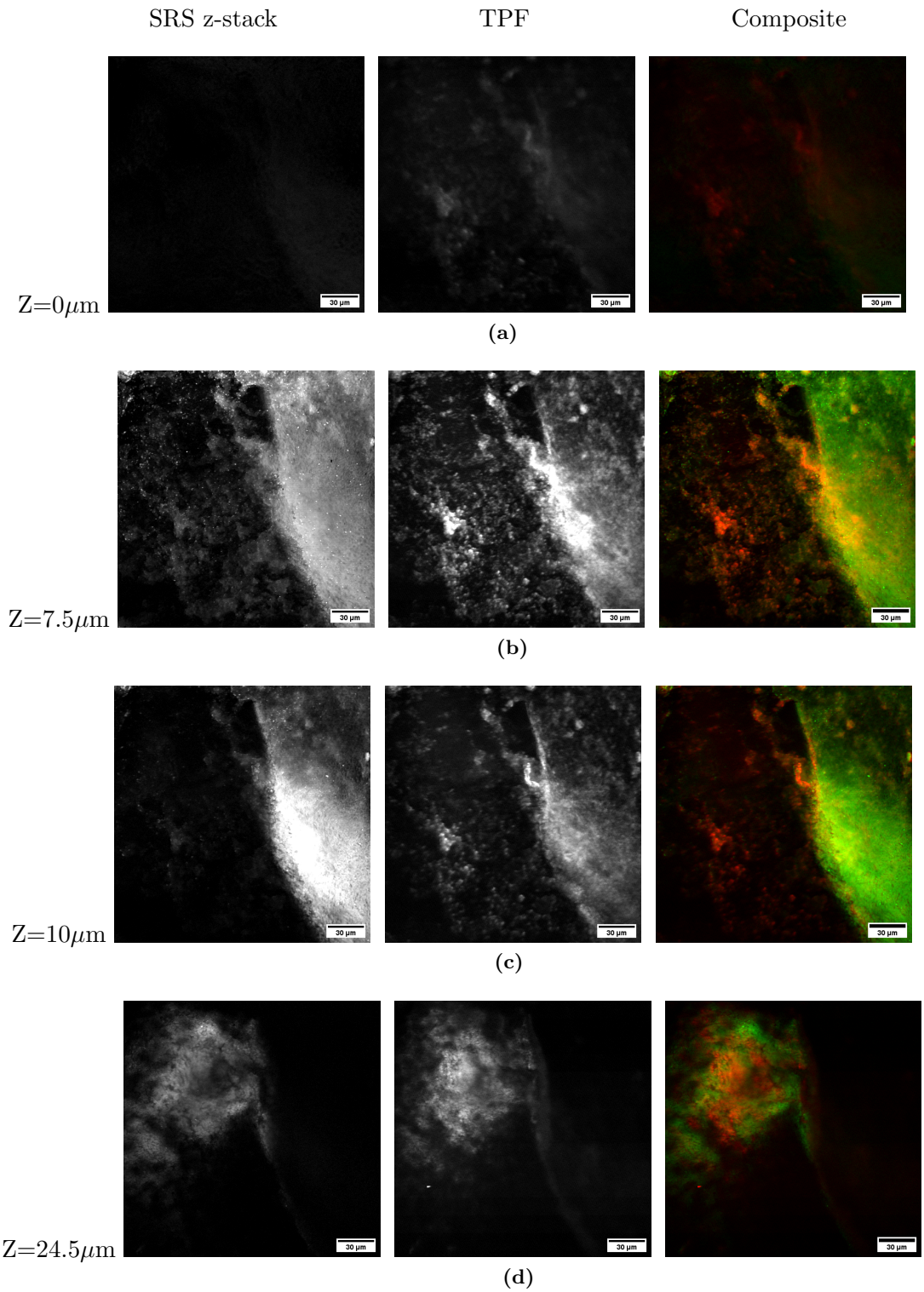

Figure 4.11: Day 5 *S.salivarius* biofilm showing z-stacks of SRS at 2930 cm^{-1} (left), TPF (middle), and SRS (green) + TPF (red) composite (right). Each slice is 0.5 μm and taken at a) 0 μm, b) 7.5μm, c) 10 μm, d) 24.5 μm. (Scale bar = 30 μm).

As the biofilm height increases to 10 μm in **Figure 4.11c**, the maximum intensity of the SRS 2930 cm^{-1} peak is seen along the biofilm border. TPF continues to show the autofluorescence across the biofilm, particularly in this dense region, but now at a lower intensity. As we reach the top of the biofilm at 24.5 μm in **Figure 4.11d**, the biofilm is now showing on the left hand side of the image and nothing on the right. This is showing the 3D nature of biofilms as this portion of biofilm may have been attached originally but has since become detached, except for the line down the middle anchoring it to the biofilm below (shown in both SRS and TPF). The biofilm is not attached to the top of the microfluidic chamber as at this, 24.5 μm, is to low for the height of the chamber, 150 μm. The SRS and TPF of this portion of biofilm show similar intensities confirming the presence of both matrix and bacteria in this portion of biofilm.

Compared to Day 1, Day 5 is naturally a much thicker biofilm, 24.5μm compared to 10.5 μm. The biofilm is more established and uniform in appearance, though the TPF indicates the distribution of bacteria favours the outer edge. In both Day 1 and Day 5, the maximum intensity of SRS (2930 cm^{-1}) and TPF do not correspond to each other, instead TPF occurs first, lower in the biofilm. SRS is detecting bacteria and matrix while TPF alone is suggesting the majority of the bacteria is located towards the bottom of the biofilm, or at least the bacteria that was most metabolically active prior to fixation. It should be remembered that these biofilms are fixed and the autofluorescence intensity for dead bacteria is much lower. It could potentially be the case that bacteria at the top of the biofilm, which is less dense and trapped, could have lost falvins and have lower fluorescence intensity levels. The impact of fixation on the SRS intensity of these biofilms is also unknown at this stage, and should be looked into in the future.

Live/dead confocal images of biofilms shown in Chapter 3 were able to give an overview of the biofilm and suggest that most live bacteria was on the edges of the biofilm close to nutrients, whereas those at the base were more likely to be dead. However, these images were found to not be representative of biofilms as often it was not possible to image the middle of the biofilm. The TPF images here also show the dense clustering of bacteria on the edges of the biofilms, with the inner biofilm showing lower intensity TPF and thus less bacteria. This may be due to there being less bacteria in

general in these areas, or the fact that when these bacteria were fixed, they were already dead and potentially being recycled into the biofilm, thus their metabolism, and flavin production, was low resulting in low TPF.

4.3 *A.naeslundii* Mono-species Biofilm

4.3.1 Day 1

4.3.1.1 Hyperspectral SRS

Hyperspectral SRS and k-means clustering analysis of Day 1 *A.naeslundii* biofilms is shown in **Figure 4.12**. The hyperspectral image in **Figure 4.12a** shows a uniform biofilm with a clear boundary where the biofilm gets thinner and tapers off leaving bacteria on the surface. The k-means clustering colour map demonstrates this in **Figure 4.12b** as it has defined the biofilm into four clusters, the spectra of which are shown in **Figure 4.12c-f**.

Cluster 1 (dark blue), shown in **Figure 4.12d** has a very strong 2938 cm^{-1} peak, representing planktonic bacteria, or small clusters, on the surface. There are small contributions from CH_2 bands at 2873 and 2895 showing some matrix production, as well as the CH_3 peak at 2969 cm^{-1}. There is a peak identified at 2918 cm^{-1}, previously unseen but could attributed to the fermi resonance of CH_2 [245]. As with *S.salivarius*, the CH_3 peak at 2938 cm^{-1} can be considered a primary indicator of *A.naeslundii* bacteria, though the peak is at a slightly higher wavenumber than *S.salivarius* (2930 cm^{-1}).

Cluster 3 (yellow) represents thinner biofilm, the intermediary boundary between the surface planktonic bacteria and the thicker inner biofilm. The spectra in **Figure 4.12e** has a strong 2937 cm^{-1} peak, but with greater 2873 and 2902 cm^{-1} CH_2 contributions, showing more matrix is present. Cluster 4 (red) in **Figure 4.12f** has a similar profile and peak contribution as cluster 3, but presents as a much broader peak. The intensity of 2935 cm^{-1} is also decreased, suggesting there is more matrix but slightly

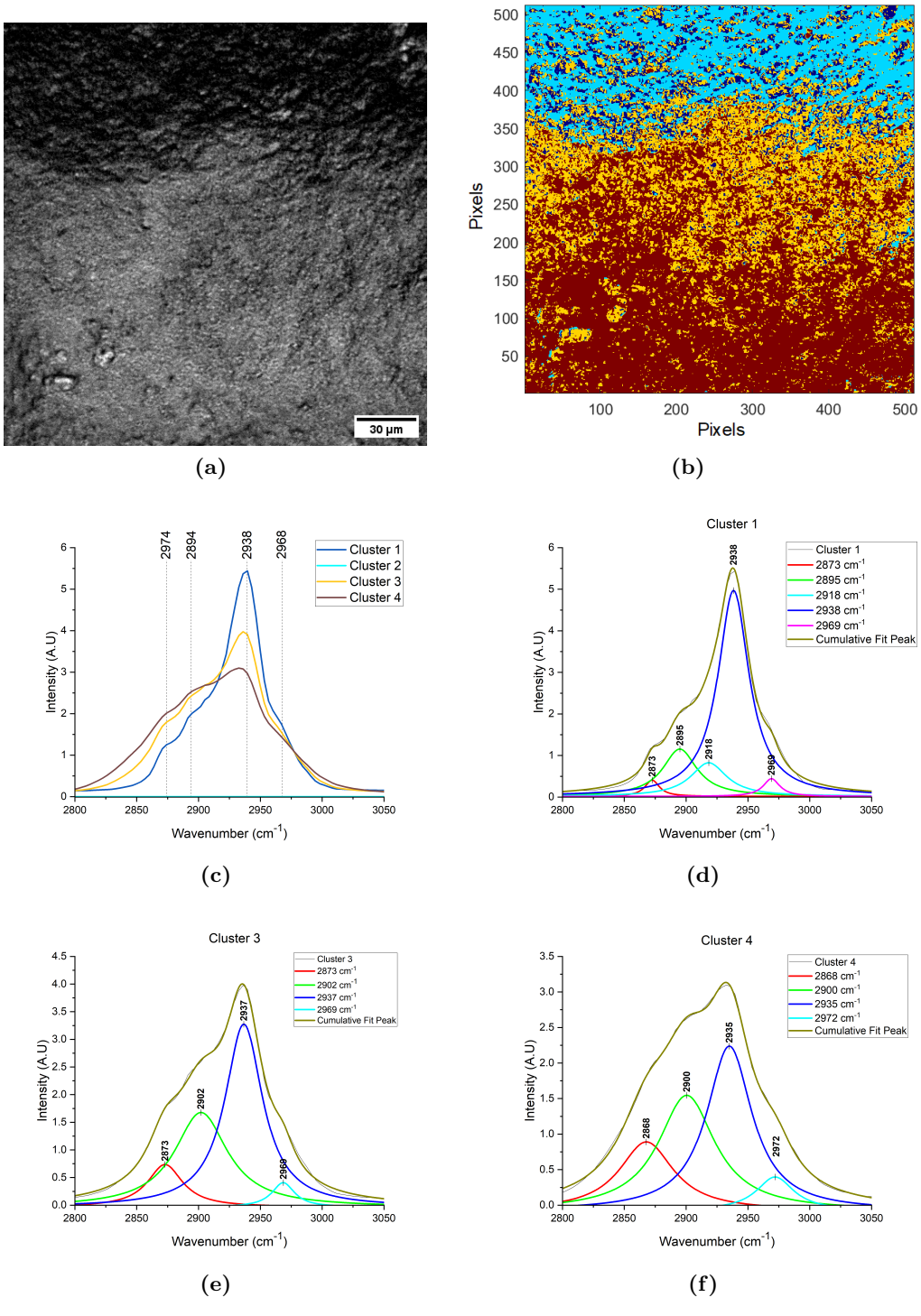

Figure 4.12: Hyperspectral SRS data of *A.naesundii* Day 1 biofilms. a) Hyperspectral image, b) K-means clustering colour map,Cluster 1 (dark blue), cluster 2 (light blue), cluster 3 (yellow), cluster 4 (red) c) average Raman spectra of the 4 k-means clusters, d), e) and f) show the deconvolution of cluster 1, 3 and 4 respectively. A Lorentzian fit was used for multiple peak deconvolution.

less bacteria present within the inner biofilm. This would support previous findings in **Section 4.2.2.2** that there are increased bacterial cells present on the biofilm edges due to nutrients access and rapid growth rates.

At this stage, the peak position of the CH_2 2873 cm^{-1}) and CH_3 2937 cm^{-1} peaks for *A.naeslundii* are slightly shifted compared to *S.salivarius* biofilms, 2881 and 2930 cm^{-1} respectively. Furthermore, there is no 2850 cm^{-1} CH_2 peak present in any spectra thus far, making the *A.naeslundii* matrix production distinct from *S.salivarius*.

4.3.1.2 Z-stacks and two-photon fluorescence (TPF)

SRS and TPF z-stacks for *A.naeslundii* Day 1 biofilm are shown in **Figure 4.13**. The stacks are 16 μm in height and images are shown at 0, 4.5, 8 and 16 μm. The SRS images (taken at 2930 cm^{-1}) show little difference across the z-stack from 0 - 8μm, **Figure 4.13a - c**. The biofilm looks uniform with no significant changes. By **Figure 4.13d** at the very top of the biofilm there is very little SRS or TPF signal, potentially only picking up scattering.

TPF shows autofluorescence in only specific areas of the images, showing small clusters of apparent bacteria, with the largest cluster featuring in the bottom left and top right corner of the biofilm. The TPF does not indicate any gradient through the biofilm or boundary, as is seen in the SRS. The fluorescence intensity is at its maximum for different areas between 4.5 - 8 μm, **Figure 4.13b-c**, but again only in selected areas. The TPF does not provide as much detail about the *A.naeslundii* biofilm as *S.salivarius* do, this could be due to the fact that *A.naeslundii* has a slower growth rate than *S.salivarius* and therefore is not metabolising at the same rate by Day 1. It is possible that *A.naeslundii* may also just not produce as many flavins and therefore not autofluorescence to the same degree, or the fact the bacteria are dead may be reducing the intensity or fading completely those in less dense areas.

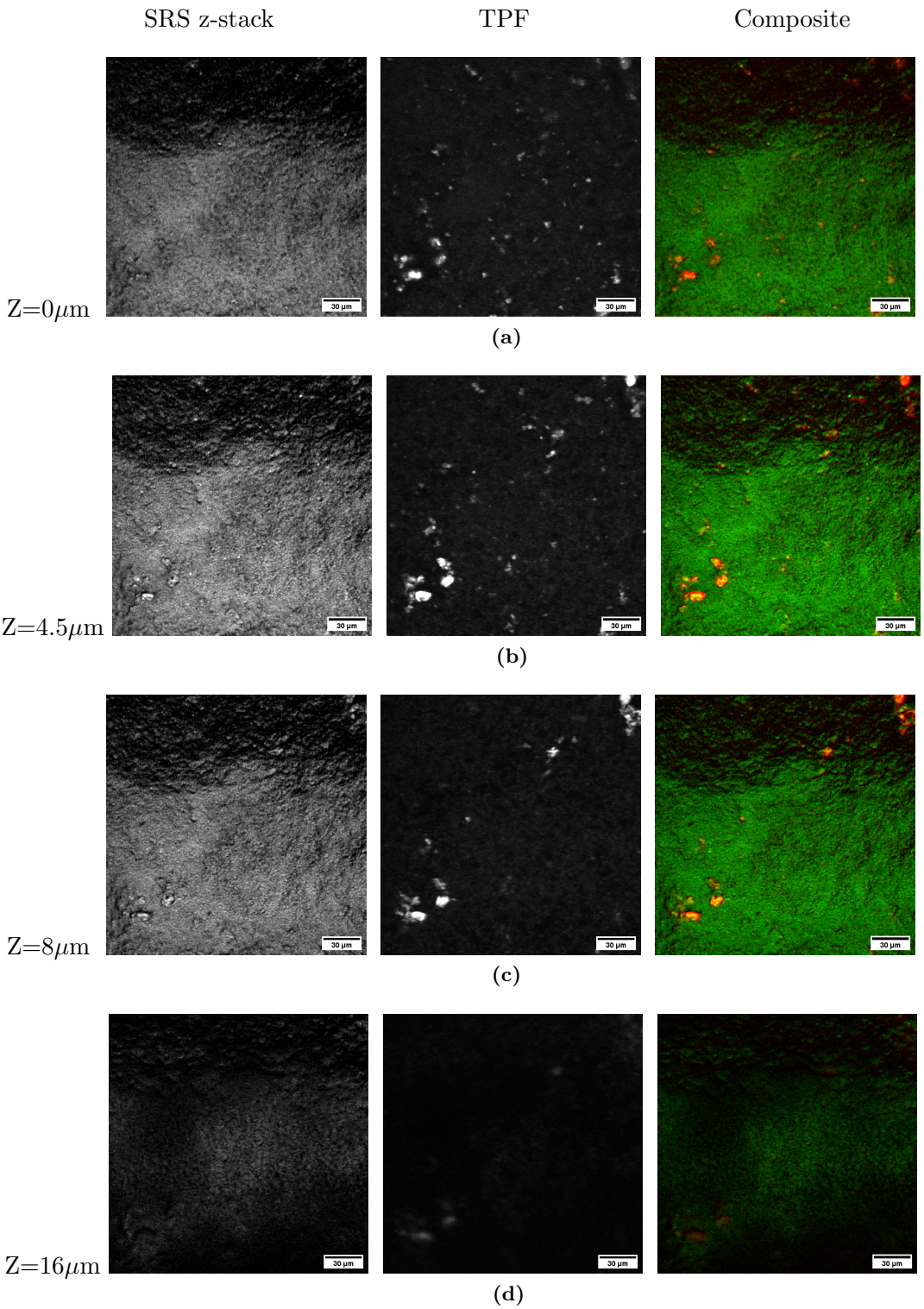

Figure 4.13: Day 1 *A.naeslundii* biofilm showing z-stacks of SRS at 2930 cm^{-1} (left), TPF (middle), and SRS (green) + TPF (red) composite (right). Each slice is 0.5 μm and taken at a) 0 μm, b) 4.5μm, c) 8 μm, d) 16 μm. (Scale bar = 30 μm).

4.3.2 Day 5

4.3.2.1 Hyperspectral SRS

Day 5 hyperspectral images of *A.naeslundii* biofilms, and the k-means clustering analysis is shown in **Figure 4.14**. From the hyperspectral image in **Figure 4.14a** taken at 2930 cm^{-1}, the biofilm appears thick and textured in areas showing the 3D nature of the biofilm. The k-means cluster analysis in **Figure 4.14b - f** shows the main biofilm is spilt into 2 clusters, cluster 1 (dark blue) and 4 (red), which are very similar in profile, **Figure 4.14d and f**. Both have a main 2926-9 cm^{-1} peak with shoulders at around 2845 and 2875 cm^{-1}. Cluster 1 represents the central biofilm, which appears potentially less thick and textured, whereas cluster 4 covers biofilm at the bottom for the image that appears thicker. The spectra for cluster 4 is also broader and has an additional peak contribution at 2893 cm^{-1}, suggesting higher matrix contribution in this area. Cluster 3 (yellow), **Figure 4.14e**, highlights bacterial aggregates on the surface, separate from the biofilm. The spectra has a 2927 cm^{-1} peak but is different from cluster 1 and 4 in that it is much broader spectra due to an additional peak at 3046 cm^{-1}, which could be due to asymmetric CH stretching [246].

For this data set, the deconvolution of the clusters does not produce as good of a fit as the previous biofilms. This is noticeable for cluster 1 and 3 in **Figure 4.14d**and **e** respectively. For Cluster 3, the lorentzian peak fitting was unable to fit the peak at 2902 cm^{-1}. The deconvolution is therefore very useful in predicting the peaks present, but the peak positioning and intensities may not be accurate. Compared to Day 1 *A.naeslundii* biofilms, Day 5 biofilms have introduced a 2845 cm^{-1} CH_2 peak, though at only very low intensities. This peak is therefore not as significant in *A.naeslundii* than *S.Salivarius*.

4.3.2.2 Z-stacks and two-photon fluorescence (TPF)

The SRS and TPF z-stacks for *A.naeslundii* Day 5 biofilm are shown in **Figure 4.15**, with z-stack height 20 μm, and images given at 0, 6.5, 16, and 20 μm. At 0 μm in

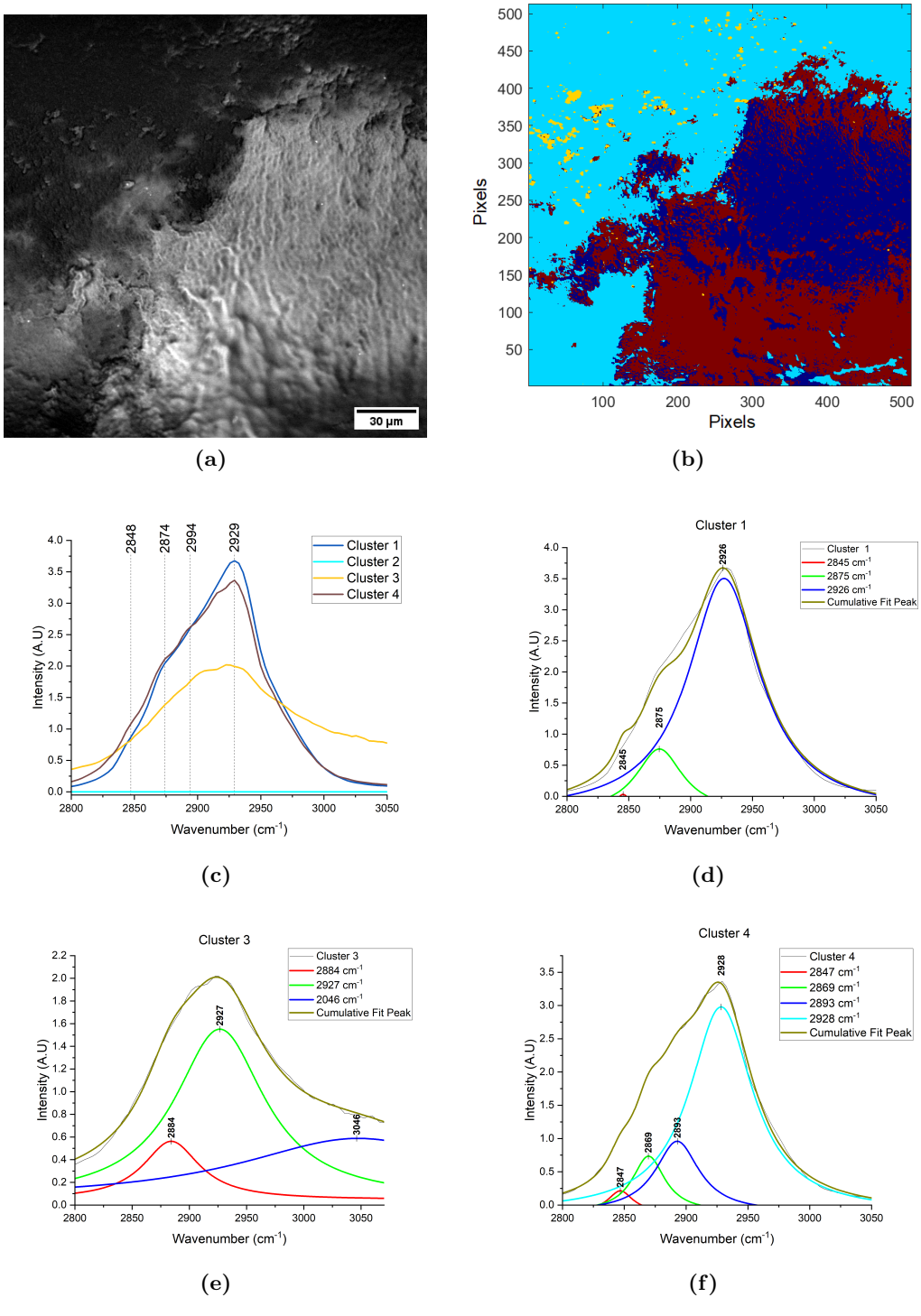

Figure 4.14: Hyperspectral SRS data of *A.naesundii* Day 5 biofilms. a) Hyperspectral image, b) K-means clustering colour map, Cluster 1 (dark blue), cluster 2 (light blue), cluster 3 (yellow), cluster 4 (red), c) average Raman spectra of the 4 k-means clusters, d), e) and f) show the deconvolution of cluster 1, 3 and 4 respectively. A Lorentzian fit was used for multiple peak deconvolution.

Figure 4.15a, there is very low intensity SRS and TPF seen across the images. The SRS is beginning to show the biofilm structure, as was seen in the hyperspectral image in **Figure 4.14a**, whereas the TPF image shows bright clusters in the centre of the image providing detail about bacteria within the biofilm that is not seen in the SRS. This is highlighted in the composite images.

Figure 4.15b at 6.5 μm shows intense detail of the biofilm through both SRS and TPF. The SRS shows the whole biofilm structure and architecture. There appears to be folds and ripples in the biofilm matrix, which could also be due to impressions from *A.naeslundii* bacteria forming chains, though the uniform intensity suggests matrix. The TPF highlights the bacteria clusters in the biofilm, particularly on the edge of the biofilm in the centre of the image. This level of detail wasn't observed for the Day 1 biofilm, showing that *A.naeslundii* does in fact autofluoresce but not until more established. TPF also shows a broad, uniform fluorescence intensity that spans the whole biofilm region. The uniformity of this fluorescence suggests this is embedded in the matrix rather than coming from bacteria cells. It has been shown that bacteria can secrete flavins into their supernatant, thus it is possible that *A.naeslundii* may do the same [247].

As the biofilm reaches 16 μm, the SRS in **Figure 4.15c** continues to show the architecture and thickness of biofilm, only on the right hand side of the image. The TPF shows how the bacteria weaves in the architecture shown in the SRS, with significantly brighter areas and some matrix fluorescence too only in the middle region. At 20 μm, the pinnacle of the biofilm is shown in specific detail by the SRS, **Figure 4.15d**. There is low intensity TPF in this region, confirming that the final layer of the biofilm is matrix, with all bacteria encased within.

Both z-stacks for Day 5 *A.naeslundii* provide and incredible amount of detail about the biofilm structure, much more so than Day 1. When comparing to *S.salivarius*, *A.naeslundii* shows a more uniform biofilm from the start but the biofilm itself appears to have more 3D architectural features.

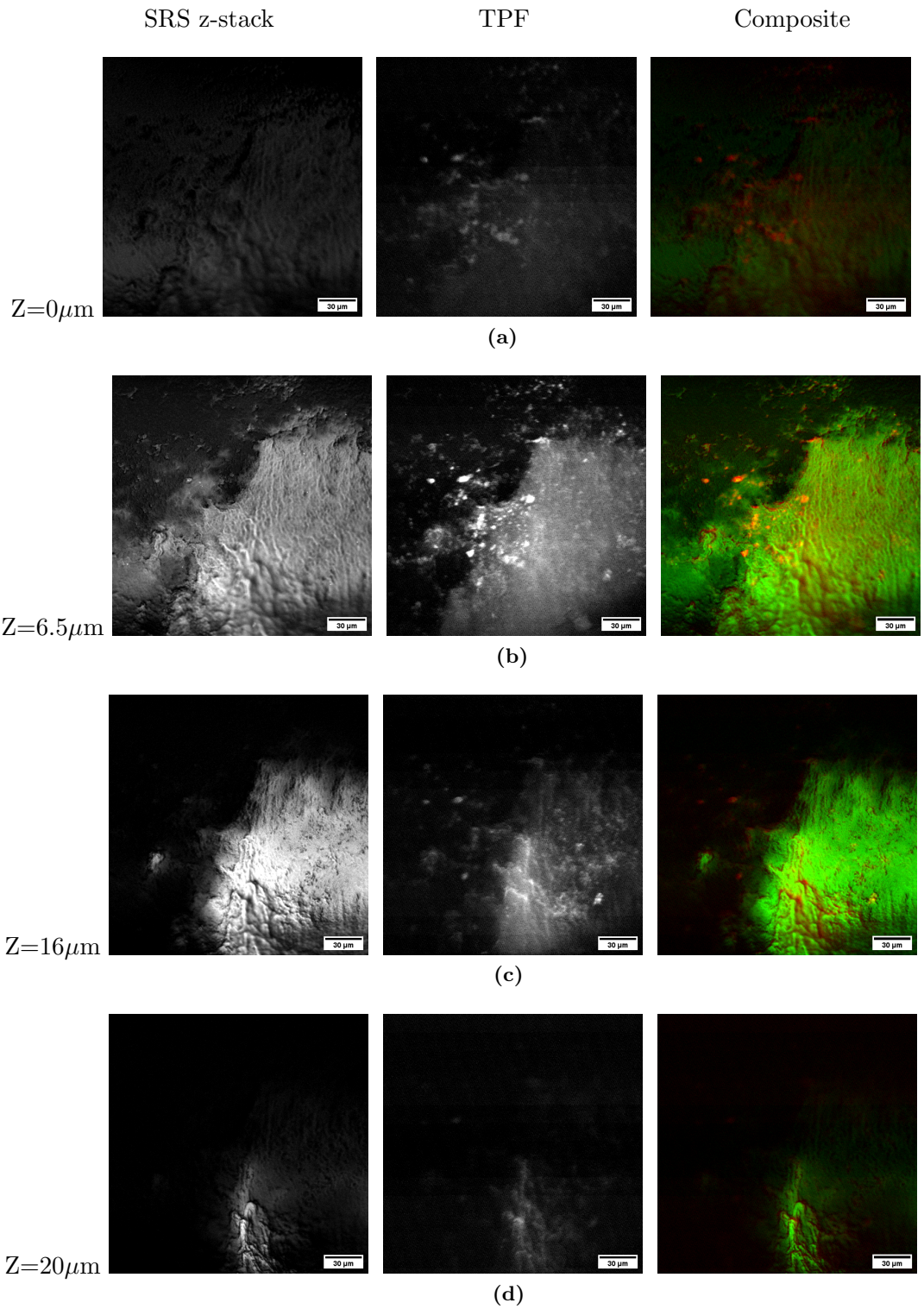

Figure 4.15: Day 5 *A.naeslundii* biofilm showing z-stacks of SRS at 2930 cm^{-1} (left), TPF (middle), and SRS (green) + TPF (red) composite (right). Each slice is 0.5 μm and taken at a) 0 μm, b) 6.5μm, c) 13 μm, d) 20 μm. (Scale bar = 30 μm).

4.4 2-Species Biofilms

Having seen the results for mono-species biofilms on Day 1 and 5, we now move on to looking at 2-species biofilms. Having the ability to compare the 2-species to the mono-species data allows for further interpretation of the results and understanding of the biofilm.

4.4.1 Day 1

4.4.1.1 Hyperspectral SRS

2-species Day 1 hyperspectral SRS images and k-means clustering analysis are shown in **Figure 4.16**. The hyperspectral SRS image in **Figure 4.16a** shows a high intensity, dense region in the centre of the image, as well as a very bright spot. From previous data, such bright intensity spots have not been bacteria relate but lipid clusters. **Figure 4.16b - f** show the k-means clustering colour map and the corresponding spectra, and the deconvolution of the spectra. The colour map shows three distinct regions of the biofilm, transitioning from top to bottom. Cluster 2 (light blue) and cluster 4 (red) are the most similar, having a dominant 2932 cm^{-1} CH_3 peak and shoulders at CH_2 2870 - 80 and 2889 - 2907 cm^{-1}. However, cluster 2 shows increased intensity in these regions therefore more matrix and thicker biofilm.

The yellow region, cluster 3, has the most distinct spectra with a dominant peak at 2902 cm^{-1}. A spectra of this style was only seen in *S.salivarius* biofilms, all *A.naeslundii* biofilms had a spectral profile similar to Cluster 2 and 4. In *S.salivarius*, this spectra denoted areas of majority matrix with little bacteria present, thus it can be assumed that the yellow regions may have a high density of *S.salivarius* matrix contribution.

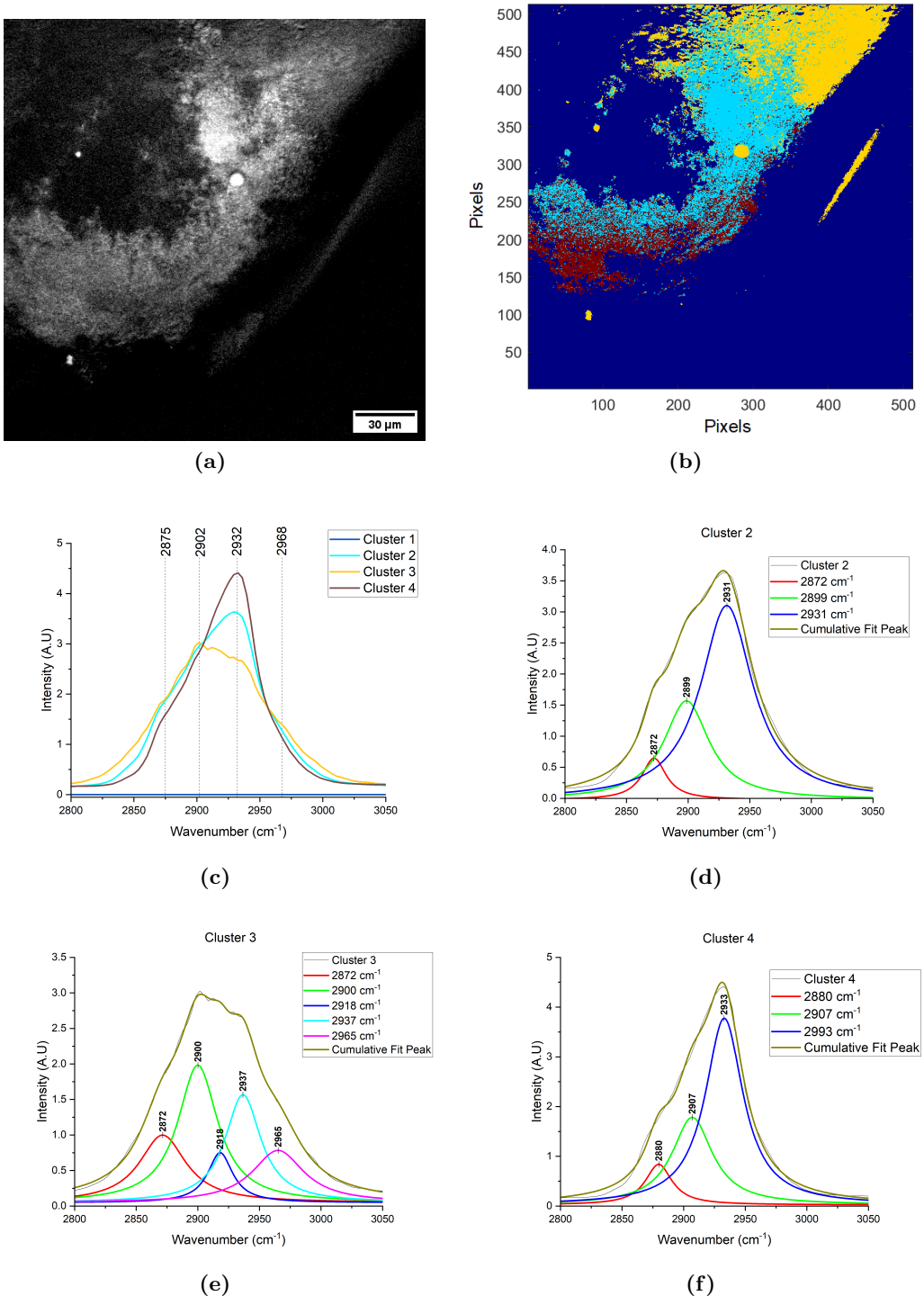

Figure 4.16: Hyperspectral SRS data of Day 1 2-species *S.salivarius* and *A.naesundii* Day 1 biofilms. a) Hyperspectral image, b) K-means clustering colour map, Cluster 1 (dark blue), cluster 2 (light blue), cluster 3 (yellow), cluster 4 (red), c) average Raman spectra of the 4 k-means clusters, d), e) and f) show the deconvolution of cluster 2, 3 and 4 respectively. A Lorentzian fit was used for multiple peak deconvolution.

4.4.1.2 Z-stacks and two-photon fluorescence (TPF)

The Day 1 2-species *S.salivarius* and *A.naeslundii* biofilm is much thicker than the previously seen mono-species biofilms, reaching 74 μm, as shown in **Figure 4.17**. For the SRS (2930 cm^{-1}) and TPF stacks, images at 0, 6.5, 24, 37.5, 57, and 74 μm are shown, along with the composite images. At 0 μm, **Figure 4.17a**, there is some SRS signal at the top of the image where there is initial biofilm attachment and the bright spot in the middle showing this feature is attached to the base of the biofilm. The TPF shows fluorescence across the centre and small clusters of bacteria. By 6.5 μm, **Figure 4.17b**, more detail emerges in both the SRS and TPF. The SRS shows the structure of the biofilm, with a brightspot where the top/central region appear more intense and an area of biofilm now introduced on the right. The TPF shows in great detail the location and structure of the bacteria within the biofilm. The bacteria in the lower portion of the biofilm shows the long chains of bacteria that is often found with *S.salivarius*. There is however, no bacteria, or fluorescence indicator, seen in the top of the biofilm, confirming the idea that this region is mostly *S.salivarius* matrix production. The TPF has picked up an area not seen in the SRS, at the centre bottom of the image.

By 24 - 37.5 μm, **Figure 4.17c - d**, the biofilm is still growing in thickness and producing matrix as shown by the increased intensity across the SRS image. The TPF shows clustering of bacteria and uniform fluorescence across the biofilm, as well as in the right hand region suggestingthere may be biofilm growth unseen in the SRS. The top portion of the biofilm from 57 - 74 μm, **Figure 4.17e - f** shows growth in the top left corner of the biofilm, where there was none previously, and the TPF still shows fluorescence on the right hand side. These SRS and TPF z-stacks show that the majority of the bacteria, as indicated to by the autofluorescence intensity, resides in the bottom half of the biofilm, and there may be areas which were developed solely by one species.

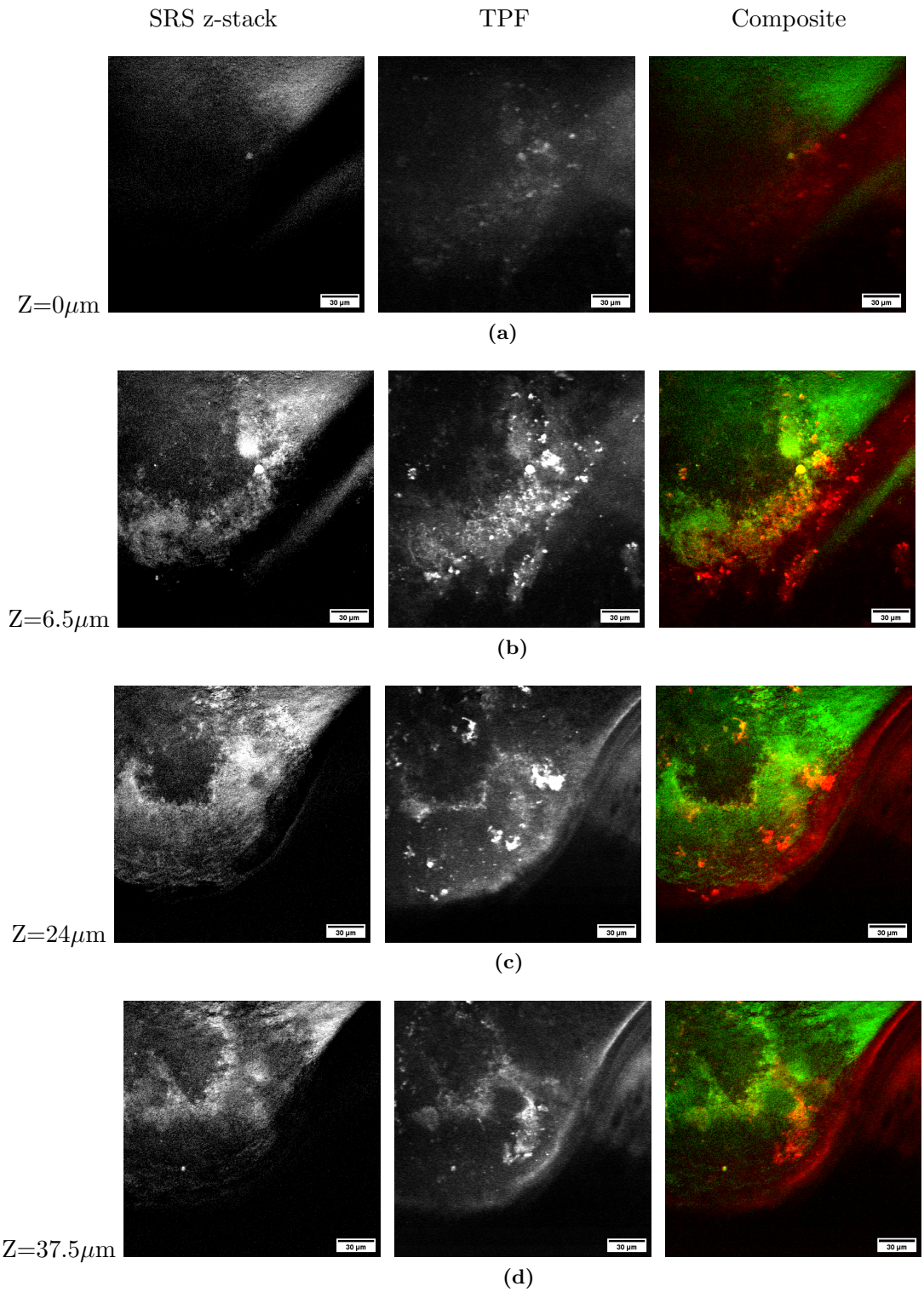

Figure 4.17: Day 1 2-species *S.salivarius* and *A.naeslundii* biofilm showing z-stacks of SRS at 2930 cm^{-1} (left), TPF (middle), and SRS (green) + TPF (red) composite (right). Each slice is 0.5 μm and taken at a) 0 μm, b) 6.5μm, c) 13 μm, d) 20 μm. (Scale bar = 30 μm).

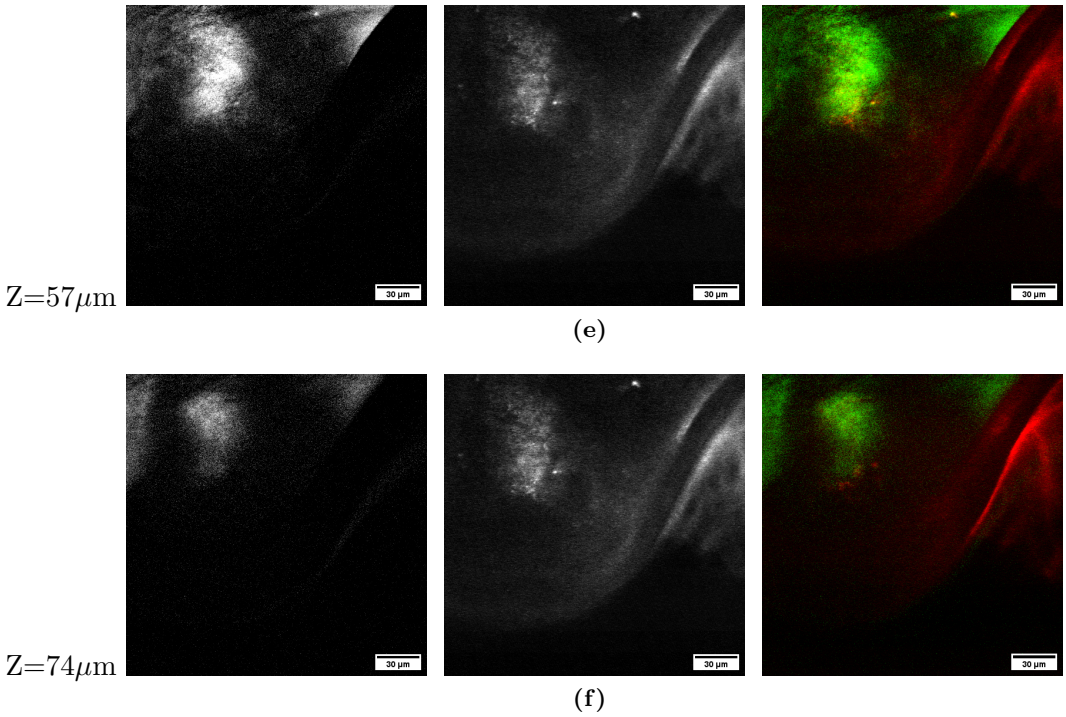

Figure 4.17: Day 1 2-species *S.salivarius* and *A.naeslundii* biofilm showing z-stacks of SRS at 2930 cm^{-1} (left), TPF (middle), and SRS (green) + TPF (red) composite (right). Each slice is 0.5 μm and taken at a) 0 μm, b) 6.5μm, c) 13 μm, d) 20 μm. (Scale bar = 30 μm).

4.4.1.3 Day 5

4.4.1.4 Hyperspectral SRS

By Day 5, 2-species *S.salivarius* and *A.naeslundii* biofilms have matured, but the inner workings of the biofilm and how the bacteria interact to produced a complex biofilm structure is still unknown. Hyperspectral SRS and k-means clustering analysis for this biofilm is given in **Figure 4.18**. The hyperspectral SRS image in **Figure 4.18a** shows the thick biofilm attached to the PDMS chamber wall (bright white band across the bottom of the image), spanning out and getting thinner, until single strands of bacteria are seen on the surface. The dense biofilm attached to the wall creates a semi-circular region that seems separate from the rest, but under close inspection does look to remain attached.

The k-means clustering colour map and corresponding spectra are given in **Figure**

4.18b - e. The strongest and most notable feature is the PDMS contribution in red, cluster 4, giving a saturated spectra with peaks at 2891 and 2950 cm^{-1}, consistent with PDMS CH stretching [248]. Cluster 1 (dark blue) denotes high bacteria density, high matrix biofilm regions with a broad spectra and peaks at 2919, 2887, 2862 and 2836 cm^{-1}. Though the spectra itself are consistent with previous biofilms, the peak positions all appear red shifted, having consistently lower wavenumber for the CH_2 and CH_3 peaks seen previously. This is consistent with repeats from the same sample, though it was only possible to analyse one biofilm for this experiment. A red shift is caused by the molecules vibrating at a lower frequency, often caused by increased crystallinity or tensile strain expanding the material. It is not clear why this may happen at this stage, and as this was not featured in other biofilms, it is not thought to be as a result of the biofilm fixing process.

Cluster 3 (yellow), has lower CH_2 peak contributions in thinner areas of biofilm where bacteria details can be seen in detail, which is as expected. From the hyperspectral data, it is not possible to discern the species of bacteria at this stage. Z-stacks may provide more information on bacterial species and how the biofilm structure changes with height.

4.4.1.5 Z-stacks and two-photon fluorescence (TPF)

The Day 5 2-species biofilm spans 43.5 μm. This Day 5 biofilm is not as thick as Day 1, this could be due to a number of reason. Firstly, as SRS is not taken of the same biofilm on Day 1 and Day 5 (due to biofilms being fixed prior analysis), the nature of biofilm growth means they grow in slightly different ways and to different thicknesses. Furthermore, as biofilms mature they break off and disperse, this could cause a reducion in thickness, or it could be due to general disruption during fixation and transport of the biofilms for the SRS facility. SRS (2930 cm^{-1}), TPF, and composite images are shown in **Figure 4.19**, featuring images at 0, 1.5, 3.5, 9.5, 21, and 43.5 μm. Already at 0 μm, **Figure 4.19a**, the SRS and TPF are showing very different structures of the base of the biofilm. The TPF shows autofluorescence across the base of the biofilm, with details showing the bacteria formation so it is not just uniform fluorescence in the matrix. This

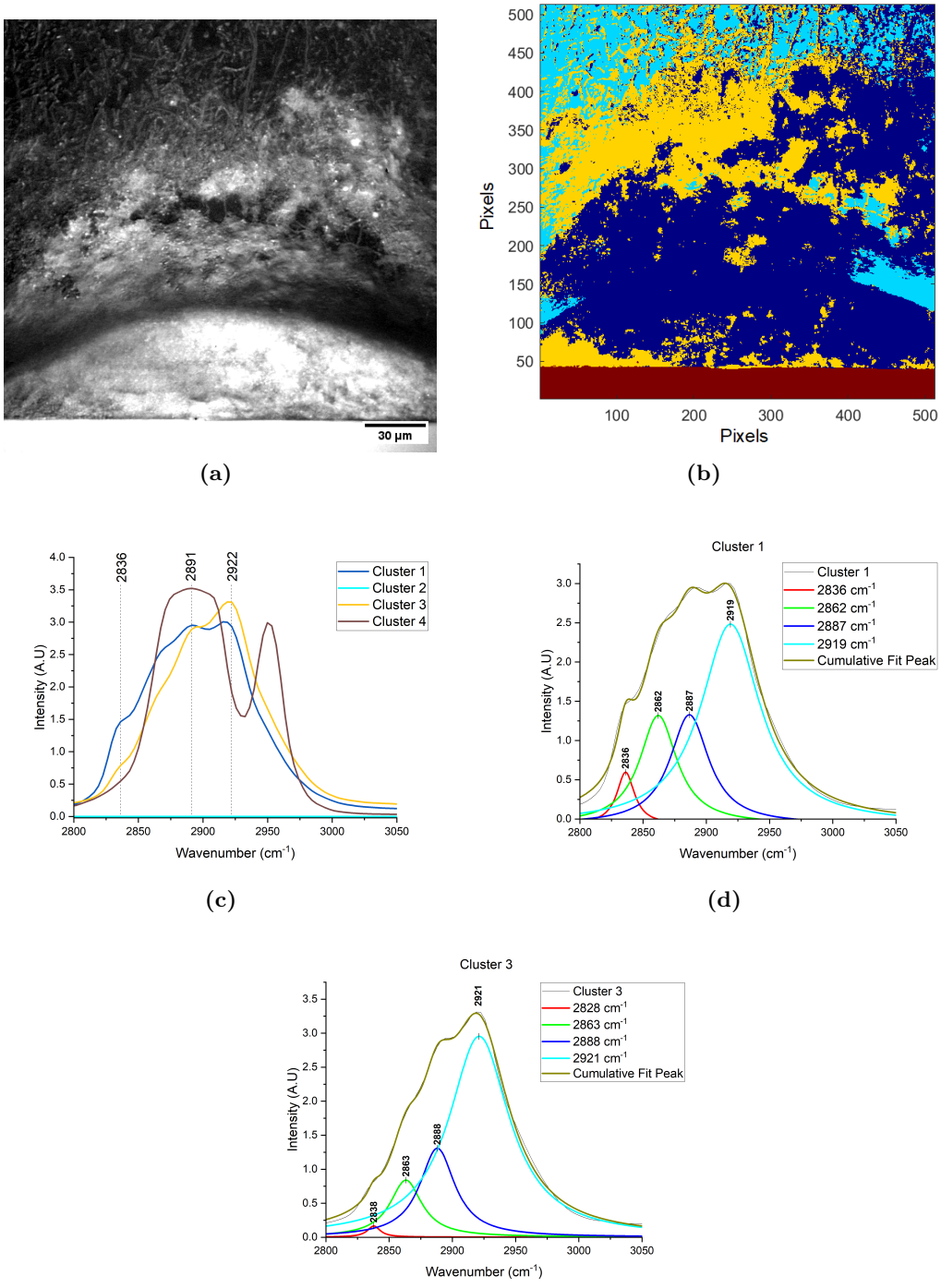

Figure 4.18: Hyperspectral SRS data of Day 5 2-species *S.salivarius* and *A.naeslundii* Day 1 biofilms. a) Hyperspectral image, b) K-means clustering colour map, Cluster 1 (dark blue), cluster 2 (light blue), cluster 3 (yellow), cluster 4 (red) c) average Raman spectra of the 4 k-means clusters, d), and e) show the deconvolution of cluster 1, and 3 respectively. Cluster 4 is PDMS, therefore the deconvolution is not shown here. A Lorentzian fit was used for multiple peak deconvolution.

visual image the TPF provides is very different from the SRS, and is the same until the top half of the biofilm. There is no semi-circular boundary, or added depth given to the biofilm in the TPF, as seen in the SRS. Typically, the whole biofilm structure and matrix is seen in detail in the SRS, with the TPF giving extra detail on the bacteria. Therefore, if the structure seen in the TPF was due to flavins being secreted into the matrix causing the autofluorescence, we would expect to see this in the SRS. This raises the question of whether the SRS is experiencing scattering or is unable for some reason to detect these regions.

By 1.5 μm, the TPF is at is maximum intensity as shown in **Figure 4.19b**. The TPF does not pick up the planktonic bacteria on the surface, which likely had a lower metabolism and flavin production than those within the biofilm. The most intense region appears to follow and cross over the dark semi-circular boundary seen in the SRS, where nothing is present, best shown in the composite image. The maximum intensity of TPF at this stage again shows the majority of bacteria may be at the bottom of the biofilm. At 3.5 μm, **Figure 4.19c**, this is where the most detail of the biofilm is seen with intricate details showing individual strands of bacteria and how they connect across the biofilm. Each species may be somewhat identified, where the long straight hair-like chains are *A.naeslundii* and smaller chains or clusters are likely to be *S.salivarius*. It is not possible at this stage, using SRS and TPD, to identify species within the biofilm without the addidtional information of the fingerprint region (500 - 1800 cm^{-1}).

As the biofilm gets thicker and grows up the chamber wall, **Figure 4.19d - f**, the width of the biofilm in the y-direction gets smaller, reducing to the semi-circular shape in both the SRS and TPF. At 21 μm, specific detail is seen within the biofilm, where intense ares in the SRS are carved out showing highly dense regions of bacteria and matrix. Even though the majority of bacteria may reside at the base of the biofilm, SRS and TPF can be used to see the structural details and intricacies of the biofilm can be seen throughout the whole biofilm.

The SRS and TPF data of Day 5 2-species *S.salivarius* and *A.naeslundii* biofilms, shows specific bacteria detail on the surface and then how the structure changes as

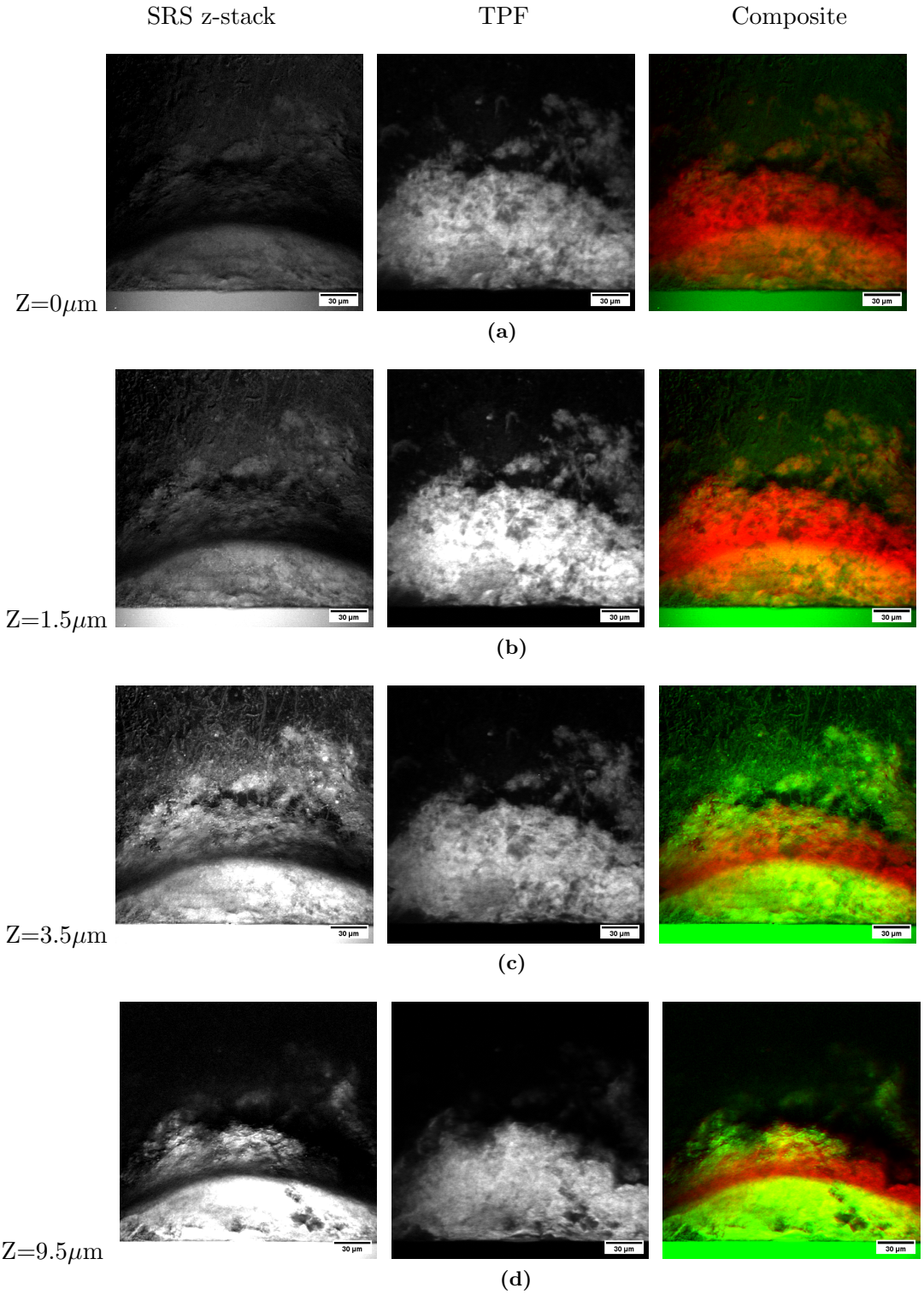

Figure 4.19: Day 5 2-species *S.salivarius* and *A.naeslundii* biofilm showing z-stacks of SRS at 2930 cm^{-1} (left), TPF (middle), and SRS (green) + TPF (red) composite (right). Each slice is 0.5 μm and taken at a) 0 μm, b) 1.5μm, c) 3.5 μm, d) 9.5, e) 21.5 μm, and f) 43.5 μm. (Scale bar = 30 μm).

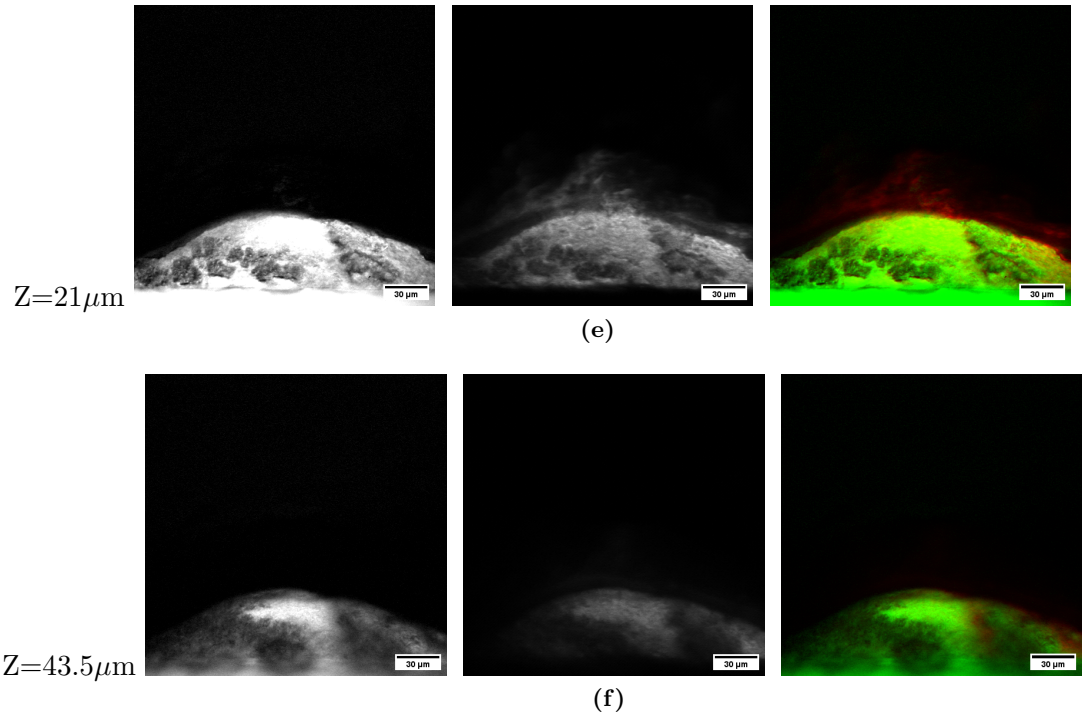

Figure 4.19: Day 5 2-species *S.salivarius* and *A.naeslundii* biofilm showing z-stacks of SRS at 2930 cm^{-1} (left), TPF (middle), and SRS (green) + TPF (red) composite (right). Each slice is 0.5 μm and taken at a) 0 μm, b) 1.5μm, c) 3.5 μm, d) 9.5, e) 21.5 μm, and f) 43.5 μm. (Scale bar = 30 μm).

the biofilm grows. TPF on live biofilms would provide more information on how the metabolism rates grow and change throughout the biofilm as it develops, and may potentially show at what stage, if any, the autoflourescence (flavins) may secrete into the matrix. At this stage it is hard to determine any specific details about the individual species within the biofilm or how each has contributed to the growth. Specific labelling of the bacteria, using a method such as Fluorescence *in situ* hybridisation (FISH) would be able to show the individual species location withn the biofilm.

4.5 2-Species FISH Biofilms

Using Fluorescence *in situ* hybridisation (FISH), *S.salivarius* and *A.naeslundii* within a 2-species biofilm were individually labelled with Cy3 and Cy5 fluorescent probes, respectively. In doing so, z-stacks mapping each species throughout the biofilm were taken

for Day 1 and Day 5 biofilms, as well as SRS.

4.5.1 Day 1

4.5.2 Hyperspectral SRS

2-species Day 1 biofilms were treated with FISH prior to fixing, and the hyperspectral image and k-means clustering analysis can be seen in **Figure 4.20**. The hyperspectral image in **Figure 4.20a** shows an area of biofilm with lots of clusters across the surface. The k-means clustering colour map and spectra are given in **Figure 4.20b - f**, showing the biofilm divided into three clear clusters. Cluster 2 (light blue) and cluster 3 (yellow) both have a dominant 2896 cm^{-1} peak, while cluster 4 (red) has a dominant 2925 cm^{-1} peak and represents most of the biofilm. As found in *S.salivarius* biofilms, regions with a stronger 2895 - 2905 cm^{-1} peak have more matrix and less bacterial contribution, or at least a lower bacterial density. Furthermore, seeing this at this stage of the 2-species biofilm suggests that *S.salivarius* may be be the dominant species at this stage. Looking at the FISH z-stacks will be able to show the species distribution within the biofilm.

4.5.2.1 FISH z-stacks

SRS and TPF z-stacks were taken for FISH Day 1 2-species biofilms, however for TPF, the excitation wavelength was chosen to excite the fluorescent FISH probes. For *S.salivarius* labelled with Cy3, a 1045 nm excitation laser was used, and for *A.naeslundii* labelled with Cy5, a 1220 nm laser was used. As TPF requires the absorption of two photons, the actual excitation for *S.salivarius* and *A.naeslundii* were 522.5 and 610 nm respectively. The 10 μm z-stack is shown in **Figure 4.21**, with images at 0, 5, 8 and 10 μm.

At 0 μm, **Figure 4.21a**, there is very low intensity SRS and *S.salivarius* fluorescence in areas of biofilm growth. By 5 μm in **Figure 4.21b**, full detail of the biofilm can be seen in the SRS, and the fluorescence images show this is mostly made up of *S.salivarius*

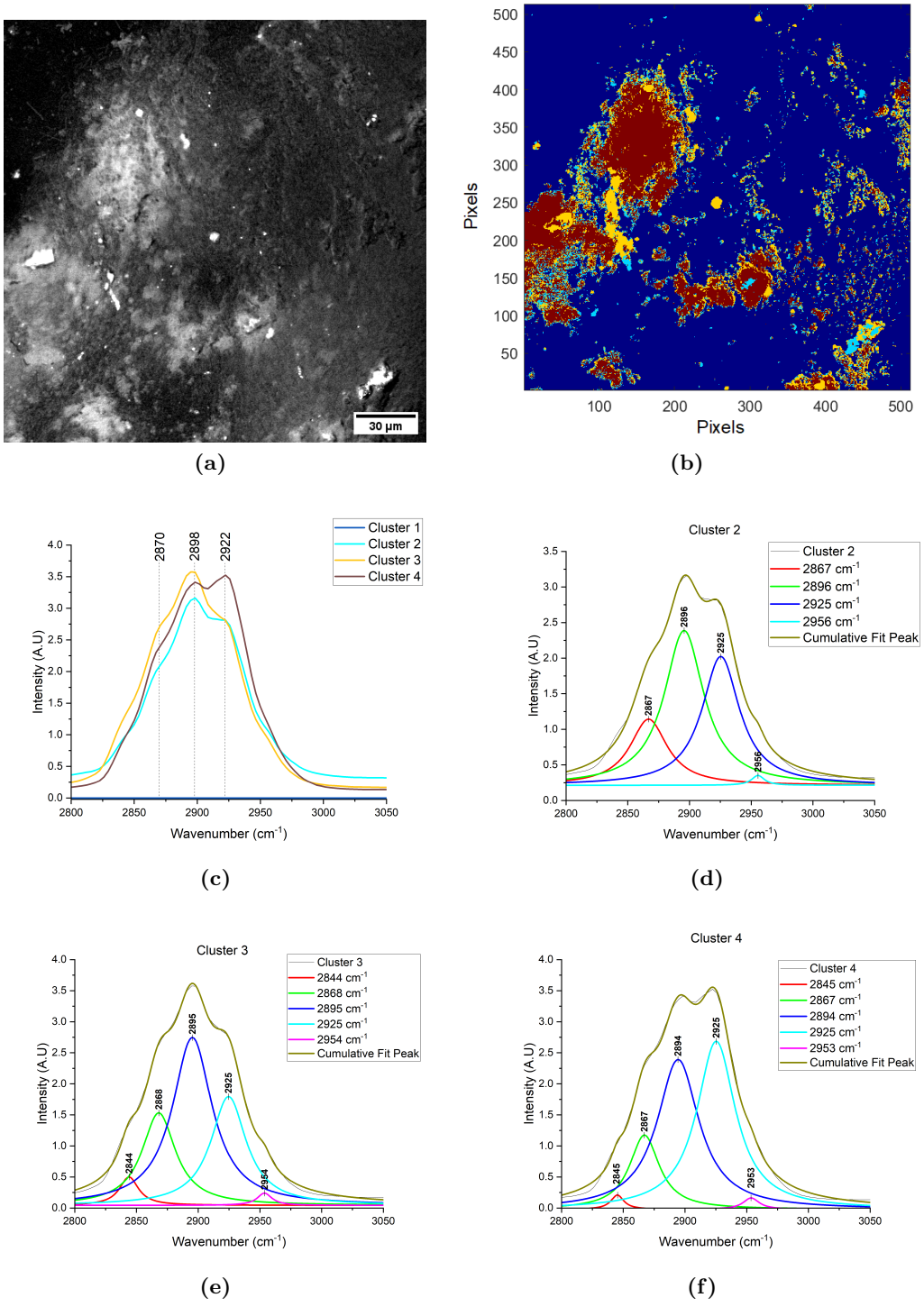

Figure 4.20: Hyperspectral SRS data of Fluorescent *in situ* hybridisation (FISH) Day 1 2-species *S.salivarius* and *A.naeslundii* Day 1 biofilms. a) Hyperspectral image, b) K-means clustering colour map,Cluster 1 (dark blue), cluster 2 (light blue), cluster 3 (yellow), cluster 4 (red), c) average Raman spectra of the 4 k-means clusters, d), and e) show the deconvolution of cluster 2, 3 and 4 respectively. A Lorentzian fit was used for multiple peak deconvolution.

bacteria as there is almost no *A.naeslundii* fluorescence present. This changes by 8 μm, when *A.naeslundii* appears as shows high intensity in some biofilm clusters. Looking at the composite images shows regions which are mixed, or small areas which are just one species. At the top of the biofilm by 10 μm, **Figure 4.21d**, there is little signal except for some *A.naeslundii* fluorescence.

The FISH z-stacks have shown that for Day 1 2-species biofilms, *S.salivarius* forms the base of the biofilm and *A.naeslundii* attaches on top. From this it can be deduced that there is a greater amount of *S.salivarius* in the 2-species biofilm at this stage. This supports the findings from the k-means clustering analysis, which shows spectra most similar to that of *S.salivarius* biofilms at this stage. As the hyperspectral image is taken at one fixed z-point, this point was likely to have been lower in the biofilm, at 5 μm where *S.salivarius* is thriving, wheras if the image had been taken higher at 8 μm, the k-means may have shown different spectra with more of a *A.naeslundii* contribution.

4.5.3 Day 5

4.5.3.1 Hyperspectral SRS

Hyperspectral k-means clustering analysis of Day 5, 2-species FISH biofilms, is seen in **Figure 4.22**. This biofilm is not as thick as previous Day 5 biofilms, this is either due to the nature of biofilm variability, or the fact the FISH process required many washing steps which could have disrupted the biofilm. Nevertheless, the hyperspectral image in **Figure 4.22a** shows dense regions of biofilm across the centre and top right, as well as the individual bacteria throughout. The k-means clustering analysis in **Figure 4.22b - f** divides this biofilm into spectral clusters which all have a very strong, narrow, 2902 cm^{-1} peak, and a very low intensity 2937 cm^{-1}.

Cluster 1 (dark blue) covers a lot of the background, minimal matrix area on the left of the image. This cluster for the first time only has the one CH_2 2902 cm^{-1} peak, and two CH_3 2937 and 2956 cm^{-1}. There may be a decrease in the lipid content in the matrix due to the lacking CH_2 contribution. Cluster 3 (yellow) covers the main part

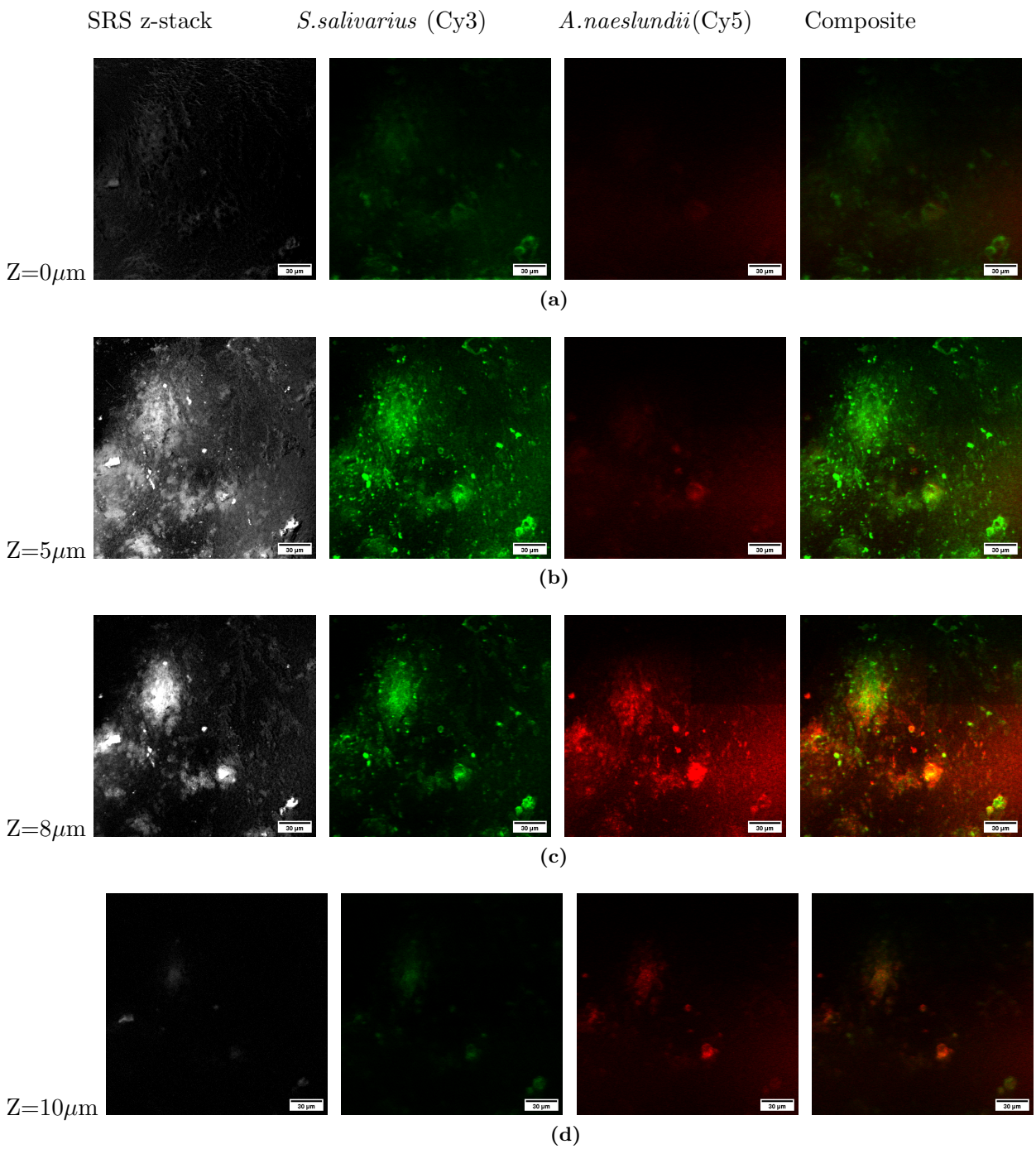

Figure 4.21: Fluorescent *in situ* hybridisation (FISH) Day 1 2-species *S.salivarius* and *A.naeslundii* biofilm showing z-stacks of SRS at 2930 cm^{-1}, TPF of Cy3 *S.salivarius* (green), TPF of Cy5 *A.naeslundii* (red) and the composite images. and SRS (green) + TPF (red) composite (right). Each slice is 1 μm and taken at a) 0 μm, b) 5μm, c) 8 μm, and d) 10 μm. Cy3 ex/em: 1045/575 nm, Cy5 ex/em: 1220/660 nm. (Scale bar = 30 μm).

of the biofilm where individual bacteria is seen, and consequently has the greatest 2931 cm^{-1} protein contribution, which thus far has been shown to be associated with bacteria. Cluster 4 (red) has the strongest, and narrowest, 2900 cm^{-1} peak, showing the matrix contribution across the main biofilm area. The z-stacks may provide more information on how the species of bacteria at Day 5 contribute to this 2 species biofilm.

4.5.4 FISH Z-stacks

To see how the *S.salivarius* and *A.naeslundii* species are distributed within a Day 5 2-species biofilm, SRS and TPF z-stacks are shown in **Figure 4.23** for a 100 μm stack. Images are shown at 0, 15, 45, 80, and 100 μm. As with Day 1, at 0μm, **Figure 4.23a**, *S.salivarius* is the only bacteria seen on the surface, nor is there any SRS signal. By 15 μm, **Figure 4.23b**, there is clear biofilm formation and areas of high density bacteria where the individual strands of *S.salivarius* can be seen, which is also present in the SRS. There is also now *A.naeslundii* present, in the main biofilm region, though the top right corner of the image remains just *S.salivarius*.

In the middle of the biofilm at 45 μm, **Figure 4.23c**, the density of both species increases, with a particularly strong *S.salivarius* fluorescence signal along the inner edge of the biofilm. The SRS image does not show this same detail, particularly along the inner edge of the biofilm this region appears sparse and low intensity in the SRS. At 80 μm, **Figure 4.23d**, the area of biofilm grows larger, potentially indicating the biofilm has taken on a 'mushroom' like shape which is common with mature biofilms. This area still shows clear bacteria contribution from both species. By 100 μm, **Figure 4.23e**, at the top of the biofilm there is still a great amount of bacteria with the *S.salivarius* species being easily identifiable.

FISH biofilms are an extremely valuable way of identifying multiple species within a biofilm which compliments SRS. By utilising z-stack, the distribution and contribution of each species of bacteria throughout the biofilm can be seen, and with enough precision that individual species can be seen and identified. As with Day 1, *S.salivarius* is the species that is seen at the base of the biofilm adhering to the surface, and from the images

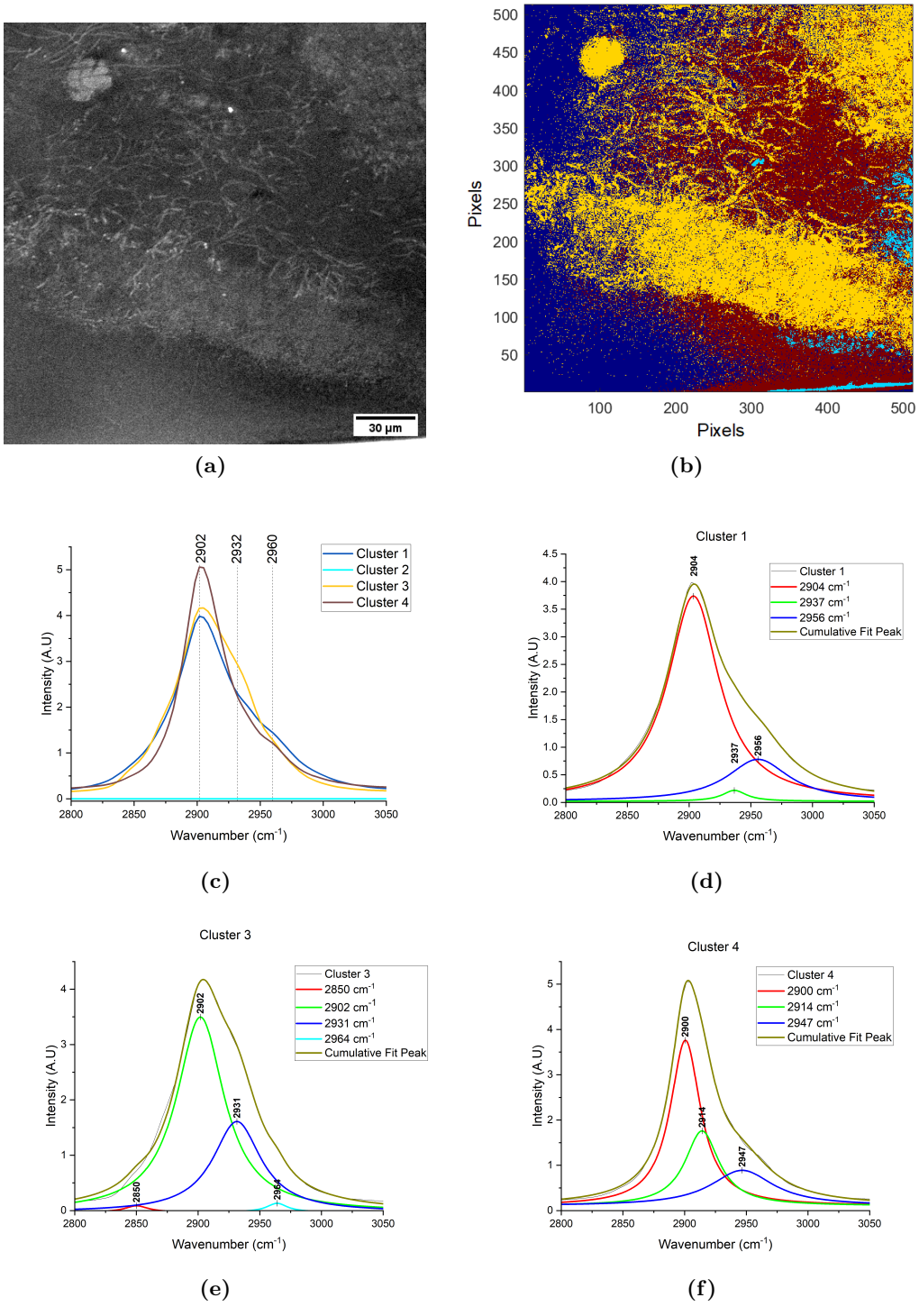

Figure 4.22: Hyperspectral SRS data of Fluorescent *in situ* hybridisation (FISH) Day 5 2-species *S.salivarius* and *A.naeslundii* Day 5 biofilms. a) Hyperspectral image, b) K-means clustering colour map, Cluster 1 (dark blue), cluster 2 (light blue), cluster 3 (yellow), cluster 4 (red), c) average Raman spectra of the 4 k-means clusters, d), and e) show the deconvolution of cluster 1, 3 and 4 respectively. A Lorentzian fit was used for multiple peak deconvolution.

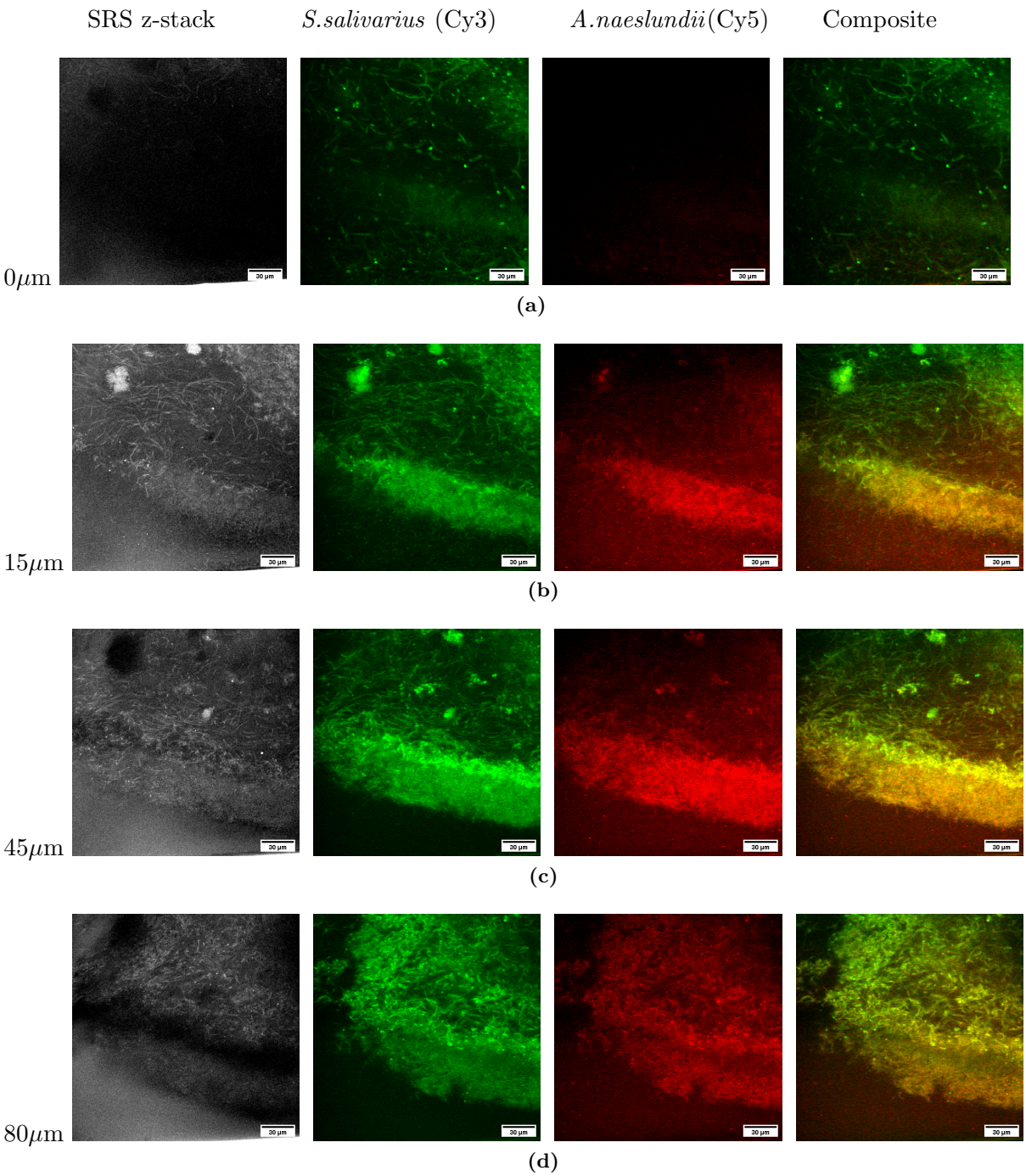

Figure 4.23: Fluorescent *in situ* hybridisation (FISH) Day 5 2-species *S.salivarius* and *A.naeslundii* biofilm showing z-stacks of SRS at 2930 cm^{-1}, TPF of Cy3 *S.salivarius* (green), TPF of Cy5 *A.naeslundii* (red) and the composite images. and SRS (green) + TPF (red) composite (right). Each slice is 1 μm and taken at a) 0 μm, b) 15μm, c) 45 μm, d) 80 μm, e) 100 μm, f) 130 μm. Cy3 ex/em: 1045/575 nm, Cy5 ex/em: 1220/660 nm. (Scale bar = 30 μm).

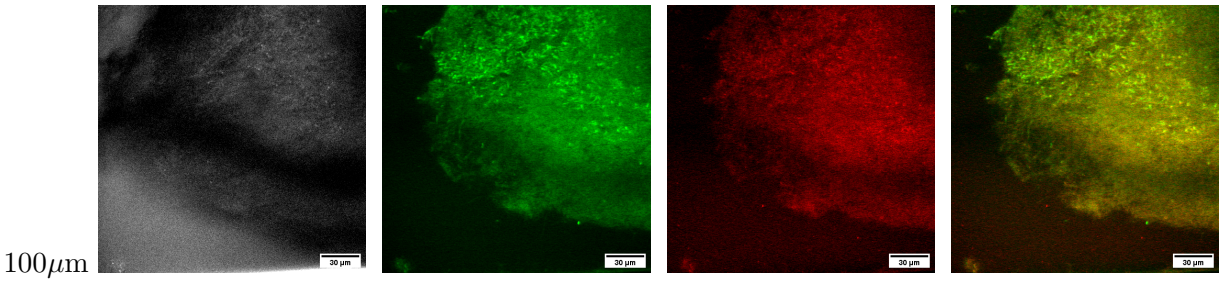

Figure 4.23: Fluorescent *in situ* hybridisation (FISH) Day 5 2-species *S.salivarius* and *A.naeslundii* biofilm showing z-stacks of SRS at 2930 cm^{-1}, TPF of Cy3 *S.salivarius* (green), TPF of Cy5 *A.naeslundii* (red) and the composite images. and SRS (green) + TPF (red) composite (right). Each slice is 1 μm and taken at a) 0 μm, b) 15μm, c) 45 μm, d) 80 μm, e) 100 μm, f) 130 μm. Cy3 ex/em: 1045/575 nm, Cy5 ex/em: 1220/660 nm. (Scale bar = 30 μm).

may have a higher quantity of bacteria within the biofilm after 5 days. However, both species thrive in the biofilm and although some areas show individual species clusters, both species mix and grow together in the biofilm.

4.6 Conclusion

This chapter has shown that SRS and TPF can be used successfully to produce high-resolution, detailed images and z-stacks of mono-species and 2-species biofilms, on chip. This novel method of biofilm analysis looks at the CH_2 and CH_3 peaks in the high wavenumber region, which correspond to the lipid and protein contributions from the bacteria cells and the matrix. Hyperspectral SRS provides a great amount of information and there are numerous ways one could analyse and interpret this data, for example by only selecting data from areas of interest, dividing the data into a grid, or by k-means analysis. As this project was interested in comparing biofilms over time, and different species types, a standardised method of analysis was required to ensure consistent analysis. After comparing different methods of analysis, k-means clustering analysis proved reliable and sufficient to accurately present the hyperspectral data into 4 clusters and their subsequent average spectra. Using multiple peak fitting to deconvolute the spectra provided further information on the individual peak contributions to the spectra,

allowing conclusions to be drawn about whether the region had high bacteria or matrix contribution.

It was found that high contributions of the lipid CH_2 peaks, at approximately 2850, 2880, and 2905 cm^{-1} were associated with increased matrix contribution, whereas the CH_3 2937 cm^{-1} protein peak identifies bacteria cells. Most spectra had contributions from all peaks, therefore the relative intensities of each of them highlighted if a region had high or low bacteria density, or matrix. *S.salivarius* biofilms were the only mono-species biofilms to have spectra with a dominating 2905 cm^{-1}. All biofilms grew thicker and denser by Day 5, and had greater matrix contributions. The 2-species biofilms had a similar spectral profile to the mono-species with all the expected peaks, though it is not possible to identify the individual species with the hyperspectral spectra at this stage.

SRS and TPF z-stacks were complimentary tools that provided higher level of detail about how the biofilms varied with height. To have a variable z-position, SRS was taken at a fixed wavenumber, 2930 cm^{-1} (CH_3), therefore the stacks were able to show the biofilm structure, individual bacterium, the matrix contribution, and indicate high and low regions of bacteria density. TPF detects the autofluoresence of endogenous fluorophores within the biofilm, and at ex/em 802(401)/550 nm these were specifically flavins. Flavins are a part of the metabolic system, thus are found within bacteria and can be secreted into the matrix. This allowed TPF to provide specific detail of the bacteria location within the biofilm that was previously unseen in the SRS. These methods are therefore perfectly complimentary, providing different information to show a complete biofilm picture. It was noted that the peak TPF intensity always occurred slightly before the maximum SRS intensity, therefore when using SRS to show the density of bacteria at a point (using 2930 cm^{-1} CH_3 peak as the marker), this did not directly correspond to the z-position the TPF would find. This is not something that was important for this work, but is worth noting.

Using TPF, it was shown that the highest density of bacteria is within the bottom half of the biofilm, and for Day 1 *A.naeslundii* biofilms there was not a high density of bacteria. However, the biofilms used in this project were fixed prior to analysis and it

is known that dead bacteria cells have lower intensity autofluorescence. It is not known for *S.salivarius* and *A.naeslundii* if the autofluorescence remains stable after death or gradually decreases, and if this process is slowed down by being trapped within a biofilm. TPF in this chapter was solely used as a location marker for the bacteria. Research has shown that bacteria under stress have increased autofluorescence as they increase their metabolism to try fight off any dangers [237]. Whether under stress, or just generally undergoing fluctuations in the metabolism, detecting the autofluorescence of flavins can be a useful marker to monitor the biofilm metabolism process and how this changes over time, or with multiple species. In the future, this process colud therefore be repeated on live biofilms in order to track the metabolism of multi-species biofilms.

Although TPF was used as a marker for bacteria location within the biofilm, a more accurate method was using FISH *S.salivarius* and *A.naeslundii* within a 2-species biofilm were fluorescently labelled with Cy3 and Cy5, respectively, and TPF taken. By seeing the specific location and distribution of each species within the biofilm, it was found that *S.salivarius* was always found at the base of the biofilm attached to the surface whereas *A.naeslundii* was not. Furthermore, Day 1 biofilms were primarily *S.salivarius* bacteria, though by Day 5 each species seemed equally present.

Combining multiple methods of analysis such as hyperspectral SRS, SRS and TPF z-stacks, and FISH TPF, was able to provide a significant amount of detail about the structure, architecture, bacteria density and distribution, and matrix contribution within mono- and 2-species biofilms. In the future, experiments could be completed on live biofilms on chip, so that the same biofilm would be analysed of time, and information about the metabolic activity of the biofilm could be tracked with TPF.

Chapter 5

Biofilm Treatment with Microbubbles, Ultrasound and IK8

5.1 Work aims and motivation

Biofilms are notoriously stubborn, hard to penetrate, and less susceptible to antibiotics, and with the rise of antibiotic resistance, new methods of treatments are being sourced. Microbubbles and ultrasound have been shown to have a disrupting and damaging effect on biofilms, and when combined with a therapeutic agent the damaging effect is only increased [174, 249]. With the aim of providing an alternative to antibiotics, an antimicrobial peptide is used in this work, which will be delivered via liposome, and combined with microbubbles and ultrasound for the most impact. To date there are no reports in the literature on the combination of antimicrobial peptides with microbubbles and ultrasound.

5.2 Biofilm growth

Biofilm growth reported in this chapter was performed using a 96-well plate, rather than the previously described microfluidic device. The large number of experimental repeats and testing conditions required for the optimisation of biofilm treatment made using the microfluidic devices unfeasible for this work. A 96-well plate allowed for a simpler set-up and high-throughput of experiments, before moving onto microfluidics once the optimal treatment parameters had been determined.

5.3 Free IK8 against bacteria and biofilms

5.3.1 Minimum Inhibitory Concentration (MIC) and Minimum Bactericidal Concentration (MBC)

The Minimum Inhibitory Concentration (MIC) values are a measure of the minimum concentration of antimicrobial required to inhibit further bacterial growth. Depending on the concentration, the bacterial effect may be bacteriostatic or bactericidal.

The MIC for IK8 against *S.salivarius* and *A.naeslundii* was determined by as the IK8 concentration that showed no visual increase in turbidity or further visible growth of bacteria. The results for both species can be seen in **Figure 5.1** where the MIC values are highlighted in red. IK8 concentration was tested in doubling dilutions from 200 - 1.56 μg/ml, and for *S.salivarius* and *A.naeslundii* the MIC value was determined to be 100 μg/ml and 12.5 μg/ml respectively. These values were confirmed over three experimental repeats. For wells with concentrations lower than these values, a visible increase in turbidity was seen as well as some biofilm formation on the base of the well, despite well plates shaking during incubation. Optical density measurements were also taken to quantify the results, however due biofilm formation the results were unreliable and discounted.

For the minimum bactericidal concentration (MBC), an antimicrobial may only be

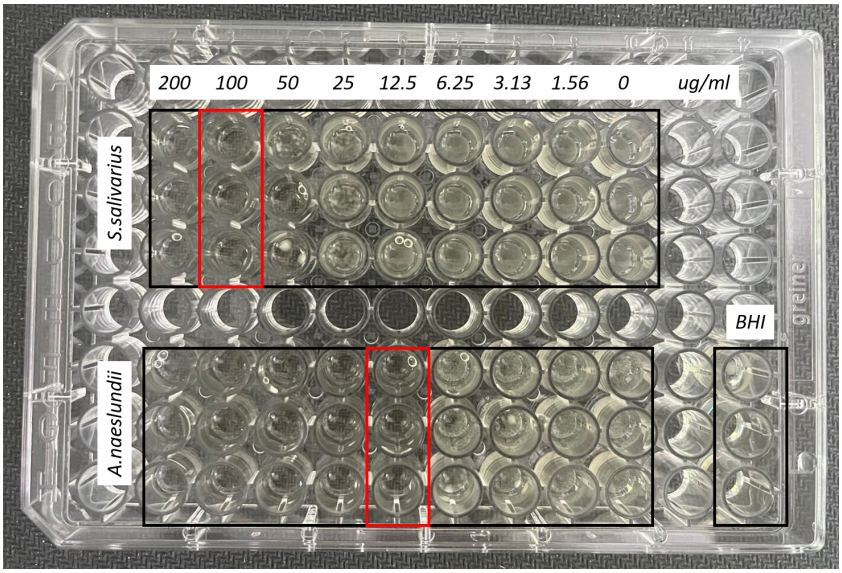

Figure 5.1: The minimum inhibitory concentration (MIC) for *S.salivarius* (top) and *A.naelsundii* (bottom) after 18 hours incubation with the antimicrobial peptide IK8. The concentrations of IK8 for each well are shown at the top, in μg/ml. The red boxes show the minimum inhibitory concentration identified for each species. Brain heart infusion (BHI) wells were used as a control. Initial bacteria concentrations were 0.5 McFarland standard.

considered bactericidal if it kills $\geq$ 99.9% of bacteria, or a 3-log reduction in viable cell density, and is no more than 4 times the MIC value [59, 250, 251]. Once the MIC was determined, 10 μl aliquots from each well were spread on agar plates to determine the cell density, and see if the MIC value corresponds to the Minimum bactericidal concentration (MBC). **Figure 5.2** shows the cell density of both species after 18 hours treatment with IK8. For both species the MBC matches the MIC. For *S.salivarius* the cell density decreases to 0 at 100 μg/ml of IK8, and for *A.naeslundii* the cell density shows a 3-log reduction at 12.5 μg/ml. The cell densities show an overall decrease with increasing concentration, but remain within 1-log of each other up to the MBC where there is a sharp drop.

The MIC and MBC are used across microbiology and clinical medicine with their values showing the susceptibility or resistance of a strain to the antimicrobial, and therefore directly impacting the therapeutic strategy chosen for a patient. There are however some limitations to the use of MIC and MBC, with the most obvious being that the test does not account for the impact the patient's body may have on the antimicrobial efficacy and

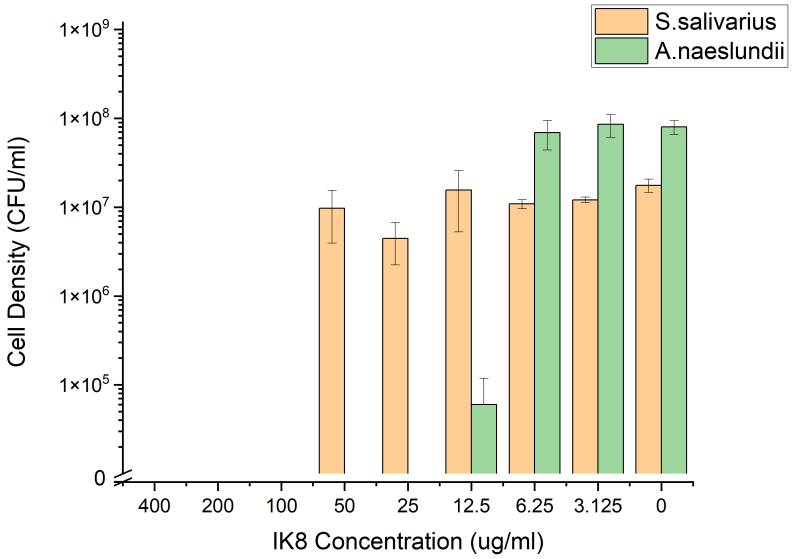

Figure 5.2: Cell density (CFU/ml) of *S.salivarius* (orange) and *A.naeslundii* (green) after 18 hours incubation at 37°C with a range of IK8 concentrations .

is only specific to the inoculum used for testing, nor does it assess the difference between planktonic bacteria and biofilms. There is no specific reason given for the 18-24 hour time frame, and perhaps a longer incubation time could prove lower concentrations to be bactericidal and not bacteriostatic [59]. There are also questions about the reliability of MIC results as repeats of the same strain can vary by a 2-fold dilution [252, 253]. For example an MIC of 2 μg/ml could actually be 1 or 4 μg/ml, thus providing unreliable outcomes during treatment. The MIC and MBC are of course extremely valuable and the best current methods for assessing and creating a standard for the effectiveness of antimicrobials, but it should noted that the effectiveness in practice may vary from the measured results.

5.3.2 Time-Kill Study

To compliment the MIC and MBC measurements, a time-kill study was undertaken to determine how long it takes for the antimicrobial to take effect, and whether inhibitory concentrations are actually bacteriostatic for short or long periods of time. **Figure 5.3**

shows how the cell density (CFU/ml) of *S.salivarius* and *A.naeslundii* changes over 24 hours for a range of IK8 concentrations above and below the MIC.

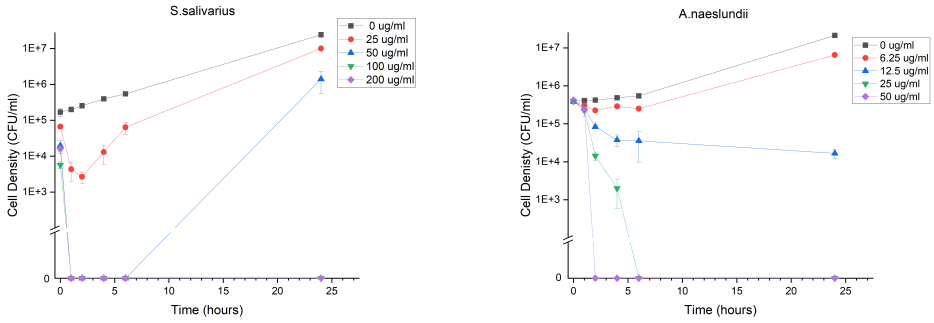

(a) **(b)**

Figure 5.3: Scatter plots showing the cell density (CFU/ml) of a) *S.salivarius* and b) *A.naeslundii* over 24 hours. Samples were incubated at 37°C with IK8 concentrations of 0, 25, 50, 100, 200 μg/ml and 0, 6.25, 12.5, 25, 50 μg/ml respectively.

For *S.salivarius* it is shown that IK8 takes effect after 1 hour incubation, causing complete cell death for concentrations 100 and 200 μg/ml. For 25 μg/ml, IK8 initially causes cell death as a 1-log reduction in cell density is seen after 2 hours, however cells are revived and cell density increases from this point on. 50 μg/ml shows complete cell death for 6 hours, but recovers after 24 hours. It is possible that at this concentration, *S.salivarius* may go into a "viable but not culturable" (VBNC) state. This is a survival response bacteria have evolved to take when in stressful environments, which allows them to remain alive and metabolically active, yet notculturable on media [254]. Once this stress has been removed or no longer a threat, they can revive and proceed as "normal" culturable bacteria cells again . This data shows that for *S.salivarius* IK8 of 100μg/ml and above are bactericidal.

Cell density results for *A.naeslundii* show that for 50μg/ml IK8, complete cell death is seen after 2 hours, however only after 6 hours for 25μg/ml, suggesting that for this species time dependence is an important factor in treatment. The MIC value of 12.5μg/ml proves to be bacteriostatic, while 6.25 and 0μg/ml show standard growth over 24 hours. Considering both these results, a minimum of 2 hour IK8 incubation time should be used when treating these bacteria simultaneously. For future biofilm experiments, a 3 hour incubation time was chosen as it was assumed the addition of extracellular matrix

within the biofilm would slow down the IK8 kill time, and a 24 hour incubation time was also tested for comparison.

5.3.3 Free IK8 against 2-species biofilms

2-species biofilms were grown in well plates as described in **Section 2.7.3** for 24 or 48 hours. To begin with 24 hour biofilms were used for IK8 testing but this was later increased to 48 hours to represent a more mature biofilm. *A.naeslundii* is known to grow slower than *S.salivarius* and experimentally has shown that a 24 hour biofilm is dominated by *S.salivarius*, so the effect of IK8 on a 24 hour biofilm may not be representative of a mature 2-species biofilm.

Biofilms were incubated with 2-fold dilutions of IK8 from 800 - 6.25 μg/ml, no IK8, and with 1% Virkon as a positive kill control, for 3 or 24 hours.

5.3.3.1 Live/dead and crystal violet staining techniques

Live/dead (SYTO9/Propidium Iodiode (PI)) and crystal violet (CV) staining was used as a method of quantifying biofilm viability and biomass after IK8 treatment. A plate reader was used to take all measurements, and for fluorescent measurements a single point well scan can be taken with the focus on the centre of the well, or a 9-point well scan can be done where nice measurements are taken in a 3x3 grid across the well and averaged to give the final value. It was noted that biofilm growth tended to be sparse in the centre of the well and thicker around the edge of the well, a comparison of both scan methods was first performed to see if a single point scan was able to provide a representative reading across the well.

2-species *S.salivarius* and *A.naeslundii* biofilms were used to test these settings and **Figure 5.4** shows that a 9-point scan detects slightly more fluorescence but both show the same overall trend, therefore a single point scan was deemed to be sufficient to measure the fluorescence of well plate biofilms.

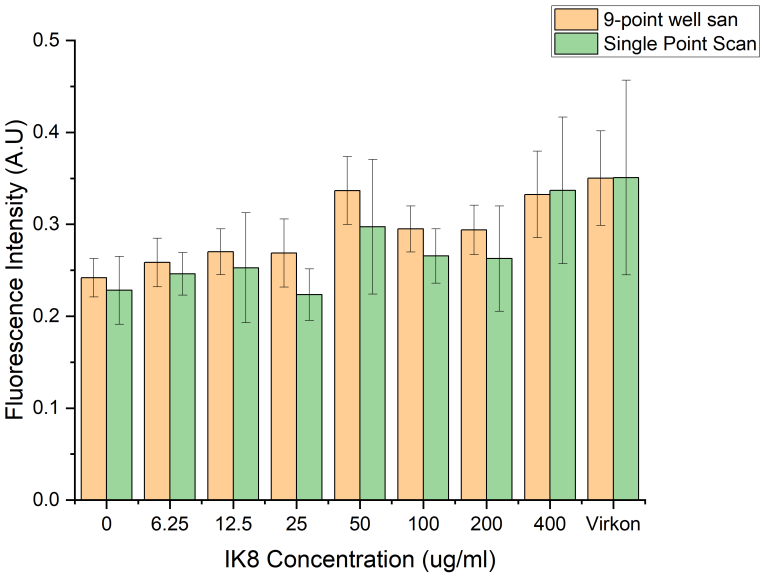

Figure 5.4: Comparison of a single point scan (green) or 9-point well scan (orange) of 2-species *S.salivarius* and *A.naeslundii* biofilms, showing fluorescence of Propidium Iodide stained biofilms after incubation with IK8 of concentration 0 - 400 μg/ml, and 1% Virkon. Each concentration is an average of 6 wells. Ex/Em:535/617 nm.

The experimental procedure of staining biofilms with PI to quantify dead bacteria was repeated twice, and did not prove as reliable as anticipated. It was expected that the fluorescence values would increase with increasing cell death (IK8 concentration), and show maximum fluorescence with 1% Virkon, which should kill the biofilm. While the first repeat shown in **Figure 5.5a** does show a slight trend with overall increasing fluorescence with IK8, the biofilm with no IK8 treatment still has a high fluorescence intensity which is only one-third less than the Virkon sample. The overall increase in intensity is low in comparison to that found in the literature, and the fluctuations across the concentration ranges are inconsistent [2]. The second repeat in **Figure 5.5b** shows no trend, and the validity is diminished by the fact the Virkon biofilms show the lowest fluorescence when it should be the highest - regardless of whether the IK8 is having any effect on the biofilms.

While this method of quantifying dead bacteria in biofilms has been followed before, seemingly successfully, some literature suggests the use of PI in biofilms is unreliable. PI only penetrates bacteria with damaged membranes and binds to nucleic acids, but the

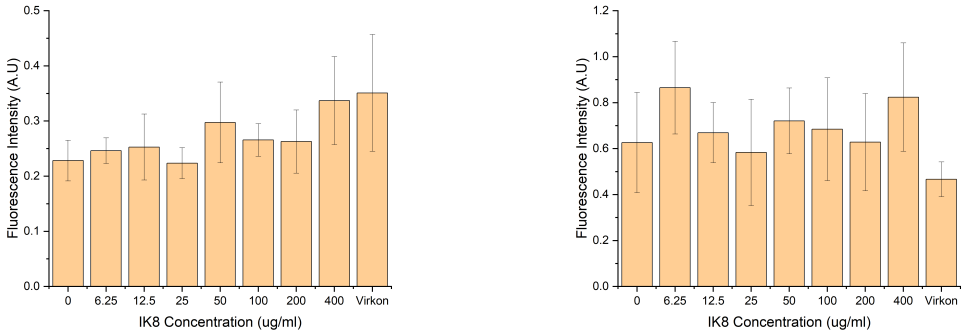

(a) **(b)**

Figure 5.5: Two experimental repeats showing the florescence intensity of PI stained 2-species biofilms after treatment with IK8. Ex/Em:535/615 nm.

presence of extracellular DNA (eDNA) and potentially eRNA, within the biofilm matrix may cause false positive results and is a factor rarely mentioned or considered when used to quantify the viability of a biofilm [255, 256]. Biofilms in well plates are also delicate and despite being grown in the same conditions, being rinsed and treated with care, biofilms may get disrupted and vary across the experiment, thus one sample may simply have more biofilm than another and therefore have a higher fluorescence intensity.

To quantify biofilm biomass CV stain was used, and similar to PI, the results were inconsistent across three experimental repeats, as shown in **Figure 5.6**. Compared to biofilm with no IK8, often the results show a higher absorbance thus greater biomass. IK8 may well be killing the bacteria, but dead cells remain incorporated within the biofilm and contribute to the CV fluorescent intensity, skewing the results. This is the main limitation of CV staining, and therefore is not a viable method of quantifying the effectiveness of IK8 treatments.

5.3.3.2 Cell density quantification

As PI and CV quantification methods proved unreliable, a more robust method is to measure the viable cell density (CFU/ml) of the biofilm after treatment by aspirating the biofilm, spreading on agar plates, and counting the colony forming units by eye [257].

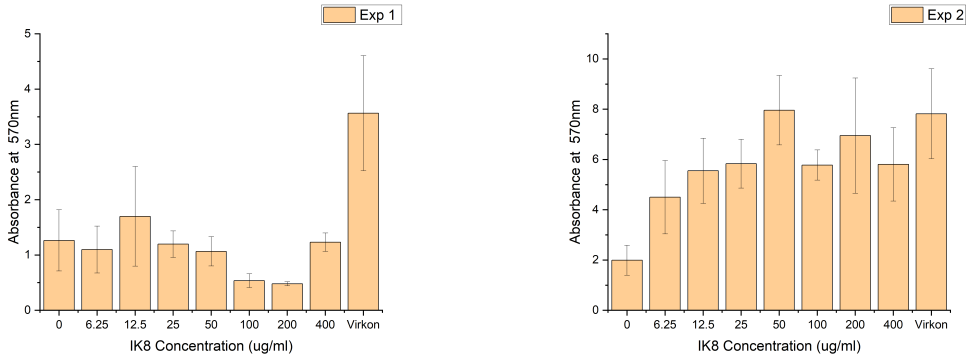

(a)

(b)

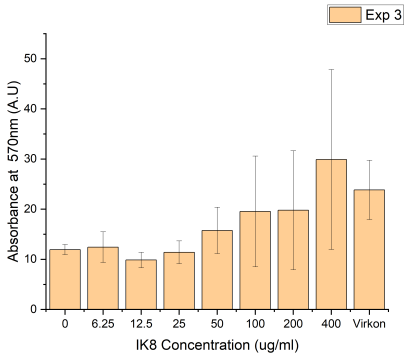

(c)

Figure 5.6: Three experimental repeats quantifying biofilm biomass after IK8 treatment by measuring the absorbance of Crystal Violet at 570 nm. Repeats shown in separate figures to emphasise the lack of reproducibility.

24 and 48 hour 2-species biofilms were incubated with IK8 for 3 and 24 hours. Neither incubation time showed bactericidal effect on either biofilm, **Figure 5.7**. For the 24 hour biofilm, a 3 hour incubation proved more effective as a reduction in cell density began at 100 μg/ml with a 78% reduction and showed a maximum at 800μg/ml with a 96% reduction. For a 24 hour incubation no substantial reduction was seen until 800 μg/ml showing a 99.6% reduction in cell density. This suggests that within 3 hours 100 μg/ml IK8 may start to take effect on biofilms, but if left to incubate for 24 hours the biofilm could recover and start growing again. There may also be poor penetration of IK8 into the biofilm which allows all remaining bacteria to recover and replicate over the 24 hour period. Increased penetration, a higher concentration, or longer incubation periods could all improve the efficacy of IK8.

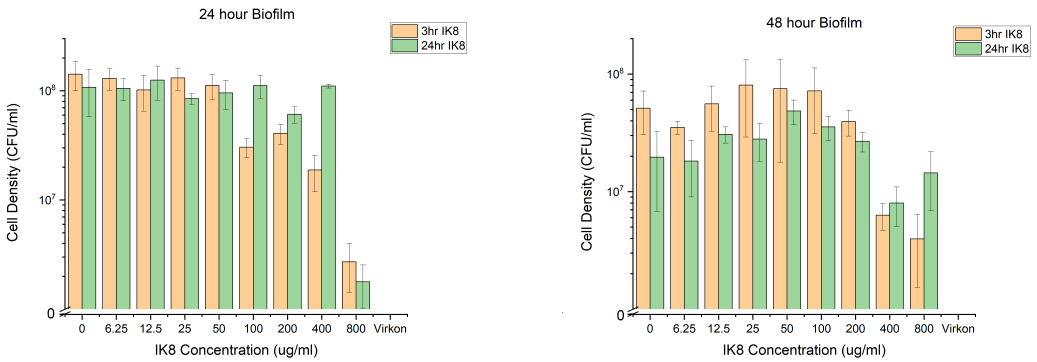

(a) **(b)**

Figure 5.7: Figures showing the cell density (CFU/ml) of 2-species *S.salivarius* and *A.naeslundii* biofilms at a) 24 hour and b) 48 hour biofilms incubated at 37°C with free IK8 for 3 hours (orange) and 24 hours (green). Results are an average of 6 wells.

2-species biofilms grown for 48-hours are more mature, denser biofilms with increased matrix contribution, therefore may respond differently to IK8 treatment. For biofilms incubated with IK8 for 3 and 24 hours, a decrease in cell density is only seen to begin at 400 μg/ml, however cell density increases again when IK8 is incubated for 24 hours, showing that IK8 is not able to inhibit the growth of biofilms for 24 hours. Compared to biofilms grown for 24 hours, 48 hour biofilms require a higher concentration of IK8 to induce cell due to the increase in extracellular matrix limiting IK8 penetration.

Cell density results show that free IK8 is not enough to cause any bactericidal effect

on 2-species biofilms, likely due to the inability to penetrate through the complex matrix - a problem well known with antibiotics. The efficacy of IK8 on planktonic bacteria was well demonstrated in **Section 2.7**, therefore IK8 itself is an ideal candidate in tackling antimicrobial resistance but faces the same challenges as antibiotics. An effective method of increasing antimicrobial uptake and penetration into the biofilm is to combine IK8 delivery with liposomes, microbubbles (MBs) and ultrasound (US). MBs and liposomes are used as a delivery vehicle for IK8 which can be released on demand with US, ensuring site specific delivery. Furthermore, the cavitation effect of MBs and US have been shown to disrupt and damage the surface of biofilms, increasing the therapeutic effect on biofilms [258, 259]. Longer incubation periods of IK8 only allowed the biofilm to recover and proliferate, therefore multiple rounds of IK8 treatments (with MBs and US) for short incubation periods may have a more successful bactericidal effect on 2-species biofilms. For the remainder of this chapter, 2-species biofilms grown for 24 hours are used in experiments.

5.4 Liposome Formation

5.4.1 Liposome fabrication

Liposomes contain Diyne-PC - a phospholipid containing photo-polymerisable diacetylene fatty acids. Liposomes which have been partially polymerised under UV have been shown to help with liposome stability, and also have the added benefit of being Raman active which offers the potential to track the encapsulated drug in a label free way [260, 261]. Both liposomes with and without Diyne-PC were used in the following experiments.

Liposomes were formed via extrusion as per **Section 2.5.1**. There were some problems that occurred during extrusion, such as loss of sample, and filters getting blocked making it impossible to push any sample through. This was the case for both liposomes with and without Diyne-PC. To prevent the sample leaking out of the block during extrusion, the syringes were replaced and when attaching to the block were twisted into

place to ensure complete attachment. This managed to solve the leakage problem.

Blockages and difficulty pushing through the sample began to occur every time liposomes were made. Firstly the sample was checked before extrusion to ensure the lipids were completely resuspended and no large clumps were visible which could cause blockages - this never appeared to be a problem. The metal extrusion block was pre-heated for longer so that it was definitely above the T_m of the lipids (55°C), and instead of just using a 400 nm filter, a 800 nm filter was first used to remove any large vesicles and aggregates which could cause blocking of the 400 nm filter. This approach did help to make extrusion easier. There was still quite large resistance when extruding, which may just be the nature of the lipids used, so the best approach was to push the syringes slowly which yielded a smooth and consistent batch.

Liposomes were stored a 4°C until needed. Dynamic light scattering (DLS) and particle-tracking were used to measure the size and concentration of the samples. Liposomes were approximately 106 nm in size and had a concentration of 2×10^{13} particles/ml, though the sample is poly-disperse with small concentrations of particles ¿ 200 nm,as shown in **Figure 5.8**.

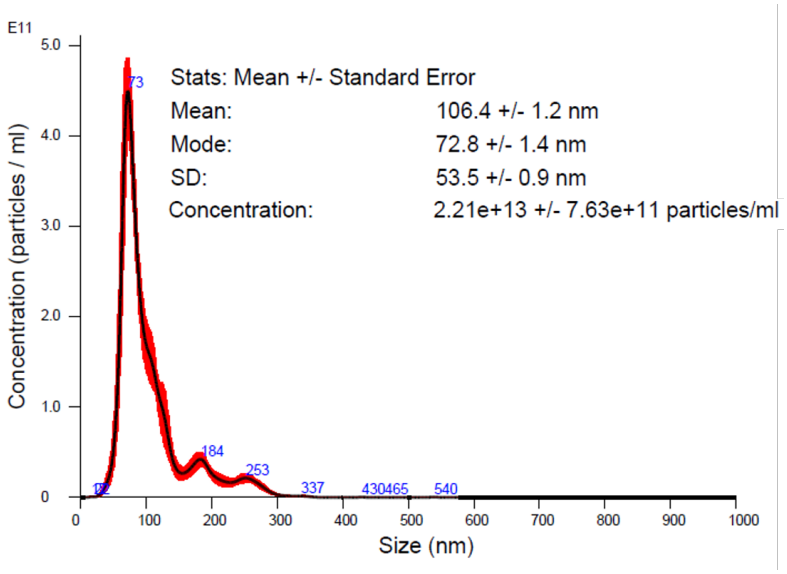

Figure 5.8: Example of a graph from particle tracking data used to find the concentration and size of Diyne-PC liposomes extruded at 60°C. Lipid mixture of DPPC:Diyne-PC:Cholesterol:Peg-2000 (molar ratio 32.5:32.5:30:5). The red shaded region shows the error.

5.4.2 Diacetylene Cross-linking

5.4.2.1 UV Polymerisation

Diacetylene, or Diyne-PC, polymerises at 254 nm, shifting from a blue to a red state, and corresponds to a visible colour change in the liposome sample from 'white' to 'red'. As this is a topochemical reaction were the monomers must be aligned in a crystalline lattice, the level of polymerisation is dependent on the packing of the monomers, as well as the amount of irradiation [262]. One crucial aspect of Diyne-PC is that the photosensitivity is dependent on its thermal history, such that it will lose sensitivity when heated above the transition temperature ($> 40°C$) and remain insensitive even when returned to room temperature, but will regain sensitivity when cooled to near 0°C [263]. Cooling the liposomes at $4°C$ for at least 10 minutes prior to UV exposure was therefore found to be a crucial part of the protocol. Without this step, no polymerisation would occur which was instantly noticeable as there would be no colour change in the sample.

A range of UV exposure times were tested and polymerisation quantified with UV-Vis and Raman Spectroscopy, as shown in **Sections 5.4.2.2** and **5.4.2.3** respectively. The aim for these liposomes was to achieve partial polymerisation which would be enough to aid in the stability of the bilayers and drug encapsulation, as research by Guoting Qin *et al* and Megha Goshi *et al* has shown, and also provide the distinct Raman signal [260, 264, 265]. Full polymerisation can have the opposite effect on stability, and has been used for triggered release from liposomes as the Diyne-PC phospholipids create pores in the bilayer releasing the encapsulated contents. Diyne-PC is thought to self assemble and create aggregates in the bilayer which shrink and cause defects in the membrane upon polymerisation, releasing the contents of the liposome [266–268].

5.4.2.2 UV-Vis Absorbance

Upon polymerisation of Diyne-PC, the absorbance peaks shift from blue to red state, showing an increase in peaks at 495 and 525 nm and decrease in peak at 600 nm, due

to the relaxation of the polymer backbone and shortening of the effective π conjugation chain length. It was anticipated that over exposure of UV could cause photodegredation damaging the chemical bonds. This is shown by a decrease in the absorption (and Raman) peaks, which is beginning to occur at the 90 min 525 nm peak in **Figure 5.9**.

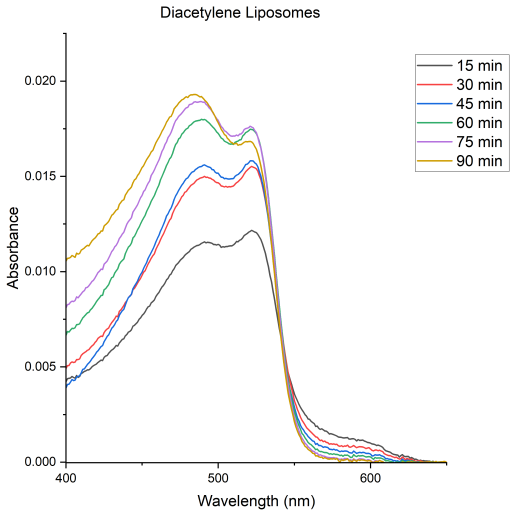

Figure 5.9: Absorbance spectra of Diyne-PC liposomes after 15-90 minute UV (254 nm) exposure. 0 minute UV exposure showed no absorbance peaks and was thus subtracted from all spectra as a baseline.

5.4.2.3 Raman spectroscopy

Raman spectra of Diyne-PC show an increase in C=C and C≡C bonds after polymerisation, corresponding to Raman peaks at 1510 and 2110 $cm^{-}1$ respectively. These peaks lie within the 'silent region' of biological Raman spectra, making them very clear, noticeable peaks [269].

The Raman intensity of Diyne-liposomes exposed to UV for varying lengths of time is shown in **Figure 5.10**. It was expected that longer polymerisation would show as increased Raman intensity, however the results show 15 minutes as the maximum intensity, after which the overall intensity decreases yet consistent fluctuations are seen, which has not been seen in the literature thus it is unlikely to be of true significance. The decrease

in Raman intensity could be due to the degradation of some polymer chains, which are then replaced after after another 15 min polymerisation causing an increase in intensity again.

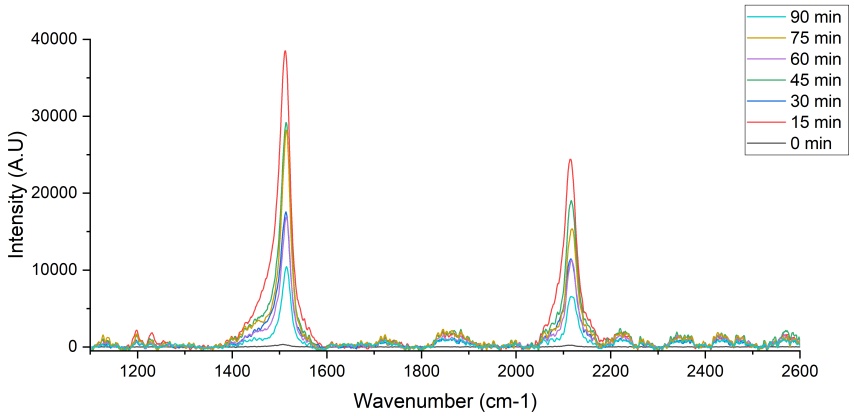

(a)

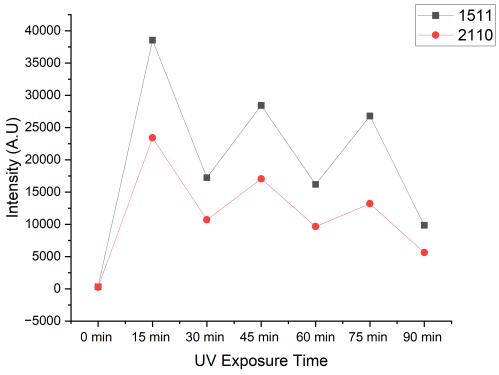

(b)

Figure 5.10: Figures showing a) the Raman spectra for Diyne-liposomes irradiated for 0-90 mins, b) scatter plot showing the intensity for 1511cm^1 (black) and 2110 cm^1 (red)for UV exposure time

5.5 Fluorophore Leakage Assay

5.5.1 Calcein characterisation and self quenching

A fluorophore leakage assay is a standard method of assessing the passive leakage from vesicles by encapsulating a fluorophore such as calcein, which self-quenches at high concentrations, but then fluoresces as it is released from the vesicle at low concentrations (**Figure 5.11**).

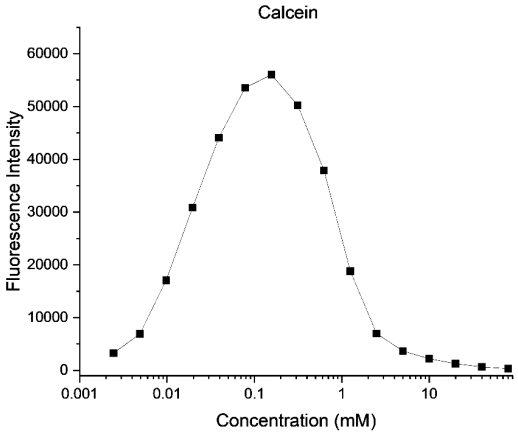

Figure 5.11: Calcein calibration curve demonstrating the self quenching behaviour at high concentrations. Calcein dissolved in PBS at room temperature.

5.5.2 Problems and troubleshooting

A standard protocol was followed as described in **Section 2.5.2**, and successfully demonstrated in similar work by J. Tinkler and S. Moorcroft , however unexpected problems arose[2, 4]. In order to keep calcein in solution at high, self-quenching, concentrations of NaOH was added, raising the pH to 12. When this calcein solution was added to the lipids to re-hydrate, the lipids would clump and become gel-like. Fresh lipids and calcein were also tested, and the fluorophore changed to carboxyfluorescein (another commonly used fluorophore assays), but the problem still persisted. The high pH of the calcein solution was found to be the problem, but reducing the pH would cause calcein to fall out of solution. There is no literature mentioning this problem, or how to achieve

self-quenching calcein at pH 7 despite it commonly being used. This problem is also potentially specific to DPPC lipids, as J. Tinkler and S. Moorcroft both used DSPC as the primary lipid component (all other factors in the protocol were the same) and found no problems with this assay. DPPC lipids were used in this thesis as previous work with L. Marsh, a collaborator at the University of Oxford, had used DPPC:Diyne-PC liposomes. The same liposome protocol was used (and slightly modified) for work in this thesis as experiments during that collaboration had shown successful UV polymerisation and Raman effects with the DPPC:Diyne-PC lipid composition [270].

Due to time limitations and prioritising experiments, this assay was never completed. In future work, DPPC could be replaced with DSPC, or the problem with pH could solved by reversing the assay so that a decrease in fluorescence is measured during leakage by encapsulating calcein in a fluorescent state which is then quenched upon release by cobalt chloride [271].

5.6 IK8 Loaded Liposomes

5.6.1 Encapsulation efficiency

The amount of IK8 encapsulated within liposomes was quantified using HPLC. Liposomes were prepared with and without Diyne-PC for comparison at a concentration of 5.5×10^{12}/ml and size of 110 $\pm$12 nm, lysed with 1% Triton-X, and diluted 5 times for analysis, as described in **Section 2.6.5**. The chromatographs for liposomes with and without Diyne-PC show a small IK8 peak after 1.6 and 1.8 mins, which can be seen in **Figure 5.12a and b** respectively. The large peak at 4 mins is due to the presence of Triton-X in the sample. The area under the IK8 peaks was calculated and the IK8 encapsulation was found to be 31.8 μg/ml for diyne-liposomes and 205.92 μg/ml for no diyne liposomes, taking into account sample dilution and injection volume. This corresponds to an encapsulation efficiency of 0.64% and 4.12%, respectively. For non-diyne liposomes, this is lower than the IK8 encapsulation efficiency found by J. Tinkler, 5.9%, both of which are considerably lower than that found by S. Moorcroft, 15% (despite the

conditions for J. Tinkler and S. Moorcroft being exactly the same) [2, 4].

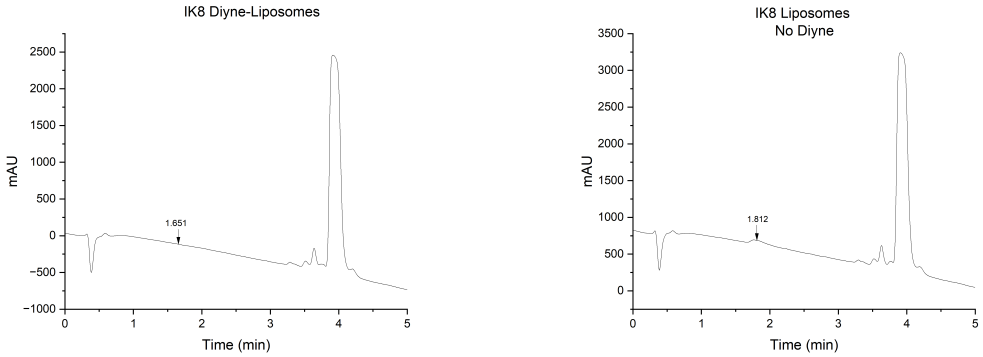

(a) **(b)**

Figure 5.12: HPLC chromotographs showing IK8 peaks for a) Diyne-liposomes (1.651 min) and b) no diyne liposomes (1.812 min).The large peak at 4 mins is Triton-X.

Liposomes with Diyne-PC have a much lower encapsulation efficiency, likely due to IK8 leaking out of the liposome. When forming the lipid bilayer during liposome formation, it has been shown that rather than DSPC and Diyne-PC assembling in a 1:1 formation, it is more likely that Diyne-PC will form clusters, thus during polymerisation these bonds shrink and creating pores in the bilayer, releasing its contents. This is the mechanism for triggered release therapeutics, however it was anticipated during these experiments that a UV exposure of 15 mins was long enough to partially polymerise and provide added stability to the liposomes, however 15 mins may prove too long. Going forward liposomes without Diyne-PC were used in biofilm treatment experiments to maximise the deliverable amount of IK8.

5.7 Biofilm Treatment with Microbubbles, IK8 Liposomes and Ultrasound

Free IK8 treatment of 2-species biofilms was previously shown in **Section 5.3.3** to start taking effect at 100 μg/ml and show a maximum of a 1-log reduction in cell density at 800 μg/ml with a 3 hour incubation period. The effectiveness of IK8 against biofilms

would be increased if it could penetrate further into the biofilm. MBs and US are increasingly being used for biofilm treatment and drug delivery due to the sonoporation effects damaging the surface of the biofilm and allowing for deeper penetration and delivery of drugs into the biofilm [175, 259]. Ultrasound alone has shown to break down the biofilm, so combined with microbubbles and ultrasound, it is hypothesised that the effectiveness of IK8 will be increased.

IK8 is a peptide which is degraded by enzymes in the blood, so loading it into a liposomes is a way of protecting the peptide and safely delivering it to the intended site. As this thesis is working on oral biofilms, an area of the body which is directly accessible, the degradation of IK8 may not be an issue in practice, though bleeding gums are a common issue with poor oral health. Despite this, using a loaded liposome to deliver the IK8 may have the added benefit of extra sonoporation effects on the biofilm, and US may propel the liposomes further into the biofilm allowing for deeper delivery. Liposomes in these experiments are not attached to the MBs, however this is an option and allows for specific targeted drug delivery. In the following experiments 2-species biofilms were grown for 24 hours in well plates, and the following treatment conditions were compared: untreated, MBs+US, free IK8 + US (1 treatment), free IK8 + US (3 treatments), IK8 Liposomes+MBs+US (LMBUS) (1 treatment), LMBUS (3 treatments), 1% Virkon (positive kill control). Three analysis methods were used: Live/Dead stain for confocal z-stack images and fluorescent intensity measurements to quantify dead cell death, crystal violet stain to quantify biomass, and agar plates to measure cell density (CFU/ml).

5.7.0.1 Microbubble production

MBs (DSPC:Peg-2000, 95:5 mol) were prepared as described in **Section 2.4** via mechanical agitation no more than 30 minutes before biofilm treatment. Images of MBs were taken to assess their size and concentration, which was determined using MATLAB code, examples of which can be seen below in **Figure 5.13**. Previous work by J. Tinkler had found that a MB concentration of $5\times\ 10^8$ ml^{-1} and 2 seconds of US at 2.25MHz,

would achieve 94% MB destruction in well plates, anything higher would only achieve 89% and show visible MB clustering [2]. For all biofilm treatments, MBs were therefore diluted so that the final concentration in the well was $5\times10^{8}\text{ml}^{-1}$. The average MB size was 1.5-2 μm.

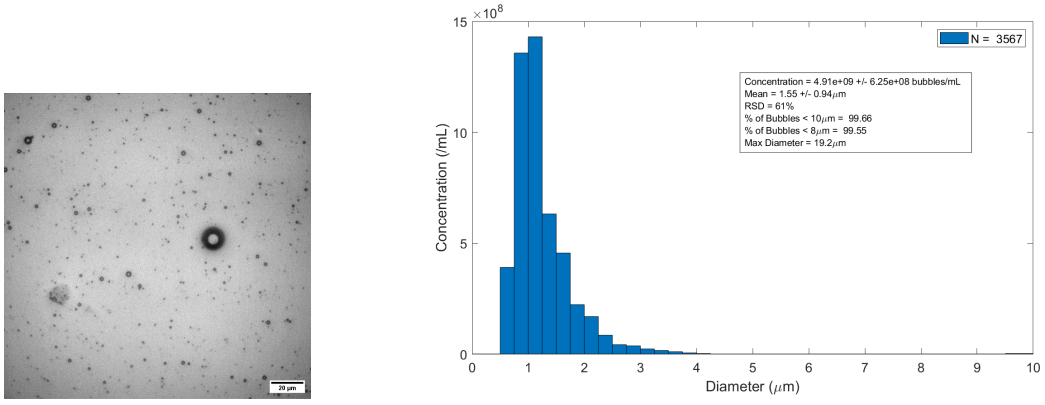

(a) **(b)**

Figure 5.13: a) Example image of MBs (DSPC:Peg-2000, 95:5 mol) taken with 40x obj, diluted 25 times, b) histogram showing size distribution and concentration of the MB sample.(1.55μm, 4.9×10^{9}MB/ml). Sample taken 15 minutes after MB production.

For biofilm where 3 repeat treatments were required over 3 hours, the same sample of MBs was used. MB stability was measured over the course of 4 hours to ensure MBs were of consistent sizing and concentrations. **Figure 5.14a** shows the concentration remains approximately stable over 4 hours at around 1×10^{9} MB/ml, and while **Figure 5.14b** shows the MB size also remains at approx 1.5μm, the standard error doubles by hour 4. The size and concentration within 3 hours was deemed consistent and acceptable for the same sample of MBs to be used for repeated treatments.

5.7.0.2 Liposome deliverable dose of IK8

From the previous HPLC results in **Section 5.6.1**, it was found that 1 ml of liposomes at concentration 2 $\times10^{13}$/ml, size 106 nm containing no Diyne-PC, encapsulated 206 μg/ml of IK8 - this represents the maximum deliverable dose possible. When free IK8 was incubated for 3 hours with 24 hour biofilms, a decrease in cell density started to happen at a concentration of 100 μg/ml (**Section 5.3.3.2**), thus a deliverable dose of

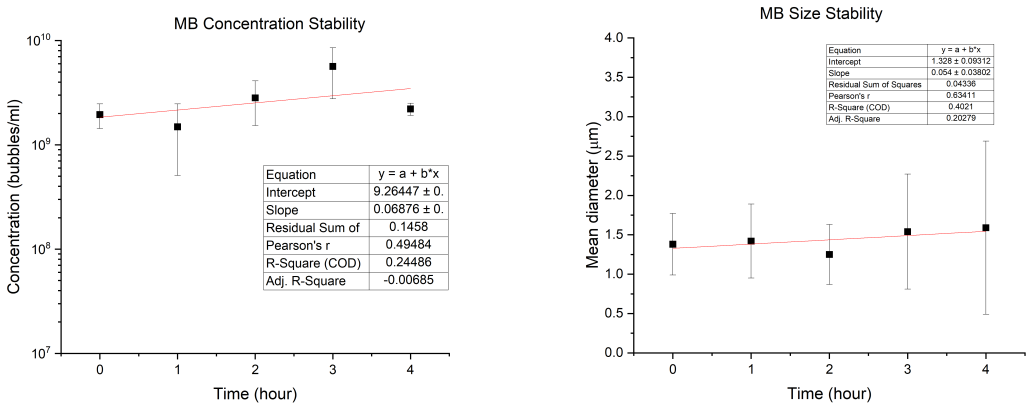

(a) **(b)**

Figure 5.14: MB stability showing a) the concentration and b) the size over 4 hours, with error bars showing the standard error. MB lipids: DSPC:Peg-2000, C_4F_10 gas core, room temperature.

100 μg/ml IK8 was anticipated to be sufficient to have an effect when combined with MBs and US, and maximised sample usage across all experiments.

5.7.0.3 Biofilm Treatment

2-species biofilms grown for 24 hours were exposed to 7 different treatments: untreated, MB+US, Free IK8 + MBs (x1), Free IK8 (x3), liposomes, MBs and US (LMBUS) (x1), LMBUS (x3), or 1% Virkon. Free IK8 on biofilms was already tested and shown in **Figure 5.7** to have a 78% reduction in cell density. Free IK8 + MBs was not included as a control in this experiment to save time and resources as this scenario would be unlikely to ever be used in clinic. For all experiments, the total dose of IK8 delivered to the biofilms was 100 μg/ml. For liposomes, the total dose encapsulated and delivered to the biofilm was 100 μg/ml, assuming all contents were released (which may not be the case). It has been demonstrated that multiple treatments of IK8 and MBs + US can have a greater impact than a single exposure, and multiple rounds of treatment is more clinically representative [2]. Some biofilms had one exposure and were incubated for 3 hours, while some had 3 exposures within the 3 hour incubation period - one every hour. The IK8 incubation period between each exposure is shorter (only 1 hour) but this is

expected to be offset by the benefit of multiple exposures.

The cell density of biofilms post treatment were counted and results of one experimental repeat (average of 3 wells) are shown in **Figure 5.15**. Free IK8+MBs+US shows the greatest decrease in cell density of all treatment methods, 62%, though there is no difference between 1 and 3 exposures. This is less than the 78% reduction in cell density reported in **Section 5.7** for 100 μg/ml free IK8, but is within the range of the standard deviation. There is no expected reason that MBs and US should have a negative effect on free IK8, thus it would be expected that if the MBs+US had no effect, the free IK8 would still obtain similar results to those found previously. One exposure of LMBUS shows no change in cell density compared to the untreated wells, but shows a small decrease after 3 exposures, however this is approximately the same reduction as just MB+US. LMBUS appears to have the least effect of all treatment methods, potentially due to IK8 not being released from the liposomes or having enough time to treat the biofilm.

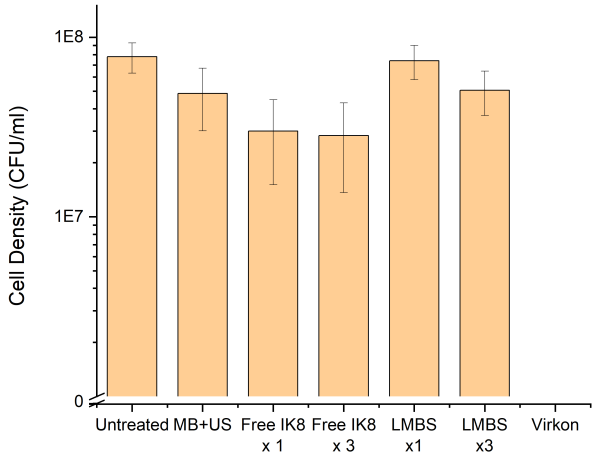

Figure 5.15: Cell density (CFU/ml) of biofilms after no treatment, MB+US, Free IK8+MBs+US x1 exposure, Free IK8+MBs+US x3 exposure, liposomes+MBs+US (LMBUS) x1 exposure, LMBUS x3 exposure, 1% Virkon.

Confocal images of live/dead stained 2- species 24 hour biofilms were taken after each treatment to visualise the effect of IK8 and MBs+US. **Figure 5.16** shows z-stack images of control biofilms: untreated and treated with 1% Virkon. Untreated biofilms

were dominated by live (green) bacteria with some areas of dead cells as expected, while those treated with Virkon are mostly dead (red).

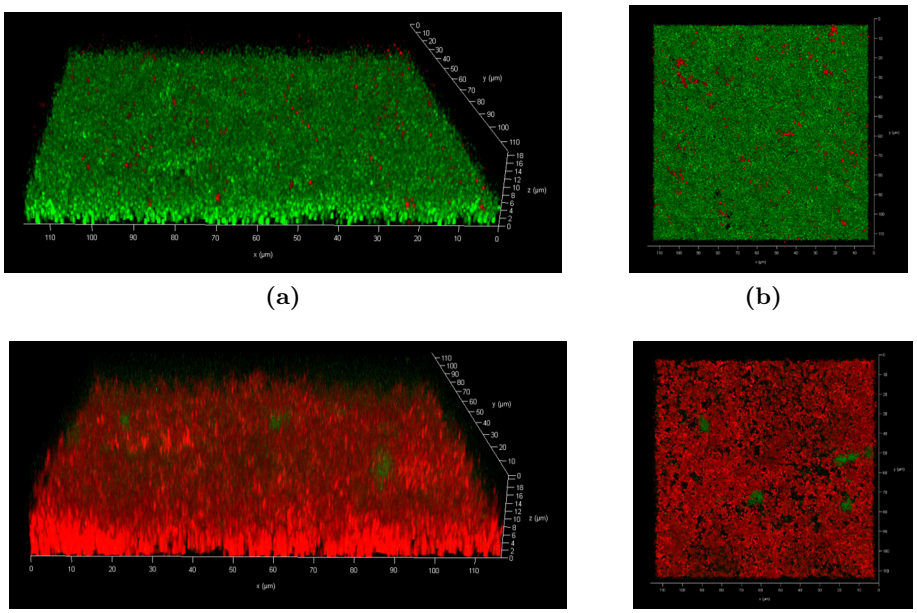

(a) **(b)**

(c) **(d)**

Figure 5.16: Confocal images of Live (green)/Dead (red) stained 2 species biofilms after treatment. Untreated biofilms (a,b) and treated with 1% Virkon (c,d). Z-stack images taken on 100x oil objective, 115x115x20 μm. b) and d) show the top of the biofilm z-stack. Biofilms grown for 24 hours.

Images after MB+US treatment can be seen in **Figure 5.17 a) and b)**. There is an increase in dead bacteria compared to untreated biofilms, but shows a similar profile to Free IK8+MBs+US 1x exposure, in **Figure 5.17 c) and d)**. Free IK8+MBs+US 3x exposure in **Figure 5.17 e) and f)** shows an increase in dead bacteria in a more uniform layer across the surface of the biofilm. The repeated exposure may help damage the biofilm and break down larger aggregates into smaller free bacteria.

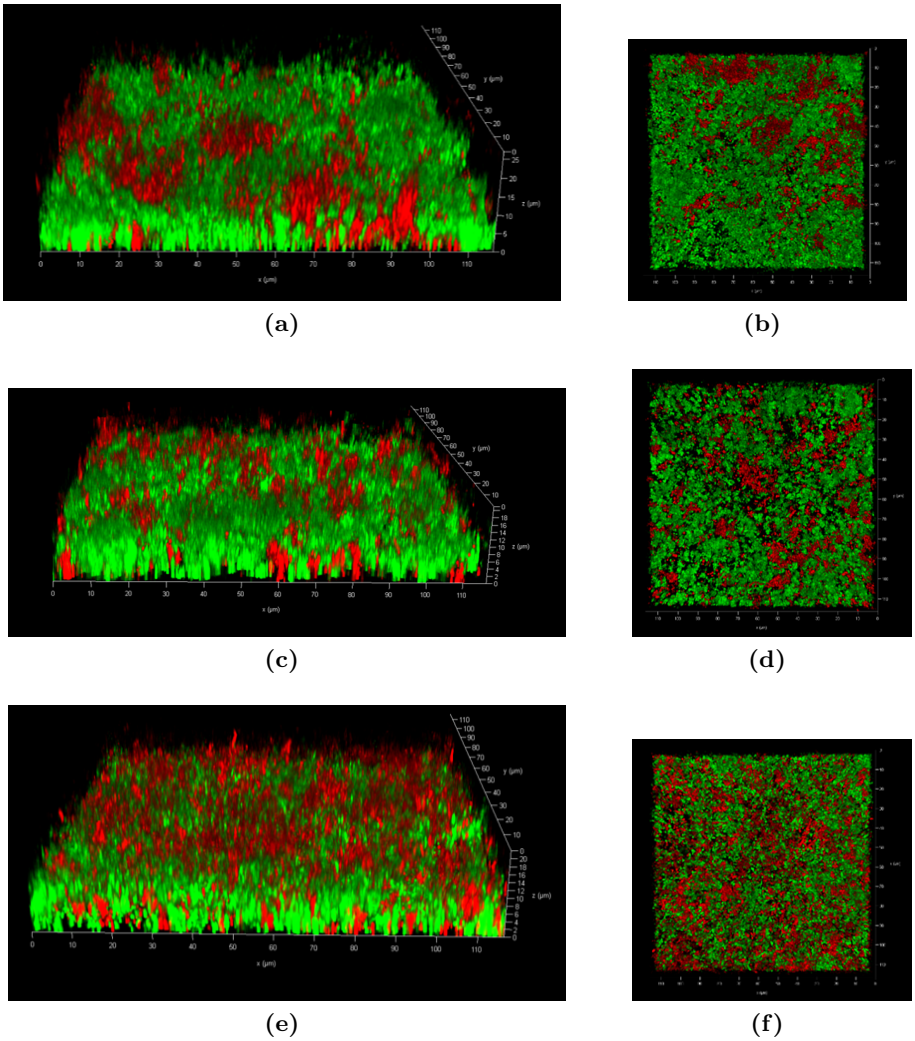

Figure 5.17: Confocal images of Live(green)/Dead (red) stained biofilms after treatment. MBS+US (a,b), Free IK8+MBS+US x1 exposure (c,d). Free IK8+MBS+US x3 exposure (e,f). Z-stack images taken on 100x oil objective, 115x115x20 μm. b), d) and e) show the top of the biofilm z-stack.

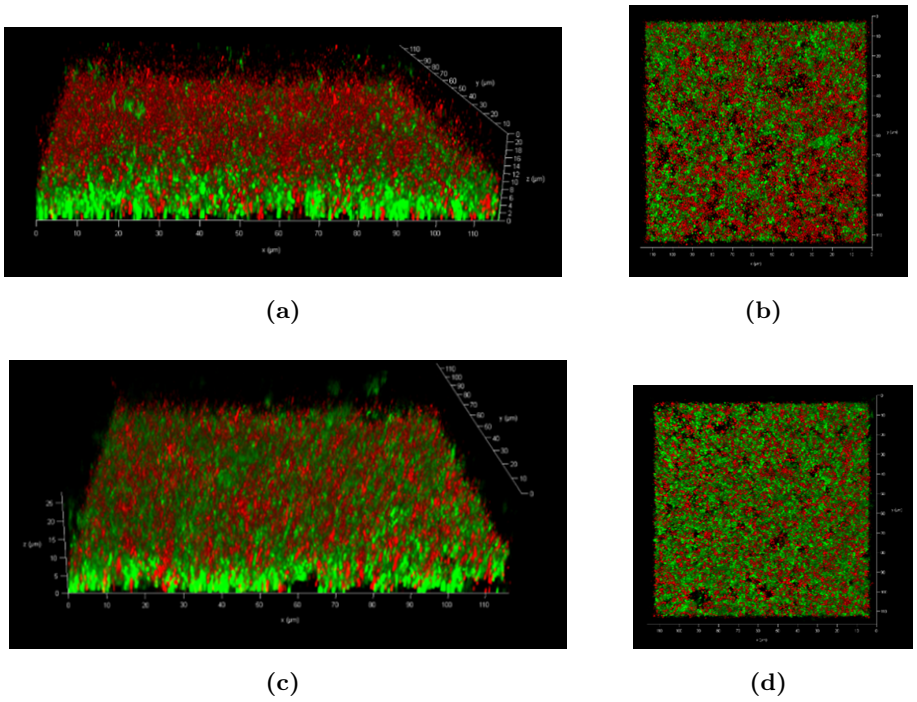

Figure 5.18: Confocal images of Live(green)/Dead (red) stained biofilms after treatment. LMBUS x1 exposure (a,b), LMBUS x3 exposure (c,d). Z-stack images taken on 100x oil objective, 115x115x20 μm. b), d) show the top of the biofilm z-stack.

Similar to the images of Free IK8+MBs+US x3 exposure, both LMBUS x1 and x3 exposure show a layer of dead bacteria on the top of the biofilm **Figure 5.18**. LMBUS x1 exposure appears to have a significant amount of dead bacteria on its surface, which is contrary to the cell density results which found there was relatively no change in cell density compared to untreated biofilms. The image also shows more dead bacteria than LMBUS x3 exposure, which the cell density results showed had a greater decrease, i.e more dead. Dead bacteria from LMBUS x3 exposure may have detached and washed away during the rinsing process before imaging.

Confocal imaging is a useful tool in visualising the how different treatments effect biofilms, however on its own is not enough to quantify dead bacteria or accurately claim the resulting effects. Multiple images were taken across each biofilm and the images presented for this work were deemed a good average representation of the biofilm.

A third method of quantification was to measure the biomass after crystal violet

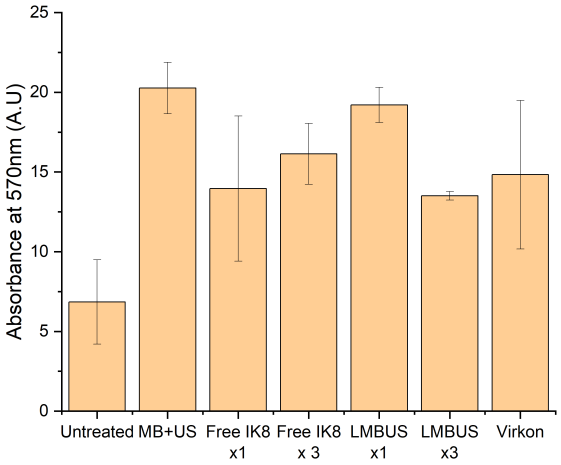

Figure 5.19: CV absorbance at 570nm for biofilms after no treatment, MB+US, Free IK8+MBS+US x1 exposure, Free IK8+MBS+US x3 exposure, LMBUS x1 exposure, LMBUS x3 expsure, 1% Virkon. The results are the average of 3 wells from 1 experimental repeat.

staining. As with previous experiments, the results, shown in **Figure 5.19**, are inconsistent and show no trend, particularly as the untreated biofilm is showing a much lower biomass than the treated biofilms. For these experiments where a pre-existing biofilm is being treated, CV staining is not a useful method of analysis.

One of the limitations of this experiment is that US was applied to the biofilms from underneath as this was the only feasible way using a well plate. Applying US from above would force the MBs down towards the surface of the biofilm, rather than away from the surface as carried out here. For MBs to have the greatest impact on a biofilm research has shown that the distance between the MB and biofilm surface should be no more than 0.68 the diameter of the MB, thus approx 1μm in this case [161]. Although US was applied immediately after MBs were added, MBs will rise thus reducing their impact on the biofilm. Having targeted MBs which bind to the biofilm would be extremely beneficial and increase the biofilm disruption from MBs alone, as well as potentially increase IK8 uptake.

5.8 Chapter Conclusions

This chapter has explored how antimicrobial peptides such as IK8 can be used as an effective treatment against 2-species biofilms, and how using a delivery system of liposomes, microbubbles and ultrasound may increase cell death. This is the first report of using the synthetic IK8 peptide against 2-species biofilms, and the first method of using liposomes, MBs and US as a treatment for oral biofilms. The effect of IK8 on both planktonic species was first assessed by finding the MIC and MBC: 100 and 12.5 μg/ml (MIC), 100 and 25 μg/ml (MBC) for *S.salivarius* and *A.naeslundii* respectively, and a time-kill study found IK8 had a bactericidal effect after 2 hours. Once it was found that IK8 was successful in treating planktonic bacteria, IK8 was incubated for 3 or 24 hours with 2-species biofilms (of either 24 or 48 hour growth). Counting the cell density (CFU/ml) of biofilms after treatment was found to be the best method of quantification, as fluorescent intensity of propidium iodide (dead bacteria) and CV staining proved unreliable. IK8 treatment of biofilms incubated for 3 hours had the best results, showing a maximum of a 1-log reduction at 800 μg/ml, though a decrease began at 100 μg/ml.

Combining loaded liposomes, microbubbles and ultrasound has been shown to damage the surface of biofilms and increase the penetration of antimicrobials into the biofilm, so the next part was to compare the effect of different treatment methods on 2-species biofilms. Liposomes with Diyne-PC in the bilayer increased leakage of IK8 due to the pores created in the bilayer during polymerisation, thus standard liposomes without Diyne-PC were used and had an encapsulation efficiency of 4.6% or 206μg/ml of IK8. This encapsulation efficiency is quite low and in future works should be investigated further. The deliverable dose of IK8 to each biofilm via liposomes was 100 μg/ml. It was found that free IK8+MBs+US had the greatest decrease in cell density after treatment (62%), however there was no difference between 1 or 3 exposures, and this is less than the 78% reduction found previously from free IK8 on biofilms. LMBUS after 1 exposure showed no change in cell density compared to untreated biofilms, while after 3 exposures a 35% decrease was seen. Confocal images showed similar trends, interestingly showing that both after free IK8+MBs+US x3 and LMBUS treatments there was a layer of dead

bacteria on top of the biofilm, suggesting an increase in breakdown of the biofilm at the surface.

The results of cell density show that incorporating a MBs + US into the delivery system does not increase bacterial cell death within the biofilm. While it is still believed and proven that MBs and US does have a positive impact on biofilm treatment, more research and an improved experimental set up is required to obtain these results. Treatments were limited by the application of US from below, lack of MB binding to the surface, and still relatively low encapsulation of IK8 into liposomes.

Chapter 6

Conclusions and Future Work

6.1 Conclusion

The aim of this work was to use microfluidics as a biofilm growth method to characterise multi-species oral biofilms over time using Raman spectroscopy (RS), and to offer an alternative to antibiotic treatment using microbubbles (MBs), ultrasound and antimicrobial peptides. The 2-species oral biofilm was used in this thesis as a model to test the capabilities of RS as a non-destructive method of real-time biofilm analysis, and the effectiveness of MBs as a treatment option. Oral biofilms, if left untreated can lead to periodontitis which is a significant public health problem, though perception of this is still relatively low. Periodontitis affects over 1 billion people world wide, creating a large economic burden, social inequalities, and is linked to many non-communicable diseases such as diabetes mellitus, cardiovascular disease, Alzheimer's, and adverse-pregnancies [272]. Generally, periodontal diseases can be controlled first and foremost with good oral hygiene habits, regular tooth cleaning and plaque removal via scaling and root polishing. Nevertheless, greater understanding of oral biofilms is therefore pivotal in combating this pubic health concern so that pathogenic biofilm formation can be prevented, or subsequently caught in the early stages so treatment, where necessary, can be started as soon as possible. Most current methods of biofilm analysis are destructive and do not allow for

real-time characterisation of the same biofilm over time, therefore RS and microfluidics is presented here as a new alternative method.

Biofilms are difficult to treat, being up to 1000x less susceptible to antibiotics than planktonic bacteria, often requiring mechanical removal particularly in the oral cavity where biofilms form dental plaque [16]. Antimicrobial resistance is another public health concern making the treatment of biofilms more difficult. Over exposure and misuse of antibiotics are causing a rapid increase in resistant strains of bacteria, therefore alternative methods of treatment are being sought as a result. MBs and ultrasound have already been shown to aid in biofilm destruction and removal and when loaded with therapeutic antimicrobial peptides, MBs can be used for site specific drug delivery and biofilm treatment [2, 172].

The work described in Chapter 3 develops a method of growing *S.salivarius* and *A.naeslundii* 2-species oral biofilms, under constant flow, using microfluidic devices. By using microfluidics, these biofilms could be analysed every day for 5 days using spontaneous RS. The microfluidic growth system was initially designed using a piezo-pump, making the system small and compact and able to fit inside an incubator. However, the piezo-pump was not able to withstand the low flow rates (and subsequent high back pressures) required, therefore a syringe pump was used to drive the flow, proving consistent and reliable. The final microfluidic design was simplified to a straight channel with two inlets, one for constant media flow and one for bacteria injection (and any other additions such as fluorescent stains or buffer). Air bubbles were the one main factor that had the potential to disrupt the biofilm growth. These were kept to a minimum by removing any bubbles via the injection loop, and ensuring all media were at 37°C prior to injection on chip. Nevertheless, some air bubbles were still present, likely due to air seeping in through the connecting taps.

RS was able to successfully compare and identify planktonic *S.salivarius* and *A.naeslundii* via individual peaks and principle component analysis (PCA). *S.salivarius* had distinct peaks at 850, 980, 1414 and 1604 cm^{-1}, compared to *A.naeslundii* with distinct peaks at 748, 1127 and 2850 cm^{-1}. Following planktonic analysis, RS was used

on chip to analyse mono- and 2-species *S.salivarius* and *A.naeslundii* biofilms over the course of 5 days. For each biofilm significant peak intensities were tracked over time, showing for *S.salivarius* biofilms the greatest increase in DNA, proteins and lipids were seen between Day 3 - 5. For *A.naeslundii* this was seen between Day 4 - 5. When subtracting the planktonic spectra from the mono-species to just identify the extracellular matrix components, both species had a clear peak at approximately 2905 cm^{-1} which could be used henceforth as matrix identifier. *S.salivarius* had additional peaks at 2850 and 2881 cm^{-1}, unique to the matrix of this species. Both species lacked the 2937 cm^{-1} peak which was present in planktonic, therefore the CH_3 2937 cm^{-1} protein peak is considered to signify the bacterial cells in the biofilm.

Linear discriminant analysis (LDA) was used to compare 2-species biofilms at Day 1, 3 and 5, and to mono-species biofilms. Day 1 2-species biofilms are distinct from Day 3 and 5, which are very similar with increased DNA, lipid and protein contributions - as expected from the matrix. When comparing 2-species biofilms to mono-species, it is clear from the LDA that 2-species biofilms are not simply the sum of the individual mono-species biofilms. The 2-species biofilm has unique characteristics due to inter-species interactions, which causes a separation of the biofilm LDA clusters. The LDA results suggest the Day 1 2-species biofilm is most similar to *S.salivarius*, whereas by Day 5 the biofilms shows features of both species with LD1 and LD2 positive loadings showing peaks at 600 - 750, 747, 1003, 1000 - 1100 and 2960 cm^{-1}.

A limitation of the work in Chapter 3 was that the results were an average of RS across the whole biofilm, and didn't consider the variations that occur within the biofilm. Furthermore, spontaneous RS has limited spatial resolution, long acquisition times, and mapping of areas proved unreliable due to drift. Therefore another RS method, Stimulated Raman Spectroscopy (SRS), was pursued in Chapter 4 which was able to provide high resolution hyperspectral SRS images, SRS z-stacks, and two-photon fluorescence (TPF) z-stacks of biofilms at a fraction of the time of spontaneous RS. This novel method of on-chip biofilm characterisation compared the high wavenumber region, 2740 - 3084 cm^{-1}, for mono- and 2-species biofilms at Day 1 and 5, though samples were fixed in advance of transport to the University of Exeter where experiments took place.

SRS provides a great amount of data which can be presented in numerous ways. For consistency of analysis across datasets, k-means clustering proved a reliable and time efficient method of hyperspectral analysis and is thus recommended for this style of biofilm analysis. By comparing k-means clusters for each biofilm species on Day 1 and 5, along with the SRS hyperspectral images, both species demonstrated 2937 cm^{-1} is a marker of bacteria cells in the biofilm. *S.salivarius* in particular had more peaks associated with the matrix, notably CH_2 2850, 2881, and 2905 cm^{-1}, and had areas of biofilm that appeared to be just matrix and no bacteria. 2-species biofilms on Day 1 demonstrated similar spectra features to *S.salivarius* biofilms, and even showed areas of biofilm which appeared to be just *S.salivarius*, showing a domination of this species on Day 1. Though SRS was not able at this stage to confidently locate individual species within the 2-species biofilm, fluorescent *in situ* hybridisation (FISH) biofilms were also analysed which showed the distribution of each fluorescently labelled species within the biofilm, and confirmed that on Day 1, 2-species biofilms appears to be *S.salivarius* dominant. SRS and FISH analysis also demonstrated that by Day 5, 2-species biofilms are thick and densely populated with both species, and have high density regions along the outer edges of the biofilm closest to the nutrients. The visual images SRS provides along with the spectra provides great information and helps visualise how the biofilm may be evolving and changing over time.

TPF was also used as a complimentary tool in visualising the bacterial species within the biofilm. TPF located the autofluorescence of flavins, which are a part of the metabolic process, and located within the bacterial cell, though have been shown to secrete into the matrix. As the biofilms were fixed, it was not possible to use the autofluorescence to understand the more about the metabolic process of the biofilm and how it changes with growth or species development, therefore in this chapter the fluorescence was just used to locate the bacteria. Furthermore, it is known that the autofluorescence of dead bacteria is lower than live, but it was unclear how this changed for *S.salivarius* and *A.naeslundii* specifically, and whether bacteria embedded within the matrix maintained their fluorescence better than those exposed on the surface. Nevertheless, TPF was an valuable method of biofilm analysis, and supported SRS z-stacks and FISH results

showing that the greatest density of bacteria is found in the bottom half of the biofilm.

Chapter 5 explores using MBs, US and synthetic antimicrobial peptides (IK8) as a novel method of treating 2-species oral biofilms. Individually, MBs, Ultrasound (US) and IK8 have been shown to effectively treat biofilms and have a bactericidal effect, however the work in this chapter needs optimising to have similar results. IK8 was demonstrated to work against planktonic *S.salivarius* and *A.naeslundii*, having a MIC of 100 and 12.5 μg/ml and MBC of 100 and 25 μg/ml, respectively. The bactericidal effect occurred after 2 hours incubation. For IK8 testing on biofilms, biofilms grown for 24 hours were used and cell density quantification was the preferred method of analysis. It was found that biofilm incubation with IK8 for 3 hours had the best results, showing a 1-log reduction at 800 μg/ml. This however, does not achieve the 3-log reduction required for something to be considered bactericidal. Combining IK8 with MBs and US, and loading IK8 into liposomes was thought to increase this effect.

Initially, Diyne-PC liposomes were trialled as it was thought the Raman properties of Diyne-PC would allow tracking of the liposomes once they had been applied to the biofilm. This would show details on how well liposomes and MBs attach and penetrate the biofilm surface. While in some instances this may have worked, Diyne-PC liposomes had a much lower encapsulation efficiency of IK8 compared to liposomes with no Diyne-PC, likely caused by the polymerisation of the polymer causing pores in the bilayer. Liposomes with no Diyne-PC were therefore used, but still only reached an encapsulation efficiency of 4.6%, or 206 μg/ml of IK8. The maximum deliverable dose for encapsulated liposomes ws 100 μg/ml. Treatment of biofilms included: untreated, free IK8, free IK8+MBs+US (1x and 3x exposures), IK8 liposome+MBs+US (1x and 3x exposures) (LMBUS). It was found that free IK8+MBs+US produced the greatest decrease in cell density, 62 %, but there was no difference between 1x and 3x exposures. Confocal images showed after treatment a layer of dead bacteria on the biofilm surface, showing the destructive effect of the treatment. The treatment results in Chapter 5 show the beginnings of how synthetic IK8, MBs and US can be used for 2-species oral biofilm treatment, though further experiments and optimisation is required to reach its full potential, which were unable to be performed here due to time constraints.

6.2 Future Works

Chapter 3 saw the use of spontaneous RS for the characterisation of on chip oral biofilms. When using this technique for biofilm analysis in the future, the areas of analysis should be split into the regions of biofilm (inner edge, middle other edge, top, bottom, etc) rather than taking the average spectra from random points across the biofilm. The variation that occurs within the biofilm on each day will go further in explaining what is causing the day to day biofilm variation. As spontaneous RS did not have the capability to do Raman maps or z-stacks, along with the limitation of long acquisition times, for this technique it is therefore ideal to have a more specific approach with clear objectives in mind, rather than starting broad and trying to deduce conclusions from the average results. Furthermore, Raman spectra of dead biofilms should also be taken to see how spectra differs from live bacteria, and if dead species can therefore be identified within the growing biofilms.

The microfluidic growth system could be improved to include more chambers on the devices to maximise throughput. Although uneven growth can sometimes be a factor in these devices, incorporating a 'pre-chamber' as described by Blanco-Cabara *et al* can result in uniform growth across three chambers on one device [91]. For future works where the number of species within the biofilm is increased and anaerobic biofilms are grown, the system will be required to be inside an anaerobic chamber. It is important therefore that appropriate syringe pumps are used which can withstand the temperature and humidity of the chamber.

For work in Chapter 4 using SRS to characterise biofilms, the main objective would be to use this method on live biofilms to gather real time, *in situ* biofilm images. This could be compared to the fixed biofilms and a comparison drawn from the spectra of live and dead biofilms. If it were possible, performing SRS using equipment that allowed the full spectra to be taken, rather than just the high wavenumber region, would provide a great amount of high resolution detail about the biofilm and allow species identification and direct monitoring of the biofilm and how it changes over time. TPF on live biofilms would also provide information about the rates of metabolism in different areas

of the biofilm and across the days, as flavin autofluorescence is known to increase when metabolism increases. Furthermore, when treating biofilms with IK8, the effectiveness of the treatment could be monitored and quantified using TPF as research has shown that when under stress from antibiotics, bacteria increase their metabolic rate in response, producing more flavins and thus increasing their autofluorescence. This method would be a quick, non-destructive way of measuring treatment effectiveness of biofilms on chip.

The work in Chapter 5 proved promising but optimisation of the IK8 delivery system is still required. One initial factor was that the liposome encapsulation efficiency of the IK8 was very low, 4.8%. Changing the composition of the liposome could improve this as work by S.Moorcroft used DSPC and achieved an encapsulation efficiency of 15% [4], where this work used DPPC as the main lipid component. Although free IK8+MB+US was shown to reduce the cell density of the biofilms the most, attaching the loaded liposomes to the MBs may aid in delivery and allow further penetration into the biofilm. Creating targeted MBs and liposomes would also help attached the MB+liposomes delivery vesicle to the biofilm, and increase the sonoporation effect. The poor results of MBs+US in this chapter were most likely due to the MBs not being close enough to the biofilm surface to have any effect, therefore MB targeting, or at least inverting the biofilm after adding MBs so that MBs rise and stick to the biofilm, would help with sonoporation.

Once the treatment options have been optimised using biofilms grown in 96-well plates, experiments would be conducted on-chip, so that the whole biofilm experiment, from growth, analysis to treatment can be conducted on-chip for consistency. As mentioned, TPF would also be an excellent method of treatment quantification as the biofilm response could be monitored via autofluorescence rather than using live/dead stains, which reduces outside interference with the biofilm. Once the autofluorescnece of bacteria at different stages is known (e.g. stationary, exponential, increased metabolism, and dead), the biofilm response to IK8 may be tracked in a non-destructive, real time manner.

The long term goal is to apply these methods to a 5-species, pathogenic oral biofilm.

Understanding biofilms using RS is not trivial and will only get more complex as more species are added. However, having a well defined method and process of analysis that is shown to work with 2-species, will make the process of understanding 5-species easier. By understanding the 5-species biofilm, how it grows, and how it may be reduced to a non-pathogenic state, or to a more manageable, treatable biofilm, will help inform the treatment methods (such as how many rounds of MBs+US may be required, or specific targeting agents), which may in the future be applied in dental clinics as an alternative to antibiotics.

Bibliography

[1] Keiji Tanaka and Koichi Shimakawa. Structure. In *Amorphous Chalcogenide Semiconductors and Related Materials*, pages 31–65. University of Texas Medical Branch at Galveston, 7 1996.

[2] Jordan M. Tinkler. Microbubbles for the treatment of Staphylococcus aureus biofilms: Tackling Antimicrobial Resistance in New Ways. 2022.

[3] Aisha Farhana and Yusuf S. Khan. Biochemistry, Lipopolysaccharide. *StatPearls*, 4 2023.

[4] Samuel Moorcroft. *Light-responsive delivery and photothermal enhancement of antimicrobial peptides to combat bacterial wound infections.* PhD thesis, 2020.

[5] Megan Wilson, Ryan Martin, Seth T. Walk, Carol Young, Sylvia Grossman, Erin Lin Mckean, and David M. Aronoff. Clinical and Laboratory Features of Streptococcus salivarius Meningitis: A Case Report and Literature Review. *Clinical Medicine & Research*, 10(1):15, 2 2012.

[6] Beaumont Health. Infective endocarditis due to Streptococcus salivarius presenting as septic arthritis. 2021.

[7] Ghalia Kaci, Denise Goudercourt, Véronique Dennin, Bruno Pot, Joël Doré, S. Dusko Ehrlich, Pierre Renault, Hervé M. Blottière, Catherine Daniel, and Christine Delorme. Anti-Inflammatory Properties of Streptococcus salivarius, a Commensal Bacterium of the Oral Cavity and Digestive Tract. *Applied and Environmental Microbiology*, 80(3):928, 2 2014.

[8] Alexander Bertuccioli, Marco Gervasi, Giosuè Annibalini, Beatrice Binato, Fabrizio Perroni, Marco B.L. Rocchi, Davide Sisti, and Stefano Amatori. Use of Streptococcus salivarius K12 in supporting the mucosal immune function of active young subjects: A randomised double-blind study. *Frontiers in Immunology*, 14:1129060, 3 2023.

[9] Paul Vielkind, Holger Jentsch, Klaus Eschrich, Arne C. Rodloff, and Catalina Suzana Stingu. Prevalence of Actinomyces spp. in patients with chronic periodontitis. *International journal of medical microbiology : IJMM*, 305(7):682–688, 10 2015.

[10] Florent Valour, Agathe Sénéchal, Céline Dupieux, Judith Karsenty, Sébastien Lustig, Pierre Breton, Arnaud Gleizal, Loïc Boussel, Frédéric Laurent, Evelyne Braun, Christian Chidiac, Florence Ader, and Tristan Ferry. Actinomycosis: etiology, clinical features, diagnosis, treatment, and management. *Infection and Drug Resistance*, 7:183, 7 2014.

[11] L. J. Bergeron and R. A. Burne. Roles of fructosyltransferase and levanase-sucrase of Actinomyces naeslundii in fructan and sucrose metabolism. *Infection and Immunity*, 69(9):5395–5402, 2001.

[12] Hans-Curt Flemming and Jost Wingender. The biofilm matrix. *Nature Publishing Group*, 2010.

[13] L Karygianni, Z Ren, H Koo, and T Thurnheer. Biofilm Matrixome: Extracellular Components in Structured Microbial Communities. 2020.

[14] Ian W Sutherland. Review Review Review Review The biofilm matrix-an immobilized but dynamic microbial environment. *TRENDS in Microbiology*, 9(5), 2001.

[15] Hans Curt Flemming, Thomas R. Neu, and Daniel J. Wozniak. The EPS matrix: The "House of Biofilm Cells". *Journal of Bacteriology*, 189(22):7945–7947, 11 2007.

[16] Divakar Sharma, Lama Misba, and Asad U. Khan. Antibiotics versus biofilm: an emerging battleground in microbial communities. *Antimicrobial Resistance & Infection Control 2019 8:1*, 8(1):1–10, 5 2019.

[17] Niels Høiby, Thomas Bjarnsholt, Michael Givskov, Søren Molin, and Oana Ciofu. Antibiotic resistance of bacterial biofilms. *International Journal of Antimicrobial Agents*, 35:322–332, 2010.

[18] Thomas K. Wood, Stephen J. Knabel, and Brian W. Kwan. Bacterial persister cell formation and dormancy. *Applied and Environmental Microbiology*, 79(23):7116–7121, 12 2013.

[19] Jan Ulrich Kreft. Biofilms promote altruism. *Microbiology (Reading, England)*, 150(Pt 8):2751–2760, 2004.

[20] Veronica Georgiana Preda and Oana Săndulescu. Communication is the key: biofilms, quorum sensing, formation and prevention. *Discoveries*, 7(3):e10, 9 2019.

[21] Zohra Khatoon, Christopher D McTiernan, Erik J Suuronen, Thien-Fah Mah, Emilio I Alarcon, and Emilio I Alarcon Bacterial. Bacterial biofilm formation on implantable devices and approaches to its treatment and prevention. *Heliyon*, 4:e01067, 2018.

[22] Steven L. Percival, Sara M. McCarty, and Benjamin Lipsky. Biofilms and Wounds: An Overview of the Evidence. *Advances in Wound Care*, 4(7):373, 7 2015.

[23] Daniela Berger, Aviva Rakhamimova, Andrew Pollack, and Zvi Loewy. Oral Biofilms: Development, Control, and Analysis. *High-Throughput*, 7(3), 8 2018.

[24] Mukesh Kumar Yadav, Jorge E Vidal, and Jae-Jun Song. Microbial biofilms on medical indwelling devices. 2020.

[25] Darren Dhananthat Chawhuaveang, Ollie Yiru Yu, Iris Xiaoxue Yin, Walter Yu Hang Lam, May Lei Mei, and Chun Hung Chu. Acquired salivary pellicle and oral diseases: A literature review. *Journal of Dental Sciences*, 16(1):523, 1 2021.

[26] Karin Sauer, Paul Stoodley, Darla M. Goeres, Luanne Hall-Stoodley, Mette Burmølle, Philip S. Stewart, and Thomas Bjarnsholt. The biofilm life cycle: expanding the conceptual model of biofilm formation. *Nature Reviews Microbiology*, 20(10):608–620, 2022.

[27] Yuanzhe Li, Xiang Li, Yu Hao, Yang Liu, Zhili Dong, and Kexin Li. Biological and Physiochemical Methods of Biofilm Adhesion Resistance Control of Medical-Context Surface. *International Journal of Biological Sciences*, 2021(7):1769–1781, 2021.

[28] Milos Krsmanovic, Dipankar Biswas, Hessein Ali, Aloke Kumar, Ranajay Ghosh, and Andrew K Dickerson. Historical Perspective Hydrodynamics and surface properties influence biofilm proliferation. 2020.

[29] M. B. Miller and B. L. Bassler. Quorum sensing in bacteria. *Annual review of microbiology*, 55:165–199, 2001.

[30] Xinyi Li, Yanmei Liu, Xingyou Yang, Chengwen Li, and Zhangyong Song. The Oral Microbiota: Community Composition, Influencing Factors, Pathogenesis, and Interventions. *Frontiers in Microbiology*, 13(April):1–19, 2022.

[31] Allan Radaic and Yvonne L. Kapila. The oralome and its dysbiosis: New insights into oral microbiome-host interactions. *Computational and Structural Biotechnology Journal*, 19:1335–1360, 1 2021.

[32] Ruijie Huang, Mingyun Li, and Richard L. Gregory. Bacterial interactions in dental biofilm. 2011.

[33] Mattias Collin, Ana Carolina Morandini, Ralph Goethe, Bernd Kreikemeyer, Masanobu Nakata, Katja Kriebel, Cathleen Hieke, and Brigitte Müller-Hilke. Oral Biofilms from Symbiotic to Pathogenic Interactions and Associated Disease –Connection of Periodontitis and Rheumatic Arthritis by Peptidylarginine Deiminase. 2018.

[34] Meng Xuan Chen, Yu Jie Zhong, Qian Qian Dong, Hai Ming Wong, and Yi Feng Wen. Global, regional, and national burden of severe periodontitis, 1990–2019: An analysis of the Global Burden of Disease Study 2019. *Journal of Clinical Periodontology*, 48(9):1165–1188, 2021.

[35] S. Listl, J. Galloway, P. A. Mossey, and W. Marcenes. Global economic impact of dental diseases. *Journal of Dental Research*, 94(10):1355–1361, 10 2015.

[36] Ignacio Neumann, Holger Schunemann, Lisa Bero, Graham Cooke, Nicola Magrini, and Lorenzo Moja. Global access to affordable direct oral anticoagulants.

[37] Shalini Kanagasingam, Sasanka S Chukkapalli, Richard Welbury, and Sim K Singhrao. Porphyromonas gingivalis is a Strong Risk Factor for Alzheimer's Disease. *Journal of Alzheimer's Disease Reports*, 4:501–511, 2020.

[38] Shaneen J. Leishman, Hong Lien Do, and Pauline J. Ford. Cardiovascular disease and the role of oral bacteria. *Journal of Oral Microbiology*, 2(2010), 2010.

[39] Rafael Scaf de Molon, Carlos Rossa Jr., Rogier M. Thurlings, Joni Augusto Cirelli, and Marije I. Koenders. Linkage of Periodontitis and Rheumatoid Arthritis: Current Evidence and Potential Biological Interactions. *International Journal of Molecular Sciences*, 20(18), 9 2019.

[40] Ying Zhou and Guang Hua Luo. Porphyromonas gingivalis and digestive system cancers. *World Journal of Clinical Cases*, 7(7):819, 4 2019.

[41] Jebamercy Gnanasekaran, Adi Binder Gallimidi, Elias Saba, Karthikeyan Pandi, Luba Eli Berchoer, Esther Hermano, Sarah Angabo, Hasnaa Makkawi, Arin Khashan, Alaa Daoud, Michael Elkin, and Gabriel Nussbaum. Intracellular Porphyromonas gingivalis Promotes the Tumorigenic Behavior of Pancreatic Carcinoma Cells. *Cancers*, 12(8):1–14, 8 2020.

[42] Nicolaas H. Fourie, Dan Wang, Sarah K. Abey, Lee Anne B. Sherwin, Paule V. Joseph, Bridgett Rahim-Williams, Eric G. Ferguson, and Wendy A. Henderson. The microbiome of the oral mucosa in irritable bowel syndrome. *Gut Microbes*, 7(4):286, 7 2016.

[43] Y. W. Han. Oral Health and Adverse Pregnancy Outcomes – What's Next? *Journal of Dental Research*, 90(3):289, 3 2011.

[44] Chapple IL and Genco R. Diabetes and periodontal diseases: consensus report of the Joint EFP/AAP Workshop on Periodontitis and Systemic Diseases. *Journal of periodontology*, 84(4 Suppl):S106–S112, 4 2013.

[45] Jontana Allkja, Frits van Charante, Juliana Aizawa, Inés Reigada, Clara Guarch-Pérez, Jesus Augusto Vazquez-Rodriguez, Paul Cos, Tom Coenye, Adyary Fallarero, Sebastian A.J. Zaat, Antonio Felici, Livia Ferrari, Nuno F. Azevedo, Albert E. Parker, and Darla M. Goeres. Interlaboratory study for the evaluation of three microtiter plate-based biofilm quantification methods. *Scientific Reports*, 11(1):1–10, 2021.

[46] Christopher G. Pierce, Priya Uppuluri, Amanda R. Tristan, Jr. Floyd L. Wormley, Eilidh Mowat, Gordon Ramage, and Jose L. Lopez-Ribot. A simple and reproducible 96 well plate-based method for the formation of fungal biofilms and its application to antifungal susceptibility testing. *Nature protocols*, 3(9):1494, 8 2008.

[47] Lorena Pesciaroli, Maurizio Petruccioli, Stefano Fedi, Andrea Firrincieli, Federico Federici, and Alessandro D'annibale. Characterization of Pleurotus ostreatus Biofilms by Using the Calgary Biofilm Device. 2013.

[48] B. Guggenheim, E. Giertsen, P. Schüpbach, and S. Shapiro. Validation of an in vitro biofilm model of supragingival plaque. *Journal of Dental Research*, 80(1):363–370, 2001.

[49] Areum Han and Sun Young Lee. An overview of various methods for in vitro biofilm formation: a review. *Food Science and Biotechnology*, 32(12):1617–1629, 10 2023.

[50] Yichen Liao, Pedram Fatehi, and Baoqiang Liao. Surface properties of membrane materials and their role in cell adhesion and biofilm formation of microalgae. *Biofouling*, 39(8):879–895, 2023.

[51] Joana Azeredo, Nuno F Azevedo, Romain Briandet, Nuno Cerca, Tom Coenye, Ana Rita Costa, Mickaël Desvaux, Giovanni Di Bonaventura, Michel Hébraud, Zoran Jaglic, Miroslava Kačániová, Susanne Knøchel, Anália Lourenço, Filipe Mergulhão, Rikke Louise Meyer, George Nychas, Manuel Simões, Odile Tresse, and Claus Sternberg. Critical review on biofilm methods. *Critical Reviews in Microbiology*, 43(3):313–351, 2017.

[52] Henryke Rath, Sascha Nico Stumpp, and Meike Stiesch. Development of a flow chamber system for the reproducible in vitro analysis of biofilm formation on implant materials. 2017.

[53] B Purevdorj, J W Costerton, and P Stoodley. Influence of Hydrodynamics and Cell Signaling on the Structure and Behavior of. *Society*, 68(9):4457–4464, 2002.

[54] Claus Sternberg, Bjarke B. Christensen, Tove Johansen, Alex Toftgaard Nielsen, Jens Bo Andersen, Michael Givskov, and Søren Molin. Distribution of bacterial growth activity in flow-chamber biofilms. *Applied and Environmental Microbiology*, 65(9):4108–4117, 1999.

[55] Mervyn Y.H. Chin, Henk J. Busscher, Robert Evans, Joseph Noar, and Jonathan Pratten. Early biofilm formation and the effects of antimicrobial agents on orthodontic bonding materials in a parallel plate flow chamber. *European Journal of Orthodontics*, 28(1):1–7, 2006.

[56] Sahra Kırmusaoğlu. The Methods for Detection of Biofilm and Screening Antibiofilm Activity of Agents. In *Antimicrobials, Antibiotic Resistance, Antibiofilm Strategies and Activity Methods*. 2019.

[57] Philip Bowler, Christine Murphy, and Randall Wolcott. Biofilm exacerbates antibiotic resistance: Is this a current oversight in antimicrobial stewardship? *Antimicrobial Resistance and Infection Control*, 9(1):1–5, 2020.

[58] C Lee Ventola. The Antibiotic Resistance Crisis Part 1: Causes and Threats. 40(4), 2015.

[59] G. A Pankey and L. D Sabath. Clinical relevance of bacteriostatic versus bactericidal activity in the treatment of gram-positive bacterial infections [2]. *Clinical Infectious Diseases*, 39(5):755–756, 2004.

[60] Garima Kapoor, Saurabh Saigal, and Ashok Elongavan. Action and resistance mechanisms of antibiotics: A guide for clinicians. 2017.

[61] Thu D.M. Pham, Zyta M. Ziora, and Mark A.T. Blaskovich. Quinolone antibiotics. *MedChemComm*, 10(10):1719–1739, 10 2019.

[62] Michael R. Mulvey and Andrew E. Simor. Antimicrobial resistance in hospitals: How concerned should we be? *CMAJ. Canadian Medical Association Journal*, 180(4):408–415, 2009.

[63] Xihong Zhao, Zixuan Yu, and Tian Ding. Quorum-sensing regulation of antimicrobial resistance in bacteria. *Microorganisms*, 8(3):1–21, 2020.

[64] Elizabeth M. Darby, Eleftheria Trampari, Pauline Siasat, Maria Solsona Gaya, Ilyas Alav, Mark A. Webber, and Jessica M.A. Blair. Molecular mechanisms of antibiotic resistance revisited. *Nature Reviews Microbiology*, 21(5):280–295, 2023.

[65] Wanda C Reygaert. An overview of the antimicrobial resistance mechanisms of bacteria. *AIMS Microbiology*, 4(3):482, 2018.

[66] Jun Lei, Lichun Sun, Siyu Huang, Chenhong Zhu, Ping Li, Jun He, Vienna Mackey, David H Coy, and Quanyong He. The antimicrobial peptides and their potential clinical applications. *Am J Transl Res*, 11(7):3919–3931, 2019.

[67] Zhan Yuin Ong, Shu Jun Gao, and Yi Yan Yang. Short synthetic β-sheet forming peptide amphiphiles as broad spectrum antimicrobials with antibiofilm and endotoxin neutralizing capabilities. *Advanced Functional Materials*, 23(29):3682–3692, 2013.

[68] Ali Adem Bahar and Dacheng Ren. Antimicrobial Peptides. *Pharmaceuticals*, 6:1543–1575, 2013.

[69] Ling Juan Zhang and Richard L. Gallo. Antimicrobial peptides. *Current Biology*, 26(1):R14–R19, 2016.

[70] Patrícia G Lima, Jose T A Oliveira, Jackson L Amaral, Cleverson D T Freitas, and Pedro F N Souza. Synthetic antimicrobial peptides: Characteristics, design, and potential as alternative molecules to overcome microbial resistance. *Life Sciences*, 278:119647, 2021.

[71] Zhan Yuin Ong, Junchi Cheng, Yuan Huang, Kaijin Xu, Zhongkang Ji, Weimin Fan, and Yi Yan Yang. Effect of stereochemistry, chain length and sequence pattern on antimicrobial properties of short synthetic b-sheet forming peptide amphiphiles. 2013.

[72] Zhan Yuin Ong, Junchi Cheng, Yuan Huang, Kaijin Xu, Zhongkang Ji, Weimin Fan, and Yi Yan Yang. Effect of stereochemistry, chain length and sequence pattern on antimicrobial properties of short synthetic β-sheet forming peptide amphiphiles. *Biomaterials*, 35(4):1315–1325, 2014.

[73] Yi Liu and Hang Lu. Microfluidics in systems biology - hype or truly useful? *Current Opinion in Biotechnology*, 39:215–220, 2016.

[74] George M. Whitesides. The origins and the future of microfluidics. *Nature*, 442(7101):368–373, 2006.

[75] Skarphedinn Halldorsson, Edinson Lucumi, Rafael Gómez-Sjöberg, and Ronan M.T. Fleming. Advantages and challenges of microfluidic cell culture in polydimethylsiloxane devices. *Biosensors and Bioelectronics*, 63:218–231, 1 2015.

[76] Carlie Rein, Mehmet Toner, and Derin Sevenler. Rapid prototyping for high-pressure microfluidics. *Scientific Reports 2023 13:1*, 13(1):1–9, 1 2023.

[77] Kiran Raj M and Suman Chakraborty. PDMS microfluidics: A mini review. *Journal of Applied Polymer Science*, 137(27), 7 2020.

[78] Fluid Dynamics: The Navier-Stokes Equations Classical Mechanics.

[79] Neil Convery and Nikolaj Gadegaard. 30 Years of Microfluidics. *Micro and Nano Engineering*, 2(November 2018):76–91, 2019.

[80] Francesca Bragheri, Rebeca Martinez Vazquez, and Roberto Osellame. Microfluidics. In *Three-Dimensional Microfabrication Using Two-Photon Polymerization: Fundamentals, Technology, and Applications*, pages 310–334. Elsevier Inc., 1 2016.

[81] Hervé Straub, Leo Eberl, Manfred Zinn, René M. Rossi, Katharina Maniura-Weber, and Qun Ren. A microfluidic platform for in situ investigation of biofilm formation and its treatment under controlled conditions. *Journal of Nanobiotechnology*, 18(1):1–12, 12 2020.

[82] Wen Bin Lee, Chien Yu Fu, Wen Hsin Chang, Huey Ling You, Chih Hung Wang, Mel S. Lee, and Gwo Bin Lee. A microfluidic device for antimicrobial susceptibility testing based on a broth dilution method. *Biosensors and Bioelectronics*, 87:669–678, 1 2017.

[83] Po Cheng Tang, Olle Eriksson, Josefin Sjögren, Nikos Fatsis-Kavalopoulos, Johan Kreuger, and Dan I. Andersson. A Microfluidic Chip for Studies of the Dynamics of Antibiotic Resistance Selection in Bacterial Biofilms. *Frontiers in Cellular and Infection Microbiology*, 12(May):1–14, 2022.

[84] Sowmya Subramanian, Ryan C. Huiszoon, Sangwook Chu, William E. Bentley, and Reza Ghodssi. Microsystems for biofilm characterization and sensing – A review. *Biofilm*, 2:100015, 12 2020.

[85] Guanju Wei and Judy Q. Yang. Microfluidic investigation of the impacts of flow fluctuations on the development of Pseudomonas putida biofilms. *npj Biofilms and Microbiomes 2023 9:1*, 9(1):1–11, 10 2023.

[86] Olga I Guliy, Stella S Evstigneeva, and Victor D Bunin. Microfluidic bioanalytical system for biofilm formation indication. *Talanta*, 247:123541, 2022.

[87] Lu Yuan, Hervé Straub, Liubov Shishaeva, and Qun Ren. Microfluidics for Biofilm Studies. *Annual Review of Analytical Chemistry*, 2023.

[88] N Liu, T Skauge, D Landa-Marbán, B Hovland, B Thorbjørnsen, F A Radu, B F Vik, T Baumann, G Bødtker, and Gunhild Bødtker. Microfluidic study of effects of flow velocity and nutrient concentration on biofilm accumulation and adhesive strength in a microchannel.

[89] Hee Cheah and Sungwoo Bae. Multichannel Microfluidic Platform for Temporal-Spatial Investigation of Niche Roles of Pseudomonas aeruginosa and Escherichia coli within a Dual-Species Biofilm. *Applied and Environmental Microbiology*, 89(7), 7 2023.

[90] Jeongyun Kim, Manjunath Hegde, Sun Ho Kim, Thomas K Wood, and Arul Jayaraman. A microfluidic device for high throughput bacterial biofilm studies †.

[91] Núria Blanco-Cabra, Maria José López-Martínez, Betsy Verónica Arévalo-Jaimes, María Teresa Martin-Gómez, Josep Samitier, and Eduard Torrents. A new BiofilmChip device for testing biofilm formation and antibiotic susceptibility. *npj Biofilms and Microbiomes 2021 7:1*, 7(1):1–9, 8 2021.

[92] William C Nance, Scot E Dowd, Derek Samarian, Jeffrey Chludzinski, Joseph Delli, John Battista, and Alexander H Rickard. A high-throughput microfluidic dental plaque biofilm system to visualize and quantify the effect of antimicrobials.

[93] Raymond H.W. Lam, Xin Cui, Weijin Guo, and Todd Thorsen. High-throughput dental biofilm growth analysis for multiparametric microenvironmental biochemical conditions using microfluidics. *Lab on a Chip*, 16(9):1652–1662, 2016.

[94] Caryn S Hughes Matthew J Baker and Katherine A Hollywood. Chapter 3 Raman spectroscopy. *Biophotonics: Vibrational Spectroscopic Diagnostics*, 2016.

[95] R S Krishnan and R K Shankar. Raman Effect: History of the Discovery. *Journal of Raman Spectroscopy*, 10, 1981.

[96] Renishaw. Raman spectroscopy explained. Technical report, Renishaw, 2018.

[97] Julia Gala de Pablo, Fern J. Armistead, Sally A. Peyman, David Bonthron, Michael Lones, Stephen Smith, and Stephen D. Evans. Biochemical fingerprint of colorectal cancer cell lines using label-free live single-cell Raman spectroscopy. *Journal of Raman Spectroscopy*, 49(8):1323–1332, 8 2018.

[98] Michael Jermyn, Kelvin Mok, Jeanne Mercier, Joannie Desroches, Julien Pichette, Karl Saint-Arnaud, Liane Bernstein, Marie Christine Guiot, Kevin Petrecca, and Frederic Leblond. Intraoperative brain cancer detection with Raman spectroscopy in humans. *Science Translational Medicine*, 7(274):1–10, 2015.

[99] James F. Brennan, Tjeerd J. Romer, Robert S. Lees, Anna M. Tercyak, John R. Kramer, and Michael S. Feld. Determination of Human Coronary Artery Composition by Raman Spectroscopy. *Circulation*, 96(1):99–105, 7 1997.

[100] Noël J.C. Bauer, James P. Wicksted, Franciscus H.M. Jongsma, Wayne F. March, Fred Hendrikse, and Massoud Motamedi. Noninvasive assessment of the hydration gradient across the cornea using confocal raman spectroscopy. *Investigative Ophthalmology and Visual Science*, 39(5):831–835, 1998.

[101] Qingyuan Zhu, Robert G. Quivey, and Andrew J. Berger. Raman spectroscopic measurement of relative concentrations in mixtures of oral bacteria. *Applied Spectroscopy*, 61(11):1233–1237, 11 2007.

[102] Gyeong Bok Jung, Seong Won Nam, Samjin Choi, Gi-Ja Lee, and Hun-Kuk Park. Evaluation of antibiotic effects on Pseudomonas aeruginosa biofilm using Raman spectroscopy and multivariate analysis. *Biomedical Optics Express*, 5(9):3238, 9 2014.

[103] Kazuki Hashimoto, Venkata Ramaiah Badarla, Akira Kawai, and Takuro Ideguchi. Complementary vibrational spectroscopy. *Nature Communications*, 10(1), 12 2019.

[104] Derek A. Long. Classical Theory of Rayleigh and Raman Scattering. *The Raman Effect*, 8:31–48, 2002.

[105] Christoph Krafft. Raman and coherent anti-Stokes Raman scattering microspectroscopy for biomedical applications. *Journal of Biomedical Optics*, 17(4):040801, 4 2012.

[106] David W Hahn. Raman Scattering Theory, 2007.

[107] Julia Gala de Pablo. *Bio chemical phenotyping of live single cells using confocal Raman spectroscopy*. PhD thesis, University of Leeds, 9 2019.

[108] John Ferraro and Kazuo Nakamoto. *Introductory Raman Spectroscopy*. Elsevier, 2003.

[109] Peter Larkin. Introduction. In *Infrared and Raman Spectroscopy*, pages 1–5. Elsevier, 2011.

[110] Shazza Rehman Zanyar Movasaghi and Ihtesham Ur Rehman. *Vibrational Spectroscopy for Tissue Analysis*. CRC Press LLC, 2012.

[111] Derek Long. *The Raman Effect: A Unified Treatment of the Theory of Raman Scattering by Molecules*. John Wiley & Sons Ltd, 2002.

[112] Max Diem. *Modern Vibrational Spectroscopy and Micro-Spectroscopy : Theory, Instrumentation and Biomedical Applications*. John Wiley & Sons,, 2015.

[113] Patrik Callis and Karl Sebbey. Introduction to Fluorescence Spectroscopies I . Theory. pages 1–9, 2011.

[114] Robin R. Jones, David C. Hooper, Liwu Zhang, Daniel Wolverson, and Ventsislav K. Valev. Raman Techniques: Fundamentals and Frontiers. *Nanoscale Research Letters*, 14(1), 2019.

[115] Eric Olaf Potma and Shaul Mukamel. *Theory of Coherent Raman Scattering*. 2013.

[116] Robert W. Boyd. The nonlinear optical susceptibility - Chapter 1. *Nonlinear Optics*, (1941):1–67, 1961.

[117] Qian Cheng, Yupeng Miao, Joseph Wild, Wei Min, and Yuan Yang. Emerging applications of stimulated Raman scattering microscopy in materials science. *Matter*, 4(5):1460–1483, 5 2021.

[118] William J. Tipping, Martin Lee, Alan Serrels, Valerie G. Brunton, and Alison N. Hulme. Stimulated Raman scattering microscopy: An emerging tool for drug discovery. *Chemical Society Reviews*, 45(8):2075–2089, 2016.

[119] Richard C. Prince, Renee R. Frontiera, and Eric O. Potma. Stimulated Raman scattering: From bulk to nano. *Chemical Reviews*, 117(7):5070–5094, 2017.

[120] Aditya Garg, Wonil Nam, Wei Wang, Peter Vikesland, and Wei Zhou. In Situ Spatiotemporal SERS Measurements and Multivariate Analysis of Virally Infected Bacterial Biofilms Using Nanolaminated Plasmonic Crystals. 8:1132–1142, 2023.

[121] Andrew J. Berger and Qingyuan Zhu. Identification of oral bacteria by raman microspectroscopy. *Journal of Modern Optics*, 50-15(17):2375–2380, 2003.

[122] Jinsong Feng, César De La Fuente-Núñez, Michael J. Trimble, Jie Xu, Robert E.W. Hancock, and Xiaonan Lu. An in situ Raman spectroscopy-based microfluidic "lab-on-a-chip" platform for non-destructive and continuous characterization of Pseudomonas aeruginosa biofilms. *Chemical Communications*, 51(43):8966–8969, 5 2015.

[123] Haodong Shen, Petra Rösch, Lara Thieme, Mathias W. Pletz, and Jürgen Popp. Comparison of bacteria in different metabolic states by micro-Raman spectroscopy. *Journal of Molecular Structure*, 1277:134831, 4 2023.

[124] Lukas Simon Kriem, Kevin Wright, Renzo Alberto Ccahuana-Vasquez, and Steffen Rupp. Mapping of a Subgingival Dual-Species Biofilm Model Using Confocal Raman Microscopy. *Frontiers in Microbiology*, 12(October), 10 2021.

[125] Qingyuan Zhu, Robert G Quivey, and Andrew J Berger. Raman Spectroscopic Measurement of Relative Concentrations in Mixtures of Oral Bacteria.

[126] Brooke D. Beier, Robert G. Quivey, and Andrew J. Berger. Identification of different bacterial species in biofilms using confocal Raman microscopy. *Journal of Biomedical Optics*, 15(6):066001, 2010.

[127] Brooke D. Beier, Robert G. Quivey, and Andrew J. Berger. Raman microspectroscopy for species identification and mapping within bacterial biofilms. *AMB Express*, 2(1):1–6, 2012.

[128] Tatiana Ramirez-Mora, Claudia Dávila-Pérez, Fernando Torres-Méndez, and Grettel Valle-Bourrouet. Raman Spectroscopic Characterization of Endodontic Biofilm Matrices. *Journal of Spectroscopy*, 2019, 2019.

[129] Tatiana Ramirez-Mora, Cristina Retana-Lobo, and Grettel Valle-Bourrouet. Biochemical characterization of extracellular polymeric substances from endodontic biofilms. *PLOS ONE*, 13(11):e0204081, 11 2018.

[130] Lukas Simon Kriem, Kevin Wright, Renzo Alberto Ccahuana-Vasquez, and Steffen Rupp. Confocal Raman microscopy to identify bacteria in oral subgingival biofilm models. *PLoS ONE*, 15(5), 2020.

[131] Kideog Bae, Wei Zheng, Ying Ma, and Zhiwei Huang. Real-Time Monitoring of Pharmacokinetics of Antibiotics in Biofilms with Raman-Tagged Hyperspectral Stimulated Raman Scattering Microscopy. *Theranostics*, 9(5), 2019.

[132] S. R. Sirsi and M. A. Borden. Microbubble Compositions, Properties and Biomedical Applications. *Bubble science engineering and technology*, 1(1-2):3, 2009.

[133] Fabrizio Calliada, Rodolfo Campani, Olivia Bottinelli, Anna Bozzini, and Maria Grazia Sommaruga. Ultrasound contrast agents: Basic principles. In *European Journal of Radiology*, volume 27. Elsevier Sci Ireland Ltd, 5 1998.

[134] Tzu-Yin Wang, Katheryne E Wilson, Steven Machtaler, and Jürgen K Willmann. Ultrasound and Microbubble Guided Drug Delivery: Mechanistic Understanding and Clinical Implications. 2013.

[135] Jeane M. Tsutsui, Feng Xie, and Richard Thomas Porter. The use of microbubbles to target drug delivery. *Cardiovascular Ultrasound*, 2:23, 11 2004.

[136] Mihai Strachinaru and Folkert J. ten Cate. Microbubble Enhanced Echocardiography in Current Cardiology Practice. *Reviews in Cardiovascular Medicine*, 23(6):202, 5 2022.

[137] Alexander L. Klibanov. Preparation of targeted microbubbles: Ultrasound contrast agents for molecular imaging. *Medical and Biological Engineering and Computing*, 47(8):875–882, 2009.

[138] Sheng Kai Wu, Po Chun Chu, Wen Yen Chai, Shih Tsung Kang, Chih Hung Tsai, Ching Hsiang Fan, Chih Kuang Yeh, and Hao Li Liu. Characterization of different microbubbles in assisting focused ultrasound-induced blood-brain barrier opening. *Scientific Reports*, 7(March):1–11, 2017.

[139] Anush Sridharan, John R Eisenbrey, Flemming Forsberg, Norbert Lorenz, Ludwig Steffgen, and Aikaterini Ntoulia. Ultrasound contrast agents: microbubbles made simple for the pediatric radiologist.

[140] Ine Lentacker, Stefaan C. De Smedt, and Niek N. Sanders. Drug loaded microbubble design for ultrasound triggered delivery. *Soft Matter*, 5(11):2161–2170, 2009.

[141] Qian Gong, Xingxing Gao, Wenfang Liu, Tingting Hong, and Chuanpin Chen. Drug-Loaded Microbubbles Combined with Ultrasound for Thrombolysis and Malignant Tumor Therapy. *BioMed Research International*, 2019, 2019.

[142] Ilya Digel, Inna Kern, Eva Maria Geenen, and Nuraly Akimbekov. Dental Plaque Removal by Ultrasonic Toothbrushes. *Dentistry Journal 2020, Vol. 8, Page 28*, 8(1):28, 3 2020.

[143] Tatsuya Ohsumi, Shoji Takenaka, Yuuki Sakaue, Yuki Suzuki, Ryoko Nagata, Taisuke Hasegawa, Hayato Ohshima, Yutaka Terao, and Yuichiro Noiri. Adjunct use of mouth rinses with a sonic toothbrush accelerates the detachment of a Streptococcus mutans biofilm: an in vitro study. *BMC Oral Health*, 20(1), 6 2020.

[144] Katherine W Ferrara, Mark A Borden, and Hua Zhang. Lipid-shelled vehicles: engineering for ultrasound molecular imaging and drug delivery NIH Public Access. *Acc Chem Res*, 42(7):881–892, 2009.

[145] Tim Segers, Anne Lassus, Philippe Bussat, Emmanuel Gaud, and Peter Frinking. Improved coalescence stability of monodisperse phospholipid-coated microbubbles formed by flow-focusing at elevated temperatures. *Lab on a Chip*, 19(1):158–167, 12 2018.

[146] Daiki Omata, Johan Unga, Ryo Suzuki, and Kazuo Maruyama. Lipid-based microbubbles and ultrasound for therapeutic application. *Advanced Drug Delivery Reviews*, 154-155:236–244, 1 2020.

[147] Klazina Kooiman, Tom J.A. Kokhuis, Tom van Rooij, Ilya Skachkov, Alex Nigg, Johannes G. Bosch, Antonius F.W. van der Steen, Wiggert A. van Cappellen, and Nico de Jong. DSPC or DPPC as main shell component influences ligand distribution and binding area of lipid-coated targeted microbubbles. *European Journal of Lipid Science and Technology*, 116(9):1217–1227, 9 2014.

[148] Sumit Garg, Alex A Thomas, and Mark A Borden. The effect of lipid monolayer in-plane rigidity on in vivo microbubble circulation persistence. 2013.

[149] James J. Kwan and Mark A. Borden. Lipid monolayer collapse and microbubble stability, 11 2012.

[150] Expanding 3D geometry for enhanced on-chip microbubble production and single step formation of liposome modified microbubbles{, author = Peyman, Sally A and Abou-Saleh, Radwa H and Mclaughlan, James R and Ingram, Nicola and Johnson, Benjamin R G and Critchley, Kevin and Freear, Steven and Evans, J Anthony and Markham, Alexander F and Coletta, P Louise and Evans, Stephen D, url = www.rsc.org/loc, doi = 10.1039/c2lc40634a.

[151] Steliyan Tinkov, Gerhard Winter, Conrad Coester, and Raffi Bekeredjian. New doxorubicin-loaded phospholipid microbubbles for targeted tumor therapy: Part I — Formulation development and in-vitro characterization. *Journal of Controlled Release*, 143(1):143–150, 4 2010.

[152] Ine Lentacker, Stefaan C De Smedt, and Niek N Sanders. Drug loaded microbubble design for ultrasound triggered delivery.

[153] Helen Mulvana, Richard J. Browning, Ying Luan, Nico De Jong, Meng Xing Tang, Robert J. Eckersley, and Eleanor Stride. Characterization of contrast agent microbubbles for ultrasound imaging and therapy research. *IEEE Transactions on Ultrasonics, Ferroelectrics, and Frequency Control*, 64(1):232–251, 2017.

[154] Radwa H. Abou-Saleh, Aileen Delaney, Nicola Ingram, Damien V.B. Batchelor, Benjamin R.G. Johnson, Antonia Charalambous, Richard J. Bushby, Sally A. Peyman, P. Louise Coletta, Alexander F. Markham, and Stephen D. Evans. Freeze-Dried Therapeutic Microbubbles: Stability and Gas Exchange. *ACS Applied Bio Materials*, 3(11):7840–7848, 11 2020.

[155] Anne Rix, Moritz Palmowski, Felix Gremse, Karin Palmowski, Wiltrud Lederle, Fabian Kiessling, and Jessica Bzyl. Influence of Repetitive Contrast Agent Injections on Functional and Molecular Ultrasound Measurements. *Ultrasound in Medicine & Biology*, 40(10):2468–2475, 10 2014.

[156] Yung-Chu Chen, Chi-Feng Chiang, Sheng-Kai Wu, Li-Fang Chen, Wen-Yuan Hsieh, and Win-Li Lin. Targeting microbubbles-carrying TGFβ1 inhibitor combined with ultrasound sonication induce BBB/BTB disruption to enhance nanomedicine treatment for brain tumors. 2015.

[157] Nicola Ingram, Laura E. McVeigh, Radwa H. Abou-Saleh, Juliana Maynard, Sally A. Peyman, James R. McLaughlan, Michael Fairclough, Gemma Marston, Elizabeth M.A. Valleley, Jorge L. Jimenez-Macias, Antonia Charalambous, William Townley, Malcolm Haddrick, Antonia Wierzbicki, Alexander Wright, Milène Volpato, Peter B. Simpson, Darren E. Treanor, Neil H. Thomson, Paul M. Loadman, Richard J. Bushby, Benjamin R.G. Johnson, Pamela F. Jones, J. Anthony Evans, Steven Freear, Alexander F. Markham, Stephen D. Evans, and P. Louise Coletta. Ultrasound-triggered therapeutic microbubbles enhance the efficacy of cytotoxic drugs by increasing circulation and tumor drug accumulation and limiting bioavailability and toxicity in normal tissues. *Theranostics*, 10(24):10973–10992, 2020.

[158] Ching Hsiang Fan, Yu Hang Cheng, Chien Yu Ting, Yi Ju Ho, Po Hung Hsu, Hao Li Liu, and Chih Kuang Yeh. Ultrasound/Magnetic Targeting with SPIO-DOX-Microbubble Complex for Image-Guided Drug Delivery in Brain Tumors. *Theranostics*, 6(10):1542–1556, 2016.

[159] Jack A. Caudwell, Jordan M. Tinkler, Ben R.G. Johnson, Kenneth J. McDowall, Fayez Alsulaimani, Christian Tiede, Darren C. Tomlinson, Steven Freear, W. Bruce Turnbull, Stephen D. Evans, and Jonathan A.T. Sandoe. Protein-conjugated microbubbles for the selective targeting of S. aureus biofilms. *Biofilm*, 4:100074, 12 2022.

[160] Joop J.P. Kouijzer, Kirby R. Lattwein, Inés Beekers, Simone A.G. Langeveld, Mariël Leon-Grooters, Jean Marc Strub, Estefania Oliva, Gaëtan L.A. Mislin, Nico de Jong, Antonius F.W. van der Steen, Alexander L. Klibanov, Willem J.B. van Wamel, and Klazina Kooiman. Vancomycin-decorated microbubbles as a theranostic agent for Staphylococcus aureus biofilms. *International Journal of Pharmaceutics*, 609(September), 2021.

[161] Long Meng, Feiyan Cai, Peng Jiang, Zhiting Deng, Fei Li, Lili Niu, Yan Chen, Junru Wu, and Hairong Zheng. On-chip targeted single cell sonoporation with

microbubble destruction excited by surface acoustic waves. *Applied Physics Letters*, 104(7), 2 2014.

[162] Y. Zhou, K. Yang, J. Cui, J. Y. Ye, and C. X. Deng. Controlled permeation of cell membrane by single bubble acoustic cavitation. *Journal of Controlled Release*, 157(1):103–111, 1 2012.

[163] Aladin Carovac, Fahrudin Smajlovic, and dzelaludin Junuzovic. Application of Ultrasound in Medicine. *Medicine Review — AIM*, 19(3):168–171, 2011.

[164] Iacopo Chiavacci and Patricia O'Gorman. Propagation speed. *Radiopaedia.org*, 7 2016.

[165] Ho Chul Shin, Richard Prager, Henry Gomersall, Nick Kingsbury, Graham Treece, and Andrew Gee. Estimation of Average Speed of Sound Using Deconvolution of Medical Ultrasound Data. *Ultrasound in Medicine and Biology*, 36(4):623–636, 4 2010.

[166] Christa Brown. *Smart Biomaterials: Embedding Microbubbles into Folded Protein Hydrogels*. PhD thesis, University of Leeds, 2022.

[167] Dui Qin, Shuang Lei, Xia Wang, Xianhua Zhong, Xiaojuan Ji, and Zhangyong Li. Resonance behaviors of encapsulated microbubbles oscillating nonlinearly with ultrasonic excitation. *Ultrasonics Sonochemistry*, 94:106334, 2023.

[168] Valerio Pereno, Junjun Lei, Dario Carugo, and Eleanor Stride. Microstreaming inside Model Cells Induced by Ultrasound and Microbubbles. *Langmuir*, 36(23):6388–6398, 6 2020.

[169] Zhenzhen Fan, Ronald E. Kumon, and Cheri X. Deng. Mechanisms of microbubble-facilitated sonoporation for drug and gene delivery. *Therapeutic delivery*, 5(4):467, 2014.

[170] Yanye Yang, Qunying Li, Xiasheng Guo, Juan Tu, and Dong Zhang. Mechanisms underlying sonoporation: Interaction between microbubbles and cells. *Ultrasonics Sonochemistry*, 67, 10 2020.

[171] Pier Paolo Claudio, Candace Howard, and Rounak Nande. Ultrasound-mediated oncolytic virus delivery and uptake for increased therapeutic efficacy: state of art. *Oncolytic Virotherapy*, page 193, 11 2015.

[172] Kirby R. Lattwein, Himanshu Shekhar, Willem J.B. Van Wamel, Tammy Gonzalez, Andrew B. Herr, Christy K. Holland, and Klazina Kooiman. An in vitro proof-of-principle study of sonobactericide. *Scientific Reports 2018 8:1*, 8(1):1–12, 2 2018.

[173] Ying Dong, Yaling Xu, Pan Li, Chuanqing Wang, Yun Cao, and Jialin Yu. Antibiofilm effect of ultrasound combined with microbubbles against Staphylococcus epidermidis biofilm. *International Journal of Medical Microbiology*, 307(6):321–328, 9 2017.

[174] Weijun Xiu, Lili Ren, Huayu Xiao, Yue Zhang, Dou Wang, Kaili Yang, Siyu Wang, Lihui Yuwen, Xiao Li, Heng Dong, Qiang Li, Yongbin Mou, Yuqian Zhang, Zhaowei Yin, Bin Liang, Yu Gao, and Lianhui Wang. Ultrasound-responsive catalytic microbubbles enhance biofilm elimination and immune activation to treat chronic lung infections. 2023.

[175] Gareth LuTheryn, Charlotte Hind, Christopher Campbell, Aaron Crowther, Qiang Wu, Sara B. Keller, Peter Glynne-Jones, J. Mark Sutton, Jeremy S. Webb, Michael Gray, Sandra A. Wilks, Eleanor Stride, and Dario Carugo. Bactericidal and anti-biofilm effects of uncharged and cationic ultrasound-responsive nitric oxide microbubbles on Pseudomonas aeruginosa biofilms. *Frontiers in Cellular and Infection Microbiology*, 12:956808, 8 2022.

[176] Yu Ying Fu, Liang Zhang, Yi Yang, Cheng Wei Liu, Ying Na He, Pan Li, and Xian Yu. Synergistic antibacterial effect of ultrasound microbubbles combined with chitosan-modified polymyxin B-loaded liposomes on biofilm-producing Acinetobacter baumannii. *International Journal of Nanomedicine*, 14:1805–1815, 2019.

[177] Junki Yamada, Takashi Takiguchi, Akihiro Saito, Hibiki Odanaka, Hitoshi Soyama, and Matsuo Yamamoto. Removal of oral biofilm on an implant fixture by a cavitating jet. *Implant Dentistry*, 26(6):904–910, 2017.

[178] A. Rmaile, D. Carugo, L. Capretto, M. Aspiras, M. De Jager, M. Ward, and P. Stoodley. Removal of interproximal dental biofilms by high-velocity water microdrops. *Journal of Dental Research*, 93(1):68–73, 2014.

[179] Michael R. Parini and William G. Pitt. Dynamic removal of oral biofilms by bubbles. *Colloids and Surfaces B: Biointerfaces*, 52(1):39–46, 9 2006.

[180] Deborah Mancinelli-Lyle, Jimmy G. Qaqish, C. Ram Goyal, and Reinhard Schuller. Efficacy of water flossing on clinical parameters of inflammation and plaque: A 4-week randomized controlled trial. *International Journal of Dental Hygiene*, 21(4):659–668, 11 2023.

[181] Monika Naginyte. Environmental effects on oral biofilm communities Submitted in accordance with the requirements for the degree of Doctor of Philosophy University of Leeds School of Dentistry September 2018. (September), 2018.

[182] Ailsa S. McKee, Ann S. McDermid, D. C. Ellwood, and P. D. Marsh. The establishment of reproducible, complex communities of oral bacteria in the chemostat using defined inocula. *The Journal of applied bacteriology*, 59(3):263–275, 1985.

[183] D. J. Bradshaw, A. S. McKee, and P. D. Marsh. Effects of carbohydrate pulses and pH on population shifts within oral microbial communities in vitro. *Journal of dental research*, 68(9):1298–1302, 1989.

[184] Monika Naginyte. *Environmental effects on oral biofilm communities*. PhD thesis, 2018.

[185] Jr Palmer, K. Kazmerzak, M. C. Hansen, and P. E. Kolenbrander. Mutualism versus Independence: Strategies of Mixed-Species Oral Biofilms In Vitro Using Saliva as the Sole Nutrient Source. *Infection and Immunity*, 69(9):5794, 2001.

[186] Fern J Armistead. *Mechanical phenotyping of single cells using shear and inertial microfluidics*. PhD thesis, University of Leeds, 2019.

[187] Alexandra Borók, Kristóf Laboda, and Attila Bonyár. PDMS Bonding Technologies for Microfluidic Applications: A Review. *Biosensors*, 11(8), 8 2021.

[188] T. Thurnheer, R. Gmür, E. Giertsen, and B. Guggenheim. Automated fluorescent in situ hybridization for the specific detection and quantification of oral streptococci in dental plaque. *Journal of Microbiological Methods*, 2001.

[189] T. Thurnheer, R. Gmür, and B. Guggenheim. Multiplex FISH analysis of a six-species bacterial biofilm. *Journal of Microbiological Methods*, 56(1):37–47, 2004.

[190] National Genome Research Institute: Fluorescence in situ Hybridisation (FISH), 2024.

[191] Damien V. Batchelor. DamienBatchelor/UoL_MicrobubbleCount: First public release of MATLAB Microbubble Code, doi.org/10.5281/zenodo.3952714, 2020.

[192] Roberto Diego Ortuso, Ugo Cataldi, and Kaori Sugihara. Mechanosensitivity of polydiacetylene with a phosphocholine headgroup. *Soft Matter*, 13(8):1728–1736, 2017.

[193] Beata Kowalska-Krochmal and Ruth Dudek-Wicher. The Minimum Inhibitory Concentration of Antibiotics: Methods, Interpretation, Clinical Relevance. *Pathogens*, 10(2):1–21, 2 2021.

[194] Matthias Koch, Christian Suhr, Bernhard Roth, and Merve Meinhardt-Wollweber. Iterative morphological and mollifier-based baseline correction for Raman spectra. *Journal of Raman Spectroscopy*, 48(2):336–342, 2017.

[195] Jake Lever, Martin Krzywinski, and Naomi Altman. Points of Significance: Principal component analysis. *Nature Methods*, 14(7):641–642, 2017.

[196] University of Exeter. CONTRAST Facility, 2023.

[197] Education Ecosystem (LEDU). Understanding K-means Clustering in Machine Learning, 2018.

[198] N. B.S. Silva, L. A. Marques, and D. D.B. Röder. Diagnosis of biofilm infections: current methods used, challenges and perspectives for the future. *Journal of Applied Microbiology*, 131(5):2148–2160, 2021.

[199] Christina Wilson, Rachel Lukowicz, Stefan Merchant, Helena Valquier-Flynn, Jeniffer Caballero, Jasmin Sandoval, Macduff Okuom, Christopher Huber, Tessa Durham Brooks, Erin Wilson, Barbara Clement, Christopher D Wentworth, and Andrea E Holmes. Quantitative and Qualitative Assessment Methods for Biofilm Growth: A Mini-review HHS Public Access. *Res Rev J Eng Technol*, 6(4), 2017.

[200] Ce Fern andez, MB Aspiras, MW Dodds, C Gonz alez Cabezas, Ah Rickard, and Correspondence H Alexander Rickard. The effect of inoculum source and fluid shear force on the development of in vitro oral multispecies biofilms. 2016.

[201] Alexander L.M. Chun, Ali Mosayyebi, Arthur Butt, Dario Carugo, and Maria Salta. Early biofilm and streamer formation is mediated by wall shear stress and surface wettability: A multifactorial microfluidic study. *MicrobiologyOpen*, 11(4), 8 2022.

[202] Bartels. Micropumps: For liquids, mixtures and gases, 2023.

[203] Thomas J. Tewes, Isabella Centeleghe, Jean Yves Maillard, Frank Platte, and Dirk P. Bockmühl. Raman Microscopic Analysis of Dry-Surface Biofilms on Clinically Relevant Materials. *Microorganisms*, 10(7), 7 2022.

[204] Datasheet. FilmTracer ™ LIVE / DEAD ® Biofilm Viability Kit. *Image (Rochester, N.Y.)*, pages 1–4, 2009.

[205] Gavin Melaugh, Jaime Hutchison, Kasper Nørskov Kragh, Yasuhiko Irie, Aled Roberts, Thomas Bjarnsholt, Stephen P. Diggle, Vernita D. Gordon, and Rosalind J. Allen. Shaping the growth behaviour of biofilms initiated from bacterial aggregates. *PLoS ONE*, 11(3), 2016.

[206] Pallee Shree, Chandra Kant Singh, Kushneet Kaur Sodhi, Jaya Niranjane Surya, and Dileep Kumar Singh. Biofilms: Understanding the structure and contribution towards bacterial resistance in antibiotics. *Medicine in Microecology*, 16:100084, 6 2023.

[207] Yusong Ye, Mnar Ghrayeb, Sarah Miercke, Sania Arif, Susann Mü, Thorsten Mascher, Liraz Chai, and Vasily Zaburdaev. Residual cells and nutrient availability guide wound healing in bacterial biofilms †. 2024.

[208] K. Czamara, K. Majzner, M. Z. Pacia, K. Kochan, Agnieszka Kaczor, and M. Baranska. Raman spectroscopy of lipids: a review. *Journal of Raman Spectroscopy*, 46(1):4–20, 1 2015.

[209] Giuseppe Pezzotti. Raman spectroscopy in cell biology and microbiology. *Journal of Raman Spectroscopy*, 52(12):2348–2443, 2021.

[210] Nikki Kuhar, Sanchita Sil, Taru Verma, and Siva Umapathy. Challenges in application of Raman spectroscopy to biology and materials. *RSC Advances*, 8(46):25888–25908, 7 2018.

[211] Zanyar Movasaghi, Shazza Rehman, and Ihtesham U. Rehman. Raman spectroscopy of biological tissues. *Applied Spectroscopy Reviews*, 42(5):493–541, 2007.

[212] Yury V. Kistenev, Alexei V. Borisov, Alisa A. Samarinova, Sonivette Colón-Rodríguez, and Igor K. Lednev. A novel Raman spectroscopic method for detecting traces of blood on an interfering substrate. *Scientific Reports*, 13(1):1–15, 2023.

[213] David Gani, Patrick J. Hendra, William F. Maddams, Catherine Passingham, Isabelle A.M. Royaud, Harry A. Willis, Veronica Zichy, and Michael E.A. Cudby. Fourier transform Raman spectroscopy in the analysis of polypeptides. *The Analyst*, 115(10):1313–1318, 1990.

[214] Klytaimnistra Katsara, Konstantina Psatha, George Kenanakis, Michalis Aivaliotis, and Vassilis M Papadakis. Subtyping on Live Lymphoma Cell Lines by Raman Spectroscopy. 2022.

[215] Zheng Yong Zhang, Dong Dong Gui, Min Sha, Jun Liu, and Hai Yan Wang. Raman chemical feature extraction for quality control of dairy products. *Journal of Dairy Science*, 102(1):68–76, 2019.

[216] Vakgroep Analytische Scheikunde and Kris De Gussem. *Optimisation of Raman spectroscopy for the analysis of Basidiomycota: spores, latex and mycelium Optimalisatie van Ramanspectroscopie voor de analyse van Basidiomycota: sporen, latex en mycelium*. PhD thesis, 2006.

[217] Ioan Notingher, Isabelle Bisson, Julia M Polak, and Larry L Hench. In situ spectroscopic study of nucleic acids in differentiating embryonic stem cells. 2004.

[218] Ping Tang, Wendai Cheng, Xuanmeng He, Qinnan Zhang, Jing Zhong, Xiaoxu Lu, Shengde Liu, and Liyun Zhong. Raman spectrum spectral imaging revealing the molecular mechanism of Berberine-induced Jurkat cell apoptosis and the receptor-mediated Berberine delivery system. 2019.

[219] Haoyue Liang, Xiaodong Kong, Yansong Ren, Haoyu Wang, Ertao Liu, Fanfan Sun, Guoqing Zhu, Qiang Zhang, and Yuan Zhou. Application of serum Raman spectroscopy in rapid and early discrimination of aplastic anemia and myelodysplastic syndrome. 2023.

[220] Jing Wen, Tianchen Tang, Saima Kanwal, Yongzheng Lu, Chunxian Tao, Lulu Zheng, Dawei Zhang, and Zhengqin Gu. Detection and Classification of Multi-Type Cells by Using Confocal Raman Spectroscopy.

[221] E. V. Timchenko, L. A. Zherdeva, P. E. Timchenko, L. T. Volova, and U. V. Ponomareva. Detailed Analysis of the Structural Changes of Bone Matrix during the Demineralization Process Using Raman Spectroscopy. *Physics Procedia*, 73:221–227, 2015.

[222] Zdeněk Pilát, Silvie Bernatová, Jan Ježek, Johanna Kirchhoff, Astrid Tannert, Ute Neugebauer, Ota Samek, and Pavel Zemánek. Microfluidic cultivation and laser tweezers raman spectroscopy of E. coli under antibiotic stress. *Sensors (Switzerland)*, 18(5), 2018.

[223] Chloe J. Kirkby, Julia Gala De Pablo, Emma Tinkler-Hundal, Henry M. Wood, Stephen D. Evans, and Nicholas P. West. Developing a Raman spectroscopy-based tool to stratify patient response to pre-operative radiotherapy in rectal cancer. *Analyst*, 146(2):581–589, 2021.

[224] Jessica D. Flynn and Jennifer C. Lee. Raman Fingerprints of Amyloid Structures. *Chemical communications (Cambridge, England)*, 54(51):6983, 6 2018.

[225] Kurt W. Short, Susan Carpenter, James P. Freyer, and Judith R. Mourant. Raman spectroscopy detects biochemical changes due to proliferation in mammalian cell cultures. *Biophysical Journal*, 88(6):4274–4288, 2005.

[226] Dorota Puchowicz, Malgorzata Cieslak, Dorota Puchowicz, and Malgorzata Cieslak. Raman Spectroscopy in the Analysis of Textile Structures. *Recent Developments in Atomic Force Microscopy and Raman Spectroscopy for Materials Characterization*, 9 2021.

[227] Wei Huang, Shanshan Wu, Maowen Chen, Liqing Sun, Yongzeng Li, Meizhen Huang, Shaohua Huang, Zhihong Xu, Rong Chen, and Haishan Zeng. Study of both fingerprint and high wavenumber Raman spectroscopy of pathological nasopharyngeal tissues. *Journal of Raman Spectroscopy*, 46(6):537–544, 2015.

[228] Kurt W Short, Susan Carpenter, James P Freyer, and Judith R Mourant. Raman Spectroscopy Detects Biochemical Changes Due to Proliferation in Mammalian Cell Cultures. *Biophysical Journal*, 88:4274–4288.

[229] Runze Li, Dinesh Dhankhar, Jie Chen, Arjun Krishnamoorthi, Thomas C. Cesario, and Peter M. Rentzepis. Identification of live and dead bacteria: A raman spectroscopic study. *IEEE Access*, 7:23549–23559, 2019.

[230] E. C. Le Ru, E. Blackie, M. Meyer, and P. G. Etchegoint. Surface enhanced raman scattering enhancement factors: A comprehensive study. *Journal of Physical Chemistry C*, 111(37):13794–13803, 9 2007.

[231] Yuanqing Chao and Tong Zhang. Surface-enhanced Raman scattering (SERS) revealing chemical variation during biofilm formation: from initial attachment to mature biofilm.

[232] Fanghao Hu, Lixue Shi, and Wei Min. Biological imaging of chemical bonds by stimulated Raman scattering microscopy. *Nature Methods*.

[233] Kideog Bae, Wei Zheng, Ying Ma, and Zhiwei Huang. Real-Time Monitoring of Pharmacokinetics of Antibiotics in Biofilms with Raman-Tagged Hyperspectral Stimulated Raman Scattering Microscopy. *Theranostics*, 9(5), 2019.

[234] Zhiping Hu, Xiaoli Wang, Weirong Wang, Zhenlong Zhang, Huiping Gao, and Yanli Mao. Raman spectroscopy for detecting supported planar lipid bilayers composed of ganglioside-GM1/sphingomyelin/cholesterol in the presence of amyloid-β. *Physical Chemistry Chemical Physics*, 17(35):22711–22720, 7 2015.

[235] George Joseph Holinga. *Sum Frequency Generation Vibrational Spectroscopy of Adsorbed Amino Acids, Peptides, and Proteins at Hydrophilic and Hydrophobic Solid-Water Interfaces*. PhD thesis, University of California, Berkeley, 2010.

[236] Peter Tc So. Two-photon Fluorescence Light Microscopy.

[237] Jérémy Surre, Claude Saint-Ruf, Valérie Collin, Sylvain Orenga, Mahendrasingh Ramjeet, and Ivan Matic. Strong increase in the autofluorescence of cells signals struggle for survival. *Scientific REPORtS* —, 8:12088, 2018.

[238] Yung Jhe Yan, Bo Wen Wang, Chih Man Yang, Ching Yi Wu, and Mang Ou-Yang. Autofluorescence detection method for dental plaque bacteria detection and classification: Example of porphyromonas gingivalis, aggregatibacter actinomycetemcomitans, and streptococcus mutans. *Dentistry Journal*, 9(7), 2021.

[239] Catherine M.C. Volgenant, Monique H. van der Veen, Johannes J. de Soet, and Jacob M. ten Cate. Effect of metalloporphyrins on red autofluorescence from oral bacteria. *European Journal of Oral Sciences*, 121(3 PART1):156–161, 6 2013.

[240] Azhar Zam. *Optical Tissue Differentiation for Sensor-Controlled Tissue-Specific Laser Surgery*. PhD thesis, 2011.

[241] Scott Palmer, Karina Litvinova, Andrey Dunaev, Stewart Fleming, David McGloin, and Ghulam Nabi. Changes in autofluorescence based organoid model of muscle invasive urinary bladder cancer. *Biomedical Optics Express*, 7(4):1193, 2016.

[242] Haihua Zhu, Weiwei Lao, Qingguang Chen, Qixia Zhang, and Hui Chen. A study of the fluorescence characteristics of common cariogenic microorganisms. *International Journal of Clinical and Experimental Medicine*, 8(3):3651, 3 2015.

[243] Sabine Renggli, Wolfgang Keck, Urs Jenal, and Daniel Ritz. Role of autofluorescence in flow cytometric analysis of Escherichia coli treated with bactericidal antibiotics. *Journal of Bacteriology*, 195(18):4067–4073, 2013.

[244] James Addis, Noor Mohammed, Olorunda Rotimi, Derek Magee, Animesh Jha, and Venkataraman Subramanian. Raman spectroscopy of endoscopic colonic biopsies from patients with ulcerative colitis to identify mucosal inflammation and healing. *Biomedical Optics Express*, 7(5):2022, 5 2016.

[245] Sergei V. Bykov, Nataliya S. Myshakina, and Sanford A. Asher. Dependence of Glycine CH2 Stretching Frequencies on Conformation, Ionization State, and Hydrogen Bonding. *The journal of physical chemistry. B*, 112(18):5803, 5 2008.

[246] Miguel A. Pérez-Osorio, Qianqian Lin, Richard T. Phillips, Rebecca L. Milot, Laura M. Herz, Michael B. Johnston, and Feliciano Giustino. Raman Spectrum of the Organic-Inorganic Halide Perovskite CH3NH3PbI3 from First Principles and High-Resolution Low-Temperature Raman Measurements. *Journal of Physical Chemistry C*, 122(38):21703–21717, 2018.

[247] Irina Mihalcescu, Mathilde Van-Melle Gateau, Bernard Chelli, Corinne Pinel, and Jean Luc Ravanat. Green autofluorescence, a double edged monitoring tool for bacterial growth and activity in micro-plates. *Physical Biology*, 12(6), 2015.

[248] Juan Carlos Castro Alcántara, Mariana Cerda Zorrilla, Lucia Cabriales, Luis Manuel León Rossano, and Mathieu Hautefeuille. Low-cost formation of bulk and localized polymer-derived carbon nanodomains from polydimethylsiloxane. *Beilstein Journal of Nanotechnology*, 6(1):744–748, 2015.

[249] Chen Zhu, Nianan He, Tao Cheng, Honglue Tan, Yongyuan Guo, Desheng Chen, Mengqi Cheng, Zhi Yang, and Xianlong Zhang. Ultrasound-Targeted Microbubble Destruction Enhances Human β-Defensin 3 Activity Against Antibiotic-Resistant Staphylococcus Biofilms.

[250] Fernando Baquero and Bruce R. Levin. Proximate and ultimate causes of the bactericidal action of antibiotics. *Nature Reviews Microbiology*, 19(2):123–132, 2021.

[251] MIC & MBC Testing For New Product Formulations — Q Laboratories.

[252] Beata Kowalska-Krochmal and Ruth Dudek-Wicher. pathogens The Minimum Inhibitory Concentration of Antibiotics: Methods, Interpretation, Clinical Relevance. 2021.

[253] Meredith A Hackel, Masakatsu Tsuji, Yoshinori Yamano, Roger Echols, James A Karlowsky, and Daniel F Sahm. Reproducibility of broth microdilution MICs for the novel siderophore cephalosporin, cefiderocol, determined using iron-depleted cation-adjusted Mueller-Hinton broth. 2019.

[254] Mesrop Ayrapetyan, Tiffany Williams, and James D. Oliver. Relationship between the viable but nonculturable state and antibiotic persister cells. *Journal of Bacteriology*, 200(20), 10 2018.

[255] Merilin Rosenberg, Nuno F. Azevedo, and Angela Ivask. Propidium iodide staining underestimates viability of adherent bacterial cells. *Scientific Reports*, 9(1):1–12, 2019.

[256] Agnieszka Latka and Zuzanna Drulis-Kawa. Advantages and limitations of microtiter biofilm assays in the model of antibiofilm activity of Klebsiella phage KP34 and its depolymerase. *Scientific Reports*, 10(1):1–12, 2020.

[257] Christina Wilson, Rachel Lukowicz, Stefan Merchant, Helena Valquier-Flynn, Jeniffer Caballero, Jasmin Sandoval, Macduff Okuom, Christopher Huber, Tessa Durham Brooks, Erin Wilson, Barbara Clement, Christopher D Wentworth, and Andrea E Holmes. Quantitative and Qualitative Assessment Methods for Biofilm Growth: A Mini-review HHS Public Access. *Res Rev J Eng Technol*, 6(4), 2017.

[258] Nianan He, Jian Hu, Huayong Liu, Tao Zhu, Beijian Huang, Xueqin Wang, Yang Wu, Wenping Wang, and Di Qu. Enhancement of vancomycin activity against biofilms by using ultrasound-targeted microbubble destruction. *Antimicrobial Agents and Chemotherapy*, 55(11):5331–5337, 11 2011.

[259] Kirby R Lattwein, Himanshu Shekhar, Joop J P Kouijzer, Willem J B Van Wamel, Christy K Holland, and Klazina Kooiman. Sonobactericide: An Emerging Treatment Strategy for Bacterial Infections. *Ultrasound in Medicine & Biology*, 46:193–215, 2020.

[260] Megha Goshi, Nicholas Pytel, and Tamer Elbayoumi. Partially Polymerized Phospholipid Vesicles for Efficient Delivery of Macromolecules. *Pharmaceutical Nanotechnology: Basic Protocols, Methods in Molecular Biology*, 2000:445–490, 2019.

[261] A. Vallance Jones. Infra-red and Ram an spectra of diacetylene. 1952.

[262] Masataka Ikeshima, Masashi Mamada, Tsuyoshi Minami, Shizuo Tokito, and Shuji Okada. Synthesis and solid-state polymerization of diacetylene derivatives directly substituted with a phenylcarbazole moiety. *Polymer Journal*, 48(10):1013–1018, 2016.

[263] Avanti Polar Lipids 23:2 Diyne PC [DC(8,9)PC], 2023.

[264] Guoting Qin, Zheng Li, Rongmin Xia, Feng Li, Brian E O Neill, Jessica T Goodwin, Htet a Khant, Wah Chiu, and King C Li. Partially polymerized liposomes. 22(15), 2012.

[265] Naing Tun Thet, William David Jamieson, Maisem Laabei, June D. Mercer-Chalmers, and A. Toby A. Jenkins. Photopolymerization of polydiacetylene in hybrid liposomes: Effect of polymerization on stability and response to pathogenic bacterial toxins. *Journal of Physical Chemistry B*, 118(20):5418–5427, 2014.

[266] Min Jung Chun, Yeol Kyo Choi, and Dong June Ahn. Formation of nanopores in DiynePC-DPPC complex lipid bilayers triggered by on-demand photo-polymerization. *RSC Advances*, 8(49):27988–27994, 2018.

[267] Amichai Yavlovich, Brandon Smith, Kshitij Gupta, Robert Blumenthal, and Anu Puri. Light-sensitive lipid-base Light-sensitive lipid-based nanoparticles for drug delivery: design principles and future considerations for biological applications. *Molecular Membrane Biology*, 27(7):364–381, 2010.

[268] Parham Sahandi Zangabad, Soroush Mirkiani, Shayan Shahsavari, Behrad Masoudi, Maryam Masroor, Hamid Hamed, Zahra Jafari, Yasamin Davatgaran Taghipour, Hura Hashemi, Mahdi Karimi, and Michael R Hamblin. Stimulus-responsive liposomes as smart nanoplatforms for drug delivery applications HHS Public Access. *Nanotechnol Rev*, 7(1):95–122, 2018.

[269] Kosuke Dodo, Katsumasa Fujita, and Mikiko Sodeoka. Raman Spectroscopy for Chemical Biology Research. *Journal of the American Chemical Society*, 144(43):19651–19667, 11 2022.

[270] Laura Kay Marsh. Pt (IV) anticancer prodrugs and liposomal encapsulation Laura Kay Marsh University of Oxford A thesis submitted for the degree of Doctor of Philosophy. (August), 2022.

[271] Limin Zhai, Jinping Zhao, Mei Zhao, Yanjing Chen, and Longjun Zhang. Encapsulation and releasing of calcein by spontaneously formed zwitterionic/anionic vesicle without separation. *Journal of Dispersion Science and Technology*, 28(3):455–461, 2007.

[272] Chandrashekar Janakiram and Bruce A Dye. A public health approach for prevention of periodontal disease.